Design and development of printed acoustic sensor

Rubaiyet Iftekharul Haque

NNT : *2015 EMSE 0794*

THÈSE

présentée par

Rubaiyet Iftekharul HAQUE

pour obtenir le grade de
Docteur de l'École Nationale Supérieure des Mines de Saint-Étienne

Spécialité : Microélectronique

DESIGN ET DÉVELOPPEMENT D'UN CAPTEUR ACOUSTIQUE IMPRIMÉ

soutenue au Centre Microélectronique de Provence à Gardanne, le 20 Octobre 2015

Membres du jury

Président :	Michelle SERGENT	Professeur, LISA, Aix-Marseille Université, France
Rapporteurs :	Dago de LEEUW	Professeur, Max Planck Institute for Polymer Research, Mainz, Allemagne
	Zine FELLAH	Chargé de Recherche, LMA-CNRS, Marseille, France
Examinateurs :	Edsger SMITS	Senior Research Scientist, Holst Centre - TNO, Eindhoven, Pays-Bas
Directeur de thèse :	Patrick BENABEN	Professeur, EMSM-SE, Gardanne, France
Co-encadrant :	Xavier BODDAERT	Professeur, EMSM-SE, Gardanne, France
Co-encadrant :	Christophe LOUSSERT	Vice President, TAGSYS RFID, La Ciotat, France
Invités:	Erick OGAM	Ingénieur de Recherche, LMA-CNRS, Marseille, France

Spécialités doctorales	Responsables :	Spécialités doctorales	Responsables
SCIENCES ET GENIE DES MATERIAUX	K. Wolski Directeur de recherche	MATHEMATIQUES APPLIQUEES	O. Roustant, Maître-assistant
MECANIQUE ET INGENIERIE	S. Drapier, professeur	INFORMATIQUE	O. Boissier, Professeur
GENIE DES PROCEDES	F. Gruy, Maître de recherche	IMAGE, VISION, SIGNAL	JC. Pinoli, Professeur
SCIENCES DE LA TERRE	B. Guy, Directeur de recherche	GENIE INDUSTRIEL	A. Dolgui, Professeur
SCIENCES ET GENIE DE L'ENVIRONNEMENT	D. Graillot, Directeur de recherche	MICROELECTRONIQUE	S. Dauzere Peres, Professeur

EMSE : Enseignants-chercheurs et chercheurs autorisés à diriger des thèses de doctorat (titulaires d'un doctorat d'État ou d'une HDR)

ABSI	Nabil	CR	Génie industriel	CMP
AVRIL	Stéphane	PR2	Mécanique et ingénierie	CIS
BALBO	Flavien	PR2	Informatique	FAYOL
BASSEREAU	Jean-François	PR	Sciences et génie des matériaux	SMS
BATTAIA-GUSCHINSKAYA	Olga	CR		FAYOL
BATTON-HUBERT	Mireille	PR2	Sciences et génie de l'environnement	FAYOL
BERGER DOUCE	Sandrine	PR2	Sciences de gestion	FAYOL
BIGOT	Jean Pierre	MR(DR2)	Génie des Procédés	SPIN
BILAL	Essaid	DR	Sciences de la Terre	SPIN
BLAYAC	Sylvain	MA(MDC)	Microélectronique	CMP
BOISSIER	Olivier	PR1	Informatique	FAYOL
BONNEFOY	Olivier	MA(MDC)	Génie des Procédés	SPIN
BORBELY	Andras	MR(DR2)	Sciences et génie des matériaux	SMS
BOUCHER	Xavier	PR2	Génie Industriel	FAYOL
BRODHAG	Christian	DR	Sciences et génie de l'environnement	FAYOL
BRUCHON	Julien	MA(MDC)	Mécanique et ingénierie	SMS
BURLAT	Patrick	PR1	Génie Industriel	FAYOL
COURNIL	Michel	PR0	Génie des Procédés	DIR
DARRIEULAT	Michel	IGM	Sciences et génie des matériaux	SMS
DAUZERE-PERES	Stéphane	PR1	Génie Industriel	CMP
DEBAYLE	Johan	CR	Image Vision Signal	CIS
DELAFOSSE	David	PR0	Sciences et génie des matériaux	SMS
DELORME	Xavier	MA(MDC)		FAYOL
DESRAYAUD	Christophe	PR1	Mécanique et ingénierie	SMS
DOLGUI	Alexandre	PR0	Génie Industriel	FAYOL
DRAPIER	Sylvain	PR1	Mécanique et ingénierie	SMS
FAVERGEON	Loïc	CR	Génie des Procédés	SPIN
FEILLET	Dominique	PR1	Génie Industriel	CMP
FRACZKIEWICZ	Anna	DR	Sciences et génie des matériaux	SMS
GARCIA	Daniel	MR(DR2)	Génie des Procédés	SPIN
GAVET	Yann	MA(MDC)	Image Vision Signal	CIS
GERINGER	Jean	MA(MDC)	Sciences et génie des matériaux	CIS
GOEURIOT	Dominique	DR	Sciences et génie des matériaux	SMS
GRAILLOT	Didier	DR	Sciences et génie de l'environnement	SPIN
GROSSEAU	Philippe	DR	Génie des Procédés	SPIN
GRUY	Frédéric	PR1	Génie des Procédés	SPIN
GUY	Bernard	DR	Sciences de la Terre	SPIN
HAN	Woo-Suck	MR	Mécanique et ingénierie	SMS
HERRI	Jean Michel	PR1	Génie des Procédés	SPIN
KERMOUCHE	Guillaume	PR2	Mécanique et Ingénierie	SMS
KLOCKER	Helmut	DR	Sciences et génie des matériaux	SMS
LAFOREST	Valérie	MR(DR2)	Sciences et génie de l'environnement	FAYOL
LERICHE	Rodolphe	CR	Mécanique et ingénierie	FAYOL
LI	Jean-Michel		Microélectronique	CMP
MALLIARAS	Georges	PR1	Microélectronique	CMP
MAURINE	Philippe	Ingénieur de recherche		CMP
MOLIMARD	Jérôme	PR2	Mécanique et ingénierie	CIS
MONTHEILLET	Frank	DR	Sciences et génie des matériaux	SMS
MOUTTE	Jacques	CR	Génie des Procédés	SPIN
NEUBERT	Gilles	PR		FAYOL
NIKOLOVSKI	Jean-Pierre	Ingénieur de recherche		CMP
NORTIER	Patrice	PR1		SPIN
OWENS	Rosin	MA(MDC)		CMP
PICARD	Gauthier	MA(MDC)		FAYOL
PIJOLAT	Christophe	PR0	Génie des Procédés	SPIN
PIJOLAT	Michèle	PR1	Génie des Procédés	SPIN
PINOLI	Jean Charles	PR0	Image Vision Signal	CIS
POURCHEZ	Jérémy	MR	Génie des Procédés	CIS
ROBISSON	Bruno	Ingénieur de recherche		CMP
ROUSSY	Agnès	MA(MDC)	Génie industriel	CMP
ROUSTANT	Olivier	MA(MDC)	Mathématiques appliquées	FAYOL
ROUX	Christian	PR	Image Vision Signal	CIS
STOLARZ	Jacques	CR	Sciences et génie des matériaux	SMS
TRIA	Assia	Ingénieur de recherche	Microélectronique	CMP
VALDIVIESO	François	PR2	Sciences et génie des matériaux	SMS
VIRICELLE	Jean Paul	DR	Génie des Procédés	SPIN
WOLSKI	Krzystof	DR	Sciences et génie des matériaux	SMS
XIE	Xiaolan	PR1	Génie industriel	CIS
YUGMA	Gallian	CR	Génie industriel	CMP

ENISE : Enseignants-chercheurs et chercheurs autorisés à diriger des thèses de doctorat (titulaires d'un doctorat d'État ou d'une HDR)

BERGHEAU	Jean-Michel	PU	Mécanique et Ingénierie	ENISE
BERTRAND	Philippe	MCF	Génie des procédés	ENISE
DUBUJET	Philippe	PU	Mécanique et Ingénierie	ENISE
FEULVARCH	Eric	MCF	Mécanique et Ingénierie	ENISE
FORTUNIER	Roland	PR	Sciences et Génie des matériaux	ENISE
GUSSAROV	Andrey	Enseignant contractuel	Génie des procédés	ENISE
HAMDI	Hédi	MCF	Mécanique et Ingénierie	ENISE
LYONNET	Patrick	PU	Mécanique et Ingénierie	ENISE
RECH	Joël	PU	Mécanique et Ingénierie	ENISE
SMUROV	Igor	PU	Mécanique et Ingénierie	ENISE
TOSCANO	Rosario	PU	Mécanique et Ingénierie	ENISE
ZAHOUANI	Hassan	PU	Mécanique et Ingénierie	ENISE

Mise à jour : 11/05/2015

DESIGN AND DEVELOPMENT OF PRINTED ACOUSTIC SENSOR

Rubaiyet Iftekharul HAQUE

Doctoral Thesis

Flexible Electronics Department
Campus Georges Charpak, Provence
École Nationale Supérieure des Mines de Saint-Étienne
Gardanne, France

2015

ABSTRACT

An acoustic transducer is a device that generally generates response signal due to the change in acoustic pressure, which can be used for different applications, such as sound recording, under water object detection, hearing aids etc. An acoustic sensor can also be employed for other industrial applications as well. In recent time, an industrial research has been conducted to demonstrate that the capacitive acoustic sensor could be integrated with radio frequency identification (RFID) tag system to improve its geolocalization. However, such application requires low cost production of capacitive acoustic transducer with appropriate sensitivity and selectivity. In this regard, new design to develop the capacitive acoustic transducer has been proposed that consists of a central cylindrical rigid backplate with small radius surrounded by a flat annular cavity under a vibrating membrane clamped at its periphery. During this work, revolutionary printing techniques have been used for the device fabrication.

The optimization of the design of the transducer requires the clear understanding of the effects of different factors on the output responses of the sensor. During this work, output responses of capacitive acoustic transducer, such as membrane displacement, quality factor, and capacitance variation are considered to evaluate the sensor design. The six device parameters taken into consideration are membrane radius, backplate radius, cavity height, air-gap, membrane tension and membrane thickness. The effects of these factors on the output responses of the transducer are investigated using an integrated methodology that combines numerical simulation and Design of Experiments (DOE). A series of numerical experiments is conducted to obtain output responses for different combinations of device parameters using finite element methods (FEM). Response surface method is used to identify the significant factors and to develop the empirical models for the output responses. Finally, these results are utilized to determine the optimum device parameters using multi-criteria optimization with desirability function. Thereafter, the validating experiments are designed and deployed using the numerical simulation to crosscheck the results.

During this work, capacitive acoustic transducers have been fabricated by combining three-dimensional (3D) printing and direct write 2D inkjet technique. Patterned bottom structure with rigid backplate and cavity have been fabricated directly by 3D printing method and

then inkjet printing technique was used to print conductive layer. A novel approach has been used to fabricate diaphragm for the acoustic sensor as well, where conductive layer was printed on pre-stressed thin organic film. The resulting structure contains electrically conductive diaphragm positioned at a distance from a fixed bottom electrode. The diaphragm deflects in response to the acoustic pressure and induces variation of the capacitance between the diaphragm and the fixed electrode. The fabricated device exhibits adequate sensitivity and selectivity at its first resonant frequency with quality factor in accordance with the device requirement.

Printed piezoelectric sensor could be an alternative potential candidate to develop acoustic transducer but inkjet-printable piezoelectric ink are not yet commercially available. Therefore, within the framework of this work, stable inkjet-printable polyvinylidene fluoride – trifluoroethylene (PVDF-TrFE) ink has been developed. PVDF-TrFE is a copolymer that exhibits piezo-, pyro- and ferro-electric properties. Experiments show that the vapor pressure and viscosity of the solvent strongly influence the quality of the printed layer. Finally, the inkjet-printed PVDF-TrFE films were characterized to investigate their morphology, crystallinity and piezoelectric properties. Crystallographic studies confirm the presence of β-phase. The results were quite promising, although further improvements of the ink and printing process are required before stepping towards inkjet-printed piezoelectric based device fabrication.

Keywords: Acoustic sensor; resonator; numerical simulation; design of experiment; printed electronics; 3D printing, piezoelectric polymer; ink formulation;

ACKNOWLEDGEMENTS

This work has been performed in partnership with TAGSYS RFID and carried out at the *Centre Microélectronique de Provence - Georges Charpak* (CMP-GC) of the École nationale supérieure des Mines de Saint-Étienne (ENSM-SE), Gardanne, France. During my work, I've realized that my PhD would not have ever been possible without the help of my family members, friends and colleagues. I appreciate all of their supports to cope with the toughest time of my life.

First of all, I oblige my deepest gratitude to my supervisor Professor Xavier BODDAERT and my thesis director Professor PatricK BENABEN for giving me the opportunity to work in this interesting field of "Printed Electronics", their advices and encouragement. I wish to express my sincere thanks to my industrial advisor Christophe LOUSSERT, manager Christophe MOUTOT and others from TAGSYS for their support throughout my work. I would also like to thank everyone involved in SPINNAKER project; specially, Petr Honzik and Professor Stephane DURAND from *Laboratoire d'Acoustique de l'Université du Maine (*LAUM) for their time and help regarding theory, basics and basic design of the acoustic sensor.

Working in the CMP, and more specifically in *Flexible Electronics Department* (PS2), made my work very interdisciplinary. I want to thanks Sylvain BLAYAC, Mohammed SAADAOUI, Rémy VIÉ, Oussama BENZAIM, Jessica MAZUIR, Abdel YAKOUB, Roger DELATTRE for sharing their knowledge and experiences, and their helps. I am also grateful to Henda BASTI, Malika BELLA, Clément TALAGRAND for some wonderful time; it would have been a lonely lab without them. Many thanks to Cyril CALMES and Thierry CALILLONI for trainings and for building all kinds of parts and tools needed during this work.

I will here take the opportunity to acknowledge Eric OGAM from *Laboratoire de Mécanique et d'Acoustique* (LMA), CNRS for his time and helps with the practical experimental issues related to the acoustics measurements, Professor Michelle SERGENT from *Laboratoire Instrumentation Sciences Analytiques* (LISA), Aix-Marseille Université for her time, guidance and helps for the development of the design of experiment during

this work, and Professor Andras BORBELY from Mines Saint-Etienne for his help with XRD measurement and analysis. My appreciation also goes to my colleagues at CMP. In particular I acknowledge Jakey BLUE for helpful discussions in terms of design of experiment. Many thanks to the entire staff at the Flexible Electronics Department (PS2); it has been a pleasure to work with all of you!

Last but not least, I want to express my gratitude to my parents for all their supports, and would like to dedicate this dissertation to my father and mother.

TABLE OF CONTENTS

LIST OF PUBLICATIONS

Journals (with peer review):

1. Fabrication of capacitive acoustic resonator combining 3D printing and 2D inkjet printing techniques, Rubaiyet Iftekharul Haque, Erick Ogam, Christophe Loussert, Patrick Benaben, Xavier Boddaert, Sensors, 2015, 15(10), 26018-26038; doi:10.3390/s151026018.
2. Inkjet printing of high molecular weight PVDF-TrFE for flexible electronics, Rubaiyet Iftekharul Haque, Rémy Vié, Michel Germainy, Laurie Valbin, Patrick Benaben, Xavier Boddaert, Flexible and Printed Electronics, 2016, 1(1), 015001; doi: 10.1088/2058-8585/1/1/015001.
3. Optimization of capacitive acoustic resonant sensor using numerical simulation and design of experiment, Rubaiyet Iftekharul Haque, Christophe Loussert, Michelle Sergent, Patrick Benaben, Xavier Boddaert, Sensors, 2015, 15(4), 8945-8967; doi: 10.3390/s150408945.

Oral presentations:

1. Development of an inkjetable fluid with high molecular weight Polyvinylidene-trifluoroethylene (PVDF-TrFE) piezoelectric copolymer, Rémy Vié, Rubaiyet Iftekharul Haque, Michel Germainy, Xavier Boddaert, E-MRS Conference, 11 to 15 May 2015, Lille, France.
2. Use of numerical study and design of experiment to optimize acoustic sensor, Rubaiyet Iftekharul Haque, Chistophe Loussert, Michelle Sergent, Xavier Boddaert, Patrick Benaben, SENSO Conference, 22nd to 24th October 2014, Gardanne, France.

Poster presentations:

1. Inkjet printing of polyvinylidene fluoride – trifluoroethylene (PVDF-TrFE) layer, Rubaiyet Iftekharul Haque, Michel Germainy, Rémy Vié, Xavier Boddaert, Patrick Benaben, IPSO Conference, 20th to 21st November 2014, Gardanne,
2. Inkjet printing of high molecular weight PVDF-TrFE copolymer: from ink formulation to the characterization of deposited thin films, Rubaiyet Iftekharul Haque, Michel Germainy, Rémy Vié, Laurie Valbin, Xavier Boddaert, Patrick Benaben, Piezoelectric Micro and Nano Structures and their Applications, 25th – 26th September 2014, Blois, France.
3. Optimization of Acoustic Sensor Using Finite Element and Design of Experiment, Rubaiyet Haque, Chistophe Loussert, Michelle Sergent, Xavier Boddaert, Patrick Benaben, EuroSensors, 7th – 10th September 2014, Brescia, Italy.

Patent:

1. Réalisation d'objets électroniques par utilisation combinée de l'impression 3D et de l'impression par jet de matière, Rubaiyet HAQUE, Xavier BODDAERT, Cyril

CALMES, Patrick BENABEN, French Patent Application No. 15/51969 of 10 March 2015.

CHAPTER 1

INTRODUCTION

This work was conducted within the framework of 'Conventions Industrielles de Formation par la REcherche (CIFRE)' PhD thesis, initiated by the French Ministry of Higher Education and Research and run by the 'Association Nationale de la Recherche et de la Technologie (ANRT)'. CIFRE stands for the industrial agreement of training through research, and aims towards the research activities on the challenges of company strategy and needs. This thesis work was focused on the development of a new kind of acoustic sensor using emerging printing techniques.

The present chapter provides the general introduction and background of this thesis. Details of the motivations of the thesis both from the industrial and academic point of views are described, and the key challenges are highlighted. Finally, the chapter ends with a presentation of the organization of this thesis to guide the reader along the research roadmap adopted in order to accomplish the objectives of this thesis.

1.1. Background

A sensor is a converter, which produces an output signal in response to some input quantity including physical quantities, such as temperature and pressure, and chemical or biological quantities. Usually the output response is electrical, such as an analog voltage or current, a stream of digital voltage pulses, or possibly an oscillatory voltage [1], [2]. Sensors are used in a wide variety of applications and the significance of this technology is growing constantly. Everyday new possibilities of sensor applications are identified, which broaden the scope of the technology.

Amongst different types of sensors, an acoustic sensor is a transducer that converts acoustic energy into electrical energy. The working principle of an acoustic sensor is similar to that of a pressure sensor. An acoustic transducer provides analog output that is proportional to the variation of acoustic pressure acting upon a flexible diaphragm. Most familiar examples of acoustic sensors are microphone, earphone etc. There are different types of acoustic sensors: namely, piezoelectric, piezoresistive and capacitive [3].

For many years, acoustic sensors have been used in civilian and military applications, such as in cellular phones, hearing aids, computers and in high quality studio microphones for sound recording [4], sonar for underwater objects detection [5] and in the acoustic sensor systems for target acquisition and surveillance purposes [6]. To date, many acoustic sensors have been developed and commercialized. However, the majority of these are targeted for

audio applications with nearly uniform sensitivity over a relatively wide range of frequencies in the human hearing range, 20 Hz – 20 kHz.

Different materials have been used to fabricate acoustic transducer depending on their types. In terms of electrical properties, metals are appropriate for diaphragm and backplate application. However, metals are vulnerable to the aggressive thermal and chemical environment during device manufacturing process, as well as less resistant to corrosion during their lifetime. Therefore, to overcome these problems, most of the microelectromechanical systems (MEMS) sensors and actuators are fabricated on silicon substrates using conventional subtractive methods such as photolithographic patterning and surface micromachining. Occasionally, organic thin films with desired mechanical properties that are chemically more robust have been used as support membrane to fabricate diaphragm for the transducer [7].

Although, subtractive method, such as photolithographic patterning, is a well-established technique to fabricate acoustic transducers, this process generally involves various deposition, masking and cleaning or etching processes to build up a three-dimensional structure. Moreover, this technique generally exhibits higher production cost and process time, and generates large volumes of hazardous waste that damages the environment. On the other hand, vacuum deposition technique for electronic devices fabrication is energy intensive and provides low resolution [8]. Therefore, to meet the global market demand for high quality, cheap electronic components and to reduce the materials loss, quest for an innovative technique to fabricate electronics leads to novel materials deposition and patterning processes such as printing techniques.

Printing technique has emerged as a revolutionary way to develop electrical devices. This technology provides new opportunities for microelectronics. In recent times, cost-effective and reliable printing technologies, such as flexography, offset lithography, gravure, screen and inkjet etc., have received increasing amount of interest due to their ability to pattern a variety of functional materials, both organic and inorganic, on various type of substrates including flexible media [9]. Each technology has its advantages and disadvantages.

Printing techniques employ the printing of conductive, insulating and semi-conductive ink directly without the etching stage. Several studies show that printing processes could be an efficient and low cost way to produce different types of electronic components, such as

printed circuits, displays (OLEDs), RFID antennas, batteries, sensors etc., using conductive inks or organic polymers. Light weight and increased robustness, as the components are flexible, are the advantages of printed electronics [9]; as a result they withstand heat, rough handling and harsh environmental conditions more than the conventional electronics [10]–[12].

Amongst the well-developed techniques, inkjet printing is a contact free additive printing technique for positioning droplets of liquid material with high precision onto a substrate. Inkjet printing operates at room temperature in ambient conditions and involves the use of fewer hazardous chemicals. The shift from high vacuum, high purity manufacturing to printing processes reduces the product manufacturing cost. Moreover, this technique is flexible, versatile and can be setup with relatively low effort, as no masks or screens are needed [8], [13], [14]. Therefore, inkjet printing technique could be a potential alternative for microelectronics fabrication because of its high precision printing ability, cost efficiency and less waste production. However, further research regarding materials may still be required to achieve the finished products with greater reliability and performances; the advantages of exploring such a transition will provide a much wider array of applications [15]. Figure 1.1 shows the inkjet-printed circuit on flexible substrate developed to connect electronic components.

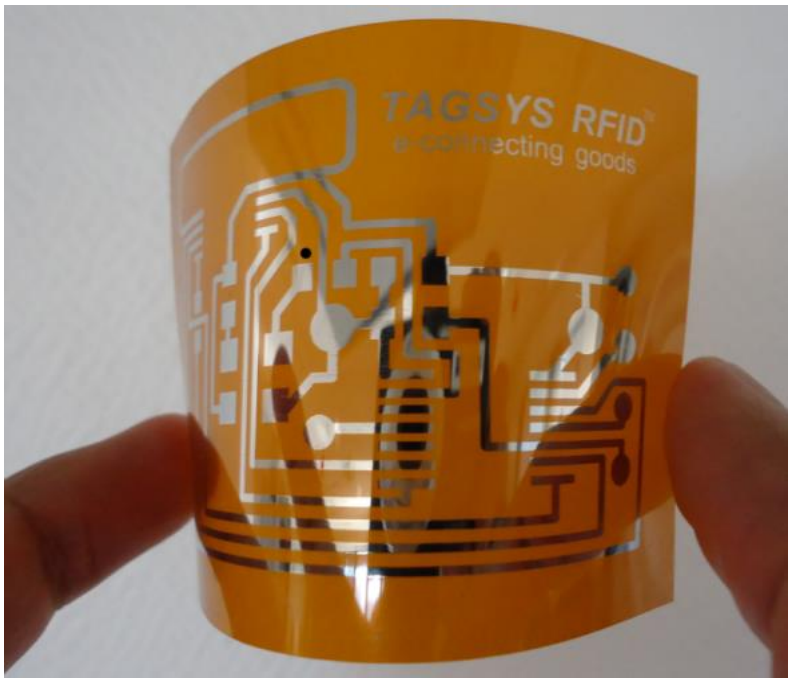

Figure 1.1: *Inkjet-printed circuit on flexible polyimide substrate.*

Furthermore, inkjet printing technology reduces the processing steps in comparison to conventional photolithography, and thus the processing complexity. Generally photolithographic technique is composed of six steps, namely, coating the base layer with several materials, masking to transfer the circuitry patterns from a dedicated mask to the substrate, and finally etching and stripping [16]. Whereas, inkjet printing is limited to the pattern direct-printing on the base layer and the subsequent curing of the deposited ink in order to remove solvents (Figure 1.2), to initiate the film cohesion and to achieve optimized functionality of the printed layer [17]. Curing step can be carried out using either conventional oven or other selective techniques such as laser, microwave, joule heating [18]–[20] and photonic sintering technique [8], [21], [22].

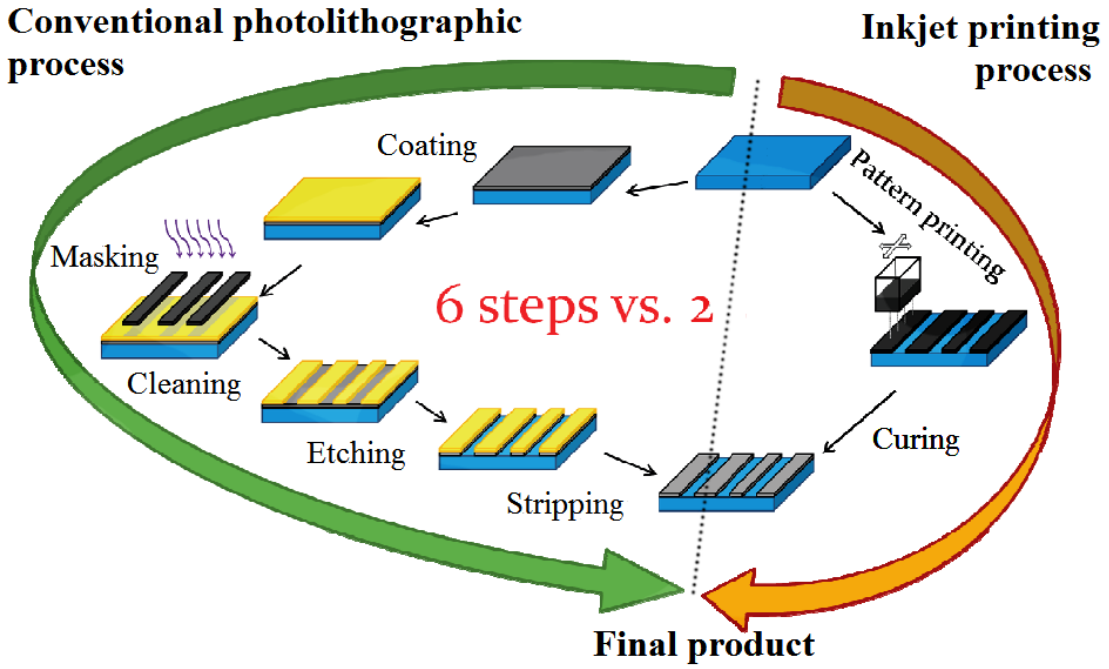

Figure 1.2: *Comparison between conventional photolithography and inkjet printing technique to fabricate a microelectronic product [17].*

The ability to design features without the requirement of additional process step enhances the yield. However, inkjet offers lower resolution compared to photolithographic technique [23], [24]. The resolution of inkjet printing is around tens of microns, although this resolution can be improved by optimizing the ink, printing substrate, drop volume, printing speed and drop spacing [24]. Generally, inkjet printing technique is more suitable for soluble materials with low-viscosity, such as organic semiconductors, whereas difficulties due to nozzle clogging occur when high-viscosity materials, such as organic dielectrics,

and ink based on dispersed particles, such as inorganic metal inks are used [14]. During inkjet printing process, ink is deposited through droplets, and thus occasionally provides reduced thickness and homogeneity. This technique normally offers throughput of around 100 m^2/h [23]. Moreover, the simultaneous use of many nozzles could improve the productivity.

Furthermore, inkjet printing can be combined with other printing techniques to manufacture new low-end high-performance electronic products on larger but cheaper substrates including flexible substrates. Printed electronics can also be used alone or in combination with conventional microelectronic components such as silicon chips for a range of different applications [16].

1.2. Thesis objectives

1.2.1. Technological objectives

As a leading provider of the item-level inventory management systems that streamline the supply chain, TAGSYS RFID, has already secured a leadership position in the global radio frequency identification technology (RFID) industry by delivering innovative and highly reliable systems [25]. In recent times, TAGSYS RFID is working on different technological advancement to improve the RFID technology, namely, static reading and geolocalization of RFID tags.

In this regard, TAGSYS RFID has built up a Research and Development project named "Spinnaker" with six industrial and eight academic partners [26]. Within this project, TAGSYS RFID is developing a system to couple the ultra-high frequency (UHF) RFID tags with acoustic sensor to improve their localization. This new approach requires the development of a new acoustic sensor at low cost to provide a highly integrated solution.

The specifications of the acoustic sensor were defined by the Spinnaker Consortium. According to the specifications, acoustic transducer should be capacitive with nominal capacitance value of around 0.5 to 3 pF so that it can be used as an active or passive device. For passive application, the sensor should provide capacitance variation of about 1 to 10 fF for 80 dB_{SPL} (equal to 0.2 Pa) incident acoustic pressure, whereas active application of the transducer requires to generate output voltage of 2 to 3 mV under 80 dB_{SPL} incident acoustic

pressure. Furthermore, the sensor should be sensitive only at certain frequency to have good selectivity.

The working principle of the proposed acoustic resonant sensor is similar to that of a condenser microphone with a difference in the response sensitivity. Generally, the expected bandwidth for the ideal microphone is flat over the large frequency range, whereas TAGSYS RFID is interested in an acoustic transducer that will provide strong detectable sensitivity at certain frequency, which is the first resonant frequency of the system. This kind of sensor is generally known as resonant acoustic sensor or acoustic resonator. However, such device is not available in the market. The comparison between the response sensitivity of ideal microphone and the desired response sensitivity of acoustic resonator under development is illustrated in Figure 1.3.

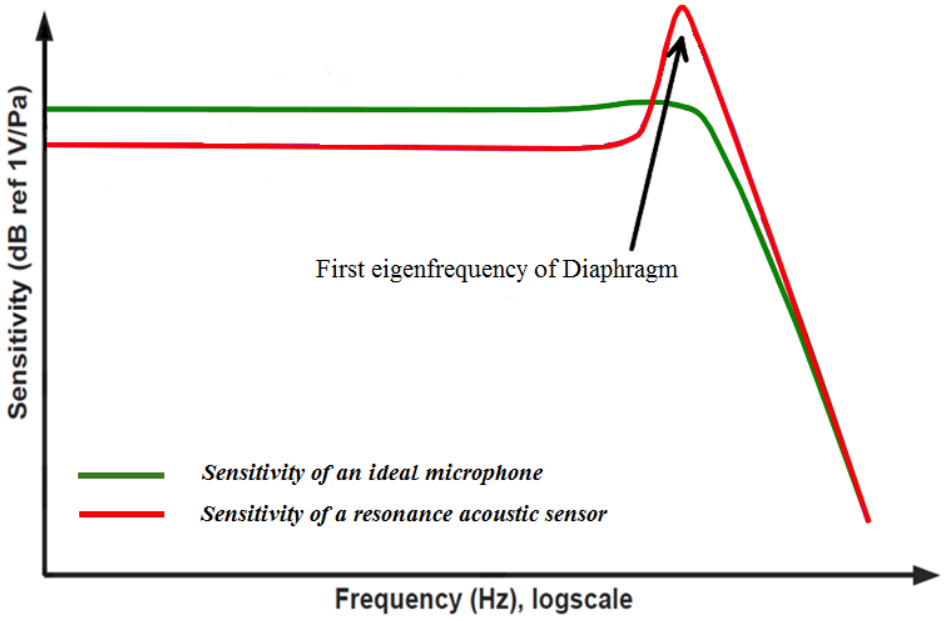

Figure 1.3: *Comparison between sensitivity of ideal condenser microphone and that of acoustic resonator proposed by Spinnaker consortium.*

To meet the requirement, a new basic design concept of the sensor has been proposed by Laboratoire d'Acoustique de l'Université du Maine (LAUM). To reduce the production cost, processing complexity as well as to take advantage of new emerging techniques, TAGSYS RFID has decided to focus on the development of the acoustic transducer using printing technologies, such as inkjet printing, with the collaboration of Centre

Microélectronique de Provence (CMP), École nationale supérieure des Mines de Saint-Étienne (ENSM-SE), Gardanne, France.

Therefore from the technological point of view, the goal of this thesis is to design and develop an acoustic resonant transducer having good sensitivity and selectivity at a fixed frequency using printing techniques based on the basic design concept. However, several issues have to be addressed to achieve this goal, namely the investigation of the suitability of the proposed acoustic transducer design to develop the capacitive acoustic resonator with good sensitivity and selectivity. Other major challenges are to inquire the possibilities of manufacturing such a device based on this design using printing technique and to achieve the targeted device specifications.

1.2.2. Scientific objectives

The goal of this thesis from an academic point of view is to contribute to the application of printing electronics technologies for device fabrication, to understand the difficulties regarding the processing complexity, and to study the behavior of the printed acoustic sensor using numerical simulation and design of experiment (DOE), and different characterization techniques. Therefore the aim is to utilize the available printing techniques and to develop processing steps to fabricate acoustic transducer that can be used as an active or as a passive sensor.

The initial scientific goal of this thesis is to understand the printing technology and the parameters related to printing of metal nanoparticle based ink and polymeric ink on different drop-on-demand (DoD) inkjet printing apparatuses, namely: Dimatix and Ceradrop inkjet printers, along with three dimensional (3D) printing system available in Centre Microélectronique de Provence (CMP). Further goal is to understand the physics involved in the acoustic sensor and apply the knowledge to fabricate printed electronics devices.

In addition to capacitive acoustic sensor, piezoelectric acoustic sensor could be an attractive alternative for acoustic resonator application, because the piezoelectric transducer directly generates an output voltage due to membrane deformation without the requirement of any additional signal conditioning circuit. Moreover, as the piezoelectric transducer does not consist of a backplate electrode, the low damping effect should lead to larger membrane displacement and thus should improve the sensitivity. Therefore, another aim is to

investigate the possibilities to develop printed piezoelectric acoustic transducer. However, suitable piezoelectric ink for DoD inkjet printing system is not commercially available. Hence, the first challenging step of this part is to develop stable inkjet printable piezoelectric polymeric ink using poly(vinylidenefluoride-trifluoroethylene) (*PVDF-TrFE*), as several parameters related to ink properties and printing system need to be taken into account. Moreover the development of the building blocks for the piezoelectric sensor, such as printing of homogenous PVDF-TrFE layer and deposition of electrodes, has to be optimized, prior to the development of the transducer.

1.3. Summary

Printed electronics technologies, especially inkjet printing technique, emerge as promising ways to fabricate electronic goods on different types of substrate and to reduce production cost. As the inkjet printing technique is a direct mask-less writing technique at ambient temperature and atmospheric pressure, this technique is cheaper than vacuum technologies and also reduces the processing steps in comparison to photolithographic technique. In order to promote improve RFID system, TAGSYS RFID in collaboration with CMP, is working on to develop acoustic resonant transducer using printed electronics techniques. In addition, for possible future applications new polymeric piezoelectric ink has been developed, which will not only provide viable alternative to fabricate printed piezoelectric acoustic sensor, but also will allow the use of such ink for a wide range of other applications, such as pressure sensor, energy harvesting, etc.

The main theme of this thesis is to design and develop the printed acoustic transducer with good selectivity at resonant frequency. This thesis is organized into six chapters. Besides the current chapter which intends to give a brief introduction of the topics and the motivations of this thesis, the other chapters are organized as given by the following:

Chapter 2 provides an overview of working principle of different types of acoustics sensors and presents the literature review of different types of acoustic sensors. In addition, this chapter also describes different printed electronics technologies, especially the inkjet printing technique and its working principle.

Chapter 3 presents the details design of the capacitive acoustic sensor and a brief theoretical analysis. Thereafter, the development of the numerical modeling of the capacitive acoustic transducer is discussed along with identification of important parameters of the device that

influence the responses. Finally, the optimization of the transducer is performed using numerical simulation and design of experiment.

Chapter 4 describes the detailed fabrication process of the printed capacitive acoustic transducer. Each development step along with the characterization involved in it is discussed as well. Finally, the characterization of the capacitive acoustic device is presented.

Chapter 5 describes the development process of polymeric piezoelectric ink formulation in details. Effects of different printing parameters and the printing process of the piezoelectric layer are presented. Thereafter, the printed piezoelectric layers are characterized and compared with the spin coated polymeric piezoelectric layer.

Chapter 6 concludes this thesis work, and proposes possible future research directions to improve the efficiency of the printed acoustic transducer and briefly describes the future application.

References

[1] D.S. Ballantine, R.M. White, S.J. Martin, and A.J. Ricco, *Acoustic Wave Sensors: Theory, Design, and Physico-Chemical Applications*. London, UK: Academic Press, 1997.

[2] Dr. Tom Kenny, "Sensor Fundamentals," in *Sensor Technology Handbook*, Jon Wilson, Ed. USA: Elsevier, 2005, pp. 1–20.

[3] P.R. Scheeper, A.G.H. van der Donk, W. Olthuis, and P. Bergveld, "A Review of Silicon Microphones," *Sensors and Actuators A: Physical*, vol. 44, pp. 1–11, 1994.

[4] D. T. Martin, "Design, Fabrication, and Characterization of a MEMS Dual-backplate Capacitive Microphone," Doctoral Thesis, University of Florida, Gainesville, FL, USA, 2007.

[5] Dimitrios Chatzopoulos, "Modeling the Performance of MEMS Based Directional Microphones," Master's Thesis, Naval Postgraduate School, Monterey, CA, USA, 2008.

[6] B. Kaushik, D. Nance, and K. K. Ahuja, "A Review of the Role of Acoustic Sensors in the Modern Battlefield," in *11th AIAA/CEAS Aeroacoustics Conference*, Monterey, CA, USA, 2005, p. AIAA 2005–2997.

[7] Alan W. Mitchell, Yuebin B. Ning, and Niall Tait, "Fabrication of a Surface Micromachined Capacitive Microphone using a Dry-etch Process," US 5573679 A, Nov-1996.

[8] Alexander Kamyshny, Joachim Steinke, and Shlomo Magdassi, "Metal-based Inkjet Inks for Printed Electronics," *Open Applied Physics Journal*, vol. 4, pp. 19–36, 2011.

[9] A. Blayo and B. Pineaux, "Printing Processes and Their Potential for RFID Printing," presented at the Joint sOc-EUSAI conference, Grenoble, 2005, pp. 27–30.

[10] Abi Bliss, "Printed Electronics: the Future at Your Fingertips," May-2013. [Online]. Available: http://www.computerarts.co.uk/blog/printed-electronics-future-your-fingertips-133664. [Accessed: 14-Dec-2014].

[11] Acreo Swedish ICT, "Printed Electronics." [Online]. Available: https://www.acreo.se/expertise/printed-electronics. [Accessed: 26-Jun-2015].

[12] Thin Film Electronics ASA, "Thinfilm Receives First Order for Brand Protection Solution," *Thinfilm: Memory Everywhere*, 2013. [Online]. Available: http://www.thinfilm.no/news/thinfilm-receives-first-order-for-brand-protection-system/. [Accessed: 26-Jun-2015].

[13] W. T. Wondmagegn, N. T. Satyala, H. J. Stiegler, M. A. Quevedo-Lopez, E. W. Forsythe, R. J. Pieper, and B. E. Gnade, "Simulation Based Performance Comparison of Transistors Designed Using Standard Photolithographic and Coarse Printing Design Specifications," *Thin Solid Films*, vol. 519, no. 6, pp. 1943–1949, 2011.

[14] Matthias Nagel and Thomas Lippert, "Laser-Induced Forward Transfer for the Fabrication of Devices," in *Nanomaterials: Processing and Characterization with*

Lasers, S. C. Singh, H. B. Zeng, C. Guo, and W. P. Cai, Eds. Weinheim, Germany: Wiley-VCH, 2012, pp. 255–306.

[15] K.K.B. Hon, L. Li, and I.M. Hutchings, "Direct Writing Technology-Advances and Developments," *CIRP Annals - Manufacturing Technology*, vol. 57, no. 2, pp. 601–620, 2008.

[16] Y. Li, D. Lu, and C. P. Wong, *Electrical Conductive Adhesives with Nanotechnologies*. New York, NY, USA: Springer, 2009.

[17] Romain Cauchois, "Microstructuring Inkjet-Printed Deposits: from Silver Nanoparticles Coalescence to the Fabrication of Interconnections for Electronic Devices," École Nationale Supérieure des Mines de Saint-Étienne, Gardanne, 2012.

[18] J. Perelaer, B.-J. de Gans, and U. Schubert, "Ink-jet printing and microwave sintering of conductive silver tracks," *Advanced Materials*, vol. 18, no. 16, pp. 2101–2104, 2006.

[19] M.L. Allen, M. Aronniemi, T. Mattila, A. Alastalo, K. Ojanperä, M. Suhonen, and H. Seppä, "Electrical Sintering of Nanoparticle Structures," *Nanotechnology*, vol. 19, no. 17, p. 175201, 2008.

[20] S. H. Ko, H. Pan, C. P. Grigoropoulos, C. K. Luscombe, J. M. J. Fréchet, and D. Poulikakos, "All-Inkjet-Printed Flexible Electronics Fabrication on a Polymer Substrate by Low-Temperature High-Resolution Selective Laser Sintering of Metal Nanoparticles," *Nanotechnology*, vol. 18, no. 34, p. 345202, 2007.

[21] K. A. Schroder, "Mechanisms of Photonic Curing™: Processing High Temperature Films on Low Temperature Substrates," in *Nanotech*, vol. 2, CRC Press, 2011, pp. 220–223.

[22] K. A. Schroder, S. C. McCool, and W. F. Furlan, "Broadcast Photonic Curing of Metallic Nanoparticle Films," *NSTI-Nanotech*, vol. 3, pp. 1–4, 2006.

[23] Ahmed Busnaina, "Nanomaterials-based Manufacturing Platform for Printed Sensors, Electronics, Energy and Material Applications," presented at the The Tenth U.S.-Korea Forum on Nanotechnology: A New Generation of Nano-technological Products & Processes, Boston, USA, 2013.

[24] K. Pataky, V. Auzelyte, and J. Brugger, "Inkjet Printing for MEMS," in *Inkjet-Based Micromanufacturing*, Jan G. Korvink, Patrick J. Smith, and Dong-Youn Shin, Eds. Weinheim, Germany: WILEY-VCH Verlag GmbH & Co. KGaA, 2012, pp. 331–345.

[25] TAGSYS, "TAGSYS…Global Leader in Item-Level Inventory Management Systems," *TAGSYS RFID*, 06-May-2013. [Online]. Available: http://tagsysrfid.com/Company/Overview.

[26] Spinnaker, "SPINNAKER," *Spinnaker*, 2012. [Online]. Available: http://www.spinnaker-rfid.com/. [Accessed: 16-Jun-2015].

CHAPTER 2

STATE OF THE ART

In this chapter, the state of the art of acoustic sensor is discussed. Different types of acoustic transducer and their operational principles are briefly described. In addition, the basic concepts of printed electronics technologies that are used for microelectronics manufacturing are presented and discussed. A specific interest has been given to the inkjet printing direct write technique. The state of the art of inkjet printing and its important parameters for microelectronics fabrication are also introduced.

2.1. Acoustic sensor

An acoustic sensor is a transducer that generates output signal in response to the acoustic wave. The acoustic wave, also known as pressure wave, is a longitudinal waveform that propagates by means of adiabatic compression and decompression. The amplitude, frequency and phase of the pressure wave carry the information. Thus, an acoustic sensor is actually a differential pressure sensor that detects pressure difference between inside and outside of the acoustic transducer enclosure. Commonly known acoustic transducers are microphone, earphone etc. The schematic diagram of a basic acoustic transducer is presented in Figure 2.1.

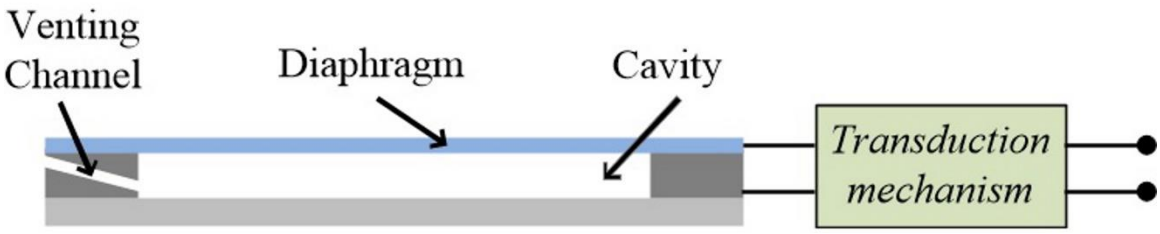

Figure 2.1: *Schematic diagram of a basic acoustic transducer structure.*

The structure of an acoustic transducer generally contains diaphragm or cantilever, which is exposed to the incident acoustic pressure. Sound pressure causes deflection of the diaphragm that is detected by the transduction mechanism of the acoustic transducer, and output is generated. Generally, acoustic transducer also contains narrow venting channel that helps to maintain the identical pressure between inside and outside of the sensor, and as a result, the sensor can detect the pressure difference due to incident acoustic pressure. Figure 2.2 illustrates the operation of an acoustic transducer in response to incident acoustic pressure.

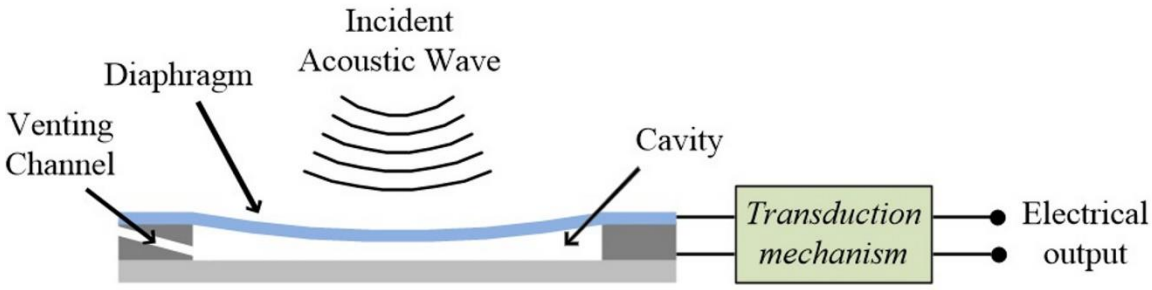

Figure 2.2: *Schematic diagram of operation of an acoustic transducer in response to incident acoustic wave.*

Acoustic transducers use different types of transduction principle, namely capacitive, piezoelectric, piezoresistive, optical, electromagnetic etc. [1], [2]. Among these piezoelectric, piezoresistive and capacitive are the most commonly adopted transduction mechanisms in transducers [2], [3]. Generally, the piezoelectric and piezoresistive sensors use the strain-detecting method, whereas the capacitive transducer adapts the position-detecting method [4]. In a piezoelectric acoustic transducer, a thin diaphragm is usually provided with a piezoelectric material or mechanically connected to a bimorph bender, a cantilever beam made of two layers of piezoelectric material having opposite polarizations. The diaphragm movement causes stress in the piezoelectric material, which in response generates an electric voltage. A piezoresistive acoustic transducer is made of a diaphragm with four piezoresistors, connected in a Wheatstone bridge configuration. The deflection of the diaphragm causes the change of strains of the piezoresistors based on their position and thus a change in resistance is observed. On the other hand, capacitive acoustic sensor detects the capacitive variation due to a change in the air gap because of deflection of the diaphragm [2].

2.1.1. Capacitive acoustic transducer

A capacitive acoustic transducer is an electromechanical-acoustic system that uses the transduction mechanism of detecting the capacitance variation. In addition to diaphragm that acts as moving electrode, backplate electrode and cavity, a capacitive acoustic sensor also consists of dielectric material, such as air, in between two electrodes, which is known as air gap. The deflection of the diaphragm induces the capacitance variation due to change in air gap.

In a capacitive acoustic transducer, the diaphragm and the backplate electrode form a parallel plate capacitor and the capacitance can be expressed as [1],

$$C = \frac{\varepsilon_0 \varepsilon_r S}{h} \quad \ldots\ldots\ldots (2.1)$$

Here S represents the overlapping surface area of the two electrodes, ε_0 is the permittivity constant, ε_r represents the relative static permittivity of the dielectric materials (for air, $\varepsilon_r = 1$) and h represents the distance between the electrodes that is equivalent to the air gap of the device. An incident sound pressure causes the diaphragm deflection, which leads to a change in the air gap and thus the capacitance variation.

There are different configurations that have often been used for the capacitive acoustic device fabrication based on the geometry and position of the backplate electrode with respect to the diaphragm, whether the backplate is perforated or not, and the size and number of backplate holes, if any etc., as presented in Figure 2.3.

Furthermore, a capacitive transducer can also be equipped with dual-backplate, one on each side of the diaphragm; or with dual-membrane. These types of differential electrostatic transducer are known as a push-pull device (Figure 2.4) [5]. The dual-backplate acoustic transducer generally exhibits higher sensitivity, which can be increased even further by applying higher bias voltage. Such transducer provides enhanced linearity and the applied electrostatic force acting on the diaphragm is symmetric compared to a single-backplate transducer. On the other hand, there is transducer structure with dual diaphragm, where two diaphragms are placed on each side of the backplate (Figure 2.4(b)) [6].

Generally, there are two types of capacitive acoustic transducer, condenser and electret. Condenser acoustic transducers are biased with an external voltage source, while electrets are biased with a fixed permanent charge [7]–[19]. In case of electret microphones thin dielectric layer, such as silicon dioxide (SiO_2) [7], [13], [19], fluorinated ethylene propylene (FEP) film [16], with implanted fixed charge, is deposited on the backplate [2]. Electret microphones are not susceptible to electrostatic pull-in. However, the fabrication process is more difficult.

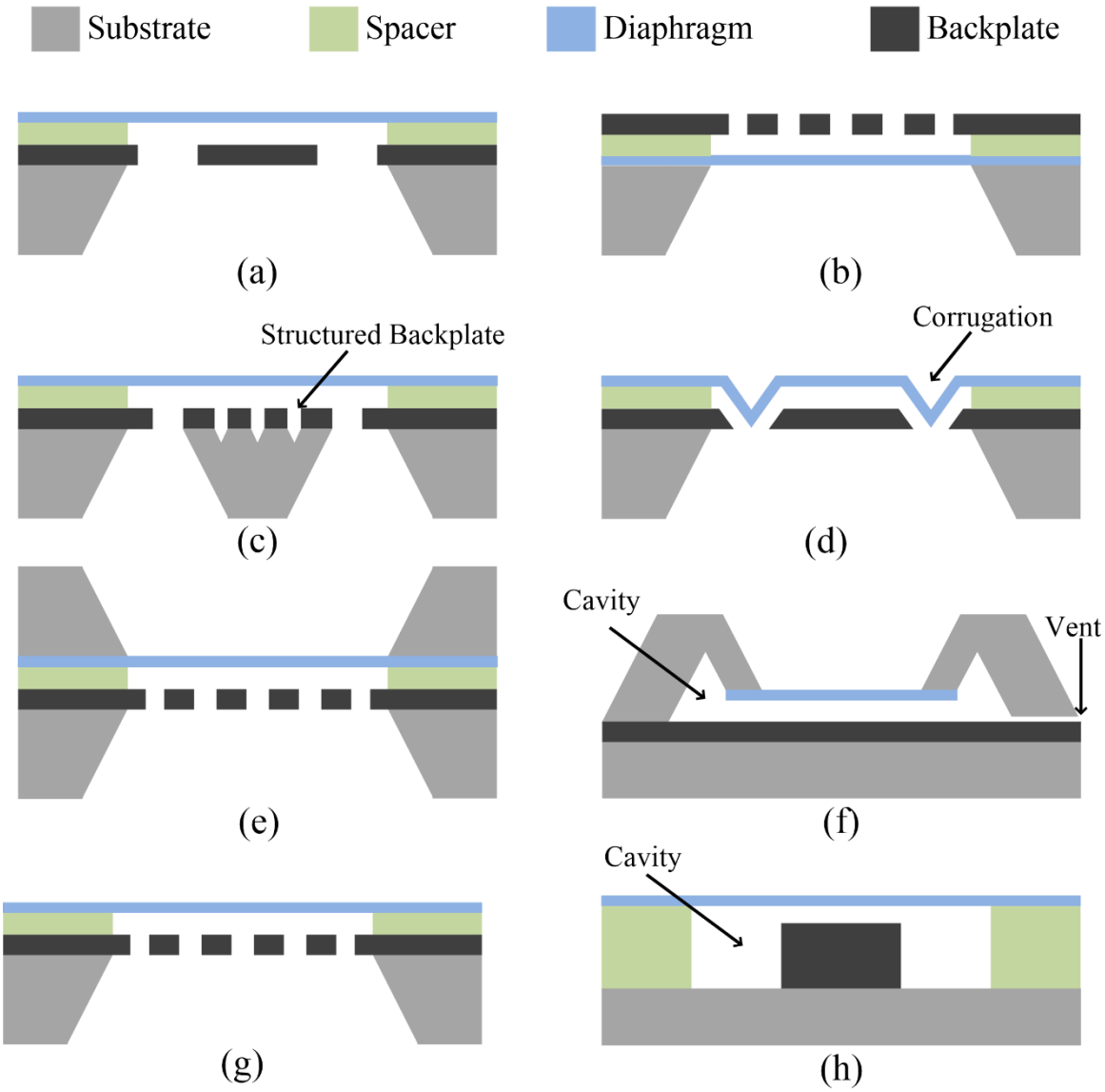

Figure 2.3: *Schematic diagrams of cross-sectional view of representative single-backplate capacitive acoustic transducers with, (a) a backplate containing small number of large holes below the diaphragm [7], (b) a highly perforated backplate above the diaphragm [20], (c) a structured backplate [21], (d) a corrugated diaphragm [22], (e) a backplate below the diaphragm and a patterned substrate above the diaphragm [8], (f) a solid backplate and small cavity [23], (g) a highly perforated backplate below the diaphragm [3], (h) a central cylindrical backplate with small radius and a flat annular cavity [24].*

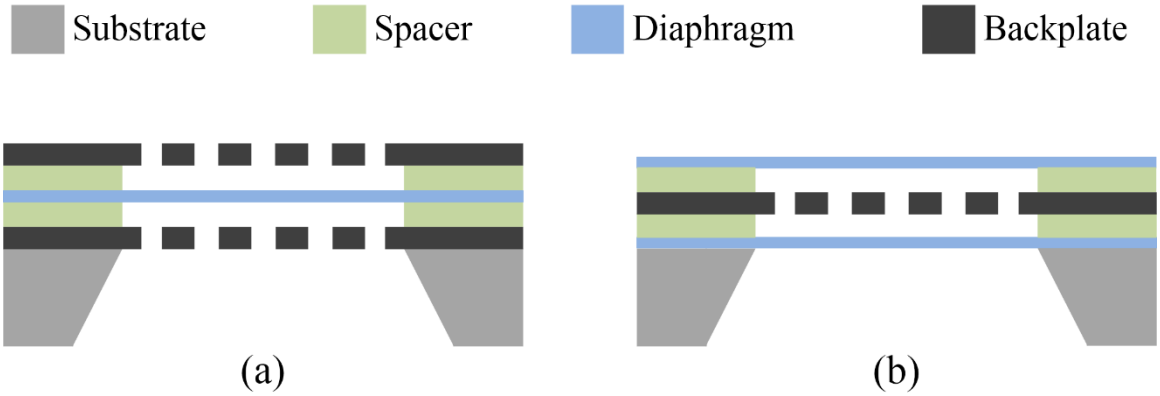

Figure 2.4: *Schematic diagram of cross-section of differential capacitive acoustic transducers (a) dual-backplate [25], and (b) dual-diaphragm [6].*

A capacitive acoustic transducer can be fabricated either using the "two wafers technique" where the diaphragm and backplate of the transducer are manufactured separately [2] and then assembled to complete the device, or by the "single wafer technology" using sacrificial layer method [2], [26]. The sensitivity of the capacitive acoustic transducer generally depends on the mechanical compliance of the diaphragm and the electric field in the air gap [2].

The electric field within the air gap of the capacitive acoustic transducer can be enhanced either by applying higher external voltage in case of condenser system or by using electrets with higher permanently embedded static electric charges. Generally, capacitive acoustic transducer suffers from over-damping as a thin layer of air is trapped in between the two electrodes. Occasionally, capacitive acoustic transducer with porous membrane or/and perforated backplate were designed and fabricated to reduce the damping effect and to increase the sensitivity of the transducer. The perforated structure also helps to tune the damping to maximize the bandwidth for free-field acoustic transducer [27].

Most of the early capacitive microphones were generally electret acoustic transducer. In 1984, Hohm *et al.* have reported the first silicon based capacitive transducer [7] that consists of Mylar diaphragm suspended above a backplate electrode having one large hole. SiO_2 was deposited on the backplate as eletret that is charged to about -350 V. The device provides a bandwidth of 100 Hz to 7 kHz, and approximately the sensitivity of 3 $mV.Pa^{-1}$ at the frequency of 1 kHz [7]. In 1989, Sprenkels *et al*. [13], [18] have developed an electret transducer having a flat bandwidth to 15 kHz with a 5% variation between devices, whereas

Murphy *et al.* [19] reported an electret transducer with a resonant frequency of about 15 kHz.

In 1990, Bergqvist *et al.* [8], provided a new microphone design concept, highly miniaturizable, that can be fabricated at low cost, having the sensitivity between 13 and 14 $mV.Pa^{-1}$ within a bandwidth of 4 to 16 kHz. The diaphragm and the backplate of the device were fabricated using two separate silicon wafers employing micromachining technique and then joined together with anodic bond.

Fabrication of a subminiaturized silicon capacitive transducer using "single wafer technology" by sacrificial layer method, having 2×2 mm diaphragm and a 1 µm air gap has been reported, which exhibits a sensitivity of 1.4 $mP.Pa^{-1}$ at low frequencies for a low bias voltage of 2 V [26]. The design was modified by incorporating backplate with highly dense acoustic holes that exhibits the sensitivity of 1-2 $mV.Pa^{-1}$ with a flat frequency response between 100 Hz and 14 kHz [28].

In 1992, Kuhnel *et al.* [21] have reported silicon based condenser transducer having structured backplate, as illustrated in Figure 2.3(c) to reduce the streaming resistance in the air gap. The device with membrane of 0.8×0.8 mm^2 and 2 µm air gap provides a sensitivity of 10 $mV.Pa^{-1}$ up to 30 kHz.

The sensitivity of a capacitive acoustic transducer can also be enhanced by increasing the compliance of the diaphragm. In this regard, transducers have been fabricated with corrugated diaphragm, as showed in Figure 2.3(d) [29]–[31]. The presence of corrugation eases the diaphragm's in-plane stress. Fabrication of hearing aid with corrugated diaphragm have been reported [32] that exhibits a sensitivity of 14 $mV.Pa^{-1}$ for 12 V bias voltage.

In 1992, Bourouina *et al.* have fabricated a condenser transducer using a p^+ silicon membrane of 1 µm thickness with integrated back-chamber as illustrated in Figure 2.3(f) that exhibits a sensitivity of 0.4 and 3.5 $mV.Pa^{-1}$ with a bandwidth between 2.5 and 20 kHz. Later on, Hsu *et al.* have reported the design and fabrication of condenser transducer using a thin low-stress polysilicon diaphragm of 2.6×2.6 mm^2, where backplate was made of p+ silicon of 13 µm thickness with periodic 60×60 μm^2 holes array, that provides a capacitance of 16.2 pF at zero bias voltage, and exhibits the sensitivity of 20 $mV.Pa^{-1}$ [3].

Most of the above described transducers have complex geometry and thus require complex fabrication steps. To reduce the fabrication complexity as well as to achieve good sensitivity, in recent time, a new design of the acoustic transducer has been introduced, having a central cylindrical backplate electrode with small radius and flat annular cavity behind the diaphragm (Figure 2.3(h)) [24], [33], [34]. The device exhibits a sensitivity of 10 mV.Pa^{-1} with a bandwidth of 20 Hz to 16 kHz for 800 V bias voltage, having the membrane radius of 50 mm and the backplate radius of 20 mm separated by 310 µm of air gap [24].

A capacitive acoustic transducer exhibits good sensitivity while maintaining low power consumption. Although, the sensitivity of such devices generally reduces at high frequencies due to the air streaming resistance of the narrow air gap [2]. Discussion above, provides insight of different geometries that can be employed to fabricate capacitive transducer with increased sensitivity. As observed, the sensitivity of the capacitive acoustic transducer can be improved mainly by reducing the damping effect which can be achieved either by employing complex backplate or diaphragm geometry, or by manufacturing device using simplified design with much larger diaphragm compared to backplate and large cavity. Table 2.1 summarized the specifications of capacitive transducer discussed above.

Table 2.1: Summary of the specifications of capacitive acoustic transducers.

Author	**Diaphragm Dimensions**	**Air gap** µm	**Capacitance** pF	**Bias Voltage (V_b)** V	**Sensitivity** mV/Pa	**Bandwidth**
Hohm et al. 1984 [7]	8.0mm*×13µm	20	9	350	3	100 Hz – 7.5 kHz
Sprenkels et al. 1989 [13], [18]	3.0mm*×2.5µm	20	N/R	300	25	100 Hz – 15 kHz
Murphy et al 1989 [19]	N/R×1.5µm	25 – 95	N/R	200	4 – 8	100 Hz – 15 kHz
Bergqvist et al 1990 [8]	2mm*×5µm	4	3.5	N/R	13	500 Hz – 2 kHz
Bergqvist et al 1990 [8]	2mm*×6µm	4	3.5	N/R	6.1	100 Hz – 5 kHz
Bergqvist et al 1990 [8]	2mm*×8µm	4	3.5	N/R	1.4	500 Hz – 20 kHz
Scheeper et al 1991 [26]	2mm*×1µm	1	20	2	1.4	40Hz
Scheeper et al 1992 [28]	2mm*×1µm	3.3	5-7	16	2	100Hz – 10 kHz
Kühnel et al 1992 [21]	0.8mm*×0.25µm	2	1	28	1.8	100 Hz – 20 kHz

Cunningham et al 1997 [29]	1mm‡×0.5µm	2	5.1	8	2.1	200 Hz – 10 kHz
Li et al 2001 [30]	1mm*×1.2µm	2.6	1.64	5	9.4	100 Hz – 19 kHz
Kressmann et al 2002 [31]	1mm*×620nm	2	2	4	3	10 Hz – 50 kHz
Schafer et al 1998 [32]	0.4mm‡×0.75µm	4	0.2	12	14	150 Hz – 10 kHz
Bourouina et al 1992 [23]	500µm*×1µm	5	N/R	N/R	0.4	N/R – 20 kHz
Bourouina et al 1992 [23]	707µm*×1µm	5	N/R	N/R	2	N/R – 7 kHz
Bourouina et al 1992 [23]	1mm*×1µm	5	N/R	N/R	3.5	N/R – 2.5 kHz
Bourouina et al 1992 [23]	1mm*×1µm	7.5	N/R	N/R	2.4	N/R – 10 kHz
Hsu et al. 1998 [3]	2.6mm*×2µm	4	16.2	10	20	100 Hz – 10 kHz
Honzik et al. 2014 [24]	50mm‡×25 um	310	N/R	800	10	20 Hz – 16 kHz

* Side length of square diaphragm ‡ Radius of circular diaphragm

2.1.2. Piezoelectric acoustic transducer

Piezoelectricity is one of the basic properties of crystals, ceramics, polymers, and liquid crystals. A material is called piezoelectric if it develops an internal dielectric displacement in response to the external mechanical stress and vice versa. This displacement is manifested as an internal electric polarization or a surface electric charge [35]–[37]. The generation of electric charges due to mechanical stress is known as the direct piezoelectric effect, whereas the generation of a mechanical strain due to application of external electric field is known as the converse or indirect piezoelectric effect [38]. The direct piezoelectric effect is generally used in sensor applications, while the converse effect is used in actuator applications.

Basically, piezoelectricity is a coupling between the mechanical properties (mechanical stress 'T_{kl}' in [Pa or N/m^2] and induced strain 'S_{ij}') and electrical properties (electric charge density 'D_i' in [C/m^2] and electric field 'E_k' in [V/m]). For unidirectional poling the piezoelectric effect of materials can be described by linear constitutive equations with respect to electrical and mechanical properties, and these equations are presented as follows [39], [40],

$$D_i = d_{ikl} \cdot T_{kl} + \varepsilon_{ik}^{T} \cdot E_k \quad \ldots \ldots \ldots (2.2)$$

$$S_{ij} = s_{ijkl}^{E} \cdot T_{kl} + d_{kij} \cdot E_k \quad \ldots \ldots \ldots (2.3)$$

where ε_{ik}^{T} is the electric permittivity at constant stress [F/m], s_{ijkl}^{E} is the elastic compliance for a constant electric field [m^2/N], and d_{kij} is the piezoelectric coefficient [C/N or m/V] that quantifies the piezoelectric response for a given strain or applied electric field [38], [40].

Piezoelectric materials are being more and more studied since their discovery in 1880 by Jacques Curie and Pierre Curie [41]. The most commonly known piezoelectric material is quartz. However, there are numerous piezoelectric materials, such as berlinite ($AlPO_4$), gallium orthophosphate ($GaPO_4$), barium titanate ($BaTiO_3$), lead zirconate titanate (PZT), zinc oxide (ZnO), aluminum nitride (AlN), polyvinylidene fluoride (PVDF) and its copolymer with trifluoroethylene (TrFE) etc. The properties of several major piezoelectric materials are listed in Table 2.2.

Table 2.2: List of physical properties of major piezoelectric materials [41]–[45].

Parameter	**Quartz**	**$BaTiO_3$**	**PZT4**	**PST5H**	**AlN**	**ZnO**	**$PbTiO_3$:Sm**	**PVDF-TrFE**
Piezoelectric coefficient (d_{33}) [pC/N]	2.3	190	289	593	5.53	10.4	65	24–38
Piezoelectric coefficient (d_{31}) [pC/N]	0.09	0.38	-123	-274	-2.65	-5.74	0	6–12
Piezoelectric constant (g_{33}) [10^{-3} Vm/N]	57.8	12.6	26.1	19.7	66–105	135	42	380
Relative dielectric constant ($\varepsilon_3^T/\varepsilon_0$)	5	1700	1300	3400	10.4	10.9	175	6
Curie Temperature (T_C) [°C]	-	120	328	193	>2000	-	355	110

A piezoelectric acoustic sensor is a transducer that converts acoustic pressure variation into an electric voltage and current for signal detection. Generally, two basic configurations have been used to develop piezoelectric transducers devices, namely, thin diaphragm (membrane or plate) and cantilever beam, that are used to couple the pressure fluctuations into mechanical displacement [46]–[50]. In such system, a piezoelectric material transfers the diaphragm strain energy into an electrical output [40]. Transducer with a diaphragm configuration consists of a layer of piezoelectric material along with bottom and top electrodes on the top of the diaphragm as illustrated in Figure 2.5(a). Figure 2.5(b) presents a basic piezoelectric transducer structure with a cantilever beam configuration, which

contains a similar layered structure of piezoelectric material and electrodes. However, it is located at the clamped end of the beam as the stresses are concentrated in this region.

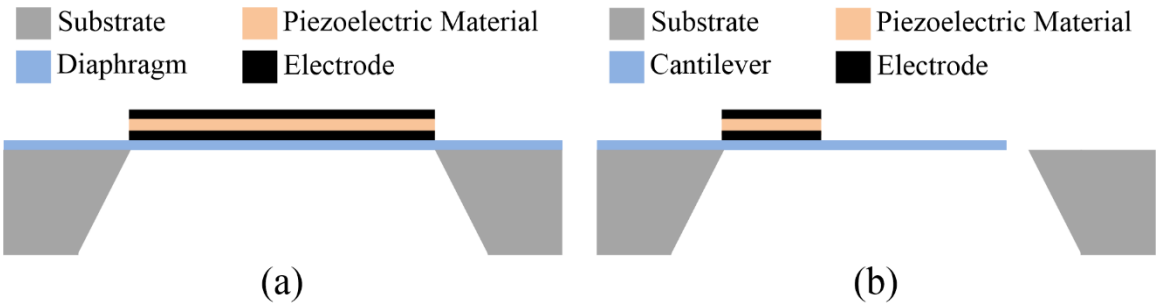

Figure 2.5: *Schematic diagram of cross-sections of basic piezoelectric transducer structures (a) diaphragm configuration [51], (b) cantilever beam configuration [49].*

The sensitivity of the diaphragm based acoustic transducers depends on the deflection of the diaphragm, which is greatly affected by the residual stress in the diaphragm; whereas, the deflection of the cantilever based acoustic transducer is greatly higher, however its mechanical stiffness is weak [52].

There are several ceramic, polymer and biological systems that exhibit piezoelectricity, which can be used as active piezoelectric element in device fabrication. ZnO is the most commonly used piezoelectric material for acoustic transducer fabrication. In addition, materials like PZT, AlN, PVDF and its copolymer PVDF-TrFE, and aromatic polyurea can also be used [53]. Different factors are taken into consideration during selecting the piezoelectric materials, namely, the magnitude of the piezoelectric coefficient, the film stability, relative permittivity, and compatibility with other processes. In addition, piezoelectric voltage constant 'g', which refers to the generation of the electric field by a piezoelectric material per unit of applied mechanical stress, also plays an interesting role for piezoelectric acoustic transducer [54].

Piezoelectric based transducer can be operated in two different modes, such as voltage mode and charge mode. In case of voltage mode, output is a voltage signal which is amplified by a voltage amplifier. On the other hand, for charge mode operation, output is a charge signal which is then converted to voltage by charge amplifier. In case of charge mode operation, the overall sensitivity remains unaffected by parasitic capacitance, for instance, change of the cable length [55].

The sensitivity of the piezoelectric transducer is proportional to the stress in the diaphragm, and the voltage across the piezoelectric element is proportional to the thickness of the piezoelectric material. Therefore, the sensitivity of the transducer reduces with the reduction of piezoelectric materials thickness, assuming the diaphragm stress is independent of the piezoelectric stress. On the other hand, the bandwidth of the transducer, which is dominated by the resonant frequency of the diaphragm (plate), increases with the decreasing size of the transducer [56].

The first piezoelectric transducer was demonstrated by Royer *et al.* in 1983 using silicon micromachining technique [51]. The transducer consists of a circular single crystal silicon diaphragm with diameter of 3 mm and thickness of 30 μm. ZnO layer of 3 - 5 μm thickness was deposited on the diaphragm using sputtering technique, sandwiched between two SiO_2 layers which contain the aluminum electrodes. A sensitivity of 0.05-0.25 $mV.Pa^{-1}$ and a flat frequency response within 5 dB between 10 Hz and 10 kHz were reported [2], [51].

Piezoelectric MEMS transducer was reported by Kim *et al*. [46], where a piezoelectrically active ZnO layer of 0.3 μm was used as the mechanical-to-electrical transducer on the square shaped diaphragm with thickness of 2 μm and dimension 3×3 mm^2. The diaphragm was made of silicon nitride, which provides almost stress free diaphragm. Polysilicon and aluminum were used as bottom electrode and top electrode respectively. The device showed approximately 9 dB variation of sensitivity from 20 Hz to 4 kHz with the typical sensitivity being 0.50 $mV.Pa^{-1}$. Kim *et al.* [47], [48] also fabricated the integrated transducer with CMOS circuit on a single chip, where ZnO is used as piezoelectric material on the silicon nitride diaphragm as well. Modified low pressure chemical vapor deposition (LPCVD) parameters were used to further reduce the residual strain in the silicon nitride diaphragm and modification of the transducer structure led to the substantial improvement in the performance of the transducer. The sensitivity was enhanced by a factor five.

Organic films, such as aromatic polyurea, PVDF and its copolymer PVDF-TrFE can also be used as active materials to fabricate piezoelectric transducer. Schellin *et al.* [57] fabricated acoustic sensor using modified integrated circuit technology process and a standard micromechanical fabrication procedure to make a 0.8 - 1 μm thick silicon membrane. Piezoelectric material, like, aromatic polyurea films of 0.25 to 1 μm thickness were deposited on the membrane by a vapor deposition polymerization method, whereas PVDF and PVDF/TrFE films of 0.25 to 1 μm thickness were spin coated on the membrane.

Aluminum was used as electrodes. Sensitivity of piezoelectric acoustic transducer with aromatic polyurea to airborne sound was around 0.13 $mV.Pa^{-1}$.

Fabrication of piezoelectric transducer with on-chip large-scale integration (LSI) CMOS circuit with improved signal-to-noise was reported by Ried *et al.* [58]. The transducer consists of square shaped silicon nitride diaphragm of 2.5×2.5 mm^2 and thickness of 3.5 μm, where ZnO was used on the diaphragm as active piezoelectric material. The transducer, with an unamplified sensitivity of 0.92 $mV.Pa^{-1}$, demonstrated a flat response from 100 Hz to 18.3 kHz.

Piezoelectric acoustic device of 3×3×0.003 mm^3, which acts as a microphone as well as a microspeaker, was reported in 2003 [59]. The device contains a low-stress LPCVD silicon nitride membrane of 1.5 μm. ZnO layer of 0.5 μm thickness was used as active piezoelectric material on the diaphragm. As a microphone, the device showed a sensitivity of 0.51 $mV.Pa^{-1}$ at 7.3 kHz with noise level of 18 dB sound pressure level (SPL). On the other hand, the output sound pressure level of the device as microspeaker was 76.3 dB SPL at 7.3 kHz, and 83.1 dB SPL at 13.3 kHz with input drive voltage of 15 $V_{0\text{-}P}$ (zero-peak).

Niu *et al.* [60] demonstrated a bimorph configuration piezoelectric transducer fabricated on micromachined parylene based diaphragm, where active piezoelectric ZnO layers of 0.4 μm thickness were deposited on both sides of a parylene supported diaphragm. The transducer exhibited a sensitivity of about 0.52 $mV.Pa^{-1}$, which was higher than the similar structured unimorph transducer built on a low stress silicon nitride. The integrated transducer based on PZT was also reported [52]. The transducer with 600×600 μm^2 to 1000×1000 μm^2 showed very flat response with sensitivity of 38 $mV.Pa^{-1}$ up to 20 kHz.

A low cost and light weight piezoelectric transducer with simplified design and improved sensitivity was reported by Hillenbrand *at el.* [61]. Cellular polypropylene films with improved piezoelectric coefficient (d_{33}) were used as active piezoelectric material. During this work, five piezoelectric films, each having the thickness of 55 μm, connected in series were used. Transducer with single film showed sensitivity of about 2 $mV.Pa^{-1}$, whereas transducer with five stacked films showed a sensitivity of 10.5 $mV.Pa^{-1}$. An ultrasonic actuator with a radially non-uniform circular composite diaphragm based on 0.8 μm thick AlN piezoelectric thin film was also presented [62].

A piezoelectric transducer for the use in a MEMS scale photoacoustic spectroscopy system as passive sensing element was reported [63], where 1 μm thick PZT was used as piezoelectric material for its large piezoelectric coefficient and low dielectric loss, and platinum (Pt) was used as electrodes. Devices with the diameter of 500 to 2000 μm were fabricated. Depending on the size, these transducers exhibit a maximum sensitivity of 0.92×10^{-3} mV.Pa^{-1}.

Saleh *et al.* [64] have demonstrated the fabrication of highly sensitive piezoelectric acoustic sensor. The structure was composed of Al/ZnO/Al/SiO_2 layers. In this case, p-type (100) orientation silicon (Si) was used to prepare the diaphragm of 25-30 μm thickness, and SiO_2 was used as barrier layer to prevent the diffusion between ZnO and silicon substrate. The frequency response was in the range of 30 Hz – 16 kHz. Average sensitivity was 0.05 mV.Pa^{-1}. Linear output was observed between 110 – 160 dB SPL.

Arora *et al.* [65] reported a piezoelectric acoustic sensor, where the structure was composed of Al/SiO_2/ZnO/SiO_2/Al. Silicon wafer was used to prepare the diaphragm of dimension 3.6×3.6 mm^2 and thickness of about 25 μm using chemical etching. SiO_2 was used as barrier layer to prevent the inter-diffusion of ZnO of thickness 1-5 μm and aluminum. The range of frequency response was 30Hz – 8 kHz and average sensitivity was about 300 $\mu V_{rms.}$/Pa. The sensor was tested at 120 – 180 dB sound pressure level (SPL). The capacitance of the device was 65-144 pF. The measured output of the device was 0.02 pC/Pa (at 140 dB SPL) with sensitivity of about 0.3 mV.Pa^{-1}.

Lee *et al.* [49] reported piezoelectric transducer with cantilever configuration. The cantilever with dimension of 2×2 mm^2 and thickness of 4.5 μm was made of a low-stress silicon nitride using low pressure chemical vapor deposition technique. Thereafter, a 0.5 μm thick layer of ZnO film was deposited on the cantilever using RF magnetron sputtering method. The high residual compression of ZnO layer and the gradient of residual stress of the silicon nitrite layer caused the cantilever to curl. Low stress silicon nitride layers were deposited on the both of the cantilever to avoid curling. The transducer exhibited approximately constant sensitivity of 30 mV.Pa^{-1} in low frequency range below the first resonant frequency, whereas close to the first resonant frequency of 890 Hz sensitivity was 200 mV/Pa^{-1}. Later on, piezoelectric transducer with cantilever configuration that demonstrated sensitivity of 30 mV.Pa^{-1} at low frequency range with a bandwidth of 1.8 kHz was reported [50]. Moreover, cantilever based piezoelectric transducers constructed out of

molybdenum (Mo) and aluminum nitride (AlN) were also reported [66], where a five-layer stack of 0.2 μm Mo/ 0.5 μm AlN/ 0.2 μm Mo/ 0.5 μm AlN/ 0.2 μm Mo was used. The device with cantilever beams of length ranging from 200 μm to 450 μm and width of 30 μm to 300 μm, exhibit sensitivity of 0.11 $mV.Pa^{-1}$ at 1 kHz.

For years, there have been numerous efforts in the development of piezoelectric transducers, where varieties of piezoelectric materials have been used as the active mechanical-to-electrical transduction. Early devices had poor frequency response due to poor control on the residual stress of the diaphragm. Generally, a piezoelectric based transducer offers two main advantages, namely, no requirement of input power and a wide dynamic range [63]. In addition, a piezoelectric sensor can be operated in two ways: voltage mode and charge mode [67]. In case of voltage mode operation the output voltage is amplified directly by a voltage amplifier, whereas in case of charge mode operation the output charge is converted to a voltage via a charge amplifier. Amongst them, charge mode operation is insensitive to parasitic capacitances. Table 2.3 summarized the specifications of the piezoelectric transducers discussed above.

Table 2.3: Summary of the specifications of piezoelectric acoustic transducers.

Author(s)	Diaphragm Dimensions	Piezoelectric Material	Sensitivity	Bandwidth
			$mV.Pa^{-1}$	
Royer *et al.* [51]	1.5mm*×30μm	ZnO	0.05–0.25	10 Hz – 10 kHz
Kim *et al.* [46]	3 mm†×2 μm	ZnO	0.5	20Hz – 5 kHz
Kim *et al.* [47]	2 mm†×1.4 μm	ZnO	0.8	3 kHz – 30 kHz
Kim *et al.* [48]	3.04 mm†×2 μm	ZnO	1	200 Hz – 16 kHz
Schelling *et al.* [57]	0.8 mm†×1 μm	Polyurea	0.126	100 Hz – 20 kHz
Ried *et al.* [58]	2.5 mm†×3.5 μm	ZnO	0.92	100 Hz – 18 kHz
Lee *et al.* [50]	2 mm‡×1.5 μm	ZnO	30	50 Hz – 1.8 kHz
Ko *et al.* [59]	3 mm†×3.0 μm	ZnO	0.51	1 kHz – 7.3 kHz
Niu *et al.* [60]	3 mm†×3.2 μm	ZnO	0.52	100 Hz – 3 kHz
Zhao *et al.* [52]	1 mm†×N/R	PZT	38	10 Hz – 20 kHz
Hillenbrand *et al.* [61]	0.3 cm^2 area×55 μm	Cellular polypropylene	2	140 kHz
Hillenbrand *et al.* [61]	0.3 cm^2 area×275 μm	Cellular polypropylene	10.5	28 kHz
Lee *et al.* [49]	2 mm‡×4.5 μm	ZnO	30	100 Hz – 890 Hz
Polcawich [63]	2 mm*×N/R	PZT	0.92×10^{-3}	N/R
Saleh *et al.* [64]	N/R×25 μm	ZnO	0.05	30 Hz – 16 kHz
Arora *et al.* [65]	3.6 mm†×25 μm	ZnO	0.3	30 Hz – 8 kHz
Littrell *et al.* [66]	0.45 mm‡×1.7 μm	AlN	0.11	N/R

* Radius of circular diaphragm
† Side length of square diaphragm.
‡ Side length of cantilever.

2.1.3. Piezoresistive acoustic transducer

Piezoresistivity generally refers to the change of the electrical resistivity of a resistor due to stress induced deformation. Certain semiconductor materials, such as silicon, exhibits much higher change in resistance when mechanical stress is applied. This effect was first observed in silicon by Smith in 1954 [68], and is known as piezoresistive effect [69], [70]. The change in resistivity occurs due to the change in the charge mobility. A positive stress causes a positive variation, whereas negative stress causes a negative variation of resistance [71]. The change of relative resistance as a function of the mechanical stress can be expressed as [56], [71],

$$\frac{\Delta R}{R} = \sum \pi_i \sigma_i \quad \ldots\ldots\ldots (2.4)$$

Where R and ΔR represent the resistivity of the resistor and the change in resistivity respectively, π_i being the piezoresistive coefficients and σ_i represents the stress along the i direction.

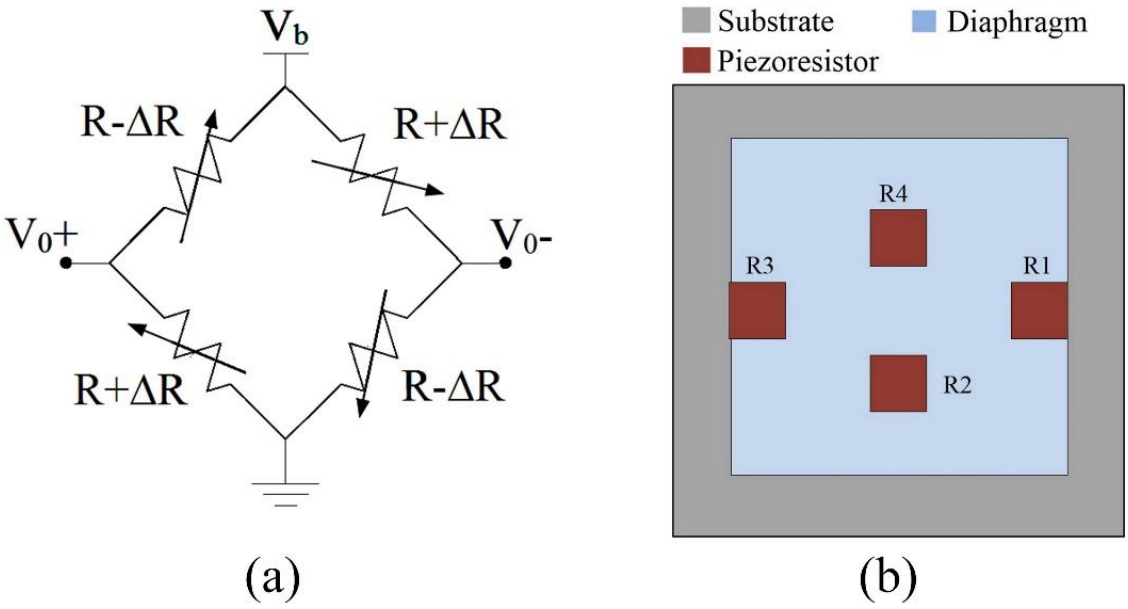

Figure 2.6: *Schematic diaphragm of (a) the Wheatstone bridge configuration, (b) Top view of a piezoresistive transducer with four active piezoresistors [72].*

The piezoresistive effect can be used to fabricate piezoresistive acoustic pressure transducer, which is similar to that of the piezoelectric transducer in terms of basic

structure, as both of them contain diaphragm, cavity and substrate [56]. In addition to that, a piezoresistive transducer also contains piezoresistors in the Wheatstone bridge configuration (Figure 2.6). In Wheatstone bridge configuration, only two of the four resistors are placed on the diaphragm while the other two are placed outside or close to the edge of the membrane. The deflection of diaphragm, due to an incident pressure, introduces a stress that leads to the change in resistance of the resistors as expressed by equation 2.4.

Initially, all four resistors have the same nominal value R. These resistors are generally arranged and sized in such a way that the resistance of two resistors located on the membrane increases by ΔR, whereas resistors located at the edge of diaphragm decrease by ΔR. The output of the transducer is a differential voltage that is given by [56], [71],

$$V_{out} = V_0^+ - V_0^- = \frac{\Delta R}{R} V_B \quad \ldots\ldots\ldots (2.5)$$

Where $\Delta R/R$ represents the relative change of resistance, and V_B and V_{out} represent the bias voltage and output voltage respectively. On the other hand, the pressure sensitivity S of the device can be expressed as [71],

$$S = \frac{\Delta V}{(\Delta P.V_B)} = \frac{\Delta R}{R}\left(\frac{1}{V_B}\right) \quad \ldots\ldots\ldots (2.6)$$

The sensitivity of the device is proportional to the stress in the diaphragm. Furthermore, high bias voltage is desirable to have better sensitivity of the device; however the maximum bias voltage is limited by the power dissipation, heating and electro-migration [56], [70]. The increment of the bias voltage also gives rise to the "$1/f$ noise" of the transducer that is also known as conductance fluctuation [73], where f represents the frequency [70].

The performance of the piezoresistive transducer is influenced by the temperature as well. The voltage fluctuation due to the random vibration of charge carriers in equilibrium with the lattice increases with temperature. The rising temperature initiates the increase in leakage current in the junction that isolates the device. As a result, a piezoresistive transducer exhibits temperature drift in the sensitivity as the operating temperature varies. The piezoresistive coefficients π_i are temperature dependent, which also impact the sensitivity. This problem can be corrected through the use of circuitry [56], [74].

Piezoresistors can be arranged in different ways on the device. Figure 2.7 illustrates the cross-sectional view of typical configurations of piezoresistive transducer. Piezoresistors can be embedded in the diaphragm structure as illustrated in Figure 2.7(a), where the piezoresistors are generally isolated from the diaphragm by a reverse biased pn-junction, or piezoresistors can be dielectrically isolated from the diaphragm as shown in Figure 2.7(b).

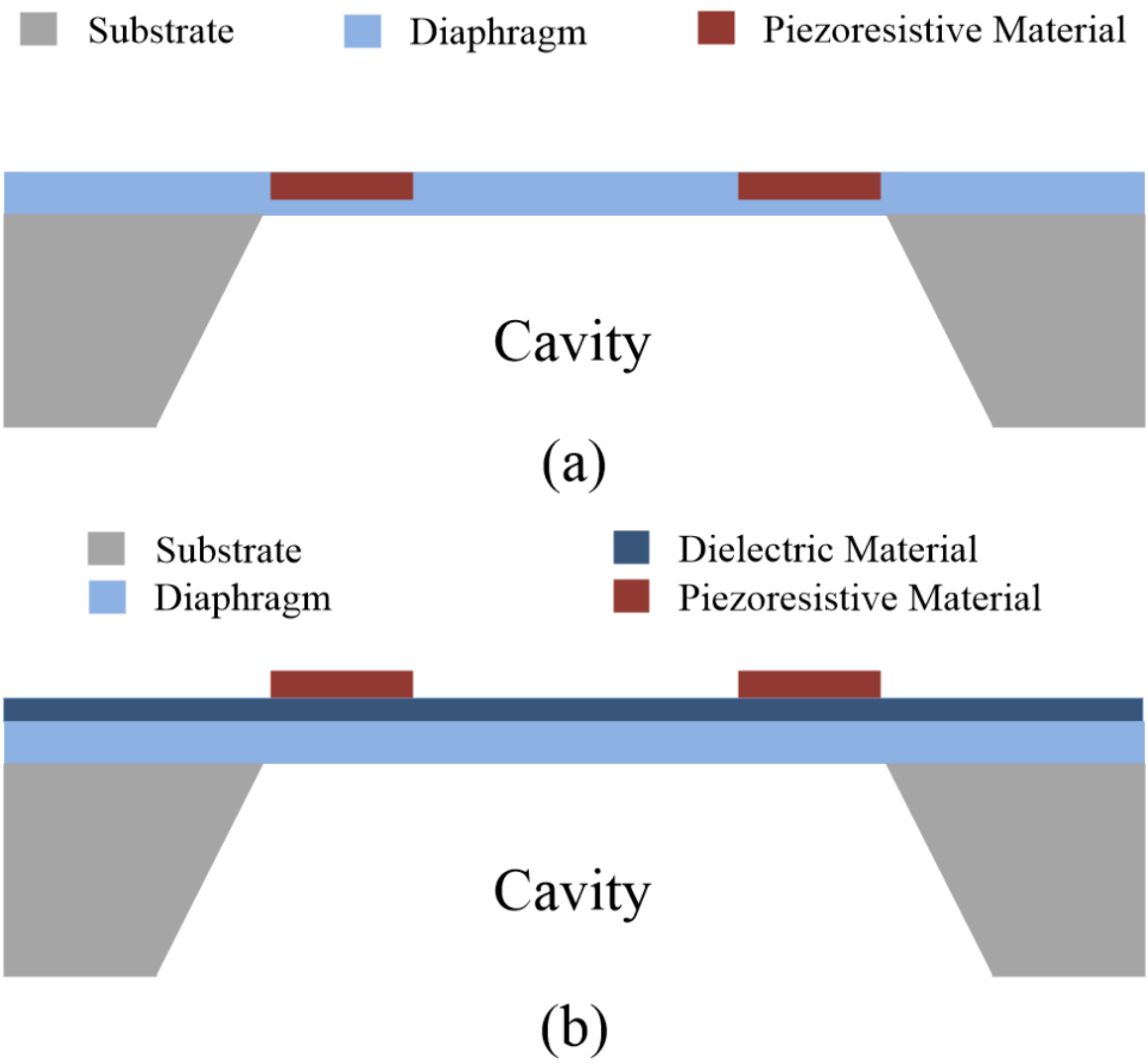

Figure 2.7: *Schematic diagram of cross sections of representative piezoresistive transducer device with (a) junction isolated piezoresistors [75], and (b) dielectrically isolated piezoresistors [72].*

Generally, the minimum detectable pressure level that can be transduced by the piezoresistive sensing device is lower than that of the others. However, the design of the diaphragm, piezoresistors and the fabrication process also play an important role for the

optimum detectable low minimum pressure level of this device [74], [76]. Piezoresistive transducer is not influenced by the parasitic capacitance, and thus allows the use of instrumentation amplifiers without great concern of the input capacitance of the amplifier. Moreover, the sensitivity of this type of transducer can be enhanced by increasing the diaphragm area [2].

The piezoresistive acoustic transducer was first demonstrated by Burns in 1957 [77], using n-type germanium. The device was constructed with a cantilever beam arrangement, based on a macro scale aluminum squared diaphragm with side length of about 20 cm. The deflection of the diaphragm was transferred to a piezoresistive bimorph cantilever that consists of two slabs of n-type germanium of 400 μm thickness. Peake *et al.* [78] proposed a piezoresistive MEMS transducer in 1969, which was constructed with two single crystalline piezoresistive p-type silicon on the n-type silicon substrate. The change of resistance due to incident pressure modulated the oscillation frequency. The surface of the wafer was passivated using thick silicon nitride layer to obtain long term stability and to avoid drift due to humidity.

Combined micromachining and microelectronics process have also been used to fabricate piezoresistive MEMS acoustic transducer with square diaphragm made of silicon, with thickness of 1 μm and an area of about 1 mm^2 [72]. The transducer was manufactured using p-type polysilicon piezoresistors, separated dielectrically from the highly boron doped silicon layer on silicon diaphragm. The resistance of the device varied from 300 Ω to 21 kΩ based on the doping concentration. The device provides a sensitivity of 25 $\mu V.Pa^{-1}$ for supply voltage of 6 V, and relative flat frequency response was observed between 100 Hz and 5 kHz with fluctuation of ±3 dB.

Kälvesten *et al.* [79] demonstrated a piezoresistive pressure transducer, based on surface micromachining techniques, for the measurement in turbulent gas flows, which consists of square diaphragm made of polysilicon with side length of 100 μm and thickness of 0.4 μm. The device exhibited flat frequency response between 10 Hz to 10 kHz with fluctuation of ±2 dB. The sensitivity and the noise of the device were recorded as 0.9 $\mu V.Pa^{-1}$ for bias voltage of 10 V, and 96 dB(A) respectively. In 1995, Kälvesten *et al.* [80] introduced piezoresistive transducers having high resonant frequencies. Two different diaphragm, made of polysilicon, with side length of 100 μm and 300 μm, and thickness of 0.4 μm, were done. Both devices were equipped with four piezoresistors arranged in the Wheatstone

bridge configuration. The sensitivity of transducers was 0.9 μV.Pa^{-1} and 0.3 μV.Pa^{-1} for smaller and larger diaphragm sizes respectively, at bias voltage of 10 V. An integrated pressure-flow sensor with square diaphragm of polysilicon was also reported, where flow sensor was fabricated based on gas cooling of a polyimide-insulated heated mass [81], that consists of pressure sensing polysilicon diaphragm of 100×100×0.4 μm^3, and exhibited sensitivity of 0.9 μV.Pa^{-1} for bias voltage of 10 V, and frequency response between 10 Hz to 10 kHz within ±2 dB variation.

An acoustic sensor, based on electrochemically etched silicon diaphragm, for airborne sound was reported [75]. The device consists of a membrane of thickness of about 1.3 μm and area of 1 mm^2, and four active piezoresistors, based on boron-implanted monocrystalline silicon, located on the diaphragm. The maximum sensitivity of the device was 80 μV.Pa^{-1} for 8 V bias voltage with flat frequency response between 50 Hz to 10 kHz with fluctuation of ±2 dB, and the lowest measured noise floor was 61 dB(A). The sensitivity of such device could be enhanced by reducing the in-plane stress of the diaphragm as well as by an improved piezoresistor design.

A piezoresistive transducer with silicon nitride diaphragm having radius of 105 μm and thickness of 0.15 μm was presented for wind-tunnel acoustic measurement by Sheplak *et al.* [82], [83]. The device was equipped with four p-type single-crystalline silicon piezoresistors, isolated dielectrically from the diaphragm, and exhibits a sensitivity of 1 μV.Pa^{-1} for 10 V bias voltage with flat bandwidth from 200 Hz to 6 kHz, and a noise floor of 92 dB at 250 Hz. In 2001, Arnold *et al.* reported a modified piezoresistive transducer with larger diaphragm, piezoresistors with lower resistance, and passivation layer to minimize the drift [84]. The device showed average sensitivity of 0.6 mV.Pa^{-1} for bias voltage of 10 V, with reduced noise floor of 40 dB.

Naguib *et al.* [85], [86] developed MEMS piezoresistive acoustic/pressure sensors, where four dielectrically isolated mono-crystalline ion-implanted p^{++} silicon piezoresistors were used. The transducers consisted of silicon nitride/oxide diaphragm with thickness of 0.4 μm, and size of 510×510 μm^2 and 710×710 μm^2, and exhibit sensitivity of 10 μV.Pa^{-1} at a bias voltage of 10 V. In 2002, Huang *et al.* [87] reported a piezoresistive MEMS sound detector, fabricated using dissolved wafer process [88] and consists of stress compensated silicon nitride/oxide membrane of 710×710 μm^2 and thickness of 0.38 μm. Poly-crystalline silicon piezoresistors were isolated dielectrically from the diaphragm. The device showed

static sensitivity of 1.1 μm.Pa^{-1}.V^{-1} over bandwidth of 100 Hz to 10 kHz with 2% nonlinearity.

A piezoresistive transducer with integrated amplifier was presented [89], [90], where four polysilicon piezoresistors were mounted on the edge of the silicon nitride membrane of 1 μm thick. The airborne sound sensitivity of the device was 50 μV.Pa^{-1} for bias voltage of 5 V, and exhibited a flat frequency between 100 Hz and 8 kHz within ±3 dB fluctuation. Beclin *et al.* demonstrated a high sensitivity piezoresistive transducer with p-type poly-silicon piezoresistors and 3D membrane for aerospace applications [71] that showed sensitivity of 50 μV.Pa^{-1}.V^{-1} with flat frequency response between 3 Hz to 600 Hz.

Therefore, several piezoresistive acoustic/pressure sensors have been reported for different applications, where silicon is generally used as piezoresistors. Studies show that the early devices have problems due to high noise floors. Moreover, sensor with single crystal silicon substrate suffers from higher temperature sensitivity than those of polycrystalline silicon. These devices have low output impedance, which make them relatively immune to interference noise, resulting in relatively simple amplifier design and packaging requirements [90]. Table 2.4 summarized the specifications of the piezoresistive acoustic/pressure sensors discussed above.

Table 2.4: Summary of the specifications of piezoresistive acoustic/pressure sensors.

Author(s)	Diaphragm Dimensions	Bias Voltage	Sensitivity	Bandwidth
			μV.Pa^{-1}.V^{-1}	
Burns [77]	20.32 cm$^{\pm}$×N/R	N/R	N/R	N/R
Peake *et al.* [78]	N/R†	N/R	N/R	N/R
Schellin *et al.* [72]	1mm*×1μm	6 V	4.17	100 Hz – 5 kHz
Kälvestin *et al.* [79]–[81]	100μm*×0.4μm	10 V	0.09	10 Hz – 10 kHz
Kälvestin *et al.* [80]	300μm*×0.4μm	10 V	0.03	10 Hz – 10 kHz
Schellin *et al.* [75]	1mm*×1.3μm	8 V	10	50 Hz – 10 kHz
Sheplak *et al.* [83]	105μm†×0.15μm	10 V	0.1	200 Hz – 6 kHz
Arnold *et al.* [84]	500μm†×1.0μm	10 V	0.6	1 kHz – 205 kHz
Naguib *et al.* [85], [86]	510μm*×0.4μm	10 V	1	1 kHz – 5.5 kHz
Naguib *et al.* [85], [86]	710μm*×0.4μm	10 V	1	1 kHz – 5.5 kHz
Huang *et al.* [87]	710μm*×0.38μm	N/R	1.1	100 Hz – 10 kHz
Li *et al.* [89]	N/R×1.0μm	5 V	10	100 Hz – 8 kHz
Beclin *et al.* [71]	N/R	N/R	50	3 Hz – 600 Hz

* Side length of square diaphragm. † Radius of circular diaphragm.
$^{\pm}$ Side length of cantilever diaphragm.

Among different types of available acoustic sensors, capacitive acoustic transducer consumes low power, while exhibits the highest sensitivity [3]. In addition, capacitive

sensing is independent of the base materials and relies on the capacitance variation due to change in the geometry of the capacitor. A capacitive acoustic transducer can also be used both as active and passive sensing devices. Moreover, to improve the localization of RFID tag, the development of the hybrid system combining existing UHF RFID tag and capacitive acoustic sensor with adequate sensitivity and selectivity is required.

Thus, within the "Spinnaker" project framework and to fulfil the low cost manufacturing of the transducer, printing techniques have been adapted during this work to develop the capacitive acoustic transducer.

2.2. Printed electronics

The term printed electronics (PE) defines the printing of electronic circuits on substrates. Different printing methods and techniques, suitable for defining patterns on materials,, can be used to fabricate electronics devices, components and interconnections on substrates. Printing techniques can also be used alone or in combination with conventional microelectronic components such as silicon chips for a range of different applications. Various kind of materials, such as conducting, semiconducting and other functional materials, can be used to create patterns on a wide range of substrates including flexible media [91], [92]. Nowadays, printing techniques are used to produce several active and passive electronic devices, such as thin film transistors, sensors and resistors.

Rapid development is going on in the field of printed electronics for a wider array of novel applications, which could lead to more efficient, affordable, and commercially and economically viable products in future. Printing techniques offer several unique features, namely, simple fabrication steps and thus less production complexity, reduced logistic costs and thus low cost final product, large area device, high volume production, high throughput, flexible structure, less materials waste during manufacturing and environmentally friendly [91], [92]. In addition to that, printed electronics process requires relatively lower processing temperature in atmospheric condition. Thus, printed electronics enable the production of electronic components or devices which are lightweight and small, thin and flexible, inexpensive and disposable [92]. Some of the interesting end applications of printed electronics are antennas, radio frequency identifications (RFIDs) tags, sensors, thin batteries, security devices, light emitting diodes (LED) and OLEDs for displays, e-paper,

photovoltaics (PV), active matrix (AM) or passive matrix (PM) display backplanes, membrane switches and flexible printed wiring boards (PWB).

Solution or liquid based printing techniques have been developed for centuries to manufacture components that are similar to conventional electronics in terms of functionality, at greater production speed, less cost and less manufacturing complexity. The reproducible printing efficiency of well-defined forms has inspired researchers to explore the potential of printing techniques to print various materials on various substrates [93]. Printing methods can be classified as: contact printing techniques, such as flexography, offset lithography, gravure printing, and screen printing, where printing plate or mesh (stencil screen) has direct contact with the substrate [94], and direct write printing techniques, such as tip-based direct writing, energy beam-based direct writing, aerosol jet direct writing and inkjet printing [95], [96]. Amongst different printing methods, direct write techniques do not require the fabrication of hard masks, facilitate the simplified processing and can be used to print on complex substrates topologies, as it is a non-contact mode of printing [97]–[100].

2.2.1. Direct write (DW) technologies

Direct write (DW) technologies, also known as direct or digital printing, refer to any technique or process capable of depositing or dispensing different types of materials on various substrates without the help of any mask or etching steps with an enhanced speed with the aid of computer. It is an unusual technology as it covers a vast length scale from tens of nanometers to several millimeters in terms of line width, which offers huge application potential. Large range of materials can be deposited using DW technologies, including metals, ceramics and polymers, electronically and optically functional materials as well as biological materials including living cells. DW technology helps the electronic industry to miniaturize the electronic circuits and enhance printing speed capability. DW technologies reduce the materials loss more effectively and thus are more cost efficient [95].

2.2.1.1. Tip-based direct write

Tip-based direct writing is a nanomanufacturing method represented by two processes, namely, dip-pen nanolithography (DPN) where molecules are diffused on to a substrate in

an ordered pattern through the micro-capillary action between tip and the surface, and nanofountain pen (NFP) where micro-pipette is used [95].

Dip-pen nanolithography is a general nanoscale direct writing or nanopatterning method that is performed by pyramidal scanning probe microscope tips, like traditional atomic force microscopy (AFM) tips, hollow tips and even tips on thermally actuated cantilevers [95], [96]. Generally during DPN direct writing, AFM probe is dipped in an ink and then the ink is transferred to the substrate of interest to create nanometric patterns by capillary transport in a positive printing mode [95]. Deposition process consists of three steps, namely, molecular deposition, lateral diffusion on a monolayer of molecules and finally termination of diffusion by chemical binding to a substrate [101], [102]. During DPN direct writing, the tip is in direct contact with the surface, either physically or through a meniscus [103], as presented in Figure 2.8 (a).

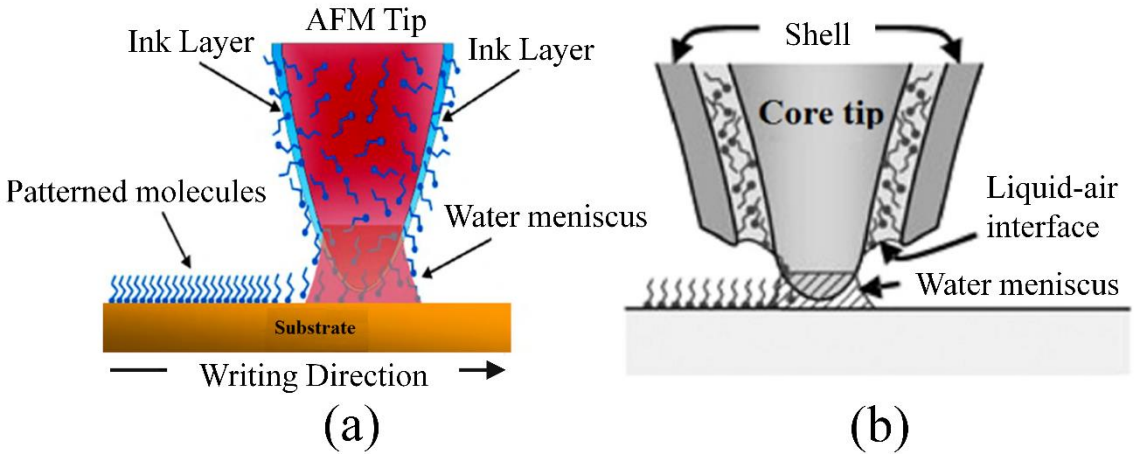

Figure 2.8: *Schematic diagram of (a) Deposition of a monolayer of molecules by DPN process where the ink molecules transfer from an AFM probe to the substrate [103], (b) the nanofountain pen [95].*

The limitation of the original DPN technique is its inability to turn the ink flow on and off, which has been solved by developing the thermal DPN (tDPN) by using easily melted solid as inks and special AFM cantilever with built-in resistive heater [95], which allows the operator to control the deposition of amount of the ink onto the substrate surface [103].

On the other hand, nanofountain pen (NFP) technique uses cantilevered nanopipette instead of the AFM tip. The pipette is filled with the solution to be deposited and the liquid flows

to the substrate when the pipette is placed in contact with the surface. Figure 2.8(b) presents the NFP technique [95].

Generally tip-based direct writing has been mainly used for the deposition of biological inks such as DNA, active enzymes, proteins or polymers. Several authors have reported the deposition of conductive traces [96]. However, this technique can also be used to deposit conducting ink with impressive line resolution, by just dipping the tip either in a metal nanoparticle based ink [104]–[106] or in an ionic solution containing metallic salt complexes [107].

2.2.1.2. Energy beam based direct writing

Energy beam based direct writing refers to the technologies that use high-power lasers to transfer and/or propel materials onto a substrate, such as laser-enhanced electroless plating (LEEP) [95], matrix-assisted pulsed laser evaporation direct-write (MAPLE-DW) [95], laser-engineered net shaping (LENS) [108], laser-guided direct write (LGDW) [109]–[111], laser-induced forward transfer (LIFT) [95], [111], etc. Amongst these, LIFT is the well-established technique.

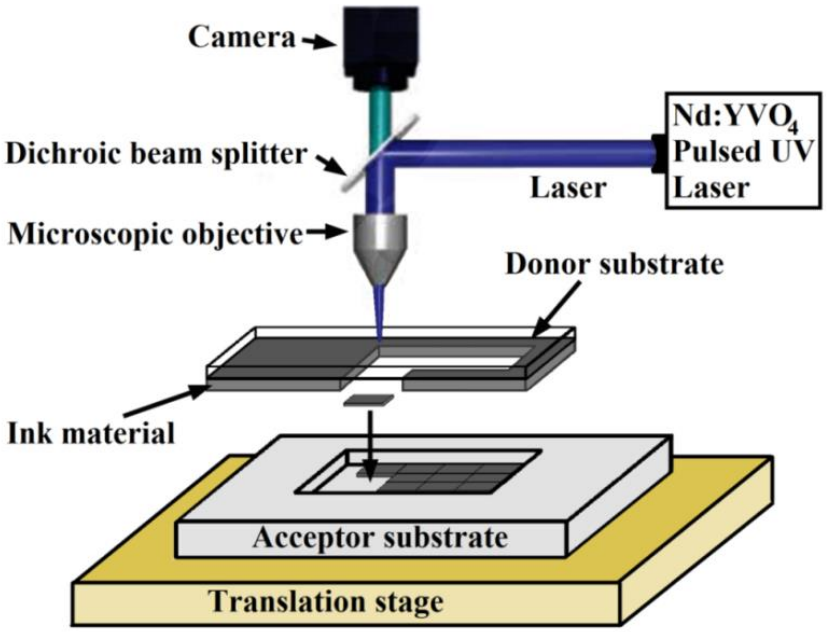

Figure 2.9: *Schematic diagram of laser direct write addition process showing deposition within the substrate.*

Laser induced forward transfer (LIFT) enables high resolution printing of varieties of functional materials, where a pulsed laser beam is used to release materials from thin donor films to a receiving substrate (Figure 2.9). During the process, donor material is initially deposited either in liquid or in solid form on an optically transparent substrate, also known as donor substrate. The application of focused laser pulses results in vaporization of a small quantity of material at the interface between the donor ink and its supporting substrate. This volumetric expansion, induced by the vaporization, propels the material forward. The material recondenses on the receiver substrate that is normally placed 25-100 microns below and parallel to the donor substrate [95], [96].

Large variety of materials, such as metals, ceramics, semiconductors and biomaterial, can be transferred and deposited using laser direct writing technologies. Ink materials are generally processed from materials in powder form and then mixed with an organic or polymer binder. The properties of the matrix materials are such that under laser irradiation, the binder absorbs the laser energy and is preferentially vaporized [111]. However, LIFT technique is incompatible with large area processing, as there are some limitations related to the preparation of the donor substrate [96].

2.2.1.3. Aerosol jet direct writing (A-DW)

Aerosol direct write, also known as Mesoscale Materials Deposition (M3D), refers to the additive process, where an aerosol beam is focused and directed toward a substrate to produce desired patterns without using masks or post-patterning [95], as illustrated in Figure 2.10. Operation of M3D consists of three steps. The aerosol jet process initiates with the atomization of an ink, using different types of atomization technique, such as ultrasonic and pneumatic, depending on the ink parameters. Generally, ultrasonic atomizer is used for low viscosity ink and pneumatic atomizer is used for relatively viscous ink. The aerosol is then entrained in a carrier gas stream, such as nitrogen (N_2), and delivered to the deposition head. Thereafter, within the printing head, an annular flow of sheath gas is introduced around the aerosol stream which acts as a focusing mechanism by occupying the outer portion of the flow tube. As a result, the aerosol droplets form a focused beam of material. The jet of droplets exits the deposition head at high velocity of 10 m/s to 100 m/s and deposited onto a substrate [95], [112].

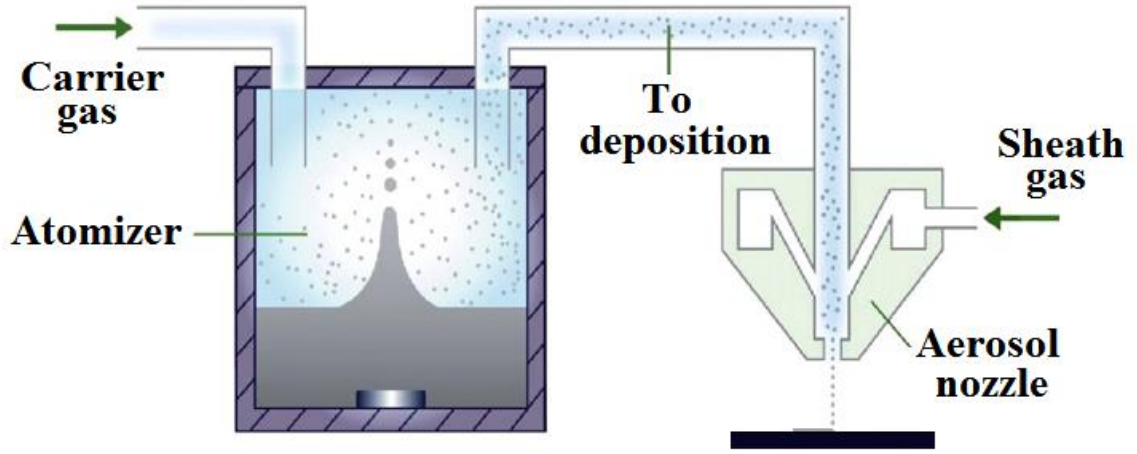

Figure 2.10: *Schematic diagram of aerosol jet direct write system [95].*

A wide range of materials, such as metals, alloys, ceramics, polymers, adhesives or even biomaterials, can be deposited using the aerosol jet process [95]. The aerosol jet technique is generally used for the deposition of 2D and 3D interconnects for micro-packaging, passive devices, and photovoltaics. However, this technique is limited by its low throughput [95], [96].

2.2.1.4. Inkjet printing technology

Inkjet printing, a non-contact method of printing, converts digital image by propelling ink droplets onto the substrate. Generally droplets of ink are formed from the repetitive jetting of ink by printing head. Thus, the basic principle of inkjet printing is the breaking-up of liquid into droplets at the nozzle boundary under imposed surface tensions, known as the Rayleigh-Tomotika instability [96]. Based on the printing head technologies, inkjet printers can be classified into two types, namely, continuous inkjet mode (CIJ) and drop-on-demand (DoD) [93], [94], [98], [99]. CIJ and DoD technologies can also be subdivided, based on their ink jetting methods. Figure 2.11 illustrates the full classification of inkjet printing technique [94].

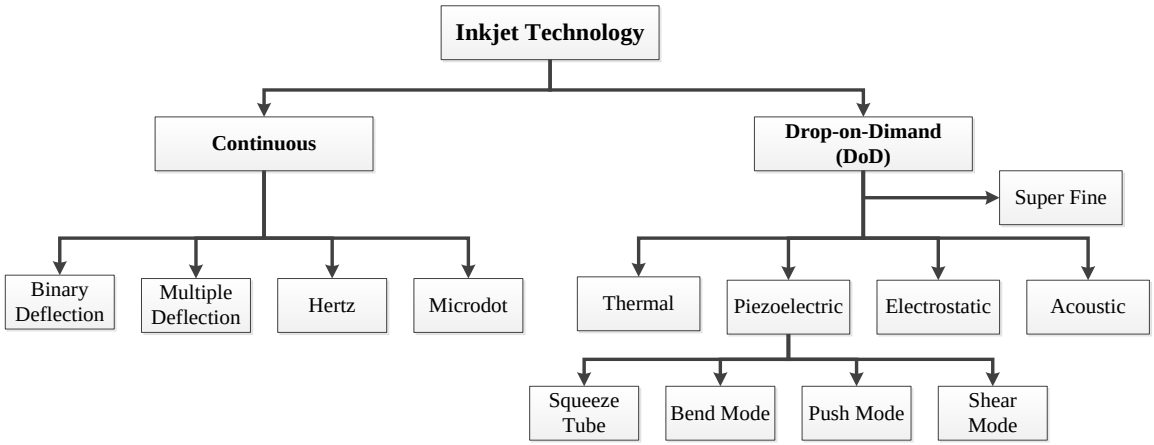

Figure 2.11: *Classification of inkjet printing techniques [94].*

2.2.1.4.1. Continuous mode inkjet printing technique

In continuous inkjet (CIJ) system, continuous stream of ink droplets are created via the Plateau-Rayleigh instability. Liquid ink from reservoir is forced by a high pressure pump through the gunbody and a microscopic nozzle. Piezoelectric crystal inside the gunbody creates an acoustic wave as it vibrates, causes the falling stream of liquid to break into droplets at regular intervals. Thereafter, droplets are subjected to the electrostatic field created by charging electrode. As a result, electrostatic charges form on the surface of the droplets, which can be adjusted by varying the electrostatic field as per desired degree of droplet deflection. Generally charged droplets are separated by one or more uncharged droplets, known as guard droplets, to minimize repulsion between neighboring droplets [93], [94], [99].

The route of these charged droplets is controlled by the electric field created by charged deflection plates, which deflects charged droplets to their intended location on the substrate. Uncharged ink droplets are not deflected by the electrostatic field and thus are not used for printing. During this technique only small fraction of ink is used for printing and the majority of the ink is collected in a collection gutter and then reused [93], [94], [99]. Figure 2.12 illustrates the continuous inkjet (CIJ) printing system.

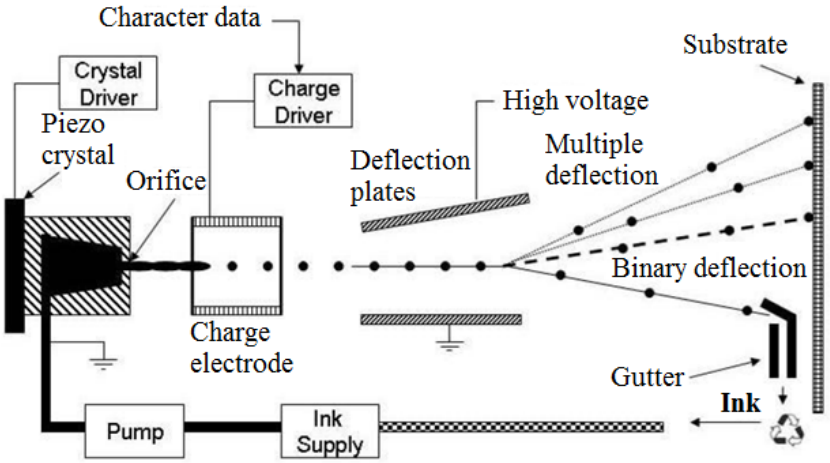

Figure 2.12: *Schematic diagram of the CIJ printing system [94].*

The continuous inkjet (CIJ) printing system produces high velocity ink droplets that allow a relatively long distance between printing head and substrate during printing. CIJ printing speed is relatively very high due to high drop ejection frequency. Moreover, in CIJ system there is no clogging of nozzle as the ink jet is always in use for all the nozzles. Generally, CIJ is commercially used to produce barcodes and labels of products and packaging [94]. However, the limitations of CIJ printing are the requirement of electrically chargeable ink and a relatively low printing quality [99].

2.2.1.4.2. Drop-on-demand inkjet (DoD) technology

DoD inkjet printing system can jet single ink droplet as per requirement [93], where the droplet is formed by increasing the pressure inside the ink reservoir. The increase in pressure inside the ink reservoir can be achieved generally by using two approaches, namely, thermal or piezoelectric printhead [93], [94], [96], [98], [99].

In the thermal inkjet system, the cartridge consists of a series of small ink chambers, and each of these chambers contains a resistive heater. In order to eject a droplet from each chamber, an electrical pulse is applied to a resistive heater that causes rapid local vaporization of the ink within the nozzle reservoir which eventually creates a bubble. The formation of bubbles causes a large increase in pressure inside the ink chamber and thus droplets are consecutively ejected from the nozzle due to the relative pressure difference with the atmosphere (Figure 2.13). The surface tension of the ink, as well as the condensation and thus the contraction of the vapor bubble during cooling, leads to the cavity refilling [93], [94], [96], [99], [98]. The inks for thermal inkjet printing contain

volatile component to form vapor bubble to facilitate the ink droplet ejection [98], [99]. Generally, water-based inks are preferable for thermal inkjet printing technique as they produce explosive bubbles more efficiently than other solvent-based inks [94].

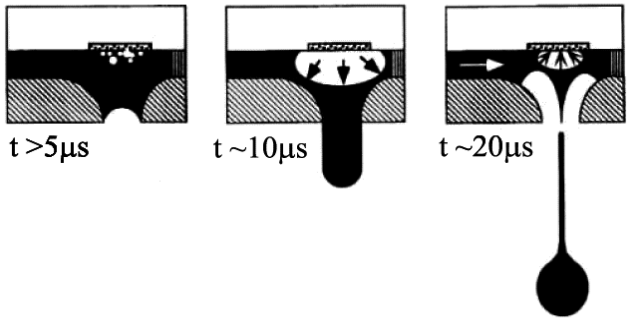

Figure 2.13: *Schematic diagram of thermal inkjet printing system.*

On the other hand, in piezoelectric DoD inkjet printer, a piezoelectric crystal, such as lead zirconium titanate (PZT), in an ink-filled chamber behind each nozzle is used instead of a heating element. The actuation is performed by the application of bipolar voltage pulse to the piezoelectric material to generate a pressure difference within the nozzle cavity forcing a droplet of ink to form [93], [94], [96], [98], [99]. Finally, the reservoir is refilled when a positive voltage is applied [96]. Wide variety of inks can be used for piezoelectric inkjet printing system. Unlike ink for thermal inkjet system, there is no requirement for any volatile component. However, the printing heads of this system are expensive due to the use of piezoelectric material. Figure 2.14 presents the piezoelectric inkjet system.

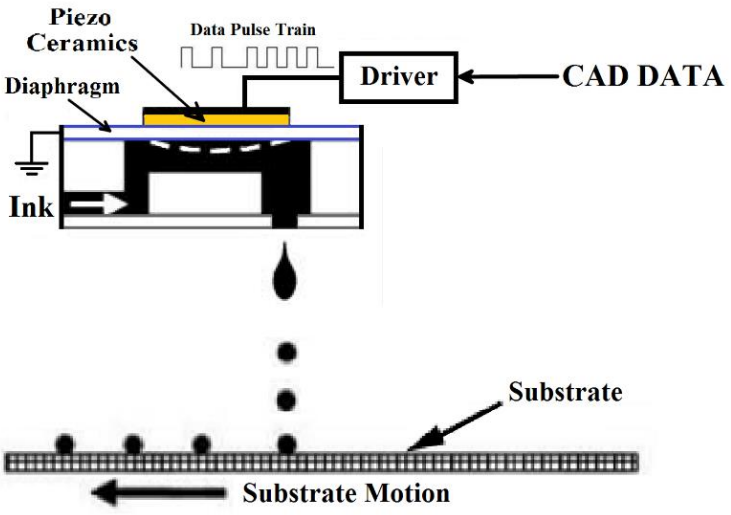

Figure 2.14: *Schematic of the DoD inkjet printing system.*

The major benefit of using inkjet printing technology is its ability to print on a large area with high printing speed and precision. However, sometimes process instabilities, such as nozzle plate defects or nozzle clogging, can trigger the generation of undesired artifacts such as deviated jets or unwanted droplets of ink. In addition, inkjet-printing is limited by the availability of functional inks with consistent rheology and properties (e.g., viscosity, surface tension, etc.) [93], [96], [98], [99], [113].

Therefore in summary, printing methods are relatively new, emerging and attractive technologies area for electronic components manufacturing in an efficient and cost effective way and can handle a large variety of materials. Table 2.5 presents a summary of the main characteristics of the previously mentioned printing technologies.

Table 2.5: Summary of the main characteristics of direct write technologies [93]–[96].

Technique	Line resolution (µm)	Deposition rate	Ink viscosity (Pa.s)
DPN	0.01 – 1	12-60 µm/min	-
NFP	0.04 – 1.15	24 µm/min	-
LIFT	10 – 100	0.18-3 m/min	-
LGDW	2	$60x10^{-4}$ mm^3/min	< 2.5
A-DW	5 – 5000	15 mm^3/min	< 2.5
CIJ	167	120-500 m/min	0.002 – 0.01
DoD inkjet	40	18 mm^3/min	0.01 – 0.1

Amongst different DW techniques, piezoelectric DoD inkjet system is flexible and versatile, and can be set up with relatively low effort [98], [99]. It is one of the most mature and its droplet ejection mechanism is well understood. During this work, the piezoelectric DoD inkjet printing system is used.

2.2.2. Inkjet printing for printed electronics

Inkjet printing, especially, piezoelectric DoD inkjet printing system has been widely applied to printed electronics technologies because of its excellent compatibility with functional inks [100]. Over the last few years, the electronic printing and materials technology become more sophisticated and efficient. With the development of printable organic semiconductors, high-resolution inkjet printing systems and low-cost, high reliability flexible substrates, the manufacture of electronics devices by high-speed inkjet printing has become an industrial reality [97].

2.2.2.1. Inkjet printable ink

Inkjet technology has been used to deposit a very wide range of materials for many different applications, namely, metals, ceramics and artificial polymers, as well as various biological materials including living cells [95], with the only restriction being that the material must be in liquid form with appropriate physical properties, such as the viscosity and surface tension, at the point of printing. The ink viscosity of inkjet should be low, typically in the range of 3-20 mPa.s [113], [114], because, when too much kinetic energy is viscously dissipated into ink, no ejection of ink droplet takes place. The surface tension of the ink should be higher than 30 mN/m to prevent dripping of the ink from the nozzle [114]. In addition, the wetting behavior of fluid and nozzle materials are also very important [113].

Generally, metal nanoparticles based ink is used as conductive ink in inkjet printing system. The reliable jetting of conductive nanoparticles depends on the careful control of the particle size, low agglomeration and their stable dispersion [97]. Smaller particles are preferable as it provides more stable suspensions, reduced sedimentation and nozzle clogging. In addition, the high surface to volume ratio leads to a low temperature sintering [95]. Generally, dispersant is used to develop stabilized nanoparticle ink, however, it coats the individual particles with insulating layer. Therefore, a post-cure at high temperature is required to drive off the additives and ensure contiguity of the particles [95], [97], [100]. For printed electronics application, the use of silver based conductive nanoparticle ink has been well established, since other metals require sintering at higher temperatures and inert atmospheres. In addition, silver exhibits the highest electrical conductivity among metals and is also resistive to oxidation [100], [115]. Furthermore, polymeric conductive ink, such as poly(3,4-ethylenedioxythiophene) polystyrene sulfonate (PEDOT:PSS), dielectric and semiconductive inks are also used for many applications. However, the polymer solution should be sufficiently diluted to maintain the viscosity of the ink within the inkjet printable range. Table 2.6 listed classification of functional inks that have been generally used in inkjet printing process. During this work, commercially available silver nanoparticle based ink, namely, SunTronic Solsys Jettable silver U5603 (20 wt.%) and U5714 (40 wt.%) from SunChemical, and Silverjet ANP DGP-HR from Advanced Nano Products (ANP) are used. Their characteristics are listed in Table 2.7.

Table 2.6: Classification of different functional inks and their properties used in inkjet printing [97]

Functional Ink	Properties	Examples
Conductive	▪ Metal-based submicron particles ▪ Bulk conductivity >10^4 S/m ▪ Low T_p <200 °C	Ag and Cu conductive inks; Ag/Cu alloys; materials containing Nickel; platinum and palladium; TCOs-ITO, AZO, GZO; PEDOT:PSS;
Dielectric	▪ Polymeric/nanoparticle based ▪ Electrical resistivity >10^{14} Ω.cm ▪ Film thickness <5µm, ▪ Permittivity (2-20) ▪ Low loss Semiconductor compatible band gap ▪ Low T_p <200 °C.	Polyvinylpyrrolidone; Poly-4-vinylphenol+Gold nanoparticles; Polyethylene, poly(vinyl alcohol); Poly(vinyl phenol); Poly(methyl methacrylate); Poly(ethylene terephthalate); Silica and Alumina;
Semiconductor	▪ Organic or inorganic ▪ Electron mobility 10^{-2}-10^1 cm^2/Vs ▪ Low T_p <200 °C.	Pentacene; Polythiophene; Poly(p-phenylene vinylene) - PPV; MEH-PPV; BEHP-PPV; Polyfluorene;
Resistive	▪ Organic or inorganic ▪ Resistance 10-100 KΩ ▪ ±10% nominal resistance tolerance	Carbon-filled vinyl-based thermoplastic binder;

T_p = Processing temperature.

Table 2.7: Characteristics of commercially available silver nanoparticle based ink

Ink	**Suntronics U5603** [116]	**Suntronics U5714** [116]	**Silverjet ANP DGP-HR** [117]
Supplier	SunChemical	SunChemical	ANP
Solvents	Ethanol, Ethanediol, Glycerol	Ethanol, Ethanediol, Glycerol	Triethylene glycol monoethyl ether (TGME)
Mean Diameter (nm)	30 – 50	30 – 50	10
Silver Content (wt.%)	20	40	30 ~ 35
Viscosity (mPa.s)	10 – 13	10 – 13	10 ~ 17
Surface Tension (mN/m)	27 – 31	27 – 31	35 ~ 38
Curing Temperature (°C)	150 – 300	150 – 300	120 ~ 250
Electrical Resistance (µΩ.cm)	5 – 30	5 – 30	11 ~ 12

2.2.2.2. Operation principle of DoD inkjet printing system

In drop-on-demand (DoD) piezoelectric inkjet printing system, the fluid is ejected in a controlled manner through the nozzle from an ink reservoir in response to a pressure or acoustic wave pulse generated by an actuator [95]. Figure 2.15 illustrates the schematic

diagram of simple piezoelectric DoD inkjet printhead. The nozzle end of the printhead geometry is considered as being closed, as the cross-sectional area of the nozzle opening is small compared to that of the capillary; whereas the ink supply end is considered as being open end, because the inside diameter of the supply tube is considerably larger than that of the capillary [118].

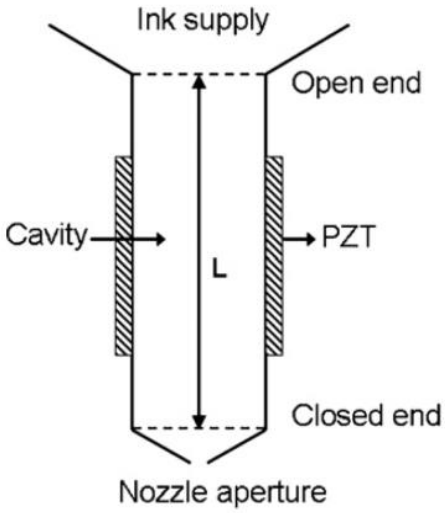

Figure 2.15: *Schematic diagram of a piezoelectric printing head [118].*

Initially the radial outward movement of the piezoelectric actuator due to the application of voltage creates a negative pressure or acoustic wave in the fluid. This negative pressure wave is then splits into two waves, travelling in opposite directions, with half amplitude. These two resultant waves are then reflected back from the two ends to meet in the middle. The reflected pressure wave from the nozzle (closed end) remains in same phase, whereas phase is reversed for the wave that is reflected from the open end [118].

At the same time, the rapid inward movement of the actuator, due to the voltage drop across the piezoelectric, initiates a positive pressure wave in the fluid. The newly formed positive pressure wave coincides with the meeting of the reflected waves, and subsequently interacts with them. The negative pressure wave is annihilated whereas the positive wave is doubled [118].

The fluid is pushed outwards when the double-amplitude positive pressure wave approaches the nozzle [118]. If the amount of kinetic energy transferred outwards is larger than the surface energy needed to form a droplet, the ejection of a droplet takes place. The velocity of the droplet depends on the amount of kinetic energy transferred. Studies showed

that, to overcome the decelerating action of ambient air, the initial velocity of a droplet has to be several meters per second [118], [119].

2.2.2.3. Drop generation

The generation of droplets in a DoD printing system is a complex process influenced by the physical fluid properties of the ink during printing, namely, density (ρ), dynamic viscosity (η), and surface tension (γ) of the fluid. Generally, number of dimensionless groupings of physical constants, such as the Reynolds (R_e), Weber (W_e), and Ohnesorge (O_h) numbers are used to characterized the behavior of the ink drops and can be expressed as follows [95], [120],

$$R_e = \frac{v\rho D}{\eta} \quad \ldots\ldots\ldots (2.7)$$

$$W_e = \frac{v^2\rho D}{\gamma} \quad \ldots\ldots\ldots (2.8)$$

$$O_h = \frac{\sqrt{We}}{\mathrm{Re}} = \frac{\eta}{(\gamma\rho D)^{1/2}} \quad \ldots\ldots\ldots (2.9)$$

Where 'v' is the velocity, and 'D' is a characteristic length, which is equal to the drop diameter.

The drop generation mechanism was explained by Fromm [118]–[120], using Z number grouping of the fluid properties that is equivalent to the inverse of the Ohnesorge number (O_h),

$$Z = (O_h)^{-1} = \frac{\mathrm{Re}}{\sqrt{We}} = \frac{(\gamma\rho D)^{1/2}}{\eta} \quad \ldots\ldots\ldots (2.10)$$

It has been established that for the DoD inkjet printing to take place, the condition $1 < Z < 10$ has to be fulfilled [118], [120], [121]. The lower limit of Z value is determined by the suspension's viscosity dissipating the pressure pulse and thus prevents drop ejection, whereas the upper limit represents the formation of satellite drops rather than a single droplet [95], [118], [120].

In addition, drop generation requires sufficient energy to overcome the influence of the fluid-air surface tension at the nozzle. The minimum required drop ejection velocity can be expressed as follow [120],

$$v = \left(\frac{4\gamma}{\rho D}\right)^{1/2} \quad \ldots\ldots\ldots (2.11)$$

Thus the fluid properties that are usually inkjet printable, can be graphically mapped in terms of R_e and W_e dimensionless groupings, as illustrated in Figure 2.16.

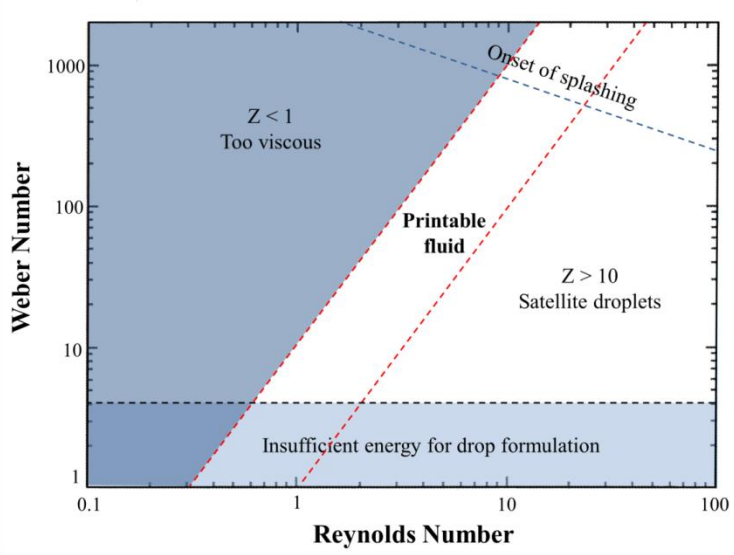

Figure 2.16: *Graphical presentation of printability and the fluid properties that are usually used for DoD inkjet system [120].*

2.2.2.4. Drop impact phenomena

The impact of the droplet on a dry solid non-porous substrate depends on the droplet size and velocity, the fluid properties, namely, density, viscosity, viscoelasticity and surface tension and substrate properties, such as roughness, surface energy and chemical homogeneity [122]. Dimensionless groupings, namely, Reynolds (R_e), Weber (W_e) and Ohnesorge numbers (O_h), are also involved in the impact process. Moreover, the Bond number (B_0), which can be expressed as follows, is also taken into consideration [122].

$$B_0 = \frac{\rho g D^2}{\gamma} \quad \ldots\ldots\ldots (2.12)$$

Here g is the gravitational acceleration.

Generally, inertial forces, capillary forces and gravitational forces drive the droplet impact phenomena. However, as the density and surface energy of the inkjet printable fluid is relative low and the diameter of the ejected droplets are usually below 100 µm, the influence of the gravitational force on the droplet impact is negligible [120].

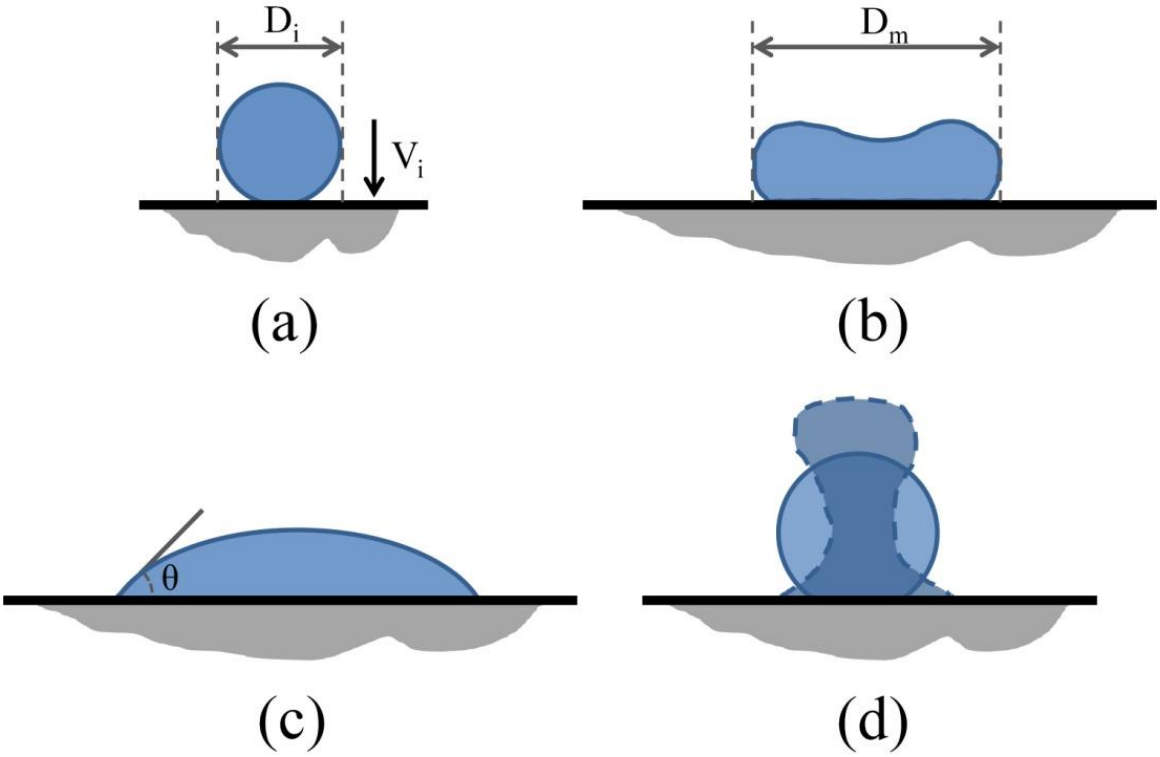

Figure 2.17: *Schematic illustration of the sequence of events that occurs after droplet impact on a substrate. Initial impact is followed by a series of damped oscillations before capillary-driven flow occurs, θ is the contact angle, D_i and D_m represents the initial droplet diameter and maximum droplet spreading diameter respectively, and V_i represents the droplet's impact velocity [95], [118], [120], [122].*

The impact of droplet on the substrate can be divided into several stages (Figure 2.17), as described by Yarin [122]. The initial stage is known as impact stage, which indicates the moment when the droplet hits the substrate, is governed by the kinematic behavior. This is followed by the impact driven spreading to an order of magnitude greater than that of the in-flight droplet radius, with an accompanying swift fluid flow that is radially outwards.

Finally, the fluid comes to rest due to damping of inertial rebound and a series of initial oscillations by viscous dissipation [95], [118], [120], [122].

In case of porous substrate, impact of droplet is strongly affected by the capillary force originated from the substrate porosity, and as a result the separation of functional material and the solvent of the ink takes place [122].

2.2.2.5. Substrate properties

Technically, inkjet printing system can deposit materials on a vast range of substrates, such as silicon wafer, glass, usual paper, textiles, other cheap substrates, and also on three-dimensional (3D) objects [97], [100]. However, because of the non-contact printing nature of inkjet technique, the dynamics of fluid setting on the substrate is substantially influenced by the properties of the substrate, and thus eventually defines the quality of the final printed layer.

Different substrates have different surface properties, such as surface energy, roughness, porosity, chemical homogeneity, which influence the liquid-surface interactions, and thus lead to different drop shapes and sizes. Therefore, different substrates provide different printing resolutions, even for the printing of same ink with identical printing parameters.

The tendency of a liquid to spread on a substrate is defined by the contact angle (θ_c). When the drops strike the substrate, the wetting of the substrate occurs according to Young's equation, which states that the surface tension pulling at the intersection of a vapor, a liquid, and a flat solid should balance along that surface, and the relationship can be expressed as [123]–[126],

$$\gamma_{sv} = \gamma_{sl} + \gamma_{lv}\cos(\theta_c) \ldots \ldots \ldots (2.13)$$

Here, γ_{SV}, γ_{SL} and γ_{LV} represent the surface energy of the solid-vapor (sv), solid-liquid (sl) and liquid-vapor (lv) interfaces respectively, and θ_c represents the measured contact angle, as presented in Figure 2.18. A contact angle greater than 90° indicates poor wetting, whereas a contact angle close to zero indicates complete wetting. A contact angle between 0° and 90° indicates good wetting [123].

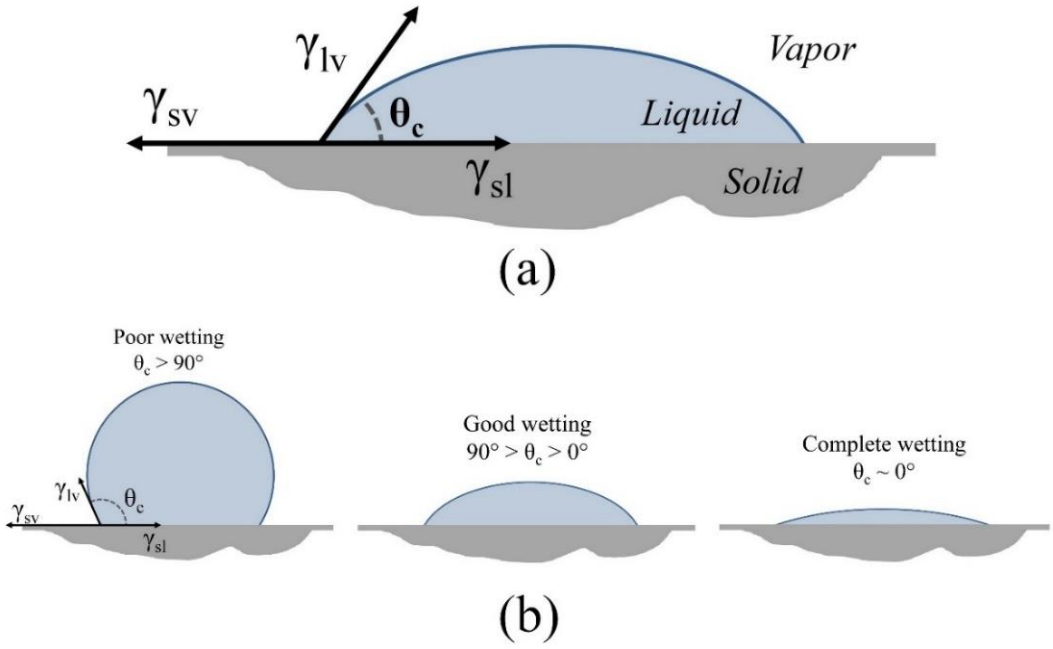

Figure 2.18: *Schematic diagram of (a) Contact angle of a liquid droplet wetted to a rigid solid surface, and (b) change in contact angle with liquid wetting.*

The wettability can be modified by physical or chemical surface treatment of the substrate. Physical treatments, such as plasma [127], [128] or corona [129], are generally employed to change the surface energy temporarily, or to clean the surface of the substrate from ambient pollution like moisture dust, whereas chemical treatments [130], e.g., chemical bath, are used for surface cleaning, and also for chemical functionalization.

During this work, different kinds of substrates have been used, namely, commercially available polyethylene terephthalate (PET) of thickness 8, 23, 480 µm, polyimide (PI) film of 125 µm, and 3D printed substrates. Table 2.8 listed the surface energy measured on PET and PI substrates, using Owens-Wendt-Rabel-Kälbe (OWRK) method [126], [131], [132].

Table 2.8: List of typical surface energy of the commercial substrate that have been used during this work measured using OWRK method

Substrate(s)	**Surface Energy (γ_{sl})** mN.m^{-1}
Polyethylene terephthalate (PET)	40.7 ± 0.2
Polyimide (PI)	43.6 ± 0.25

2.2.2.6. Printed line resolution

The resolution of the conventional inkjet printing system is limited by different factors including ejected drop size, drop-to-drop spacing during printing, viscosity and surface tension of the fluid, and surface energy or wettability of the substrate [133]. Width of the printed line (W), drop size or diameter (D_d) and drop spacing (D_S) are interconnected and illustrated in Figure 2.19. Some examples of printed lines are given in Figure 2.20.

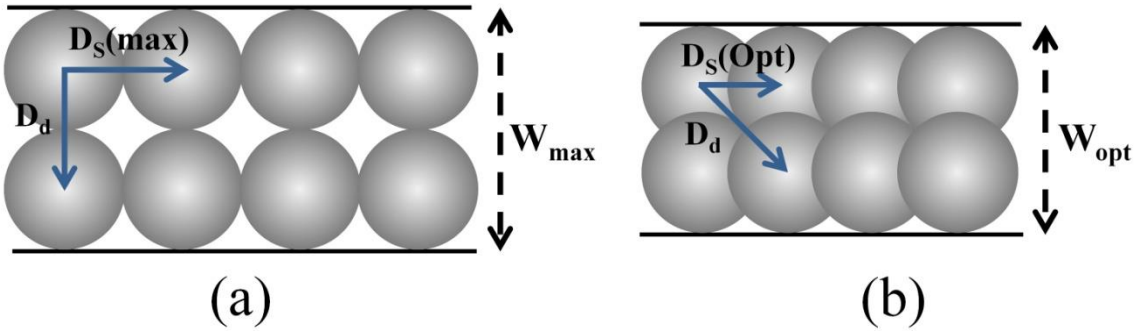

Figure 2.19: *Schematic diagram of printed line resolution that shows the relation between drop diameter, drop spacing and printed line width.*

The drop spacing calculated by equation 2.14, ensures that the diagonal dots are tangential and the adjacent dots are well connected.

$$D_S = \frac{D_d}{\sqrt{2}} \quad \ldots\ldots\ldots (2.14)$$

During inkjet printing process, the maximum drop spacing that can be used to form a continuous line is determined by the drop size or diameter of the liquid on the substrate, where two adjacent dots are barely connected as shown in Figure 2.22(a). However, the resolution of such printed pattern is low and the resistance is generally relatively high. With the decrease in drop spacing, the resolution of the printed pattern increases, and the sheet resistance decreases; however, the ink consumes increases as well. Too much reduction of the drop spacing causes the formation of bulging in the printed lines as shown in the Figure 2.22(d).

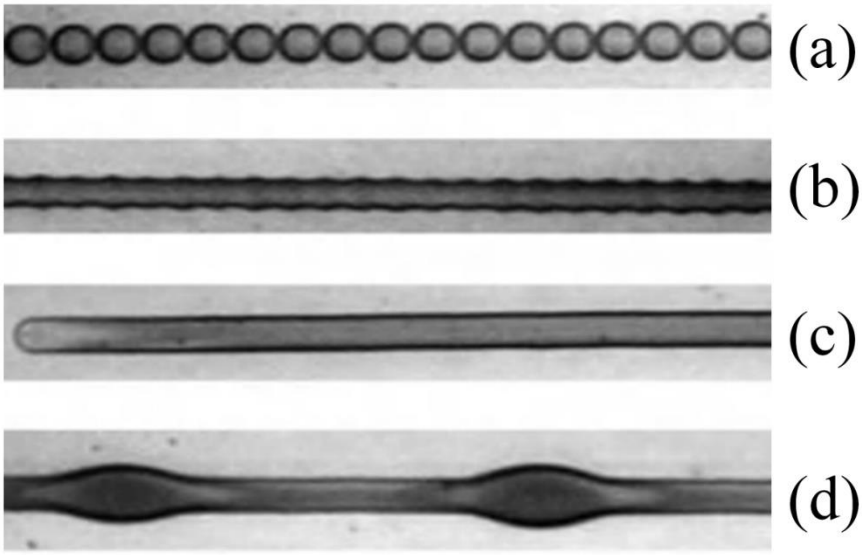

Figure 2.20: *Examples of principle printed line behavior (a) individual drops, (b) scalloped, (c) uniform and (d) bulging [134].*

2.2.3. Inkjet printing system

During this work Dimatix materials printer DMP-2800 has been used, equipped with 4 mL cartridge that can be filled with any types of ink. The printhead consists of sixteen nozzles of diameter of 23 µm, and 254 µm apart from each other, that can deposit droplet volume of either 1 pL or 10 pL, depending on their types. Figure 2.21 shows the Dimatix DMP-2800 materials printer along with cartridge.

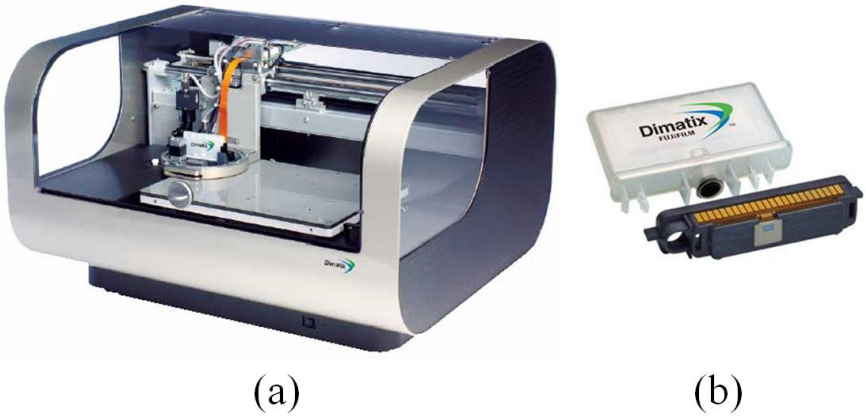

Figure 2.21: *Photographs of (a) Dimatix DMP-2800 materials printer, and (b) Cartridge for the Dimatix printer [135].*

In this system, the size, shape and speed of the droplets can be controlled by adjusting the voltage waveform applied to the nozzles. Each nozzle piezo-actuator can be tuned individually to achieve the same ejection conditions by adjusting the maximum applied voltage. A typical actuation cycle is illustrated in Figure 2.22.

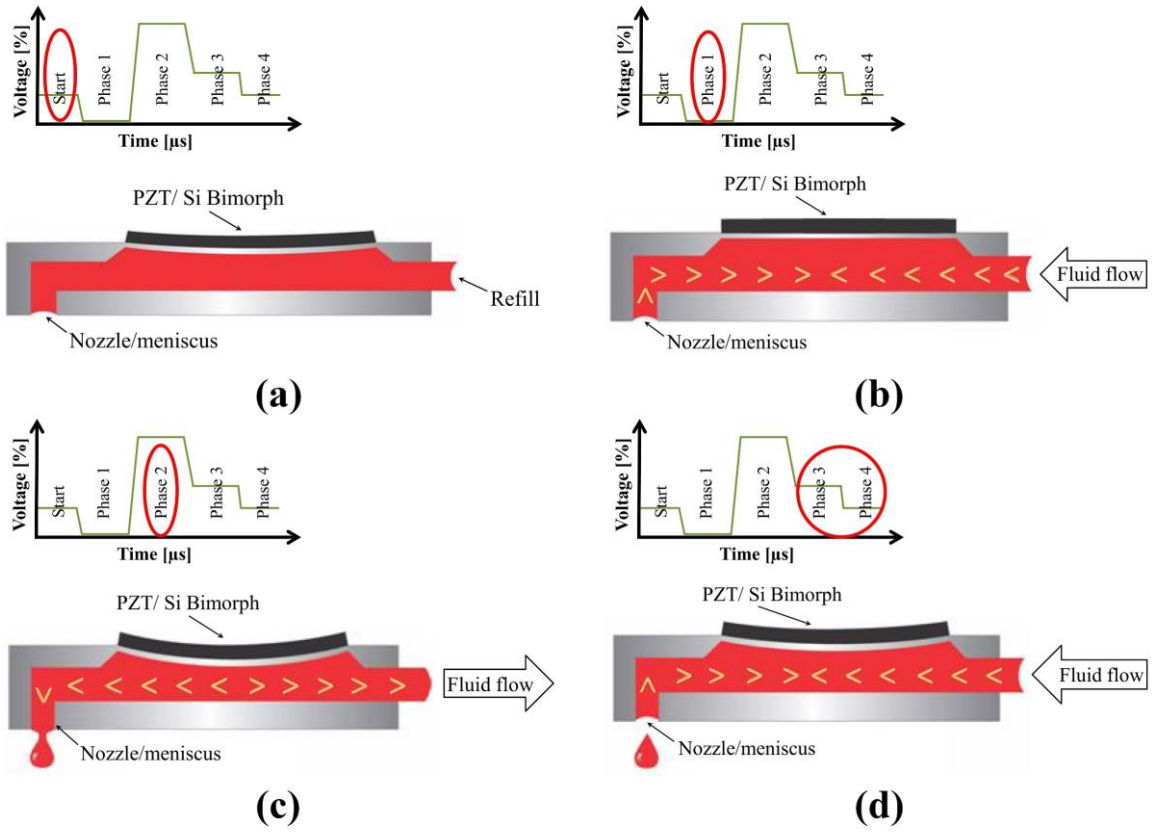

Figure 2.22: *Schematics diagram of the operation principle of inkjet printing system: (a) slight deflection of PZT bimorph prior to the initiation of drive pulse train, (b) drawing in fluid from reservoir due to decrease in voltage moves PZT upward, (c) initiation of drop formation by increase in voltage that deflects PZT, and (d) controlled motion of PZT while fluid drop break off and return to standby position [135].*

The drop spacing in X direction (D_{Sx}) is adjusted by the cartridge speed (v') and the droplet ejection frequency (f') and can be expressed as below [136],

$$D_{Sx} = \frac{v'}{f'} \quad \ldots\ldots\ldots (2.15)$$

On the other hand, the drop spacing in Y direction (D_{Sy}) can be controlled by changing the angle (sabre angle) of the axis of the nozzles array with respect to the printing translation direction in X-axis, as presented in Figure 2.23, and can be expressed as follows [136],

$$D_{Sy} = 254 * \sin(\alpha_S) \quad \ldots \ldots \ldots (2.16)$$

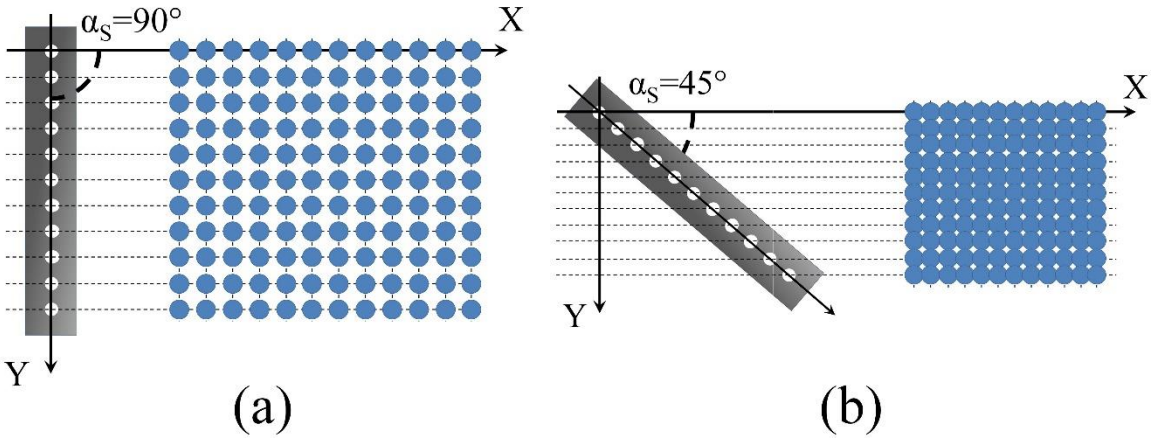

Figure 2.23: *Schematic diagram of the drop spacing setting on the Dimatix DMP-2800 materials printer.*

In Dimatix system, drop spacing is adjustable between 5 and 254 µm in one micron increment. Furthermore, the system allows to control the meniscus pressure to prevent the ink dripping, the temperature of the nozzle plate from ambient to 70 °C, the temperature of the substrate from ambient to 60 °C, and also the type and frequency of nozzle cleaning cycles [135]. The system is also equipped with two cameras, namely, fiducial camera and drop analysis camera. The fiducial camera allows the observation of the printed surface, and more importantly the alignment process. The second camera provides real-time imaging of drop ejection from the nozzles. Voltage waveforms and other cartridge settings can be actively adjusted while monitoring drop formation to set optimal values [135].

2.2.4. Post-treatment process

The deposition of the inkjet-printed layer on the substrate is followed by the curing step to obtain functional layer. During this process, the evaporation of the solvent occurs while the functional materials, such as conductive nanoparticles, polymers and pigments, remain on the surface of the substrate.

Study shows that the final shape of the inkjet-printed pattern is strongly influenced by the evaporation process of the solvent, which eventually affects the arrangement of the functional materials in the final printed pattern. The timescale for drying depends on several factors, such as the ambient temperature, humidity and the drop size [137].

Several physical phenomenon take place during solvent evaporation process, namely, convection, Marangoni effect and hydrodynamic flows driven by temperature gradients inside the droplet [96]. Initially, a gradual decrease of the droplet height occurs due to solvent evaporation. At this stage the droplet shape remains very close to a spherical cap. However, at later stages, the evaporation of the droplet becomes too shallow for convection to keep pace with evaporation near the contact line [137]. As the contact line is pinned, to prevent the shrinkage of contact area of the droplet liquid flows outwards, which transports the dispersed materials to the edge as well. Therefore an undesirable distribution of materials takes place that leads to the formation of the ring mass with time. Figure 2.24 illustrates the schematic diagram of droplet evaporation process, and Figure 2.25 shows the observed coffee-ring after the drying of a coffee droplet.

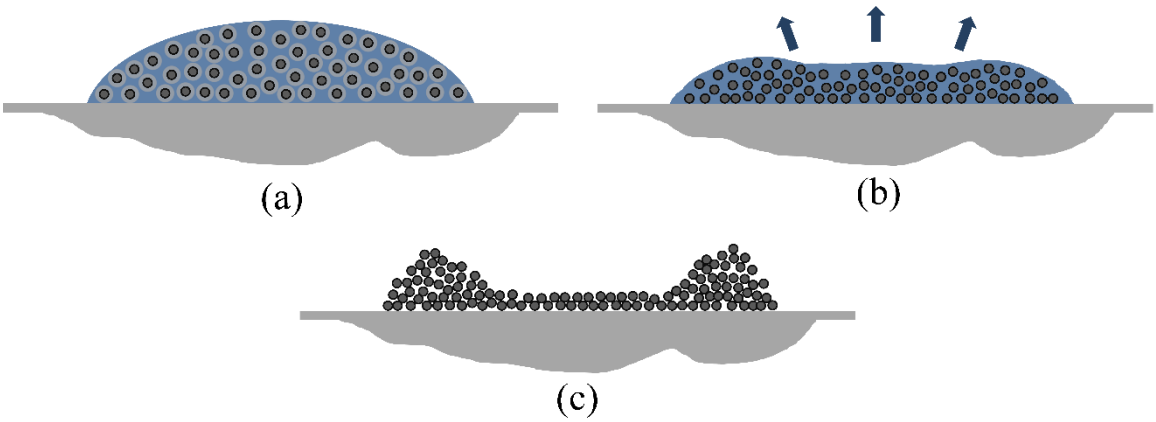

Figure 2.24: *Schematic diagram of drying process of nanoparticle based ink (a) droplet after printing, (b) during solvent evaporation, and (c) formation of coffee-ring after solvent evaporation.*

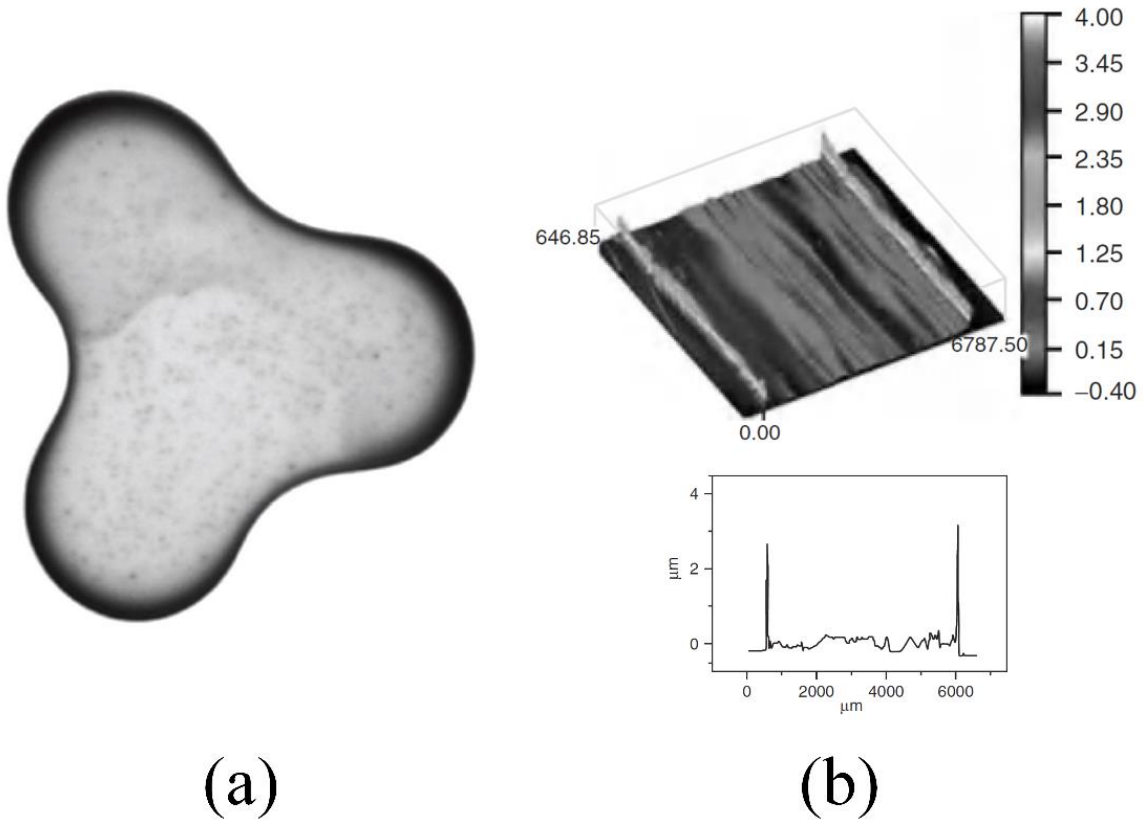

***Figure 2.25**: Illustrations of (a) coffee-rings observed after complete drying of a coffee droplet consist of 1 wt.% of solid content [138], and (b) coffee-drop effect of an inkjet-printed film [134].*

The unexpected growth of the coffee-ring can be counterbalanced by the Marangoni flow i.e., surface tension driven flow, using a mixed-solvent system [139]. Direction of the Marangoni flow is opposite to that of the convective flow, and can be enhanced by adding a small amount of solvent with high boiling temperature and low surface tension in the mixture [139].

The drying step is pursued by the sintering or annealing of the printed layers, which takes place due to applied thermal energy and describes the process of coalescence, densification and the grain size increments of the particles [140]. The driving force of the sintering is the reduction of the total interfacial energy. The solid state sintering of nanoparticles could be divided into three overlapping stages. Initially, the formation of the necks between the particles takes place, followed by occurrence of considerable densification before isolation of the pores, and at the end the densification reaches from the isolated pore state to the final densification [140]. Figure 2.26 illustrates the geometrical models for two particles model,

where the neck size increases with the increasing sintering time due to materials transport between particles and hence shrinkage occurs.

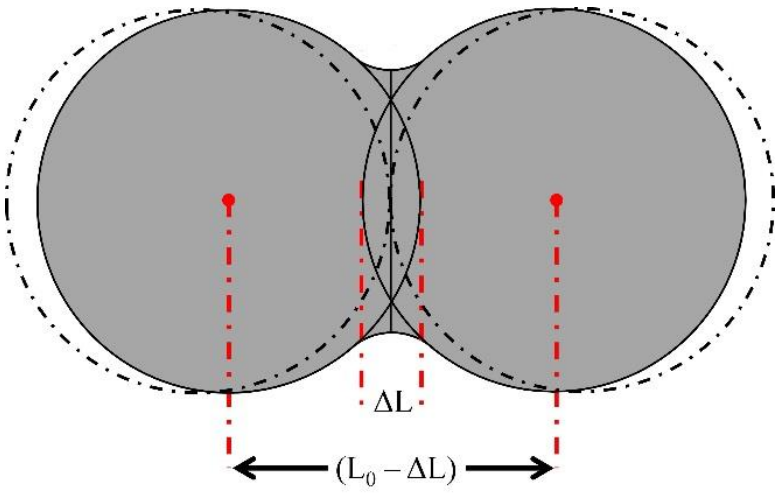

Figure 2.26: *Schematic diagram of two particle model for the initial stage of sintering with shrinkage [140].*

In printed electronics, substrates having low glass transition temperature (T_g) are generally used [141], consequently a low curing temperature of an ink is preferable to avoid any destructive heating deformation. The sintering step can be performed by exposing the printed pattern to heat (thermal sintering), intense light (photonic sintering), microwave radiation, plasma, and by applying an electrical voltage [115].

2.4.1. Thermal sintering

Thermal heating of printed patterns, also known as radiation-conduction-convection heating, leads to the evaporation of solvent and allows the particle to adhere to each other to form a dense structure. Traditional thermal heating method is an equilibrium heating process generally performed by conventional heating oven or furnace. During this process, both the thin film and the substrate are uniformly heated to elevated temperatures, and the maximum temperature is often limited by the substrate properties [142]. In order to achieve highly conductive layer using nanoparticle based conductive ink, post curing at high heating temperature of around 200 to 300 °C is required to get rid of a residual insulating layer composed of organic stabilizer molecules that surrounds the particles [115], [143], [144]. However, this requires the use of only thermally stable substrates [97].

2.4.2. Photonic sintering

Photonic curing refers to the high-temperature thermal processing of a thin film using pulsed light from a flash lamp [142], [145], [146]. As the printed layer is exposed to light during the photonic curing, the absorption of light by the printed layer causes the heating, which leads to the evaporation of liquid and the sintering [115]. The process allows the use of a low-temperature substrate, such as plastic or paper. Photonic curing is a non-equilibrium based thermal processing method, where the printed film is preferentially heated over the substrate, and thus permits the sintering of the printed film at significantly higher temperature than the substrate can normally withstand [142], [145]. This method enables the use of inexpensive low temperature substrates, and cures the films quickly enough to keep up with the high speed printing process [145].

2.4.3. Microwave sintering

Microwave sintering uses electromagnetic wave with wavelengths ranging from 1 mm to 1m in free space and frequency between 300 MHz and 300 GHz, known as microwave energy, to process various kinds of materials [147], [148]. During the process, heating of the materials as a whole, known as volumetric heating, takes place due to absorption of microwave field, by the conversion of the electromagnetic energy into thermal energy. The microwave heating process is instantaneous and fast. This is an economic and effective sintering process. Because of the volumetric heating, the heating of the material is uniform from inside-out [115], [147], [149], [150]. This method is widely used for the sintering of dielectric materials [150]. On the other hand, microwave sintering of the metal layer is limited by its very low penetration depth. Study shows that at 2.54 GHz the penetration depth for Ag, Au, and Cu ranges are from 1.3 to 1.6 μm [149], [150]. Therefore, in order to perform microwave sintering of metals successfully, the thickness of the layer requires to be of the same order as the penetration depth [115], [149], [150].

2.4.4. Plasma sintering

Plasma sintering is a selective sintering method, which is employed by exposing the printed patterns to low-pressure argon (Ar) plasma. During this process, initially the decomposition of the organic moieties around the nanoparticles occurs, and then with time the growth of skin layer takes place. Accordingly, after sufficient amount of sintering time, the complete printed pattern transforms into a bulk material structure [151].

2.2.4.5. Electrical sintering

Electrical sintering is performed by applying a voltage across the printed structure. Due to energy dissipation, the current flow through the structure leads to the local heating. This technique facilitates the sintering within short time, and reduces substrate heating [115].

During this work, both conventional thermal heating and photonic sintering techniques have been used.

2.2.5. Applications of inkjet printing in microelectronics

Inkjet printing can be used to fabricate different types of structure, such as electrical interconnections for a circuitry on a printed circuit board [151], [152]; radio frequency identification (RFID) tags [153]–[155]; embedded electrical passive structures such as conductors, resistors, and inductor [152], [156]; switch [157]; organic electronics; displays [152]; even to develop under-bump metallization [152], [158], [159].

Inkjet printing technology can also be used to develop three-dimensional (3D) microstructures, using either wet-in-wet or wet-in-dry approaches. In case of wet-in-wet method, a layer of ink is printed on the previously printed layer without sintering. On the other hand, wet-in-dry approach involves the printing of an ink layer on the previous layer after curing [160]. Sanchez-Ronaguera et al. [161] presented inkjet-printed 3D metal-insulator-metal crossover structure, where two inkjet-printed conductive silver lines are separated by a printed UV curable SU-8 insulating ink. During the process, printed conductive lines were cured on a preheated hot plate at 150 °C for 10 min and insulator was cured using UV lamp. Similarly, Cook et al. [162] demonstrated the fabrication of multi-layer capacitor.

Furthermore, inkjet technology can also be used to fabricate complex 3D microelectromechanical systems (MEMS), cantilever and other structures. S. L. Fuller *et al.* [143] exhibited 3D metallic structure formed by colloid ink having nanoparticles. Fabrication process of an inkjet-printed planar heat actuator, which contained cantilever printed out of multiple layers of silver nanoparticles onto a glass slide was reported. Figure 2.27 shows the processing steps involved in the fabrication of this actuator.

Polymethyl methacrylate (PMMA) was used as sacrificial layer, as it can easily be dissolved into acetone and retains its solubility even after sintering step at 300 ºC. Inkjet process was performed with the substrate at 250 ºC for the total printing time of 30 min, and then the structure was sintered at 300 ºC for 10 min. Afterward, the structure was lightly sonicated in an acetone bath for 5 min. However, PMMA is not an ideal sacrificial layer, as the nanoparticle ink solvent can dissolve the deposited PMMA, which could cause the leakage through the sacrificial layer to the substrate [143].

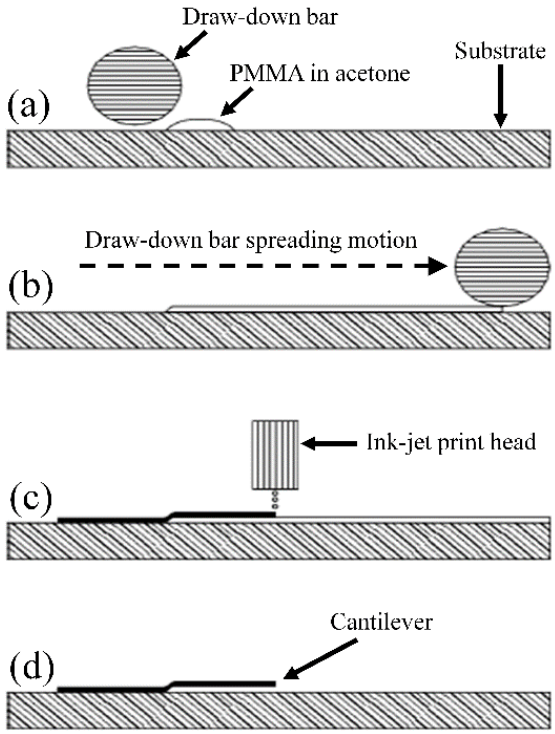

Figure 2.27: *Schematic diagram of fabrication process using inkjet printing technique [143].*

Moreover, 3D structures can be formed by printing several layers of microstructures, including sacrificial layer. The technique can be used to fabricate wide varieties of microstructures, including different forms of MEMS structures that consist of void or cavity. Horning *et al.* [163] presented the fabrication technique of MEMS structure using this approach, where void or cavity is formed after removal of the sacrificial layer (Figure 2.28). However, the inkjet printing of 3D MEMS structure is generally limited in micrometer scale, and requires the removal of the sacrificial layer.

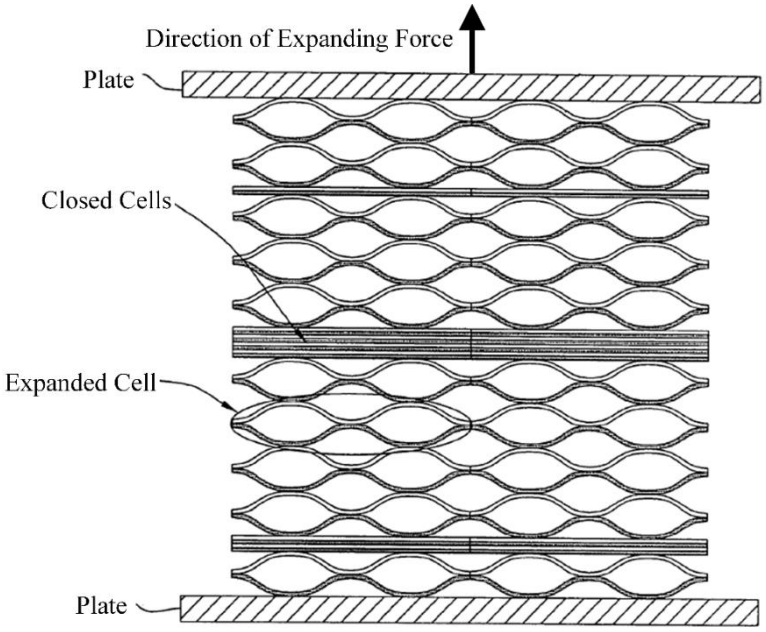

Figure 2.28: *Schematic diagram of inkjet-printed electrostatic actuator under electric field [163].*

2.3. Summary

Over the time, different types of acoustic transducer have been designed and developed, based on different transduction mechanisms. Capacitive, piezoelectric, and piezoresistive transduction mechanisms are the most well-known and commonly used techniques. It has been observed that most of the developed acoustic transducers have been targeted for audio applications, and thus exhibit a constant sensitivity over a wide bandwidth within the human hearing range between 20 Hz and 20 kHz.

Capacitive acoustic transducer, among others, exhibits high sensitivity and consume relatively low power [3], and can also be utilized as active or passive sensing device according to the requirement.

There are several printing techniques available that are generally used for microelectronics fabrication. In this chapter, direct write additive printing techniques, especially the inkjet printing method has been presented. There are several factors that influence the inkjet printing process. Inkjet allows the printing of different types of material in liquid form. Inkjettable fluid should have surface tension between 30-40 mN/m, and viscosity of 3-20 mPa.s. In addition, the surface energy and roughness of the substrate also influence strongly the quality of the printed layer. Depending on the rheological properties of the ink, the

printing system parameters, namely, waveform applied to the nozzle, voltage and nozzle temperature, need to be adjusted as well.

Printing of the film is generally followed by the curing of the layer. Among several available methods, thermal heating using conventional oven is the most commonly used technique. On the other hand, the development of the photonic sintering technique facilitates the use of low cost substrate, like paper and low temperature plastic substrates without damaging the substrates.

Inkjet printing method is generally used for developing the circuit interconnection. In addition, several electronics components, such as capacitor, resistor, inductor and thin film transistor have been developed using inkjet printing technique. This technique can also be used to fabricated 3D structures MEMS structures; however, their dimensions are limited to micrometer range.

References

[1] Elmer L. Hixson and Ilene J. Busch-Vishniac, "Transducer Principles," in *Handbook of Acoustics*, Malcolm J. Crocker, Ed. John Wiley & Sons, 1998, pp. 1375–1388.

[2] P.R. Scheeper, A.G.H. van der Donk, W. Olthuis, and P. Bergveld, "A Review of Silicon Microphones," *Sensors and Actuators A: Physical*, vol. 44, pp. 1–11, 1994.

[3] P.-C. Hsu, C. H. Mastrangelo, and K. D. Wise, "A High Sensitivity Polysilicon Diaphragm Condenser Microphone," in *The 11th Annual International Workshop on Micro Electro Mechanical Systems Proceeding*, Heidelberg, Germany, 1998, pp. 580–585.

[4] Bin Liu, "Transducers for Sound and Vibration - The Finite Element Method Based Design," Ph. D. dissertation, Technical University of Denmark, Denmark, 2001.

[5] Frederick V Hunt, *Electroacoustics the Analysis of Transduction, and Its Historical Background*. Amerocam Institute of Physics, 1954.

[6] Jesper Bay, Ole Hansen, and Siebe Bouwstra, "Design of a Silicon Microphone with Differential Read-Out of a Sealed Double Parallel-Plate Capacitor," *Sensors and Actuators A: Physical*, vol. 53, no. 1, pp. 232–236, 1996.

[7] D. Hohm and R.G. Multhaupt, "Silicon-Dioxide Electret Transducer," *Journal of the Acoustical Society of America*, vol. 75, no. 4, pp. 1297–1298, 1984.

[8] J. Bergqvist and F. Rudolf, "A New Condenser Microphone in Silicon," *Sensors and Actuators*, vol. 21, no. 1–3, pp. 123–125, 1990.

[9] G.M. Sessler, "Acoustic Sensors," *Sensors and Actuators A*, vol. 25–27, pp. 323–330, 1991.

[10] G.M. Sessler and J.E. West, "Self-Biased Condenser Microphone with High Capacitance," *The Journal of the Acoustical Society of America*, vol. 34, no. 11, pp. 1787–1788, 1962.

[11] Michael Pedersen, Wouter Olthuis, and Piet Bergveld, "A Silicon Condenser Microphone with Polyimide Diaphragm and Backplate," *Sensors and Actuators A: Physical*, vol. 63, no. 2, pp. 97–104, 1997.

[12] Quanbo Zou, Zhijian Li, and Litian Liu, "Theoretical and Experimental Studies of Single-Chip-Processed Miniature Silicon Condenser Microphone with Corrugated Diaphragm," *Sensors and Actuators A: Physical*, vol. 63, no. 3, pp. 209–215, 1997.

[13] A.J. Sprenkels, R.A. Groothengel, A.J. Verloop, and P. Bergveld, "Development of an Electret Microphone in Silicon," *Sensors and Actuators*, vol. 17, no. 3–4, pp. 509–512, 1989.

[14] Andrea Barbieri and Germano Nicollini, "A 470 μA Direct Readout Circuit for Electret and MEMS Digital Microphones," *Analog Integrated Circuits and Signal Processing*, vol. 81, no. 1, pp. 229–240, Oct. 2014.

[15] G.M. Sessler, "Electrostatic Microphones with Electret Foil," *The Journal of the Acoustical Society of America*, vol. 35, no. 4, pp. 1354–1357, 1963.

[16] J. Hillenbrand, T. Motz, and G. M. Sessler, "High Sensitivity Electret Accelerometer with Integrated FET," *IEEE Sensors Journal*, vol. 14, no. 6, pp. 1770–1777, Jun. 2014.

[17] Arie Van Rhijn, "Integrated Circuits for High Performance Electret Microphones," in *Audio Engineering Society Convention 114*, Amsterdam, The Netherlands, 2003.

[18] J.A. Voorthuyzen, P. Bergveld, and A.J. Sprenkels, "Semiconductor-Based Electret Sensors for Sound and Pressure," *IEEE Transactions on Electrical Insulation*, vol. 24, no. 2, pp. 267–276, 1989.

[19] P. Murphy, K. Hubschi, N. De Rooij, and C. Racine, "Subminiature Silicon Integrated Electret Capacitor Microphone," *IEEE Transactions on Electrical Insulation*, vol. 24, no. 3, pp. 495–498, 1989.

[20] Johan Bergqvist and Jean Gobet, "Capacitive Microphone with a Surface Micromachined Backplate Using Electroplating Technology," *Journal of Microelectromechanical Systems*, vol. 3, no. 2, pp. 69–75, 1994.

[21] Wolfgang Kuhnel and Gisela Hess, "A Silicon Condenser Microphone with Structured Back Plate and Silicon Nitride Membrane," *Sensors and Actuators A*, vol. 30, pp. 251–258, 1992.

[22] Quanbo Zou, Zhijian Li, and Litian Liu, "Design and Fabrication of Silicon Condenser Microphone Using Corrugated Diaphragm Technique," *Journal of Microelectromechanical Systems*, vol. 5, no. 3, pp. 197–204, 1996.

[23] T. Bourouina, S. Spirkovitch, F. Baillieu, and C. Vauge, "A New Condenser Microphone with a p+ Silicon Membrane," *Sensors and Actuators*, vol. 131, no. 1–3, pp. 149–152, 1992.

[24] Petr Honzík, Alexey Podkovskiy, Stéphane Durand, and Nicolas Joly, "Experimental Investigation on the Electrostatic Receiver with Small-Sized Backing Electrode," in *Forum Acusticum*, Krakow, Czech Republic, 2014, vol. 7.

[25] Pirmin Rombach, Matthias Müllenborn, Udo Klein, and Kurt Rasmussen, "The First Low Voltage, Low Noise Differential Silicon Microphone, Technology Development and Measurement Results," *Sensors and Actuators A: Physical*, vol. 95, no. 2, pp. 196–201, 2002.

[26] P. R. Scheeper, Wouter Olthuis, and Piet Bergveld, "Fabrication of a Subminiature Silicon Condenser Microphone Using the Sacrificial Layer Technique," in *TRANSDUCERS'91., 1991 International Conference on Solid-State Sensors and Actuators*, 1991, pp. 408–411.

[27] Brüel & Kjær, *Microphone Handbook: Theory*. Nærum, Denmark: Brüel & Kjær, 1996.

[28] P.R. Scheeper, A.G.H. van der Donk, W. Olthuis, and P. Bergveld, "Fabrication of Silicon Condenser Microphones using Single Wafer Technology," *Journal of Microelectromechanical Systems*, vol. 1, no. 3, pp. 147–154, 1992.

[29] Brian T. Cunningham and Jonathan J. Bernstein, "Wide-Bandwidth Silicon Nitride Membrane Microphones," in *Proceeding of Conference on Micromachining and Microfabrication Process Technology III, SPIE*, Austin, TX, USA, 1997, vol. 3223, pp. 56–63.

[30] Xinxin Li, Rongming Lin, Huatsoon Kek, Jianmin Miao, and Quanbo Zou, "Sensitivity-Improved Silicon Condenser Microphone with a Novel Single Deeply Corrugated Diaphragm," *Sensors and Actuators A: Physical*, vol. 92, pp. 257–262, 2001.

[31] R. Kressmann, M. Klaiber, and G. Hess, "Silicon Condenser Microphones with Corrugated Silicon Oxide/Nitride Electret Membranes," *Se*, vol. 100, pp. 301–309, 2002.

[32] D. Schafer, S. Shoaf, and P. Loeppert, "Micromachined Condenser Microphone for Hearing Aid Use," in *Proceeding of Solid-State Sensors and Actuator Workshop*, Hilton Head Island, SC, USA, 1998, pp. 27–30.

[33] Alexey Podkovskiy, Petr Honzík, Stéphane Durand, Nicolas Joly, and Michel Bruneau, "Miniaturized Electrostatic Receiver with Small-Sized Backing Electrode," in *Proceedings of Meetings on Acoustics*, Montreal, Canada, 2013, vol. 19, p. 030047.

[34] Petr Honzík, Alexey Podkovskiy, Stéphane Durand, Nicolas Joly, and Michel Bruneau, "Analytical and Numerical Modeling of an Axisymmetrical Electrostatic Transducer with Interior Geometrical Discontinuity," *Journal of the Acoustical Society of America*, vol. 134, no. 5, pp. 3573–3579, 2013.

[35] D.A. Berlincourt, D.R. Curran, and H. Jaffe, "Piezoelectric and Piezomagnetic Materials and Their Function in Transducers," in *Physical Acoustic: Principles and Methods*, vol. 1 Part A, W.P. Mason and R.N. Thurston, Eds. New York: Academic Press, 1964.

[36] W. G. Cady, *Piezoeletricity*, Revised ed., vol. 1. New York: Dover Publications Inc, 1964.

[37] W. P. Mason, *Piezoelectric Crystals and Their Application to Ultrasonics*. New York: Van Nostrand, 1950.

[38] Nava Setter, "ABC of Piezoelectricity and Piezoelectric Materials," in *Piezoelectric Materials in Devices*, Nava Setter, Ed. Swiss Federal Institute of Technology, 2002.

[39] "IEEE Standard on Piezoelectricity," *ANSI/IEEE Std 176-1987*, pp. 1–66, 1988.

[40] S. Horowitz, D. Mathias, J. Fox, J. P. Cortes, M. Sanghadasa, and P. Ashley, "Effects of Scaling and Geometry on the Performance of Piezoelectric Microphones," *Sensors and Actuators A: Physical*, vol. 185, pp. 24–32, 2012.

[41] A. L. Kholkin, N. A. Pertsev, and A. V. Goltsev, "Piezoelectricity and Crystal Symmetry," in *Piezoelectric and Acoustic Materials for Transducer Applications*, Ahmad Safari and E. Koray Akdoğan, Eds. Springer, 2008, pp. 17–38.

[42] D. Berlincourt, H. A. Krueger, and C. Near, "Properties of Morgan Electro Ceramic Ceramics," Morgan Electro Ceramics, Technical, 2000.

[43] Khaled S Ramadan, D Sameoto, and S Evoy, "A Review of Piezoelectric Polymers as Functional Materials for Electromechanical Transducers," *Smart Materials and Structures*, vol. 23, no. 3, p. 033001, Mar. 2014.

[44] Robert John Littrell, "High Performance Piezoelectric MEMS Microphones," Doctoral Thesis, The University of Michigan, Michigan, USA, 2010.

[45] Ruozhou Hou, David Hutson, Katherine J. Kirk, and Yong Qing Fu, "AlN Thin Film Transducers for High Temperature Non-Destructive Testing Applications," *Journal of Applied Physics*, vol. 111, no. 7, p. 074510, 2012.

[46] E. S. Kim and R. S. Muller, "IC-Processed Piezoelectric Microphone," *IEEE Electron Device Letters*, vol. 8, no. 10, pp. 467–468, 1987.

[47] E. S. Kim, R. S. Muller, and P. R. Gray, "Integrated Microphone with CMOS Circuits on a Single Chip," in *International Electron Devices Meeting, 1989. IEDM'89. Technical Digest*, 1989, pp. 880–883.

[48] E. S. Kim, J. R. Kim, and R. S. Muller, "Improved IC-Compatible Piezoelectric Microphone and CMOS Process," in *International Conference on Solid-State Sensors and Actuators*, 1991, pp. 270–273.

[49] S. S. Lee, R. P. Ried, and R. M. White, "Piezoelectric Cantilever Microphone and Microspeaker," *Journal of Microelectromechanical Systems*, vol. 5, no. 4, pp. 238–242, 1996.

[50] S. S. Lee and R. M. White, "Piezoelectric Cantilever Acoustic Transducer," *Journal of Micromechanics and Microengineering*, vol. 8, no. 3, pp. 230–238, 1998.

[51] M. Royer, J. O. Holmen, M. A. Wurm, O. S. Aadland, and M. Glenn, "ZnO on Si Integrated Acoustic Sensor," *Sensors and Actuators*, vol. 4, no. 3, pp. 357–362, 1983.

[52] H. J. Zhao, T. L. Ren, J. S. Liu, L. T. Liu, and Z. J. Li, "Fabrication of High-Quality PZT-Based Piezoelectric Microphone," in *12th International Conference on Transducers, Solid-State Sensors, Actuators and Microsystems*, 2003, vol. 1, pp. 234–237.

[53] S. Horowitz, T. Nishida, L. Cattafesta, and M. Sheplak, "Design and Characterization of a Micromachined Piezoelectric Microphone," in *11th AIAA/CEAS Aeroacoustics Conference*, 2005, p. AIAA Paper 2005–2998.

[54] Kenji Uchino, *Piezoelectric Actuators and Ultrasonic Motors*. New York: Springer, 1996.

[55] M Serridge and T R Licht, *Piezoelectric Accelerometer and Vibration Preamplifier Handbook, Brüel & Kjær*. 1987.

[56] D. T. Martin, "Design, Fabrication, and Characterization of a MEMS Dual-backplate Capacitive Microphone," Doctoral Thesis, University of Florida, Gainesville, FL, USA, 2007.

[57] R. Schellin, G. Hess, W. Kuehnel, G. M. Sessler, and E. Fukada, "Silicon Subminiature Microphones with Organic Piezoelectric Layers: Fabrication and Acoustical Behaviour," in *7th International Symposium on Electrets (ISE 7)*, 1991, pp. 929–934.

[58] R. P. Ried, E. S. Kim, D. M. Hong, and R. S. Muller, "Piezoelectric Microphone with On-Chip CMOS Circuits," *Journal of Microelectromechanical Systems*, vol. 2, no. 3, pp. 111–120, 1993.

[59] S. C. Ko, Y. C. Kim, S. S. Lee, S. H. Choi, and S. R. Kim, "Micromachined Piezoelectric Membrane Acoustic Device," *Sensors and Actuators A: Physical*, vol. 103, no. 1, pp. 130–134, 2003.

[60] M. N. Niu and E. S. Kim, "Piezoelectric Bimorph Microphone Built on Micromachined Parylene Diaphragm," *Journal of Microelectromechanical Systems*, vol. 12, no. 6, pp. 892–898, 2003.

[61] Joachim Hillenbrand and Gerhand M. Sesslet, "High-Sensitivity Piezoelectric Microphones Based on Stacked Cellular Polymer Films (L)," *Journal of the Acoustical Society of America*, vol. 116, p. 3267, 2004.

[62] B. A. Griffin, M. D. Williams, C. S. Coffman, and M. Sheplak, "Aluminum Nitride Ultrasonic Air-Coupled Actuator," *Journal of Microelectromechanical Systems*, vol. 20, no. 2, pp. 476–486, 2011.

[63] Ronald G. Polcawich, "A Piezoelectric MEMS Microphone Based on Lead Zirconate Titanate (PZT) Thin Films," U.S. Army Research Laboratory, ARL-TR-3387, 2004.

[64] Sherif Saleh, Hamed Elsimary, Amal Zaki, and Shamim Ahmad, "Design and Fabrication of Piezoelectric Acoustic Sensor," in *The 5th WSEAS Int. Conf. on Microelectronics, Nanoelectronics, Optoelectronics*, Prague, Czech Republic, 2006, pp. 92–96.

[65] A. Arora, A. Arora, V. K. Dwivedi, P. J. George, K. Sreenivas, and V. Gupta, "Zinc Oxide Thin Film-Based MEMS Acoustic Sensor with Tunnel for Pressure Compensation," *Sensors and Actuators A: Physical*, vol. 141, no. 2, pp. 256–261, 2008.

[66] R. Littrell and K. Grosh, "Modeling and Characterization of Cantilever-Based MEMS Piezoelectric Sensors and Actuators," *Journal of Microelectromechanical Systems*, vol. 21, no. 2, pp. 406–413, 2012.

[67] Stephen B. Horowitz, Dustin Mathias, Corey D. Hernandez, Mohan Sanghadasa, and Paul Ashley, "Miniaturization of Piezoelectric Microphones," in *AIAA Infotech@Aerospace*, Atlanta, Georgia, 2010, pp. 1–8.

[68] C. S. Smith, "Piezoresistance Effect in Germanium and Silicon," *Physical Review*, vol. 94, no. 1, pp. 42–49, 1954.

[69] A.A. Barlian, W.-T. Park, J.R. Mallon, A.J. Rastegar, and B.L. Pruitt, "Review: Semiconductor Piezoresistance for Microsystems," *Proceedings of the IEEE. Institute of Electrical and Electronics Engineers*, vol. 97, no. 3, pp. 513–552, Mar. 2009.

[70] Robert Dieme, "Characterization of Noise in MEMS Piezoresistive Microphones," University of Florida, 2005.

[71] S. Beclin, S. Brida, S. Metivet, P. Martins, and O. Stojanovic, "High Sensitivity Piezoresistive Silicon Microphone for Aerospace Applications," presented at the 5th ESA MNT Round Table, Noordwijk, The Netherlands, 2005.

[72] R. Schellin and G. Hess, "A Silicon Subminiature Microphone Based on Piezoresistive Polysilicon Strain Gauges," *Sensors and Actuators A: Physical*, vol. 32, no. 1, pp. 555–559, 1992.

[73] J. A. Harkey and Thomas W. Kenny, "1/f Noise Considerations for the Design and Process Optimization of Piezoresistive Cantilevers," *Journal of Microelectromechanical Systems*, vol. 9, no. 2, pp. 226–235, 2000.

[74] Melih Papila, Raphael T. Haftka, Toshikazu Nishida, and Mark Sheplak, "Piezoresistive Microphone Design Pareto Optimization: Tradeoff between Sensitivity and Noise Floor," *Journal of Microelectromechanical Systems*, vol. 15, no. 6, pp. 1632–1643, 2006.

[75] R. Schellin, M. Strecker, U. Nothelfer, and G. Schuster, "Low Pressure Acoustic Sensors for Airbrone Sound with Piezoresistive Monocrystalline Silicon and Electrochemically Etched Diaphragms," *Sensors and Actuators a*, vol. 46–47, pp. 156–160, 1995.

[76] Melih Papila, Raphael T. Haftka, Toshikazu Nishida, and Mark Sheplak, "Piezoresistive Microphone Design Pareto Optimization: Tradeoff between Sensitivity and Noise Floor," in *44th AIAA/ASME/ASCE/AHS Structural Dynamics, and Materials Conference*, Virginia, USA, 2003, pp. AIAA–2003–1632.

[77] F. P. Burns, "Piezoresistive Semiconductor Microphone," *Journal of the Acoustical Society of America*, vol. 29, no. 2, pp. 248–253, 1957.

[78] E. R. Peake, A. R. Zias, and J. V. Egan, "Solid-State Digital Pressure Transducer," *IEEE Transactions on Electron Devices*, vol. 16, no. 10, pp. 870–876, 1969.

[79] E. Kälvesten, L. Löfdahl, and G. Stemme, "A small-size silicon microphone for measurements in turbulent gas flows," *Sensors and Actuators A: Physical*, vol. 45, no. 2, pp. 103–108, 1994.

[80] E. Kälvesten, L. Löfdahl, and G. Stemme, "Small Piezoresistive Silicon Microphones Specially Designed for the Characterization of Turbulent Gas Flows," *Sensors and Actuators A: Physical*, vol. 46–47, pp. 151–155, 1995.

[81] E. Kälvesten, C. Vieider, L. Löfdahl, and G. Stemme, "An Integrated Pressure-Flow Sensor for Correlation Measurements in Turbulent Gas Flows," *Sensors and Actuators A*, vol. 52, pp. 51–58, 1996.

[82] M. Sheplak, K. S. Breuer, and M. A. Schmidt, "A Wafer-Bonded, Silicon-Nitride Membrane Microphone with Dielectrically-Isolated, Single-Crystal Silicon Piezoresistors," in *1998 Solid-State Sensor and Actuator Workshop*, Hilton Head Island, SC, 1998, pp. 23–26.

[83] M. Sheplak, M. Seiner, K. S. Breuer, and M. A. Schmidt, "A MEMS Microphone for Aeroacoustics Measurements," in *37th AIAA Aerospace Sciences Meeting*, Reno, NV, 1999, vol. AIAA 99–0606, pp. 1–7.

[84] D. P. Arnold, S. Gururaj, S. Bhardwaj, T. Nishida, and M. Sheplak, "A Piezoresistive Microphone for Aeroacoustic Measurements," in *ASME IMECE 2001, International Mechanical Engineering Congress and Exposition*, New York, 2001, pp. 281–288.

[85] A. Naguib, E. Soupos, H. Nagib, C. Huang, and K. Najafi, "A Piezoresistive MEMS Sensor for Acoustic Noise Measurements," in *5th AIAA/CEAS Aeroacoustics Conference & Exhibit*, Bellevue, WA, 1999, vol. AIAA 99–1992, pp. 1142–1149.

[86] A. Naguib, E. Soupos, H. Nagib, C. Huang, and K. Najafi, "Characterization of a MEMS Acoustic/Pressure Sensor," in *37th AIAA Aerospace Sciences Meeting*, Reno, NV, 1999, vol. AIAA 99–0520, pp. 1–7.

[87] C. Huang, A. Naguib, E. Soupos, and K. Najafi, "A Silicon Micromachined Microphone for Fluid Mechanics Research," *Journal of Micromechanics and Microengineering*, vol. 12, no. 6, pp. 767–774, 2002.

[88] Yogesh B. Gianchandani and Khalil Najafi, "A Bulk Silicon Dissolved Wafer Process for Microelectromechanical Devices," *Journal of Microelectromechanical Systems*, vol. 1, no. 2, pp. 77–85, 1992.

[89] Gang Li, Yitshak Zohar, and Man Wong, "Piezoresistive Microphone with Integrated Amplifier Realized Using Metal-Induced Laterally Crystallized Polycrystalline Silicon," *Journal of Micromechanics and Microengineering*, vol. 14, no. 10, pp. 1352–1358, 2004.

[90] Gang Li, Yitshak Zohar, and Man Wong, "Piezoresistive Pressure Sensor Using Metal-Induced Laterally Crystallized Polycrystalline Silicon," in *International Conference on Electrical Engineering (ICEE)*, Sapporo, Japan, 2004.

[91] E. Coatanéa, V. Kantola, J. Kulovesi, L. Lahti, R. Lin, and M. Zavodchikova, "Printed Electronics - Now and Future.pdf," in *Bit Bang - Rays to the Future*, Y. Neuvo and S. Ylönen, Eds. Helsinki, Finland: Helsinki University Print, 2009, pp. 63–102.

[92] A. Karwa, "Printing Studies with Conductive Inks and Exploration of New Conducting Polymer Compositions," Rochester Institute of Technology, Rochester, New York, 2006.

[93] A. Blayo and B. Pineaux, "Printing Processes and Their Potential for RFID Printing," presented at the Joint sOc-EUSAI conference, Grenoble, 2005, pp. 27–30.

[94] U. Caglar, "Studies of Inkjet Printing Technology with Focus on Electronic Materials," Tampere University of Technology, Tampere, 2009.

[95] K.K.B. Hon, L. Li, and I.M. Hutchings, "Direct Writing Technology-Advances and Developments," *CIRP Annals - Manufacturing Technology*, vol. 57, no. 2, pp. 601–620, 2008.

[96] Romain Cauchois, "Microstructuring Inkjet-Printed Deposits: from Silver Nanoparticles Coalescence to the Fabrication of Interconnections for Electronic Devices," École Nationale Supérieure des Mines de Saint-Étienne, Gardanne, 2012.

[97] Pira International Ltd., *Inkjet for Printed Electronics*. Surrey, UK: iSmithers Rapra Publishing, 2007.

[98] David Wallace, "Overview of Inkjet-Based Micromanufacturing," in *Inkjet-Based Micromanufacturing*, vol. 9, Jan G. Korvink, Patrick J. Smith, and Dong-Youn Shin, Eds. Weinheim, Germany: WILEY-VCH Verlag GmbH & Co. KGaA, 2012, pp. 1–17.

[99] Helmut Kipphan, Ed., *Handbook of Print Media: Technologies and Production Methods*. Heidelberg, Germany: Springer, 2001.

[100] Katsuaki Suganuma, *Introduction to Printed Electronics*, vol. 74. New York, NY: Springer, 2014.

[101] J Jang, S Hong, GC Schatz, and MA Ratner, "Self-assembly of Ink Molecules in Dip-Pen Nanolithography: A Diffusion Model," *Journal of Chemical Physics*, vol. 115, no. 6, pp. 2721–2729, 2001.

[102] P Manandhar, J Jang, GC Schatz, MA Ratner, and S Hong, "Anomalous Surface Diffusion in Nanoscale Direct Deposition Processes," *Physical Review Letters*, vol. 90, no. 11, pp. 1155051–1155054, 2003.

[103] A.P. Malshe, K.P. Rajurkar, K.R. Virwani, C.R. Taylor, D.L. Bourell, G. Levy, M.M. Sundaram, J.A. McGeough, V. Kalyanasundaram, and A.N. Samant, "Tip-based nanomanufacturing by electrical, chemical, mechanical and thermal processes," *CIRP Annals - Manufacturing Technology*, vol. 59, pp. 628–651, 2010.

[104] B. Basnar and I. Willner, "Dip-pen-nanolithographic Patterning of Metallic, Semiconductor, and Metal Oxide Nanostructures on Surfaces," *Small*, vol. 5, no. 1, pp. 28–44, 2009.

[105] H. Wang, L. Huang, Z. Xu, C. Xu, R. Composto, and Z. Yang, "Sintering Metal Nanoparticle Films," presented at the Flexible Electronics and Displays Conference and Exhibition, 2008, pp. 1–3.

[106] W. M. Wang, R. M. Stoltenberg, S. Liu, and Z. Bao, "Direct patterning of gold nanoparticles using dip-pen nanolithography," *ACS Nano*, vol. 2, no. 10, pp. 2135–2142, 2008.

[107] B. W. Maynor, Y. Li, and J. Liu, "Au ink for afm dip-pen nanolithography," *Langmuir*, vol. 17, no. 9, pp. 2575–2578, 2001.

[108] Weiping Liu and J.N. DuPont, "Fabrication of Functionally Graded TiC/Ti Composites by Laser Engineered Net Shaping," *Scripta Materialia*, vol. 48, no. 9, pp. 1337–1342, May 2003.

[109] Juntao Xu, Sheila A. Grant, and Robert L. Pastel, "Laser-Guided Direct Writing: A Novel Method to Deposit Biomolecules for Biosensors Arrays," *IEEE Transactions on Biomedical Engineering*, vol. 50, no. 1, pp. 126–128, 2003.

[110] David J. Odde and Michael J. Renn, "Laser-Guided Direct Writing for Applications in Biotechnology," *Trends in Biotechnology*, vol. 17, no. 10, pp. 385–389, 1999.

[111] Craig B. Arnold, Pere Serra, and Alberto Piqué, "Laser Direct-Write Techniques for Printing of Complex Materials," *MRS Bulletin*, vol. 32, pp. 23–31, 2007.

[112] Justin M. Hoey, Artur Lutfurakhmanov, Douglas L. Schulz, and Iskander S. Akhatov, "A Review on Aerosol-Based Direct-Write and Its Applications for Microelectronics," *Journal of Nanotechnology*, vol. 2012, p. Article ID 324380, 2012.

[113] B. J. de Gans, P. C. Duineveld, and U. S. Schubert, "Inkjet Printing of Polymers: State of the Art and Future Developments," *Advanced materials*, vol. 16, no. 3, pp. 203–213, 2004.

[114] Berend-Jan de Gans and Ulrich S. Schubert, "Inkjet Printing of Polymer Micro-Arrays and Libraries: Instrumentation, Requirements, and Perspectives," *Macromolecular Rapid Communications*, vol. 24, no. 11, pp. 659–666, Jul. 2003.

[115] Alexander Kamyshny, Joachim Steinke, and Shlomo Magdassi, "Metal-based Inkjet Inks for Printed Electronics," *Open Applied Physics Journal*, vol. 4, pp. 19–36, 2011.

[116] Sun Chemical Corporation, "Technical Information Leaflet: Solsys Jettable Silver EMD5714 & EMD5603." Sun Chemical Corporation, 2011.

[117] Advanced Nano Products (ANP) Co. LTD, “Silver Jet Ink.” [Online]. Available: http://anapro.com/eng/product/silver_inkjet_ink.html. [Accessed: 13-Apr-2015].

[118] Emine Tekin, Patrick J. Smith, and Ulrich S. Schubert, “Inkjet Printing as a Deposition and Patterning Tool for Polymers and Inorganic Particles,” *Soft Matter*, vol. 4, no. 4, pp. 703–713, 2008.

[119] J.E. Fromm, “Numerical Calculation of the Fluid Dynamics of Drop-on-Demand Jets,” *IBM Journal of Research and Development*, vol. 28, no. 3, pp. 322–333, 1984.

[120] Brian Derby, “Inkjet Printing of Functional and Structural Materials: Fluid Property Requirements, Feature Stability, and Resolution,” *Annual Review of Materials Research*, vol. 40, pp. 395–414, 2010.

[121] N. Reis and B. Derby, “Ink Jet Deposition of Ceramic Suspensions: Modelling and Experiments of Droplet Formation,” in *MRS Proceedings*, 2000, vol. 625, p. 117.

[122] A. L. Yarin, “Drop Impact Dynamics: Splashing, Spreading, Receding, Bouncing…,” *Annu. Rev. Fluid Mech.*, vol. 38, pp. 159–192, 2006.

[123] David B. Thiessen and Kin F. Man, “Surface Tension Measurement,” in *The Measurement, Instrumentation and Sensors Handbook*, Second., vol. 1, John G. Webster and Halit Eren, Eds. CRC Press LLC, 1999, pp. 1–14.

[124] Daniel Bonn, Jens Eggers, Joseph Indekeu, Jacques Meunier, and Etienne Rolley, “Wetting and Spreading,” *Reviews of Modern Physics*, vol. 81, no. 2, pp. 739–805, 2009.

[125] Davide Rossi, Enrico Mioni, Mirella Zancato, Antonio Bettero, and Sergio Rossi, “Development of a Tensiometric Model for Surface Energy Characterization of Raw Coffee Beans,” *Journal of Food Engineering*, vol. 112, no. 4, pp. 352–357, 2012.

[126] Dimitri Janssen, Randy De Palma, Stijn Verlaak, Paul Heremans, and Wim Dehaen, “Static Solvent Contact Angle Measurements, Surface Free Energy and Wettability Determination of Various Self-Assembled Monolayers on Silicon Dioxide,” *Thin Solid Films*, vol. 515, no. 4, pp. 1433–1438, 2006.

[127] Q.F Wei, “Surface Characterization of Plasma-Treated Polypropylene Fibers,” *Materials Characterization*, vol. 52, no. 3, pp. 231–235, 2004.

[128] B.K. Lok, P.Y. Ng, X. Hu, and H.P. Low, “Effect of Plasma Treated ITO Substrate on Inkjet Printing of Conductive Ink,” presented at the Electronics Packaging Technology Conference (EPTC), Singapore, 2006, pp. 154–160.

[129] Thomas Schuman, Britt Adolfsson, Magnus Wikström, and Mikael Rigdahl, “Surface Treatment and Printing Properties of Dispersion-Coated Paperboard,” *Progress in Organic Coatings*, vol. 54, no. 3, pp. 188–197, Nov. 2005.

[130] Phuong Q. M. Nguyen, Lip-Pin Yeo, Boon-Keng Lok, and Yee-Cheong Lam, “Patterned Surface with Controllable Wettability for Inkjet Printing of Flexible Printed Electronics,” *ACS Applied Materials & Interfaces*, vol. 6, no. 6, pp. 4011–4016, Mar. 2014.

[131] Daniel K. Owens and R. C. Wendt, “Estimation of the Surface Free Energy of Polymers,” *Journal of Applied Polymer Science*, vol. 13, no. 8, pp. 1741–1747, 1969.

[132] D. H. Kaelble, "Dispersion-Polar Surface Tension Properties of Organic Solids," *The Journal of Adhesion*, vol. 2, no. 2, pp. 66–81, Apr. 1970.

[133] Vadim Bromberg, Siyuan Ma, and Timothy J. Singler, "High-resolution inkjet printing of electrically conducting lines of silver nanoparticles by edge-enhanced twin-line deposition," *Applied Physics Letters*, vol. 102, no. 21, p. 214101, 2013.

[134] Anke Teichler, Jolke Perelaer, and Ulrich S. Schubert, "Combinatorial Screening of Materials Using Inkjet Printing as a Patterning Technique," in *Inkjet-Based Micromanufacturing*, Jan G. Korvink, Patrick J. Smith, and Dong-Youn Shin, Eds. Weinheim, Germany: WILEY-VCH Verlag GmbH & Co. KGaA, 2012, pp. 19–40.

[135] FujiFilm, "Dimatix Materials Printer." FujiFilm Dimatix, Inc., 2008.

[136] Daniele Sette, "Functional Printing: From the Study of Printed Layers to the Prototyping of Flexible Devices," Doctoral Thesis, Universite de Grenoble, Grenoble, France, 2014.

[137] Hans Kuerten and Daniel Siregar, "Drying of Inkjet-Printed Droplets," in *Inkjet-Based Micromanufacturing*, Jan G. Korvink, Patrick J. Smith, and Dong-Youn Shin, Eds. Weinheim, Germany: WILEY-VCH Verlag GmbH & Co. KGaA, 2012, pp. 97–110.

[138] Robert D. Deegan, Olgica Bakajin, Todd F. Dupont, Greb Huber, Sidney R. Nagel, and Thomas A. Witten, "Capillary Flow as the Cause of Ring Strains from Dried Liquid Drops," *Nature*, vol. 389, pp. 827–829, 1997.

[139] J. A. Lim, W. H. Lee, H. S. Lee, J. H. Lee, Y. D. Park, and K. Cho, "Self-Organization of Ink-jet-Printed Triisopropylsilylethynyl Pentacene via Evaporation-Induced Flows in a Drying Droplet," *Advanced Functional Materials*, vol. 18, no. 2, pp. 229–234, Jan. 2008.

[140] Suk-Joong L. Kang, *Sintering: Densification, Grain Growth, and Microstructure*. Amsterdam: Elsevier, 2005.

[141] By Jolke Perelaer, Antonius W. M. de Laat, Chris E. Hendriks, and Ulrich S. Schubert, "Inkjet-Printed Silver Tracks: Low Temperature Curing and Thermal Stability Investigation," *Journal of Materials Chemistry*, vol. 18, no. 27, p. 3209, 2008.

[142] Stan Farnsworth and Kurt Schroder, "Photonic Curing for Millisecond-Drying of Thin Films," *Specialist Printing Worldwide*, no. 4, pp. 34–36, 2012.

[143] Sawyer B. Fuller, Eric J. Wilhelm, and Joseph M. Jacobson, "Ink-Jet Printed Nanoparticle Microelectromechanical Systems," *Journal of Microelectromechanical Systems*, vol. 11, no. 1, pp. 54–60, 2002.

[144] S. Gamerith, A. Klug, H. Scheiber, U. Scherf, E. Moderegger, and E. J. W. List, "Direct Ink-Jet Printing of Ag–Cu Nanoparticle and Ag-Precursor Based Electrodes for OFET Applications," *Advanced Functional Materials*, vol. 17, no. 16, pp. 3111–3118, Nov. 2007.

[145] K. A. Schroder, "Mechanisms of Photonic Curing™: Processing High Temperature Films on Low Temperature Substrates," in *Nanotech*, vol. 2, CRC Press, 2011, pp. 220–223.

[146] K. A. Schroder, S. C. McCool, and W. F. Furlan, "Broadcast Photonic Curing of Metallic Nanoparticle Films," *NSTI-Nanotech*, vol. 3, pp. 1–4, 2006.

[147] Dinesh Agrawal, "Microwave Sintering of Ceramics, Composites and Metallic Materials, and Melting of Glasses," *Transactions of the Indian Ceramic Society*, vol. 63, no. 3, pp. 129–144, 2006.

[148] Romain Cauchois, Mohamed Saadaoui, Abdelwahhab Yakoub, Karim Inal, Beatrice Dubois-Bonvalot, and Jean-Christophe Fidalgo, "Impact of Variable Frequency Microwave and Rapid Thermal Sintering on Microstructure of Inkjet-Printed Silver Nanoparticles," *Journal of Materials Science*, vol. 47, no. 20, pp. 7110–7116, Oct. 2012.

[149] Jolke Perelaer, Mark Klokkenburg, Chris E. Hendriks, and Ulrich S. Schubert, "Microwave Flash Sintering of Inkjet-Printed Silver Tracks on Polymer Substrates," *Advanced Materials*, vol. 21, no. 47, pp. 4830–4834, Dec. 2009.

[150] J. Perelaer, B.-J. de Gans, and U. S. Schubert, "Ink-jet Printing and Microwave Sintering of Conductive Silver Tracks," *Advanced Materials*, vol. 18, no. 16, pp. 2101–2104, Aug. 2006.

[151] Jolke Perelaer, "Postprinting Processes for Inorganic Ink for Plastic Electronics Applications," in *Inkjet-Based Micromanufacturing*, Jan G. Korvink, Patrick J. Smith, and Dong-Youn Shin, Eds. Weinheim, Germany: WILEY-VCH Verlag GmbH & Co. KGaA, 2012, pp. 111–125.

[152] David Wallace, Donald Hayes, Ting Chen, Virang Shah, Delia Radulescu, Patrick Cooley, Kurt Wachtler, and Arunkumar Nallani, "Ink-Jet as a MEMS Manufacturing Tool," in *First International Conference on Integration and Commercialization of Micro and Nanosystems*, Sanya, Hainan, China, 2007, pp. 1161–1168.

[153] Karoliina Koski, Eveliina Koski, Juha Virtanen, Toni Björninen, Lauri Sydänheimo, L. Ukkonen, and Atef Z. Elsherbeni, "Inkjet-Printed Passive UHF RFID Tags: Review and Performance Evaluation," *The International Journal of Advanced Manufacturing Technology*, vol. 62, no. 1–4, pp. 167–182, Sep. 2012.

[154] Abdelwahhab Yakoub, Mohamed Saadaoui, Patrick Benaben, and Plamen Iliev, "High Efficiency of Low-Cost Spiral Antennas for RFID, Fully Printed by an Inline Inkjet Process," in *Large-area Organic & Printed Electronics Convention (LOPE-C)*, München, Germany, 2012.

[155] O. Benzaim, E. Bihar, D. Kaddour, D. Unnikrishnan, S. Tedjini, and M. Saadaoui, "Photonic Sintering and RF Performances of Inkjet-Printed Transmission Lines," in *Large-area Organic & Printed Electronics Convention (LOPE-C)*, München, Germany, 2013.

[156] Byung Ju Kang, Chang Kyu Lee, and Je Hoon Oh, "All-Inkjet-Printed Electrical Components and Circuit Fabrication on a Plastic Substrate," *Microelectronic Engineering*, vol. 97, pp. 251–254, Sep. 2012.

[157] Daniele Sette, Christophe Poulain, Abdelwahhab Yakoub, Mohamed Saadaoui, Béatrice Dubois, and Anne Blayo, "Study of the Electrical Contact in a Fully Inkjet Printed Membrane Switch," in *Proceedings of the 59th IEEE HOLM Conference on Electrical Contacts*, Newport, Rhode Island, 2013, pp. 1–6.

[158] D.J. Hayes, D.B. Wallace, M.T. Boldman, and R.M. Marusak, "Picoliter Solder Droplet Dispensing," *Microcircuits and Electronics Packaging*, vol. 16, no. 3, pp. 173–180, 1993.

[159] D.J. Hayes, W.R. Cox, and M.E. Grove, “Microjet Printing of Polymers and Solder of Electronics Manufacturing,” *Journal of Electronics Manufacturing*, vol. 8, no. 3–4, pp. 209–216, 1998.

[160] Wessel W. Wits and Ashok Sridhar, “Inkjet Printing of 3D Metallic Silver Complex Microstrucutres,” in *International Conference on Competitive Manufacturing*, Cape Touwn, South Africa, 2010, pp. 45–50.

[161] Veronica Sanchez-Romaguera, Marie-Beatrice Madec, and Stephen G. Yeates, “Inkjet Printing of 3D Metal–Insulator–Metal Crossovers,” *Reactive and Functional Polymers*, vol. 68, no. 6, pp. 1052–1058, Jun. 2008.

[162] Benjamin S. Cook, James R. Cooper, and Manos M. Tentzeris, “Multi-Layer RF Capacitors on Flexible Substrates Utilizing Inkjet Printed Dielectric Polymers,” *IEEE Microwave and Wireless Components Letters*, vol. 23, no. 7, pp. 353–355, Jul. 2013.

[163] Robert Horning, Thomas Ohnstein, and Daniel Youngner, “Method for Making Devices using Ink Jet Printing,” US7112463 B2, Sep-2006.

CHAPTER 3

MODELING AND OPTIMIZATION OF CAPACITIVE ACOUSTIC SENSOR

This chapter presents the design and simplified mathematical analyses of the capacitive acoustic transducer. The numerical simulation of the acoustic transducer based on finite element method (FEM) is discussed along with design of experiment (DOE). Eventually, the optimization of device is presented to achieve transducer with good sensitivity and selectivity over the experimental frequency range. This kind of device is known as capacitive acoustic resonator. The optimization of the acoustic sensor requires a clear understanding of the effect of different factors on the output responses of the sensor. During this work, output responses of capacitive acoustic transducer, such as membrane displacement, quality factor, capacitance variation and output voltage, are considered to evaluate the sensor design. The six device parameters taken into consideration are membrane radius, backplate radius, cavity height, air gap, membrane tension and membrane thickness. The effects of factors on the output responses of the transducer are investigated using an integrated methodology that combines numerical simulation and DOE. A series of numerical experiments is conducted to obtain output responses for different combinations of device parameters using FEM. Response surface method is used to identify the significant factors and to develop the empirical models for the output responses. Finally, these results are utilized to calculate the optimum device parameters using multi-criteria optimization with desirability function. Thereafter, the validating experiments are designed and deployed using the numerical simulation to crosscheck the responses.

3.1. Background

A capacitive acoustic transducer is a device [1], [2], which detects the incident acoustic pressure variation using vibrating diaphragm and provides capacitance variation in response. For years, several capacitive acoustic sensors have been developed and commercialized and majority of them were focused on audio applications that provides nearly uniform sensitivity over a wide range of frequencies [2]–[8].

Within the “Spinnaker” project framework, a simplified design has been proposed to fabricate a capacitive acoustic transducer with a central cylindrical rigid backing electrode of small radius surrounded by a flat annular cavity below a membrane clamped at its periphery, separated by an air gap [7], [8]. Honzik *et al.* [7] have reported that this design leads to a higher sensitivity, as well as a larger frequency bandwidth.

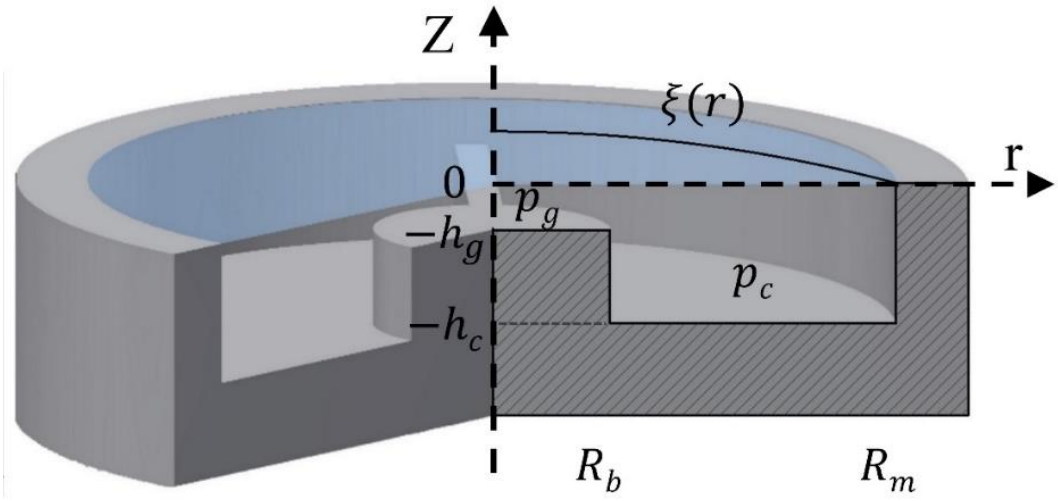

Figure 3.1: *Schematic diagram of the design of the acoustic transducer.*

A capacitive acoustic sensor, similar to that of a condenser microphone, can also be used as an acoustic resonant sensor by modifying different parameters related to the device fabrication. The characteristics of the damping material and other geometric parameters determine the transducer bandwidth. Generally, ideal microphones respond evenly to incident acoustic pressure over the entire range of relevant frequencies, whereas resonant transducers provide higher sensitivity at their natural frequencies.

During this work, we investigated the possibilities to develop the acoustic resonator based on the proposed design, as presented in Figure 3.1, to achieve strong sensitivity and selectivity at a specified frequency with narrow bandwidth. To fulfill the specific system requirement, one needs to optimize structural parameters, such as membrane radius, backplate radius, air gap, cavity height, membrane thickness, of the acoustic sensor (Figure 3.1). In addition, the membrane tension and materials used to fabricate the device needed to be optimized as well.

As a large number of parameters is involved in acoustic sensor optimization, numerical simulation can be a powerful and economical tool for virtual device prototyping. However, extensive computational effort is involved in numerical simulation and thus, it usually takes a substantial amount of time to complete simulation runs of a complex structure. In this work, a new design scheme for acoustic sensor optimization that combines numerical simulation using the COMSOL Multiphysics software and design of experiments (DOE) approach have been used. DOE helps to develop a set of experiments that provides a great deal of information about the effect of input parameters on responses. In this scheme, a set

of numerical experiments is conducted to generate responses. Thereafter, based on the numerical simulation results, the response surface method (RSM) is used to derive empirical models for each of the responses, which will later be used during the optimization process. The empirical model reduces computational efforts in the acoustic sensor optimization, since they are far less complex than the original finite element model.

In case of single response characteristic, optimization can simply be obtained by determining the experimental conditions that satisfied the expected response [9]. However, the performance of a capacitive acoustic resonant sensor is often characterized by a group of responses, such as static capacitance, capacitance variation, quality factor, etc. If more than one response comes into consideration, it is very difficult to select the optimal setting that can achieve all the required qualities simultaneously.

Vogel *et al.* [10] have applied FEM and a sequential quadratic programming (SQP) method as part of the CAPA optimization module to optimize micromachined capacitive ultrasound transducer array (CMUT), the design of comb structures for use in acceleration sensors, and the optimization of an electrostatic membrane device for an integrated silicone microphone. The SQP method is generally used for a nonlinearly constrained optimization problem that approximately solves a sequence of optimization subproblems, each of which optimizes a quadratic model of the objective subject to a linearization of the constraints. However, it is difficult to implement SQP methods so that exact second derivatives can be used efficiently and reliably [11]. The alternative of this approach, is to make use of a desirability function that transforms an estimated response into a scale-free value, known as global desirability [9], [12], [13]. With the multi-objective nature of our problem, desirability function is employed during this work to avoid the disadvantages of other methods.

A new approach that combined the numerical experiments and DOE approach to optimize the acoustic transducer with good sensitivity and selectivity is discussed. Figure 3.2 illustrates graphically the experimental process flow that has been used during this work. Initially, a set of numerical experiments are performed to predict responses of the sensor using FEM model. Thereafter, DOE approach is used to drive the empirical models based on the FEM simulation results for the acoustic sensor optimization.

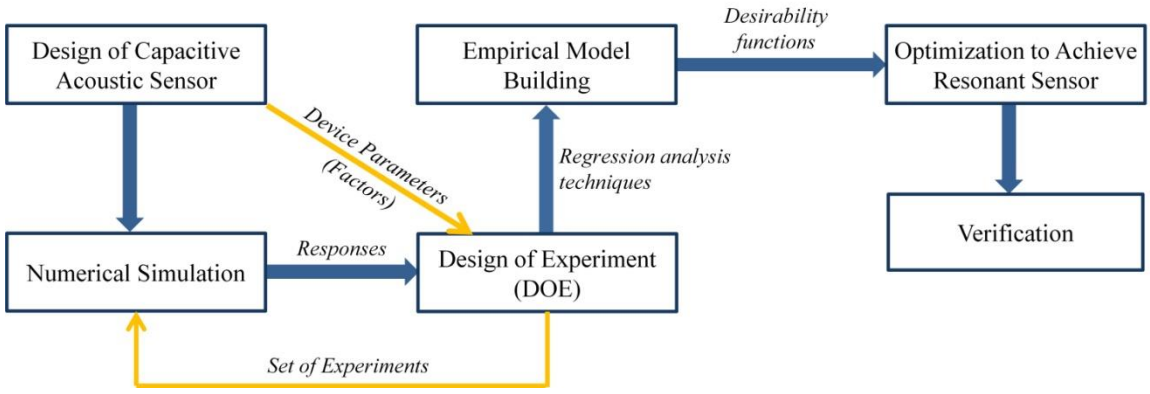

Figure 3.2: *Design scheme of the optimization process.*

Therefore, the objectives of this study are to investigate the effect of different parameters of the transducer on the output responses using the numerical analysis and DOE approach and to optimize device parameters to develop acoustic resonator that provides required sensitivity and selectivity. In this regard, the first part of this work is devoted to the theoretical analysis to understand the system, and then the construction of finite element (FE) model of the acoustic sensor (based on the design presented in Figure 3.1). Thereafter, DOE is introduced to achieve greater information with the least possible number of experiments. Finally, multi-criteria optimization is performed to obtain the optimum set of parameters, which is verified using numerical simulation.

3.2. Theoretical analysis

3.2.1. Basic description of the system and assumptions

The problem deals with the behavior of a vibrating membrane clamped at its periphery, and a thin layer of fluid that is trapped between the membrane and a central cylindrical rigid backing electrode of small radius surrounded by a flat annular cavity. For analytical solution, the backing electrode is assumed to be smooth without any holes or grooves, and the thin fluid layer in the air gap is assumed to be surrounded by a thick fluid region in the cavity. The fluid trapped in the air gap, due to movement of the membrane, is pumped back and forth in a relatively large cavity region. A schematic diagram of the corresponding device is illustrated in Figure 3.1.

In this model, the coordinate normal to the plane of the rigid backing electrode and the membrane is considered as z-axis, and 'r', the generalized coordinates defining the tangent plane. The plane of the membrane is denoted as "$z = 0$", the plane of the backing electrode

and the cavity are denoted by "$z = -h_g$" and "$z = -h_c$" respectively. The radius of the backing electrode is defined by R_e and the radius of the membrane by R_m.

It is assumed that the pressure variation in the air gap and cavity region is constant throughout the thickness of the fluid film and depends only on the tangent coordinate 'r'. As the pressure variation does not depend on the z-coordinate, thus the z-component of the particle velocity (v) can be neglected. On the other hand, the temperature variation depends on both coordinates 'r' and 'z'. The temperature variation is approximately proportional to the pressure variation outside the boundary layers. The temperature variation (τ) vanishes at the interfaces between the fluid layer and the membrane ($z = 0$), and between the fluid layer and the backing electrode ($z = -h_g$).

3.2.2. Electrostatic analysis

A capacitive acoustic sensor is an electro-mechanical transducer that transforms the mechanical deformation of the diaphragm in an output signal. The capacitance (C_0) of a parallel plate capacitor, with a fixed distance between the two electrodes h_0 and an overlapping area between the two electrodes plates S_e, also known as effective area, is given by

$$C_0 = \frac{\varepsilon_0 \varepsilon_r S_e}{h_0} \quad \dots\dots\dots (3.1)$$

Where ε_0 represents the vacuum permittivity ($\varepsilon_0 = 8.854 \times 10^{-12} F \cdot m^{-1}$) and ε_r represents the relative static permittivity of the materials between the plates (for vacuum, $\varepsilon_r = 1$). When an external DC voltage (V_0) is applied, an electrostatic force (F_{es}) as presented by equation (3.2), is created across the electrodes and induces a membrane deformation.

$$F_{es} = \frac{Q^2}{2\varepsilon_0 S_e} = \frac{\varepsilon_0 S_e}{2h_0^2} V_0^2 \quad \dots\dots\dots (3.2)$$

Thus the air gap (h_g) becomes ($h_0 + \langle \xi \rangle_{es}$), where $\langle \xi \rangle_{es}$ represents the quiescent average deformation of membrane due to the electrostatic force of the pre-polarization of the transducer. Therefore, the static capacitance (C_i) of the acoustic sensor can be expressed as,

$$C_i = \frac{\varepsilon_0 \varepsilon_r S_e}{h_0 + \langle \xi \rangle_{es}} = \frac{\varepsilon_0 \varepsilon_r S_e}{h_g} \quad \ldots\ldots\ldots (3.3)$$

The air gap of the transducer varies due to membrane deformation. If $\langle \xi \rangle_{Se}$ represents the average small signal deformation; the variable distance between the back electrode and the membrane becomes $(h_g + \langle \xi \rangle_{Se})$. Thus, the output capacitance (C_n) due to incident pressure can be expressed as follows,

$$C_n = \frac{\varepsilon_0 \varepsilon_r S_e}{h_g + \langle \xi \rangle_{Se}} = \frac{\varepsilon_0 \varepsilon_r S_e}{h_g}\left(1 - \frac{\langle \xi \rangle_{Se}}{h_g}\right) = C_i\left(1 - \frac{\langle \xi \rangle_{Se}}{h_g}\right) \quad \ldots\ldots\ldots (3.4)$$

where the expression has been expanded to the first order (Taylor series). Therefore, the capacitance variation (ΔC) can be obtained by subtracting equation (3.4) from equation (3.3),

$$\Delta C = |C_n - C_i| = C_i \frac{|\langle \xi \rangle_{Se}|}{h_g} \quad \ldots\ldots\ldots (3.5)$$

On the other hand, the total voltage (V) across the capacitor is the sum of the quiescent polarization voltage (V_0) and the small signal output voltage (V_{out}). The charge (Q) in the capacitor can be expressed as,

$$Q = CV \quad \ldots\ldots\ldots (3.6)$$

And its differentiation is given as,

$$dQ = CdV + VdC \quad \ldots\ldots\ldots (3.7)$$

We assume that the system has a constant total charge,

$$Q = \sum_i q_i = \text{const.} \quad \ldots\ldots\ldots (3.8)$$

where i represents the number of charges, and thus $dQ = 0$. The inclusion of this assumption in equation (3.7) gives

$$dV = -\frac{dC}{C}V \quad \ldots\ldots\ldots (3.9)$$

Assuming $C = C_n, dC \approx \Delta C, dV \approx V_{out}, V \approx V_0$, and introducing them into equation (3.9), the output voltage V_{out} can be expresses as:

$$V_{out} = V_0 \frac{C_i \frac{\langle \xi \rangle_{Se}}{h_g}}{C_i\left(1 - \frac{\langle \xi \rangle_{Se}}{h_g}\right)} = V_0 \frac{\langle \xi \rangle_{Se}}{h_g}\left(1 + \frac{\langle \xi \rangle_{Se}}{h_g}\right) \approx V_0 \frac{\langle \xi \rangle_{Se}}{h_g} \quad \ldots\ldots\ldots (3.10)$$

The expression has been expanded to the first order (Taylor series) and the higher order term is negligible and thus removed. Based on the analysis, it has been observed that the capacitance variation as well as output voltage of the acoustic sensor mainly depend on the membrane displacement. Therefore, to improve the sensitivity of the sensor, we have to design the sensor which will provide high membrane displacement.

3.2.3. Equations governing the membrane displacement

The equation governing the vibration of a thin circular membrane of radius R_m, thickness t_m, and density ρ_m under constant radial force per unit length (T_m) acting on its edge, driven by uniform harmonic incident acoustic pressure p_i over the membrane surface, loaded by the pressure field $p(r)$, also known as reaction pressure at the membrane surface, can be expressed as [7], [8], [14], [15],

$$T_m\left(\Delta_r + K^2\right)\, \xi(r) = p_i - p(r), \quad 0 < r < R_m \quad \ldots\ldots\ldots (3.11)$$

Here, $\xi(r)$ being the vertical membrane displacement, Δ_r (equals to ∇_r^2) represents the Laplace operator, and K^2 defines the wavenumber of the free flexural vibration of the membrane,

$$K^2 = \frac{\omega^2 \rho_{ms}}{T_m} = \frac{\omega^2}{c^2}; \quad c = \sqrt{\frac{T_m}{\rho_{ms}}} \qquad \text{and} \qquad \rho_{ms} = t_m \rho_m \quad \ldots\ldots\ldots (3.12)$$

where c denotes the speed of sound in the membrane, ρ_{ms} is the surface density of the membrane and ω is the angular frequency. The membrane is supported on a rigid circular frame at its periphery $r = R_m$ (Dirichlet boundary condition), therefore,

$$\xi(R_m) = 0 \quad \ldots\ldots\ldots (3.13)$$

The reaction pressure $p(r)$, loading the diaphragm, is due to the underlying air layer squeezed in air gap and in the annular cavity under the membrane, where

$$p(r)=\begin{cases} p_g(r) & r\in(0,R_e) \\ p_c=\text{const} & r\in(R_e,R_m) \end{cases} \quad \ldots\ldots\ldots (3.14)$$

Here $p_g(r)$ and $p_c(r)$ represent the pressure in the air gap and in the cavity volume respectively. The cavity pressure is assumed to be quasi-uniform, R_e represents the effective radius and is equal to the radius of the backplate electrode (R_b).

The incident acoustic signal (with the time factor given by $e^{j\omega t}$) triggers the membrane displacement $\xi(r)$, which is assumed to be small and harmonic ($\xi(r)e^{j\omega t}$). The general solution for the displacement of the membrane $\xi(r)$ is the eigenfunction expansion and can be written as [8],

$$\xi(r)=\sum_n \xi_n \Psi_n(r) \quad \ldots\ldots\ldots (3.15)$$

The eigenfunctions $\Psi_n(r)$ are expressed as,

$$\Psi_n(r)=\frac{1}{\sqrt{\pi}R_m J_1(K_n R_m)} J_0(K_n r) \quad \ldots\ldots\ldots (3.16)$$

Where K_n is given by the equation $J_0(K_n R_m)=0$ (zero order Bessel function of the first kind). The constants ξ_n can be expressed based on the orthogonality properties of the eigenfunctions $\Psi_n(r)$ as follows:

$$\xi_n=\frac{1}{T_m\left(K^2-K_n^2\right)}\iint_{S_m}\left(p_i-p(r)\right)\Psi_n dS_m \quad \ldots\ldots\ldots (3.17)$$

Here $S_m=\pi R_m^2$ represents the surface of the membrane.

The membrane displacement gives rise to the motion of the air in the domain below the circular membrane, composed of the air gap and the annular cavity. As assumed before, the pressure variation does not depend on the z-coordinate, thus the z-component of the particle velocity (v) can be neglected. In addition, the temperature variation (τ), which is approximately proportional to the pressure variation outside the boundary layers, vanishes

at the interfaces between the fluid layer and the membrane at "$z = 0$", and between the fluid layer and the backing electrode at "$z = -h_g$". Thus the boundary conditions associated with the system are,

$$v_{r(g,c)}(r,0) = v_{r(g,c)}(r,-h_{g,c}) = 0 \quad \ldots\ldots\ldots (3.18)$$

$$\text{and } \tau_{g,c}(r,0) = \tau_{g,c}(r,-h_{g,c}) = 0 \quad \ldots\ldots\ldots (3.19)$$

The solution of the mean displacement of the circular membrane over the backplate electrode driven by a constant incident pressure p_i due to the sound field can be expressed as follows [7], [8]:

$$\langle \xi \rangle_{Se} = \frac{1}{S_e} \iint_{S_e} \xi(r) dS_e = \frac{2}{\sqrt{\pi} R_e R_m} \sum_n \xi_n \frac{J_1(K_n R_e)}{K_n J_1(K_n R_m)} \quad \ldots\ldots\ldots (3.20)$$

For details see Appendix A.

3.2.4. Pressure sensitivity

The sensitivity level (L) of the acoustic sensor for the given bias voltage (V_0), represents the relation between the input pressure and the output voltage, and can be expressed as follows,

$$L = 20 \log\left[\left|\frac{V_{out}}{p_i}\right|\right] = 20 \log\left[\left|\frac{V_0 \langle \xi \rangle_{Se}}{p_i h_g}\right|\right] \quad \ldots\ldots\ldots (3.21)$$

3.2.5. Resonant frequency

The selectivity of the acoustic resonant sensor depends on its natural frequency or resonant frequency. At resonant frequency, all parts of the membrane vibrate sinusoidally with the same frequency and with a fixed phase relation, which provides maximum displacement of membrane and is known as the normal mode of vibration. Resonant frequencies of the membrane in vacuum are solely determined by its physical dimensions and mechanical constants, namely, Young's modulus, density of the membrane material, size of the membrane and boundary conditions. As the maximum membrane displacement occurs at resonant frequency, it leads to the maximum sensitivity for the capacitive acoustic sensor.

The natural frequencies of the pre-tensed circular vibrating membrane in vacuum is given by [16], [17],

$$f_{ij} = \frac{k_{ij}}{2\pi R_m}\sqrt{\frac{T_m}{t_m \rho_m}} = \frac{k_{ij}}{2\pi R_m}\sqrt{\frac{T_m}{\rho_{ms}}} \quad \ldots\ldots\ldots (3.22)$$

The values k_{ij} are derived from the roots of the Bessel functions of the first kind. The natural frequencies of vibration and mode shapes are identified by two integers (i, j) that characterize the mode shape. The index $i = 1, 2, 3, \ldots$ corresponds to the number of circumferential lines ($r = const.$) on the membrane that have zero displacement, while $j = 0, 1, 2, \ldots$ corresponds to the number of diametral lines ($\theta = const.$) that have zero displacement. The values k_{ij} for the first six modes are listed in Table 3.1.

Table 3.1: Values of k_{ij} derived from the roots of the Bessel functions of the first kind for first six modes

Mode number	Factor
1	$k_{10} = 2.4048$
2	$k_{11} = 3.8317$
3	$k_{11} = 3.8317$
4	$k_{12} = 5.1356$
5	$k_{12} = 5.1356$
6	$k_{20} = 5.5201$

However, in case of a capacitive acoustic resonator, the membrane is usually loaded with an air cavity rather than vibrating in free space [18]. The presence of the cavity generally detunes the membrane resonance [19]. The shift of the first resonant frequency of the system towards higher frequency than that of the membrane in vacuum occurs due to viscous damping and acoustic stiffness of the cavity [20].

3.2.6. Quality factor

The quality factor, also known as Q-factor (Q_f), which is related to the energy loss of the vibrating diaphragm [21], is characterized by a resonator's bandwidth relative to its center frequency. Generally, in frequency domain, Q-factor is expressed as,

$$Q_f = \frac{f_r}{\Delta f} = \frac{\omega_r}{\Delta \omega} \quad \ldots\ldots\ldots (3.23)$$

where f_r is the resonant frequency, Δf is the half-power bandwidth (i.e. the bandwidth over which the power of the vibration is greater than half the power at the resonant frequency), $\omega_r = 2\pi f_r$ is the angular resonant frequency and $\Delta\omega$ the angular half power bandwidth.

High Q_f value represents low damping, which indicates low rate of energy loss relative to the stored energy of the resonator [22], [23]. Q-factor is inversely proportional to the damping coefficient of the oscillating system and defined as [22],

$$Q_f = 2\pi \frac{W}{\Delta W} = \frac{m\omega_r}{\gamma} = \frac{K}{\gamma\omega_r} \quad \ldots\ldots\ldots (3.24)$$

where W is the total energy stored in the resonator, ΔW is the energy loss per cycle, K is the spring constant of the resonator, γ is the coefficient of the damping force and m is the mass of the oscillator.

Thus, higher Q-factor represents higher selectivity. The Q-factor of the system can be improved by enhancing the total stored energy, while reducing the energy loss per cycle.

3.3. Numerical simulation

3.3.1. Finite element model (FEM)

The finite element method is a numerical method, generally used for solving a differential or integral equation of engineering and mathematical physics problems, such as structural analysis, heat transfer, fluid flow, mass transport and electromagnetic potential. Basically, FEM is used as a "virtual prototyping" tool for finding approximate solution for problems involving complex geometries, loading and materials properties [24].

Generally, the FEM works by subdivision of the whole problem domain into simpler parts, known as finite elements. Thereafter, the behavior of each little element, which is regular in shape, is promptly anticipated by a set of mathematical equations. The summation of these individual element behaviors generates the expected behavior of the actual object [24]–[27].

Engineering problems are continuum problems in most cases. This means that all bodies of interest are continuous at all points in space. In general, the solution of such continuum

problems using the FEM follows a general step-by-step procedure. The finite element method is generally characterized by [24]–[27]:

1. Discretization of the domain: in this step, the body is divided into an equivalent system of finite elements with associated nodes. Appropriate element shapes need to be selected to accurately model the physical behavior. The accuracy of the solution also depends on the size or number of elements.

2. Selection of the shape functions: the second step involves the selection of the shape functions within each element, which can be defined using the nodal values to obtain the variation of the field variable over the element. Generally, linear, quadratic and cubic polynomials are the frequently used functions. The principle of selecting the shape function is that the field variable or its derivatives are continuous across the adjoining element boundaries.

3. Formulation of the element equations: after the selection of the elements and their shape functions, the matrix equations expressing the properties of the individual elements are determined. They are known as element equations.

4. Assembling the element equations to obtain the system equations: at this stage, the element equations are assembled to determine the properties of the entire domain represented by the system of elements. The assembly of the element equations provides the matrix equations that express the properties of the entire system. The principle of the assembly is that the nodal value of the field variable at a node where the elements are interconnected should be the same for all elements sharing this node.

5. Set-up of the boundary conditions: thereafter, the boundary conditions of the problem are defined prior to solve the system equations.

6. Solving of the system equations: once the element equations are assembled and the boundary conditions are included, a system of matrix equations is computed to solve the unknown nodal values of the domain. The system equations are generally expressed as follows,

$$\underset{n\times n}{[K]}\underset{n\times 1}{\{u\}} = \underset{n\times 1}{\{F\}} \quad \text{... ... ... (3.25)}$$

where $[K]$ represents the properties, like, stiffness, conductivity, viscosity, dielectric permittivity etc., $\{u\}$ is the vector of the unknown field variables or behaviors, e.g., displacement, temperature, velocity, electric potential etc., and $\{F\}$ is known as action, such as force, heat source, charge etc. The system of these matrix equations can be linear or nonlinear.

7. Post-processing: sometimes post-processing of the solution is required, which is designed to extraction of data of interest from FEM solution.

3.3.2. FEM model development of the acoustic transducer

The capacitive acoustic sensor works by transforming the mechanical deformation of a thin membrane (diaphragm), induced by an external incident pressure, into a capacitance variation or an AC voltage signal. Numerical simulation is performed using finite element method (FEM) not only to understand but also to quantify the effect of different input parameters on the membrane displacement, capacitance variation, Q-factor, output voltage. The finite element simulation of the acoustic sensor is a moving boundary problem, in which the computational air domain within the sensor changes continuously, because of membrane vibration under harmonic acoustic wave. Three-dimensional (3D) FEM model is developed using half-slice of the air domain (symmetrical part) to reduce the computational time, as illustrated in Figure 3.3.

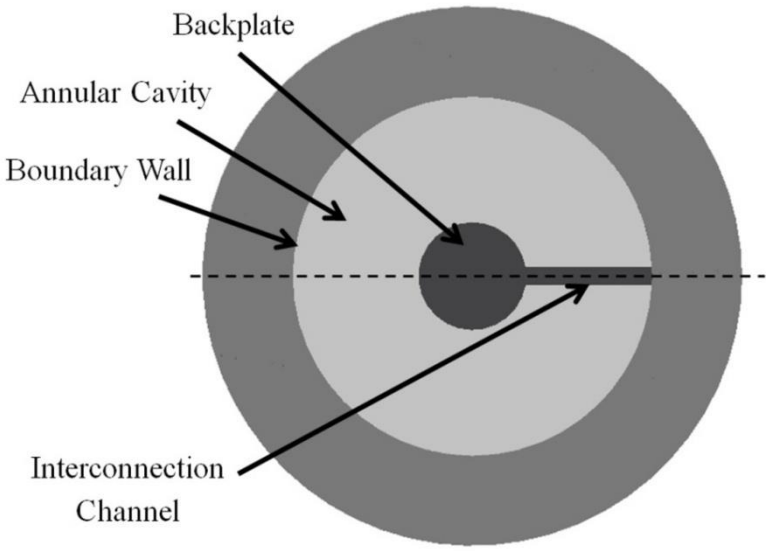

Figure 3.3: *Schematic diagram of top view of the proposed acoustic sensor without the diaphragm.*

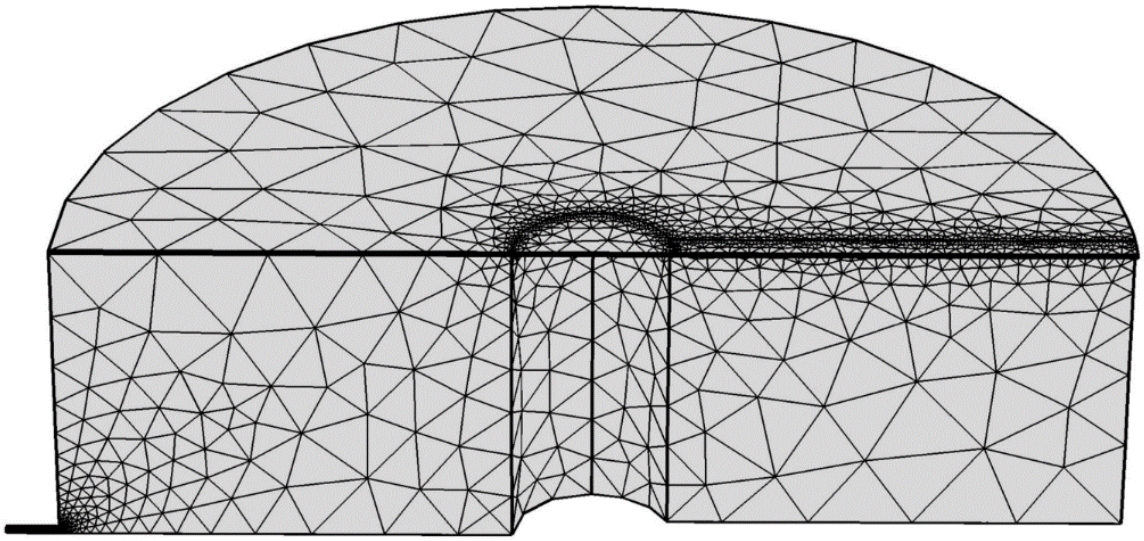

Figure 3.4: *Half-slice of air domain (symmetrical part) of the acoustic sensor with finite element mesh.*

Figure 3.4 illustrates the half-slice of the 3D air domain with finite element mesh, which was solved considering the periodicity and symmetry of the boundary value. The custom mesh is used in such a way that it resolves the acoustic boundary layer for the frequency range of 0 Hz to 250 kHz without mesh regeneration. The physical parameters of the air and the membrane materials are given in Table 3.2.

Table 3.2: Physical properties of the thermoviscous fluid (air) and material properties of the membrane

Parameter	Value	Unit
Bulk viscosity (μ_{B0})	10 x 10^{-6}	Pa·s
Gas constant (R_{s0})	281.4	J/(kg·K)
Density of Membrane (ρ_m)	1390	kg/m^3
Young's modulus of membrane (E_m)	4×10^9	Pa
Poisson's ratio of membrane (υ_m)	0.38	-

The resulting finite element model with fully coupled thermoacoustic, electrostatic, moving mesh and membrane physics interface was solved using the linear-perturbation solver, PARDISO, in the frequency domain. Solution of the numerical simulation provides the membrane displacement with respect to frequencies. Figure 3.5 presents the membrane displacement at first resonant frequency (f_r).

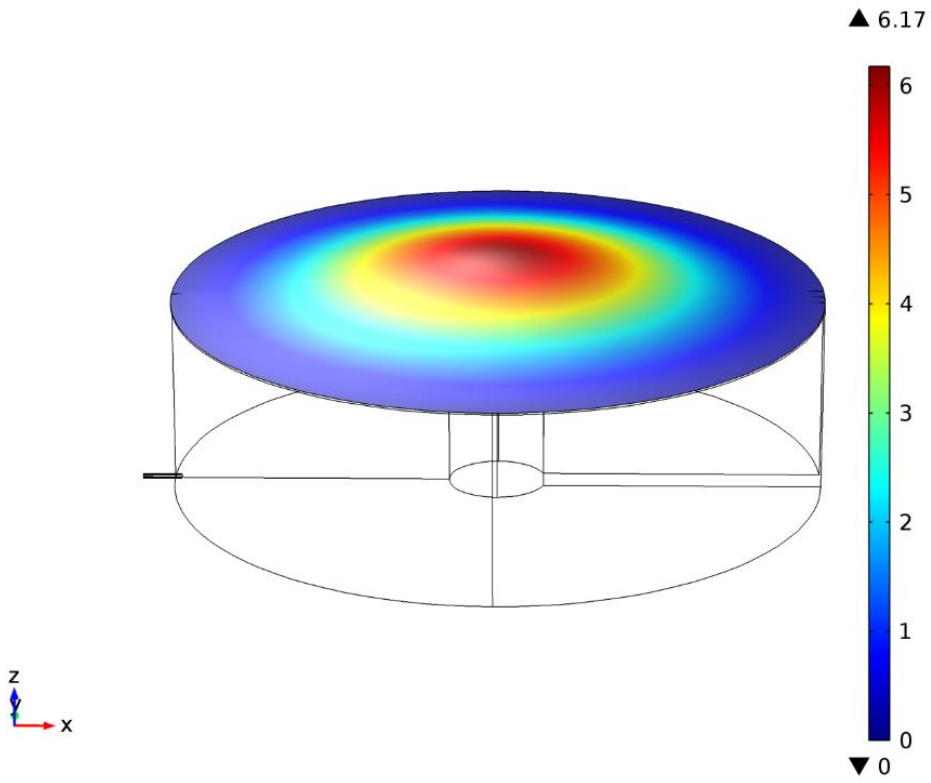

Figure 3.5: *Measured displacement field of the membrane of the acoustic sensor at first resonant frequency (f_r = 16737 Hz) for R_m=5mm, R_b=0.75mm, h_c=3000µm, h_g=30µm, T_m=500N/m and t_m=8µm.*

COMSOL Multiphysics software (version 4.4) is used to perform 3D numerical simulation. All the numerical works have been executed on a workstation, DELL PRECISION T7600, having 32 Gigabytes RAM and 16 cores (two 3.1GHz eight-core Intel Xeon E5-2687W Processors).

The validation of the numerical model is checked by comparing the maximum membrane displacement of the numerical analysis with that of the theoretical analysis as presented in equation (3.20). The results show proximate similarity as depicted in Figure 3.6. A little shift of the resonant frequency and a slightly smaller magnitude of the membrane displacement are obtained in the FEM results. They are caused by the presence of the interconnection channel to electrically connect the bottom electrode with the outside, and the venting hole as it is in the real device; whereas for simplicity the effect of the interconnecting channel and venting hole are not considered in the theoretical analysis.

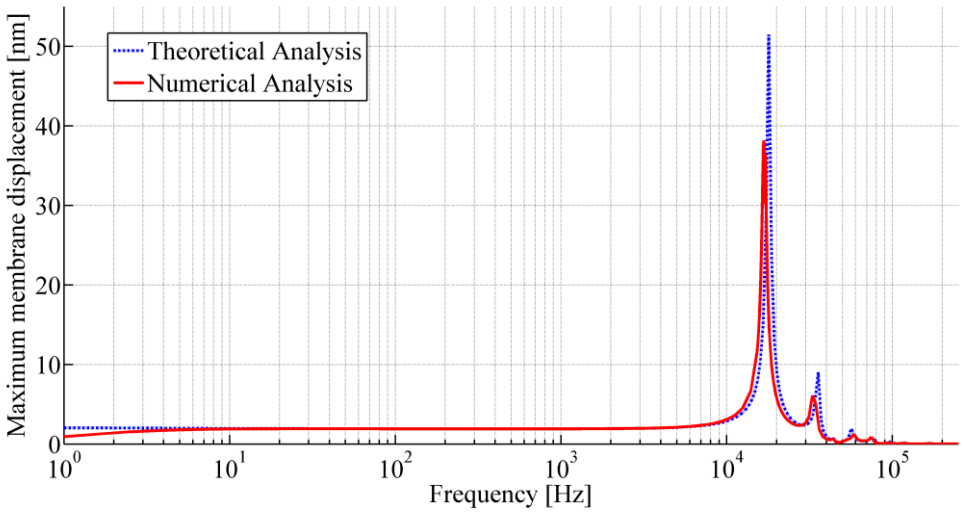

Figure 3.6: *Comparison of the membrane displacement of theoretical and numerical analysis of the acoustic transducer (for R_m=5mm, R_b=0.75mm, h_c=3000µm, h_g=30µm, T_m=500N/m and t_m=8µm).*

3.3.3. Selection of parameters and responses

Based on the theoretical analysis and the device structure, several parameters, such as membrane radius (R_m), bottom electrode radius (R_b), cavity height (h_c), air gap (h_g), membrane tension (T_m), membrane thickness (t_m), materials properties of the membrane (e.g., Young's modulus, density of the materials and Poisson ratio), and the venting hole geometry are involved with device performance. During this study, geometry of the venting hole was kept unchanged and the polyethylene terephthalate (PET) thin film was used as a membrane material, whose properties are listed in Table 3.2. Thus venting-hole geometry and material properties were omitted from the further analysis.

The static capacitance of the system is generally determined by the effective surface area of the electrodes and air gap, whereas the Q-factor depends on the damping loss mechanism that is related to the device geometry. On the other hand, the sensitivity of the acoustic sensor, is basically driven by the membrane displacement. Therefore, the first step of this work is the identification of the major input parameters that strongly influence the membrane displacement and Q-factor. In this regard, the classic "one variable at a time" method is used, where the effect of individual parameter on the membrane displacement at first resonant frequency was studied, for a fixed set of other parameters at their nominal

values, using numerical simulation. The process is repeated for each of the parameters involved in the study until all the parameters have been studied.

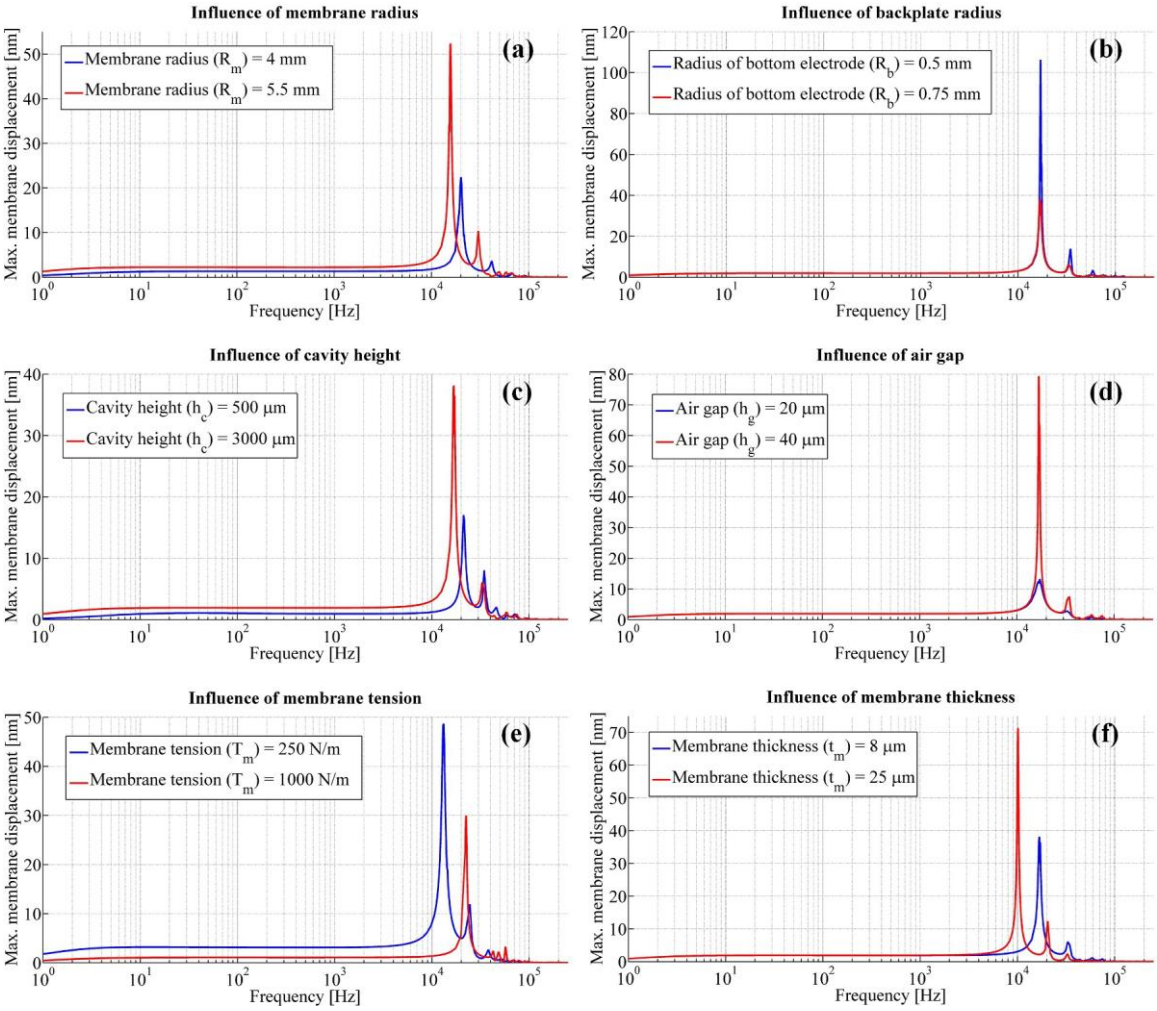

Figure 3.7: *Effect of individual input parameter on the membrane displacement (other parameters kept at constant value: R_m=5mm, R_b=0.75mm, h_c=3000µm, h_g=30µm, T_m=500N/m and t_m=8µm).*

Increase of the membrane displacement and Q-factor, and shift of the resonant frequency are observed for the increasing membrane radius, as showed in Figure 3.7(a). On the other hand, the increase of the bottom electrode radius leads to reduction of membrane displacement and Q-factor (Figure 3.7(b)). Figure 3.7(c) illustrates the effect of cavity height on the membrane displacement. Large cavity height reduces the air damping in the cavity and thus favors the increase of the membrane displacement and Q-factor. Similarly, increase in air gap provides higher membrane displacement and quality-factor (Figure 3.7(d)). However, the increase in air gap leads to a lower static capacitance. In addition, as

shows in Figure 3.7(e), higher membrane tension reduces the membrane displacement, and also shifts the resonance at higher frequency. Thickness of the membrane also affects the membrane displacement and the resonant frequency (Figure 3.7(f)).

Based on these initial tests, it has been observed that all six input parameters, namely, R_m, R_b, h_c, h_g, T_m and t_m, have some influence on the membrane displacement and Q-factor, and therefore, on the output responses. Moreover, to achieve better selectivity, the sensitivity at other natural frequencies than the first resonant frequency has to be reduced. Therefore, in order to study and eventually to optimize the capacitive acoustic resonator to fulfill the requirements, several output responses, namely, static capacitance (C_0), membrane displacement at first resonance ($|\langle \xi_{Se} \rangle|_{fr1}$), quality factor ($Q_f$), capacitance variation (ΔC), capacitance ratio ($\Delta C/C_0$), output voltage (V_{out}) and membrane displacement at second resonance ($|\langle \xi_{Se} \rangle|_{fr2}$) were studied for each experiment.

However, one-variable-at-a-time approach cannot predict the interaction between the factors. In addition, this approach is not applicable for multiple response problems and does not permit the construction of a model for the system [28]. Therefore, the study of the influence of all the input parameters and their interactions and the optimization of the system requires methodical experimental strategies based on DOE. A good experimental strategy will provide the necessary information to estimate effects of factors, to develop empirical models for each system output and to optimize the multiple responses simultaneously to fulfill the objectives.

3.4. Experimental design

DOE provides a systematic way to study the effects of the input variables of a system or process, also known as factors, on outputs or responses. It is an effective tool for maximizing the amount of information gained from a study while minimizing the number of tests to be performed. In practice, DOE is applicable to both physical processes and numerical simulation models [29], [30]. However, unlike physical measurement, numerical experimentation is not subject to noise or uncertainly [31], [32].

Compared to other experimental strategies, namely, one-variable-at-a-time [28] and sequential simplex [28], [33], RSM is intended to predict the response with a good quality all over the experimental domain. RSM approach has four basic steps: the data collection

according to an experimental design, an empirical model (e.g., polynomial) calculation by least square regression for each of the responses, generation of response-surface contour plots or maps that are examined to the region of the desired response and finally, the experimental verification of the predicted optimum [28]. DOE coupled with RSM can achieve rapid process development under minimal cost.

The selection of appropriate experiments is very important to build a reliable response surface model and therefore, its precise prediction [34]. According to the postulated model, there are different optimal designs of experiments with a guarantee of good prediction in the domain of interest. One of the best known for a second-order model is the class of central composite design (CCD), consisting of a two-level complete or fractional factorial design, an "axial" design and center points [34].

A series of FEM analysis of an acoustic sensor based on DOE has been performed to investigate the possibility of determining the optimal set of parameters to fabricate sensor with optimum sensitivity and selectivity. The optimization is carried out to maximize the membrane displacement at first resonant frequency of the system, while minimizing the membrane displacement at other frequencies. The feasible domain is defined by the six factors, namely, R_m, R_b, h_c, h_g, T_m and t_m. The ranges of the six factors used in the numerical experiments are presented in Table 3.3; these values were selected based on the process capabilities of our equipment to fabricate devices.

Table 3.3: Range of experimental variables (factors)

Factors	Code	Range
Membrane Radius (R_m)	x_1	4 – 10 mm
Bottom Electrode Radius (R_b)	x_2	0.25 – 3 mm
Cavity Height (h_c)	x_3	1000 – 4000 µm
Air gap (h_g)	x_4	3 – 80 µm
Membrane Tension (T_m)	x_5	100 – 3000 N/m
Film Thickness (t_m)	x_6	8 – 25 µm

The variation domain of the six factors defines a hypercube in six dimensions. A second-order model was postulated to represent the evolution of the responses in this domain and to optimize the acoustic resonant sensor. To estimate the coefficients of the model, a CCD was built with some additional points corresponding to a space-filling design to cover the entire domain. A total of 62 experiments were employed and listed in Table 3.4. These experiments were performed using numerical simulation, and for each experimental run,

C_0, $|\langle\xi_{Se}\rangle|_{fr1}$, Q_f, ΔC, $\Delta C/C_0$, V_{out} and $|\langle\xi_{Se}\rangle|_{fr2}$ were collected (Appendix B) for further analysis and empirical model building. During this study, "nemrodW" statistical software [35] was used to develop experimental strategies and search for optimal settings.

Table 3.4: DOE table for acoustic sensor study

N°Exp	R_m	R_b	h_c	h_g	T_m	t_m	*N°Exp*	R_m	R_b	h_c	h_g	T_m	t_m
	mm	mm	µm	µm	N/m	µm		mm	mm	µm	µm	N/m	µm
1	4	0.25	1000	3	3000	8	32	10	3	4000	80	100	25
2	10	0.25	1000	3	100	8	33	10	0.25	1000	3	3000	25
3	4	3	1000	3	100	8	34	4	3	1000	3	3000	25
4	10	3	1000	3	3000	8	35	4	0.25	4000	3	3000	25
5	4	0.25	4000	3	100	8	36	10	3	4000	3	3000	25
6	10	0.25	4000	3	3000	8	37	4	0.25	1000	80	3000	25
7	4	3	4000	3	3000	8	38	10	3	1000	80	3000	25
8	10	3	4000	3	100	8	39	10	0.25	4000	80	3000	25
9	4	0.25	1000	80	100	8	40	4	3	4000	80	3000	25
10	10	0.25	1000	80	3000	8	41	10	1.625	2500	41.5	1550	16.5
11	4	3	1000	80	3000	8	42	7	0.25	2500	41.5	1550	16.5
12	10	3	1000	80	100	8	43	7	1.625	1000	41.5	1550	16.5
13	4	0.25	4000	80	3000	8	44	7	1.625	2500	3	1550	16.5
14	10	0.25	4000	80	100	8	45	7	1.625	2500	41.5	100	16.5
15	4	3	4000	80	100	8	46	7	1.625	2500	41.5	3000	16.5
16	10	3	4000	80	3000	8	47	5.9	1.322	2266	36.9	1407	15.8
17	4	1.625	2500	41.5	1550	8	48	8.1	1.322	2266	36.9	1407	15.8
18	10	1.625	2500	41.5	1550	8	49	7	2.231	2266	36.9	1407	15.8
19	7	0.25	2500	41.5	1550	8	50	7	1.625	3202	36.9	1407	15.8
20	7	3	2500	41.5	1550	8	51	7	1.625	2500	60.1	1407	15.8
21	7	1.625	1000	41.5	1550	8	52	7	1.625	2500	41.5	2265	15.8
22	7	1.625	4000	41.5	1550	8	53	7	1.625	2500	41.5	1550	20.8
23	7	1.625	2500	3	1550	8	54	4	0.5	1000	80	100	8
24	7	1.625	2500	80	1550	8	55	4	0.5	4000	80	3000	8
25	4	0.25	1000	3	100	25	56	10	0.5	4000	80	100	8
26	10	3	1000	3	100	25	57	7	0.5	2500	41.5	1550	8
27	10	0.25	4000	3	100	25	58	7	0.5	2500	80	1550	8
28	4	3	4000	3	100	25	59	4	0.5	4000	80	100	25
29	10	0.25	1000	80	100	25	60	4	0.5	1000	80	3000	25
30	4	3	1000	80	100	25	61	10	0.5	4000	80	3000	25
31	4	0.25	4000	80	100	25	62	7	0.5	2500	60.1	1407	15.8

3.5. Results and discussions

3.5.1. Empirical model building and analysis

To perform data analysis, the experimental data are first transformed into logarithmic scale to get symmetric distribution, as presented by the box plot [9] in Figure 3.8. The coefficients of the models are then estimated using common regression analysis techniques [30], [36] to solve $\boldsymbol{X}_{62\times28}\boldsymbol{\beta}_{28\times1} = y_{62\times1}$, where $\boldsymbol{X}$ indicates the matrix of factors and factor interactions, vector y is the experimental results for one response in logarithmic scale, and

vector $\boldsymbol{\beta}$ is the unknown coefficients. Generally, $\boldsymbol{\beta}$ is estimated by resolving the linear system of equations, and can be expressed as $\boldsymbol{\beta} = (\boldsymbol{X^T X})^{-1}\boldsymbol{X^T} y$, where '$T$' and '$-1$' represent the transpose and inverse matrix respectively. Once the coefficients are computed, the equation of the empirical model for each response is entirely defined. For instance, observation reveals that the Q-factor is mainly influenced by linear terms R_b, h_c, h_g, t_m, quadratic terms R_b^2, h_c^2, and interaction terms $R_m R_b$, $R_m h_c$, $R_m T_m$, $R_b h_c$, $R_b h_g$, $R_b T_m$, $R_b t_m$, $h_c h_g$, $h_c T_m$, $h_g T_m$, $h_g t_m$ etc. For simplicity, only the most significant terms of the empirical models are mentioned in the equations (3.26) to (3.32) below, although each second order polynomial response equation consists of 28 terms.

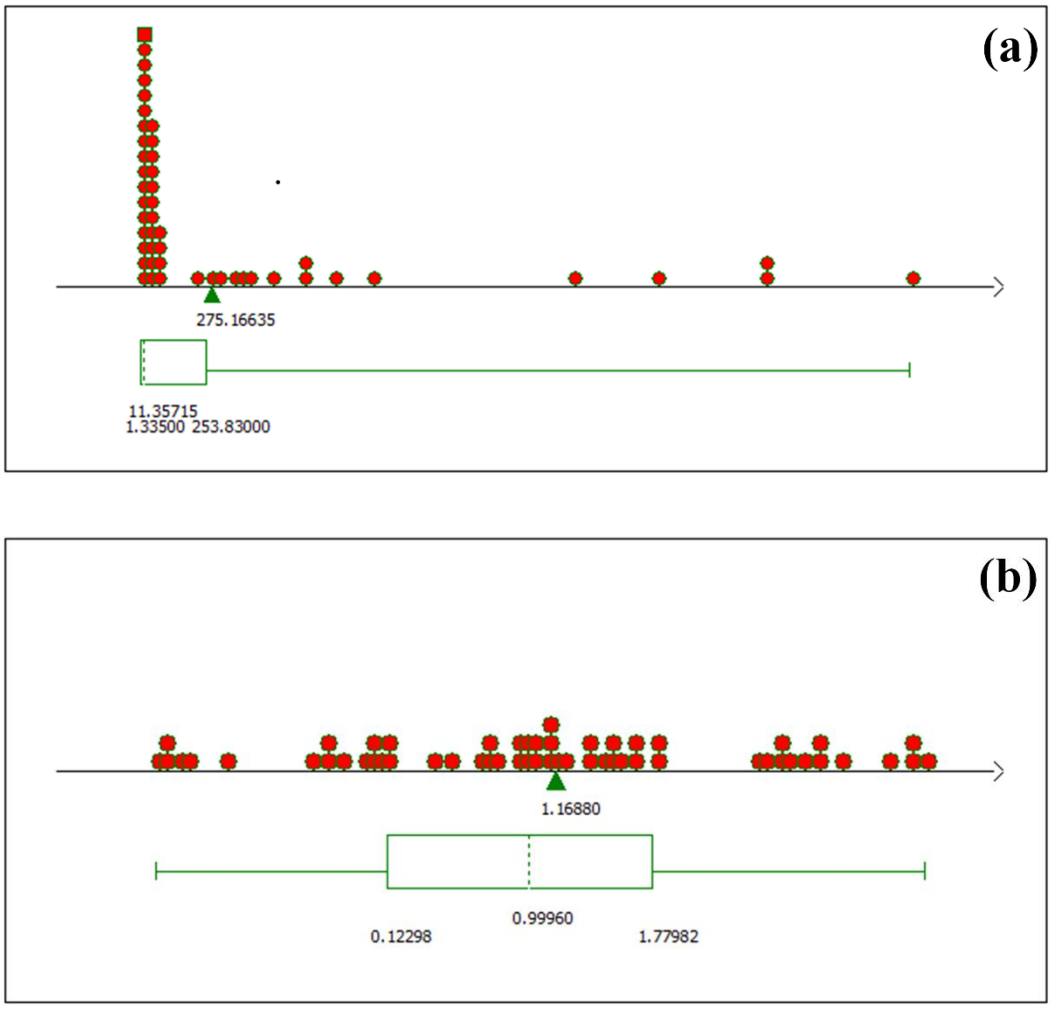

Figure 3.8: *Box plot of the response: maximum average membrane displacement at first resonant frequency ($|\langle \xi_{Se} \rangle|_{fr1}$), (a) linear scale and (b) logarithmic scale.*

$$Y_{C0} = 0.29743 + 0.09489x_1 + 0.61423x_2 - 0.71485x_4 - 0.04947x_1^2 - 0.09846x_2^2 + 0.43464x_4^2 - 0.08399x_1x_2 \quad (3.26)$$

$$Y_{|\langle\xi_{Se}\rangle|fr1} = 1.28557 + 0.22517x_1 - 0.87877x_2 + 0.25368x_3 + 0.95558x_4 - 0.24669x_5 + 0.11454x_6 + 0.51751x_2^2 - 0.46702x_4^2 - 0.29140x_5^2 + 0.14770x_1x_2 + 0.18454x_1x_3 - 0.06673x_2x_3 - 0.19040x_2x_4 + 0.09034x_1x_5 + 0.11223x_2x_5 - 0.06130x_3x_5 + 0.06152x_4x_6 + 0.13720x_5x_6 \quad (3.27)$$

$$Y_{Qf} = 1.16077 - 0.45781x_2 + 0.09958x_3 + 0.12209x_4 + 0.09090x_6 + 0.75406x_2^2 - 0.31853x_3^2 + 0.24556x_1x_2 + 0.30512x_1x_3 - 0.19310x_2x_3 - 0.61056x_2x_4 - 0.16106x_3x_4 - 0.19291x_1x_5 + 0.15244x_2x_5 + 0.19565x_3x_5 + 0.36619x_4x_5 + 0.12421x_2x_6 + 0.17754x_4x_6 \quad (3.28)$$

$$Y_{\Delta C} = -0.11475 + 0.24282x_1 + 0.16241x_2 + 0.26101x_3 - 0.44159x_4 - 0.24636x_5 + 0.11822x_6 + 0.64695x_4^2 + 0.15244x_1x_2 + 0.19087x_1x_3 - 0.20920x_2x_4 + 0.09150x_1x_5 + 0.11199x_2x_5 + 0.14269x_5x_6 \quad (3.29)$$

$$Y_{\Delta C/C0} = -1.36351 + 0.12631x_1 - 0.44107x_2 + 0.26289x_3 + 0.27584x_4 - 0.24843x_5 + 0.11406x_6 - 0.32919x_5^2 + 0.23530x_1x_2 + 0.19518x_1x_3 - 0.21663x_2x_4 + 0.08997x_1x_5 + 0.11364x_2x_5 + 0.14723x_5x_6 \quad (3.30)$$

$$Y_{Vout} = -0.06943 + 0.24247x_1 - 0.88045x_2 + 0.27537x_3 + 0.25239x_4 - 0.24694x_5 + 0.11806x_6 + 0.62291x_2^2 - 0.34230x_3^2 - 0.28377x_6^2 + 0.15129x_1x_2 + 0.18613x_1x_3 - 0.19269x_2x_4 + 0.09442x_1x_5 + 0.11221x_2x_5 - 0.08001x_3x_6 + 0.13824x_5x_6 \quad (3.31)$$

$$Y_{|\langle\xi_{Se}\rangle|fr2} = 0.43405 + 0.24954x_1 - 0.61280x_2 + 0.44395x_4 - 0.40514x_5 - 0.76316x_4^2 + 0.45812x_6^2 - 0.11145x_2x_3 + 0.21407x_2x_4 + 0.14111x_2x_5 - 0.15529x_3x_5 - 0.24556x_4x_5 - 0.24635x_5x_6 \quad (3.32)$$

where Y_{C0}, $Y_{|<\xi se>|fr1}$, Y_{Qf}, $Y_{\Delta C}$, $Y_{\Delta C/C0}$, Y_{Vout} and $Y_{|<\xi se>|fr2}$ represent the empirical models of the responses for C_0, $|\langle\xi_{Se}\rangle|_{fr1}$, Q_f, ΔC, $\Delta C/C_0$, V_{out} and $|\langle\xi_{Se}\rangle|_{fr2}$ respectively, and x_1, x_2, x_3, x_4, x_5, and x_6 are the coded values of R_m, R_b, h_c, h_g, T_m and t_m respectively.

To evaluate the significance of empirical models, analysis of variance (ANOVA) [37] is performed. The evaluated ANOVA of the model for the logarithm of the responses are summarized in Table 3.5 (for more details see Appendix C). The column "Sig." represents the p-value of the null hypothesis, which indicates the significance of the relation between factors and response, i.e., the model significance. With p-value being less than 0.01 in all five models, it can be concluded that the five response surface models are statistically significant with 99% confidence level. Furthermore, the goodness of the fit of the regression model is measured by R-Squared (R^2) and adjusted R-squared (R_a^2) values, which indicate the amount of variability in the response explained by the factors and range from 0 to 1. Therefore, the larger value is desirable. For all the models, R^2-values are closer

to 1, indicating that the regression line perfectly fits the data. On the other hand, R_a^2-value provides the predictive accuracy. From the table, it has been observed that the value of R^2 and R_a^2 are very close to each other, which indicates that the models for all responses are adequately reproducing the experimental data. This approach ensures the inclusion of only those variables that have a significant effect in the statistical model.

Table 3.5: Analysis of variance (ANOVA) table of estimated models

Symbols	Model	Source of variation	Sum of squares	Degrees of freedom	Mean square	Ratio	Sig.
Y_{C0}	$Log(C_0)$	Regression	42.2128	27	1.5634	6205.1558	< 0.01
		Residuals	0.0076	30	0.0003		
		Total	42.2204	57			
		R-Squared (R^2)	1				
		Adj. R-Squared (R_a^2)	1				
$Y_{\lvert\langle\xi_{Se}\rangle\rvert_{fr1}}$	$Log(\lvert\langle\xi_{Se}\rangle\rvert_{fr1})$	Regression	99.2762	27	3.6769	112.9190	< 0.01
		Residuals	1.0094	31	0.0326		
		Total	100.2856	58			
		R-Squared (R^2)	0.990				
		Adj. R-Squared (R_a^2)	0.981				
Y_{Qf}	$Log(Q_f)$	Regression	37.0305	27	1.3715	20.3269	< 0.01
		Residuals	2.0242	30	0.0675		
		Total	39.0546	57			
		R-Squared (R^2)	0.948				
		Adj. R-Squared (R_a^2)	0.902				
$Y_{\Delta C}$	$Log(\Delta C)$	Regression	24.8283	27	0.9196	14.0307	< 0.01
		Residuals	2.0317	31	0.0655		
		Total	26.8600	58			
		R-Squared (R^2)	0.924				
		Adj. R-Squared (R_a^2)	0.858				
$Y_{\Delta C/C_0}$	$Log(\Delta C/C_0)$	Regression	31.0535	27	1.1501	19.4959	< 0.01
		Residuals	1.7698	30	0.0590		
		Total	32.82	57			
		R-Squared (R^2)	0.946				
		Adj. R-Squared (R_a^2)	0.898				

Y_{Vout}	$Log(V_{out})$	Regression	55.9191	27	2.0711	47.4756	< 0.01
		Residuals	1.3523	31	0.0436		
		Total	57.2715	58			
		R-Squared (R^2)	0.976				
		Adj. R-Squared (R_a^2)	0.956				
$Y_{\|\langle\xi_{Se}\rangle\|_{fr2}}$	$Log(\|\langle\xi_{Se}\rangle\|_{fr2})$	Regression	43.6303	27	1.6159	18.1856	< 0.01
		Residuals	2.7546	31	0.0889		
		Total	46.3849	58			
		R-Squared (R^2)	0.941				
		Adj. R-Squared (R_a^2)	0.889				

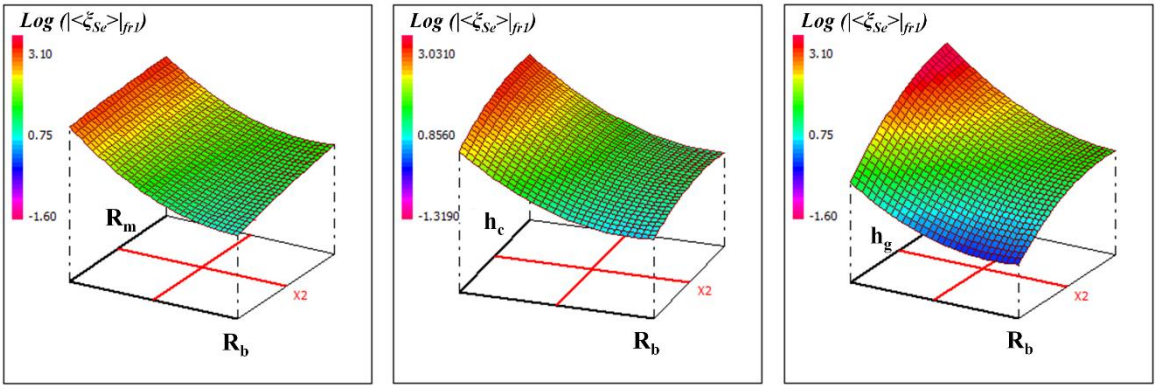

(a) In the plane: R_b, R_m *(b) In the plane: R_b, h_c* *(c) In the plane: R_b, h_g*

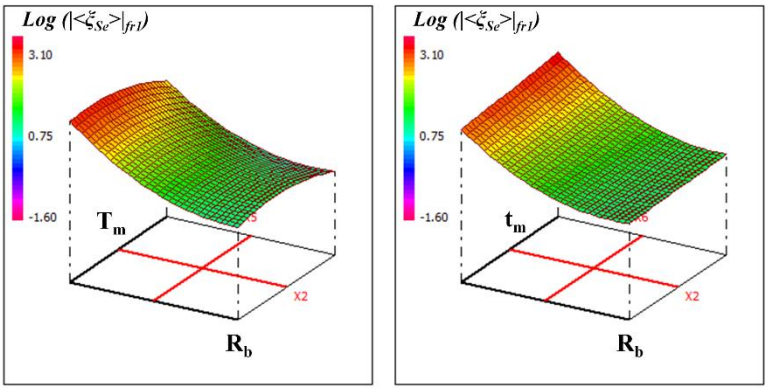

(d) In the plane: R_b, T_m *(e) In the plane: R_b, t_m*

Figure 3.9: *Response surface plots of logarithm of maximum membrane displacement at first resonant frequency ($Log(|\langle\xi_{Se}\rangle|_{fr1})$ in different planes with respect to other factors kept constants at the central level.*

To further check the model behavior response surface plots can provide a quick view of the maximum membrane displacement at first resonant frequency and of the Q_f value for different values of factors, and thus help to identify the type of interactions between these

factors. Only two factors can be displayed on a plot while other factors are kept at constant central value. For example, the 3D graphical representation of the response surface of maximum membrane displacement at first resonant frequency and quality-factor are illustrated in Figures 3.9 and 3.10.

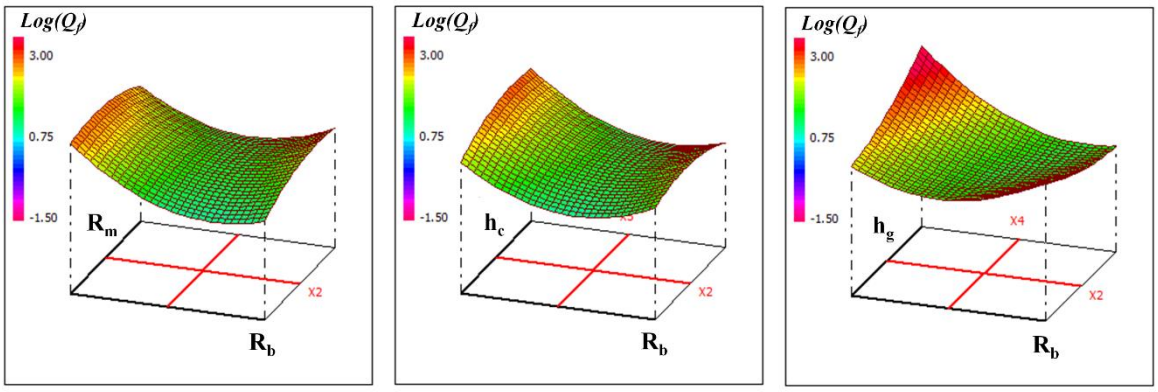

(a) In the plane: R_b, R_m (b) In the plane: R_b, h_c (c) In the plane: R_b, h_g

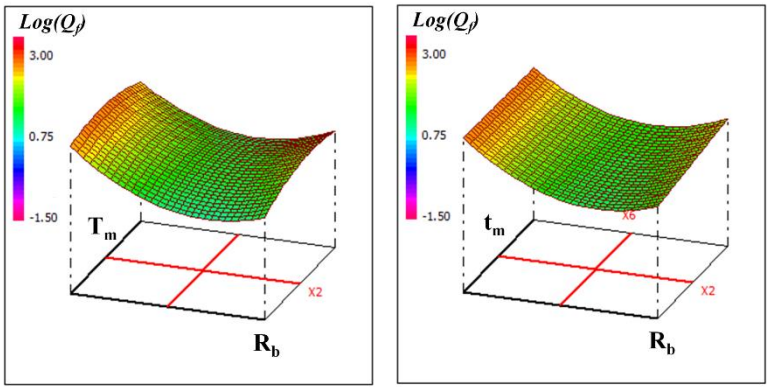

(d) In the plane: R_b, T_m (e) In the plane: R_b, t_m

Figure 3.10: *Response surface plots of logarithm of Q-factor ($Log(Q_f)$) in different planes with respect to other factors kept constants at the central level.*

Figures from 3.9(a) to 3.9(e) illustrate the interaction among different factors on the maximum membrane displacement at first resonant frequency for a fixed set of other factors at central value of their respective variation domain. It has been observed that all the six parameters, and some of the quadratic and interaction between those parameters have the strongest influence on the membrane displacement as presented by equation (3.27). On the other hand, Figures 3.10(a) to 3.10(e) show the interaction of different factors on the quality factor of the membrane displacement at first resonant frequency. The response surface plots also show the local maxima and minima of the responses in terms of different factors within

their investigated ranges. As an example, membrane displacement of an acoustic resonator can be maximized by increasing the value of R_m, h_c, h_g and t_m, and by reducing the value of R_b and T_m as illustrated by red color zone in Figure 3.9.

3.5.2. Optimization process

As observed, the effects of factors are not only additive but also interactive. The presence of interaction effects makes it imperative that all the factors have to be optimized simultaneously to determine the best compromise. Consequently, multi-criteria optimization is necessary. Therefore, desirability function approach is employed to achieve simultaneous optimization in our multi-response problem. In this approach, an objective function, also known as desirability function, is used to transform the existing values of the considered response into a scale free value called desirability. The desirability lies between 0 and 1 and it represents the closeness of a response to its ideal value.

Multi-response optimization problem generally involves several processing steps after the models being fitted with the experimental data. Initially, the desirability index (d_i) is defined for each response, based on the desirability functions as presented in equations from (3.33) to (3.35), for the cases of bilateral desirability function, maximization and minimization [9], [13].

$$d_i(\hat{Y}_i) = \begin{cases} 0 & \text{if } \hat{Y}_i < a \\ \left(\dfrac{\hat{Y}_i - a}{a_i - a}\right)^{s_{i1}} & \text{if } a < \hat{Y}_i < a_1 \\ 1 & \text{if } a_1 < \hat{Y}_i < b_1 \\ \left(\dfrac{b - \hat{Y}_i}{b - b_1}\right)^{s_{i2}} & \text{if } b_1 < \hat{Y}_i < b \\ 0 & \text{if } \hat{Y}_i > b \end{cases} \quad \dots (3.33)$$

$$d_i(\hat{Y}_i) = \begin{cases} 0 & \text{if } \hat{Y}_i < a \\ \left(\dfrac{\hat{Y}_i - a}{b - a}\right)^{s_i} & \text{if } a < \hat{Y}_i < b \\ 1 & \text{if } \hat{Y}_i > b \end{cases} \quad \dots (3.34)$$

$$d_i(\hat{Y}_i) = \begin{cases} 1 & \text{if } \hat{Y}_i < a \\ \left(\dfrac{b-\hat{Y}_i}{b-a}\right)^{s_i} & \text{if } a < \hat{Y}_i < b \\ 0 & \text{if } \hat{Y}_i > b \end{cases} \quad \ldots (3.35)$$

where a represents the lower tolerance limit, b represents the upper tolerance limit, and (a_1, b_1) represents the target interval. s_i, s_{i1} and s_{i2} in equations (3.33) to (3.35) represent the considered weights. Shape of desirability functions are respectively illustrated in Figure 3.11.

Global desirability is then calculated by accumulating the 'n' individual desirability values corresponding to the 'n' studied responses, as follows,

$$D = \left(\prod_{i=1}^{n} d_i^{w_i}\right)^{\frac{1}{\sum w_i}} \quad \ldots\ldots\ldots (3.36)$$

Here 'D' is the global desirability, 'd_i' represents the respective individual desirability, 'w_i' is the weight of individual function and '$\sum w_i$' represents the total weight.

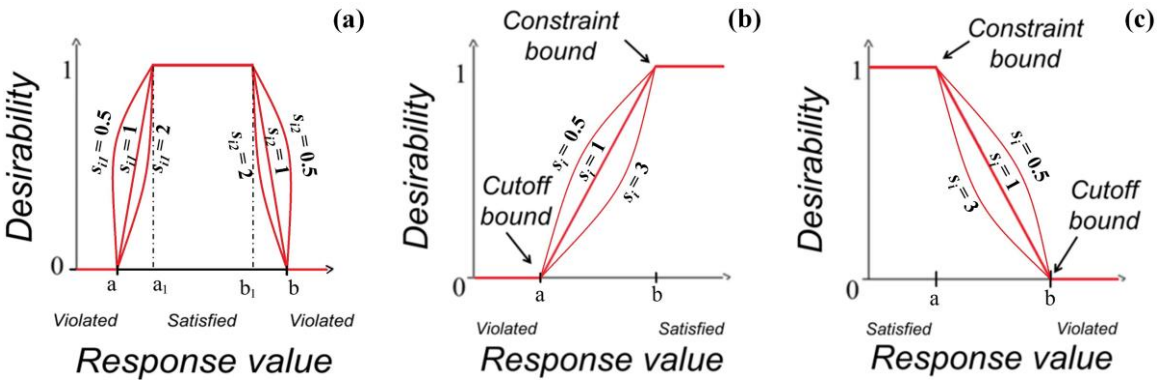

Figure 3.11: *Schematic diagram of different desirability functions: (a) bilateral desirability function, (b) maximization & (c) minimization.*

Thereafter, the optimum combination of levels of parameters is determined based on the highest global desirability value. Finally, the response of the sensor based on the optimum level of parameters is predicted and validated.

In this study, the optimization is performed to obtain acoustic resonant sensor, where the Q-factor and capacitance variation are maximized while the value of static capacitance is

held within the fixed value range and the membrane displacement at second resonant frequency is minimized to get better selectivity. Table 3.6 represents the list of optimization criteria and the desirability functions for responses that have been used during the optimization process. Figures from 3.12(a) to 3.12(d) illustrate the desirability functions.

Table 3.6: Optimization criteria and the desirability functions for the optimization of an acoustic resonant sensor

Response (unit)	**Partial desirability Code**	**Functions**	**Weight (w_i)**	***a***	***b***	**Predicted response**	**Partial desirability**
C_0 (pF)	d_1	Bilateral	1	0.5	3.2	0.5	100%
Q_f	d_2	Maximization	1	25	1450	210	52.4%
ΔC (fF)	d_3	Maximization	1	1	36	1.72	15.1%
$\lvert\langle\xi_{Se}\rangle\rvert_{fr2}$ (nm)	d_4	Minimization	1	0.03	3	1.12	21.3%

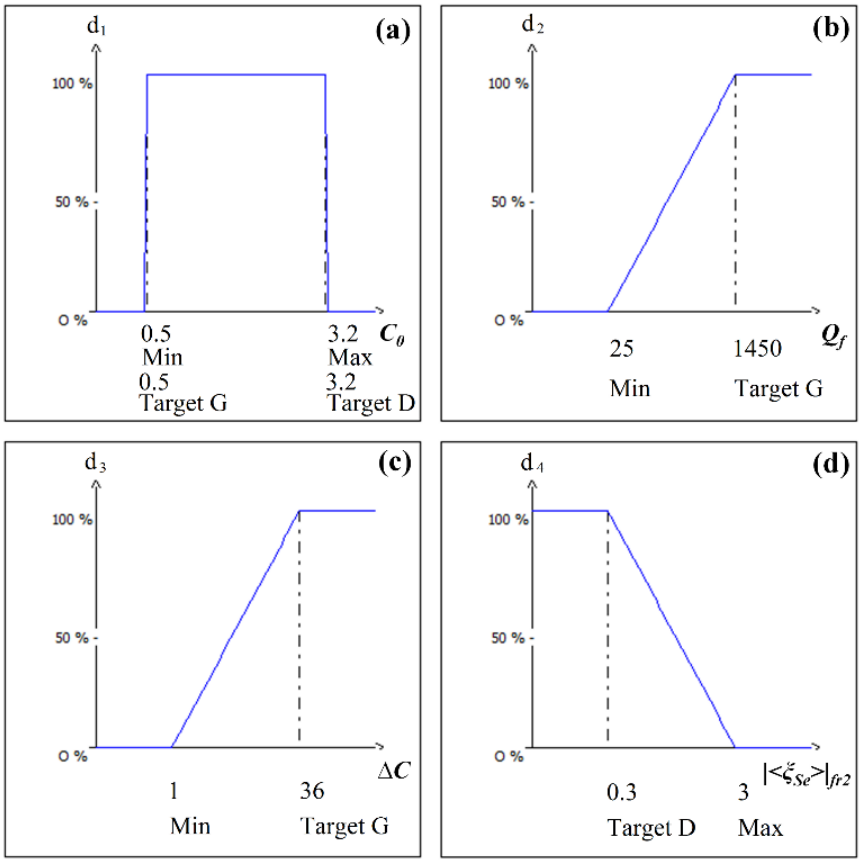

Figure 3.12: *Desirability functions for multi-criteria optimization of acoustic resonant sensor (for (a)* $0.5 \leq C_0 \leq 3.2\,pF$*; (b)* $Q_f \geq 25$*; (c)* $\Delta C \geq 1fF$*; (d)* $|\langle\xi_{Se}\rangle|_{fr2} \leq 3nm$*).*

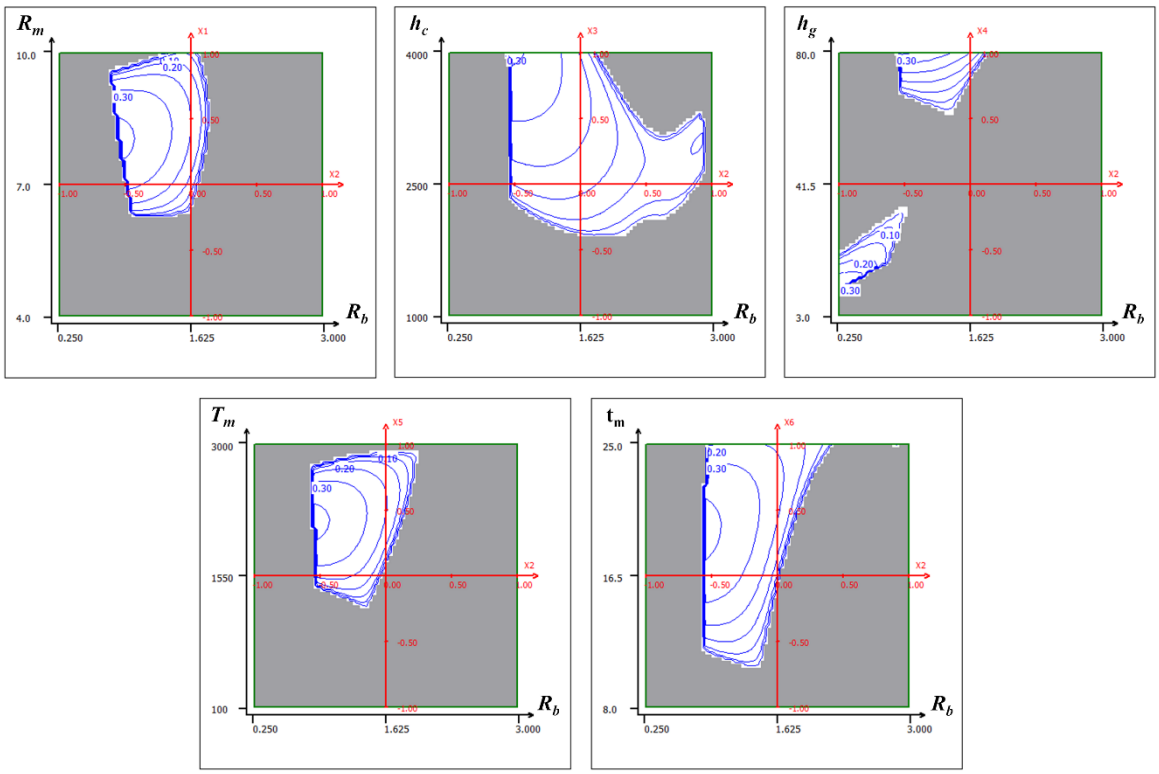

Figure 3.13: *Optimum zone for acoustic resonant sensor with desired responses.*

The solution found based on multi-criteria optimization is presented by response surface of global desirability with respect to different planes in Figures 3.13(a) to 3.13(e), where white region represents the acceptable zone that satisfies all the criteria. Finally, the values of optimum level of parameters were decided to satisfy the desirability and the global desirability is evaluated. The best estimated set of optimized parameters based on multi-criteria optimization is listed in Table 3.7, which provides the global desirability of 36%.

Table 3.7: Set of best optimized parameters based on multi-criteria desirability functions optimization

Factor	Value
Membrane radius (R_m)	8.1 mm
Backplate radius (R_b)	0.871 mm
Cavity height (h_c)	3987 µm
Air gap (h_g)	80.0 µm
Membrane tension (T_m)	2158 N/m
Membrane thickness (t_m)	19.8 µm

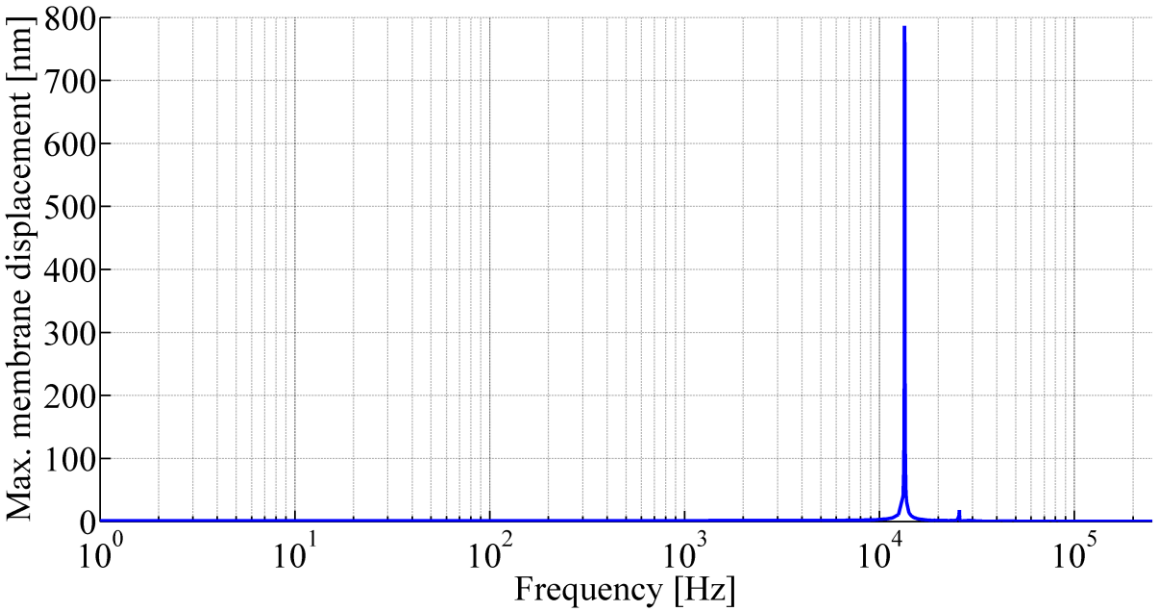

Figure 3.14: *Maximum membrane displacement of the acoustic resonant sensor with set of optimum parameters.*

3.5.3. Verification

Once the optimum set of parameters is determined, the numerical analysis has been performed to verify the responses of the acoustic sensor with these optimum parameters. Figure 3.14 shows the maximum membrane displacement of the acoustic resonant sensor with respect to frequencies. It has been observed, according to numerical analysis, that the acoustic sensor with the optimum set of parameters provides good sensitivity and selectivity, with static capacitance (C_0) of 0.50 pF, capacitance variation (ΔC) of 2.6 fF, and Q-factor (Q_f) of 522, along with capacitance ratio ($\Delta C/C_0$) of 0.52% and output voltage (V_{out}) of 19.7 mV at first resonant frequency of the acoustic sensor for an incident acoustic pressure level of (or equal to) 80 dB_{SPL}.

3.6. Summary

Numerical simulation and DOE approach have been used to investigate the virtual prototyping of an acoustic sensor to understand the linear, quadratic and interaction effects of different parameters on the outputs of the sensor. DOE helps to reduce the computation efforts in the acoustic resonant sensor optimization process since the empirical model is far less complex than the numerical simulation. RSM helps to develop empirical model for each response. It has been observed that the maximum membrane displacement at first

resonant frequency and quality-factor are influenced by several linear, quadratic and interaction terms. Based on the empirical model, the region of optimum set of parameters for acoustic resonant sensor was obtained using multi-criteria optimization. Cross-verification using numerical simulation shows that a capacitance of 0.50 pF, capacitance variation of 2.6 fF, output voltage of 19.7 mV and Q-factor of 522 can be achieved. Hence, the optimum set of parameters satisfies the targeted output responses of the acoustic resonator.

Therefore, it has been demonstrated that acoustic sensor, with good sensitivity and selectivity, can be achieved with the presented design which consists of a relatively smaller backplate electrode compared to the membrane, along with large annular cavity.

References

[1] J. J. Neumann Jr and K. J. Gabriel, "A Fully-Integrated CMOS-MEMS Audio Microphone," in *TRANSDUCERS, The 12th International Conference on Solid-State Sensors, Actuators and Microsystems*, 2003, vol. 1, pp. 230–233.

[2] P.R. Scheeper, A.G.H. van der Donk, W. Olthuis, and P. Bergveld, "A Review of Silicon Microphones," *Sens. Actuators Phys.*, vol. 44, pp. 1–11, 1994.

[3] P.-C. Hsu, C. H. Mastrangelo, and K. D. Wise, "A High Sensitivity Polysilicon Diaphragm Condenser Microphone," in *The 11th Annual International Workshop on Micro Electro Mechanical Systems Proceeding*, Heidelberg, Germany, 1998, pp. 580–585.

[4] Dietmar Hohm and Gisela Hess, "A Subminiature Condenser Microphone with Silicon Nitride Membrane and Silicon Back Plate," *J. Acoust. Soc. Am.*, vol. 85, no. 1, pp. 476–480, 1989.

[5] Zhen-Zhun Shu, Ming-Li Ke, Guan-Wei Chen, Ray-Hua Horng, Chao-Chih Chang, Jean-Yih Tsai, Chung-Ching Lai, and Ji-Liang Chen, "Design and Fabrication of Condenser Microphone Using Wafer Transfer and Micro-Electroplating Technique," in *Design, Test, Integration and Packaging of MEMS/MOEMS*, Nice, France, 2008, pp. 386–390.

[6] Q. Zou, Z. Li, and L. Liu, "Design and Fabrication of Silicon Condenser Microphone Using Corrugated Diaphragm Technique," *J. Microelectromechanical Syst.*, vol. 5, no. 3, pp. 197–204, 1996.

[7] Petr Honzík, Alexey Podkovskiy, Stéphane Durand, Nicolas Joly, and Michel Bruneau, "Analytical and Numerical Modeling of an Axisymmetrical Electrostatic Transducer with Interior Geometrical Discontinuity," *J. Acoust. Soc. Am.*, vol. 134, no. 5, pp. 3573–3579, 2013.

[8] Alexey Podkovskiy, Petr Honzík, Stéphane Durand, Nicolas Joly, and Michel Bruneau, "Miniaturized Electrostatic Receiver with Small-Sized Backing Electrode," in *Proceedings of Meetings on Acoustics*, Montreal, Canada, 2013, vol. 19, p. 030047.

[9] Gareth A Lewis, Didier Mathieu, and Roger Phan-Tan-Luu, *Pharmaceutical experimental design*. New York: Dekker, 1999.

[10] F. Vogel, H. Landes, R. Lerch, M. Kaltenbacher, and R. Peipp, "Numerical Simulation and Optimization of Capacitive Transducers," in *Proceedings of EuroSime*, Aix-en-Provence, France, 2003, pp. 399–405.

[11] Philip E. Gill and Elizabeth Wong, "Sequential Quadratic Programming Methods," in *Mixed Integer Nonlinear Programing*, vol. 154, Jon Lee and Sven Leyffer, Eds. New York: Springer, 2012, pp. 147–224.

[12] George Derringer and Ronald Suich, "Simultaneous Optimization of Several Response Variables," *J. Qual. Technol.*, vol. 12, no. 4, pp. 214–219, 1980.

[13] L. A. Sarabia and M. C. Ortiz, "Response Surface Methodology," in *Comprehensive Chemometrics*, vol. 1, Steven Brown, Romà Tauler, and Beata Walczak, Eds. Oxford: Elsevier, 2009, pp. 345–390.

[14] Tomas Lavergne, Stéphane Durand, Michel Bruneau, and Nicolas Joly, "Dynamic Behaviour of the Circular Membrane of an Electrostatic Microphone: Effect of Holes in the Backing Electrode," *J. Acoust. Soc. Am.*, vol. 128, no. 6, pp. 3459–3477, 2010.

[15] Michel Bruneau, Anne-Marie Bruneau, Zdeněk Škvor, and Pierrick Lotton, "An Equivalent Network Modelling the Strong Coupling Between a Vibrating Membrane and a Fluid Film," *Acta Acust.*, vol. 2, pp. 223–232, 1994.

[16] Allan F. Bower, *Applied Mechanics of Solids*. New York: CRC Press, 2010.

[17] Philip M. Morse and K. Uno Ingard, *Theoretical Acoustics*. Princeton, New Jersey: Princeton University Press, 1986.

[18] J. Merhaut, "A Contribution to the Theory of Electroacoustic Transducers Based on Electrostatic Principle," *Acustica*, vol. 19, pp. 283–292, 68 1967.

[19] William P. Baker, Gregory Al Kriegsmann, and Edward L. Reiss, "Acoustic Scattering by Baffled Cavity-Backed Membranes," *J. Acoust. Soc. Am.*, vol. 83, no. 2, pp. 423–432, 1988.

[20] G.L. Lamb, Jr., "Variational Principle for Scattering by a Baffled Cavit-Backed Membrane," *J. Acoust. Soc. Am.*, vol. 86, no. 2, pp. 795–801, 1989.

[21] Albert Prak, Frans R. Blom, Miko Elwenspoek, and Theo S. J. Lammering, "Q-Factor and Frequency Shift of Resonating Silicon Diaphragms in Air," *Sens. Actuators A*, vol. 25–27, pp. 691–698, 1991.

[22] Sen Ren, Weizheng Yuan, Dayong Qiao, Jinjun Deng, and Xiaodong Sun, "A Micromachined Pressure Sensor with Integrated Resonator Operating at Atmospheric Pressure," *Sensors*, vol. 13, no. 12, pp. 17006–17024, 2013.

[23] Kwan Kyu Park, Hyunjoo Jenny Lee, P. Crisman, M. Kupnik, O. Oralkan, and B. T. Khuri-Yakub, "Optimum design of circular CMUT membranes for high quality factor in air," in *Ultrasonics Symposium, 2008. IUS 2008. IEEE*, Beijing, China, 2008, pp. 504–507.

[24] Daryl L. Logan, *A First Course in the Finite Element Method*. Stamford, CT: Cengage Learning, 2012.

[25] J.T. Mottram and C.T. Shaw, *Using Finite Elements in Mechanical Design*. London, UK: McGraw-Hill Book Company, 1996.

[26] Singiresu S. Rao, *The Finite Element Method in Engineering*, 4th ed. Oxford, UK: Butterworth Heinemann, 1999.

[27] C.S. Desai and J.F. Abel, *Introduction to the Finite Element Method - A Numerical Method for Engineering Analysis*. New York, USA: Van Nostrand Reinhold Co., 1972.

[28] Gopal S. Rautela, Ronald D. Snee, and Warren K. Miller, "Response-Surface Co-optimization of Reaction Conditions in Clinical Chemical Methods," *Clin. Chem.*, vol. 25, no. 11, pp. 1954–1964, 1979.

[29] J. K. Telford, "A Brief Introduction to Design of Experiments," *Johns Hopkins APL Tech. Dig.*, vol. 27, no. 3, pp. 224–232, 2007.

[30] R. Bahloul, A. Mkaddem, Ph. Dal Santo, and A. Potiron, "Sheet Metal Bending Optimisation using Response Surface Method, Numerical Simulation and Design of Experiments," *Int. J. Mech. Sci.*, vol. 48, no. 9, pp. 991–1003, 2006.

[31] Peter Stehouwer, "Design of Experiments for Numerical Parameter Studies of Electronic Systems: Optimizing the Cooling Strategy of an Ethernet Switch," *Electronic Cooling*, May-2005.

[32] Jihua Gou, Chuck Zhang, Zhiyong Liang, Ben Wang, and James Simpson, "Resin Transfer Molding Process Optimization Using Numerical Simulation and Design of Experiments Approach," *Polym. Compos.*, vol. 24, no. 1, pp. 1–12, 2003.

[33] Fred H. Walters, Lloyd R. Parker Jr., Stephen L. Morgan, and Stanley N. Deming, *Sequential Simplex Optimization*. Florida, USA: CRC Press LLC, 1991.

[34] E. Rosales, M.A. Sanromán, and M. Pazos, "Application of Central Compostie Face-Centered Design and Response Surface Methodology for the Optimization of Electro-Fenton Decolorization of Azure B Dye," *Env. Sci Pollut Res*, vol. 19, pp. 1738–1746, 2012.

[35] LPRAI, "nemrodW," *LPRAI*, 2014. [Online]. Available: http://www.lprai.com/index.php?page=Logiciel. [Accessed: 27-Dec-2014].

[36] Douglas C. Montgomery and George C. Runger, "Multiple Linear Regression," in *Applied Statistics and Probability for Engineers*, 4th Edition., New York, USA: John Wiley & Sons, 2007, pp. 410–467.

[37] Douglas C. Montgomery and George C. Runger, "Design and Analysis for Single-Factor Experiments: The Analysis of Variance," in *Applied Statistics and Probability for Engineers*, 4th Edition., New York, USA: John Wiley & Sons, 2007, pp. 468–504.

CHAPTER 4

DEVICE FABRICATION & CHARACTERIZATION

In this chapter, the development of a capacitive acoustic resonator by combining three-dimensional (3D) printing and two-dimensional (2D) printed electronics technique is discussed in details. Patterned bottom structure with rigid backplate and cavity is fabricated directly by 3D printing method, and then direct write 2D inkjet-printed technique is employed to print conductive silver electrode. A novel approach is used to fabricate diaphragm for the acoustic sensor as well, where conductive layer is inkjet-printed on a pre-stressed thin organic film. In depth processing steps along with the characterization of each technological building block are also presented. Finally, transducers have been characterized to understand their functionalities. During operation, the deflection of the transducer in response to the incident acoustic pressure has been detected, and the corresponding change of electrical capacitance between the diaphragm and the fixed electrode has been calculated. The result confirms that the developed transducer acts as a capacitive acoustic resonator, which provides good sensitivity and selectivity at its resonant frequency.

4.1. Background

Capacitive acoustic transducer is an electromechanical-acoustic system that consists of a flexible diaphragm in parallel to a fixed backplate electrode separated by an air gap, a cavity and a venting-channel. During this work, within the SPINNAKER consortium framework, a new transducer design has been developed, that consists of a central cylindrical rigid backplate with small radius surrounded by a flat annular cavity below a vibrating membrane clamped at its periphery separated by air gap [1]–[3].

The ultimate goal of this research is to develop and fabricate printed capacitive acoustic resonator. The capacitive transducer designed for the general audio application provides flat sensitivity over a wide bandwidth. As it has been argued earlier in this thesis, it can be modified to develop an acoustic resonator by altering the device parameters, such as membrane radius, backplate radius, cavity height, air gap, membrane tension, and membrane thickness. As determined from the simulation and optimization studies, the fabrication of acoustic resonator requires large cavity and membrane structure along with optimized backplate electrode and air gap. The design to develop printed acoustic transducer is illustrated in Figure 4.1.

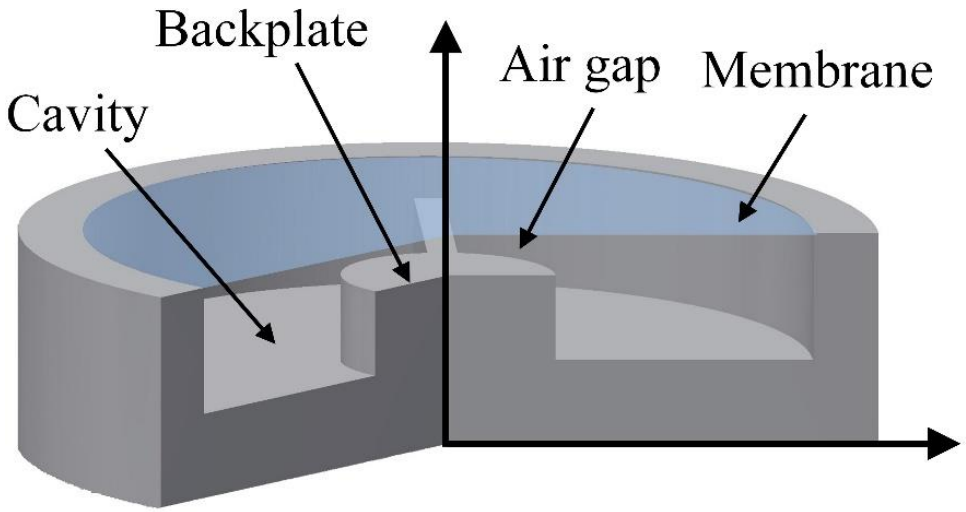

Figure 4.1: *Schematic diagram of the design of the capacitive acoustic transducer.*

Inkjet printing can be used to fabricate different types of structure, including three-dimensional (3D) microelectromechanical systems (MEMS), such as 3D metallic structures using colloid ink having nanoparticles [4], and MEMs structures with void or cavity by printing several layers of microstructures and using of sacrificial layer [5]. However, this method requires the removal of the sacrificial layer by subtractive process to create void or cavity. In addition, the printing of 3D MEMs structure by inkjet-printing technique only, is limited to micrometer scale fabrication, and thus to form devices with large cavity in millimeter scale with complex geometry is difficult using this technique. These issues can be addressed by fabricating the device using new fabrication process that combines emerging 3D printing technique and 2D inkjet direct write technique.

Three-dimensional (3D) printing method is a powerful additive manufacturing method. Materials with various properties can be printed using this technique. In addition, multiple materials can simultaneously be printed in the same structure without the requirement of any post curing. This technique can be used to fabricate complex structures directly without the requirement of any etching or micromachining [6]. Thus, patterned three-dimensional structure for the MEMs devices can be built by 3D printing method and can be used as substrate to print electrically conductive ink layer by direct write inkjet printing technique to fabricate acoustic sensor and other electronic devices.

It appears that prior art has not given rise to the fabrication of acoustic transducer combining 2D direct write inkjet printing technique and 3D printing method.

4.2. Three-dimensional (3D) printing technique

Three-dimensional (3D) printing is an emerging technology that generally works by building parts in layers. It is a relatively fast and flexible technique, allowing the production of various objects with complex geometries as prototype parts and tools directly from a computer aided design (CAD) file [6].

Generally, 3D printer builds an object by adding small amounts of material, such as polymer, in liquid or powder form, using bottom up approach, rather than starting with a block of raw material and removing. During the layer process, heat, light or chemicals are precisely applied on the deposited layer to bond and strengthen the structure [6].

Figure 4.2: *The EDEN 260V polyjet 3D printing system.*

During this work, Objet EDEN 260 V polyjet 3D printing system (Figure 4.2) has been used. It allows the printing of 3D object by dispensing materials from a printing head to form a layer of an object being built. The thickness of the dispensed material layer is altered to a predetermined height using a roller [7]. Figures 4.3(a) and 4.3(b) illustrate the process flow and the schematic diagram of polyjet printing process.

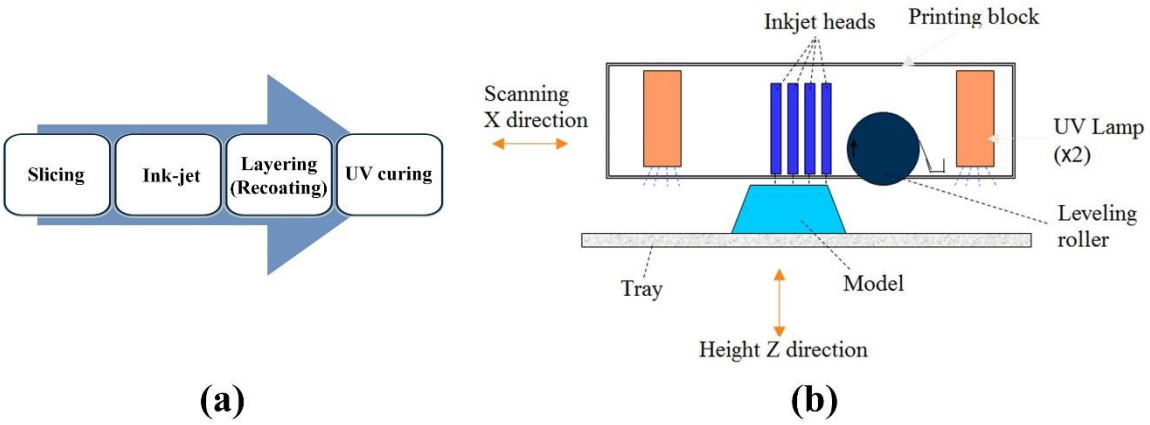

Figure 4.3: *Schematic diagram of (a) the process flow of polyjet 3D printing method, and (b) polyjet 3D printing system.*

Polyjet 3D printing system provides high resolution printing of 600 dpi with smooth surface finish. The thickness of each printed layer is 16 µm. This system allows the printing of different types of structural materials, namely, plastic, rubber-like, bio-compatible, high temperature materials, etc. Important properties of some materials that have been used for polyjet 3D printing system have been listed in Table 4.1.

Table 4.1: Summary of the materials properties uses in polyjet 3D printing system [6], [8], [9].

Materials	**Code**	**Tensile strength** MPa	**Heat deflection temperature (T_{HD})** °C	**Glass transition temperature (T_g)** °C
Bio-compatible materials	MED610	50 – 65	45 – 50	52 – 54
High Temperature	RGD525	70 – 80	75 – 80	62 – 65
Vero Clear	RGD810	50 – 65	45 – 50	52 – 54
Vero White	RGD875	50 – 65	45 – 50	52 – 54
Vero Black	RGD835	50 – 65	45 – 50	52 – 54
Vero Blue	RGD840	50 – 60	45 – 50	48 – 50

Most of the materials have similar mechanical and thermal characteristics, with the disadvantages of having low glass transition temperature (T_g), and low heat deflection temperature (T_{HD}) that refers to the temperature above which deformation of the structure takes place. As a result, these materials are generally vulnerable at high heating temperature.

4.3. Fabrication of the capacitive acoustic transducer

The fabrication of the capacitive acoustic transducer by combining 3D printing technique and 2D inkjet direct write technique, based on the design presented in Figure 4.1, has been performed in three separated major steps, as presented below.

1. Preparation of the patterned bottom structure, containing backplate, cavity, interconnecting channel, and printed backplate electrode.
2. Fabrication of diaphragm under tension with printed conductive electrode.
3. Device fabrication by assembling the bottom structure and the diaphragm separated by a spacer.

Figure 4.4 illustrates the schematic diagram of the process flow of the development of the printed acoustic transducer, and Figure 4.5 presents the image of the printed capacitive acoustic transducer. Each fabrication step of the capacitive acoustic transducer will be described in details in the later section.

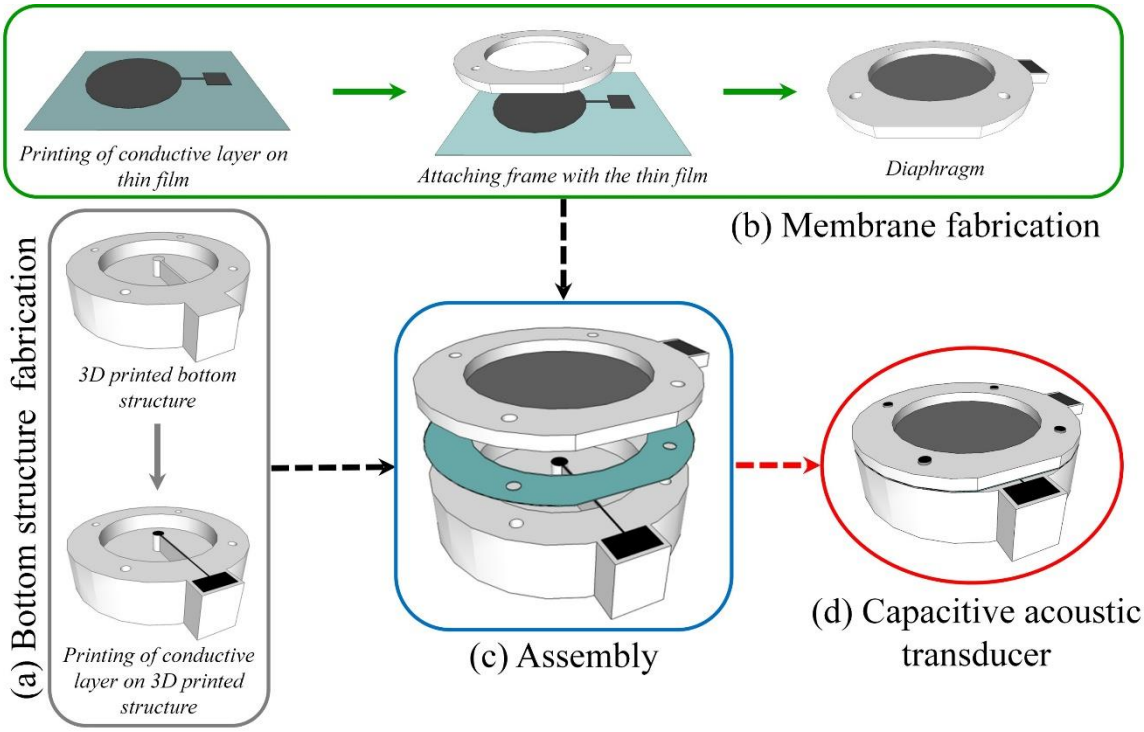

Figure 4.4: *Fabrication steps of the acoustic sensor combining inkjet printing and 3D printing technique.*

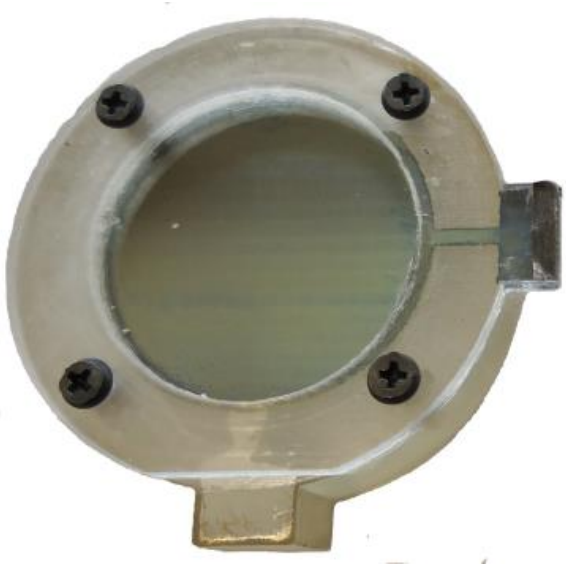

Figure 4.5: *Printed capacitive acoustic transducer.*

4.3.1. Fabrication of the bottom structure

During this work, patterned 3D bottom part of the acoustic transducer is formed without any etching step, using polyjet 3D printing method. Conductive layer is then printed on the backplate by two-dimensional (2D) direct write inkjet techniques. Occasionally, surface of the three-dimensional structure formed by 3D printing method may require polishing to reduce surface roughness before printing conductive layer. Finally, printed silver layer is sintered to obtain conductivity. Figure 4.6(a) to 4.6(c) illustrate the fabrication of process of the bottom part of the device.

Figure 4.6(a) refers to the first step of the process, where three-dimensional structure is printed directly using polyjet 3D printing method. On the other hand, Figure 4.6(b) illustrates the top view of the 3D printed structure, along with rigid backplate of small radius and flat annular cavity; it also contains narrow channel to print interconnection line. With reference to Figure 4.6(c), the electrically conductive silver ink layer is then printed by 2D inkjet techniques on the backplate, which acts as bottom electrode.

Since the materials used for polyjet 3D printing system have relatively low heat deflection temperature, as presented in Table 4.1, to avoid any structural damage of the 3D printed structure, the conductive layer is sintered using photonic sintering method.

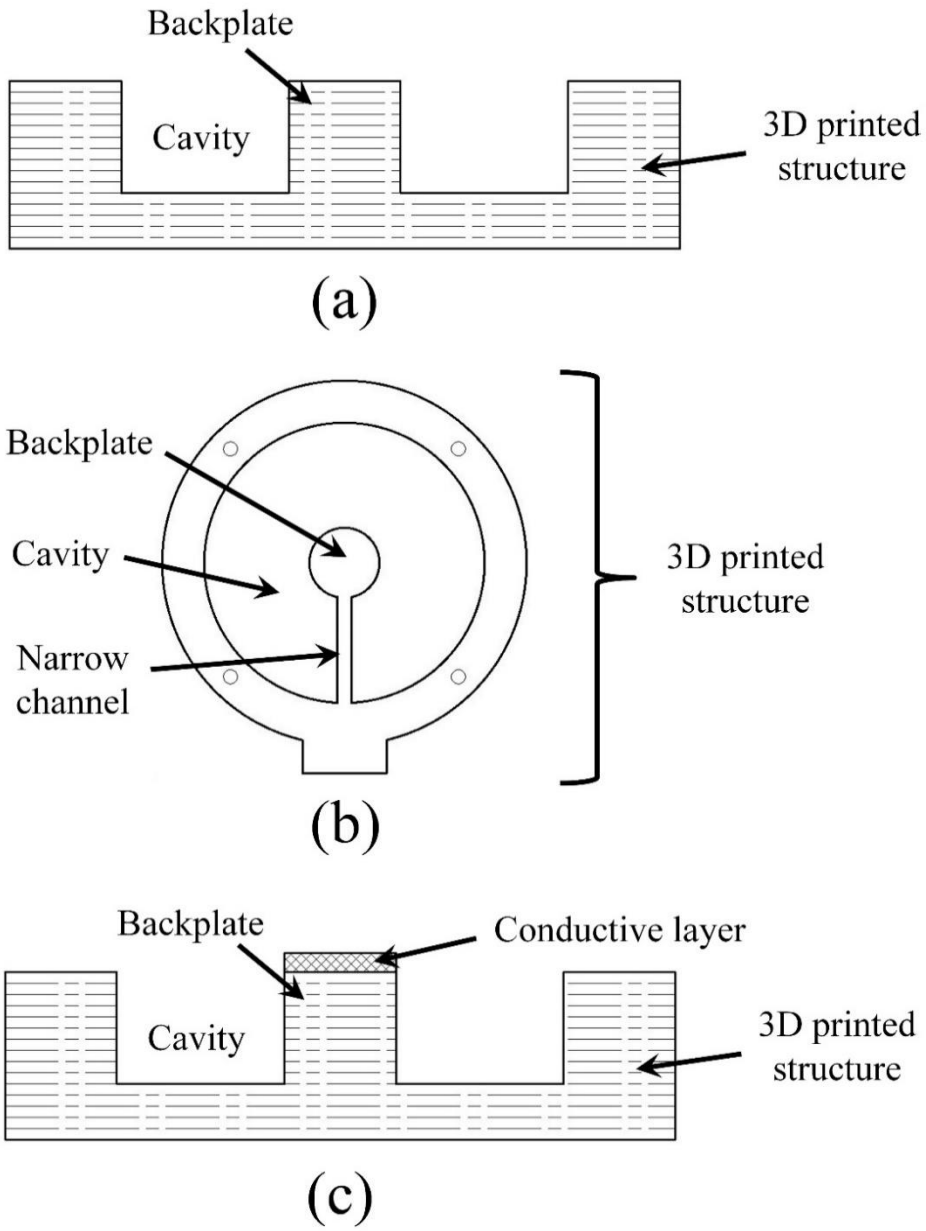

Figure 4.6: *Schematic diagram of the fabrication steps of the bottom structure of the capacitive acoustic transducer using 3D printing, (a) cross-sectional view and (b) top view of the of the 3D printed bottom structure, and (c) cross-sectional view bottom structure after printing the backplate electrode.*

4.3.2. Fabrication of the diaphragm

The diaphragm of the capacitive transducer is developed by printing conductive layer on pre-stressed organic thin film using 2D inkjet printing direct write technique. During this fabrication step, thin organic film having thickness lower than 25 µm, such as Mylar,

polyethylene napthalate (PEN) and polyimide (PI) have been used. Initially, the thin film is mounted on a specifically designed holder and tension is applied to the film. Conductive layer is then printed on the pre-stressed film using inkjet printing technique and sintered. Figures 4.7(a) to 4.7(c), and Figures 4.8(a) to 4.8(c) illustrate the fabrication sequence of the diaphragm for the acoustic transducer.

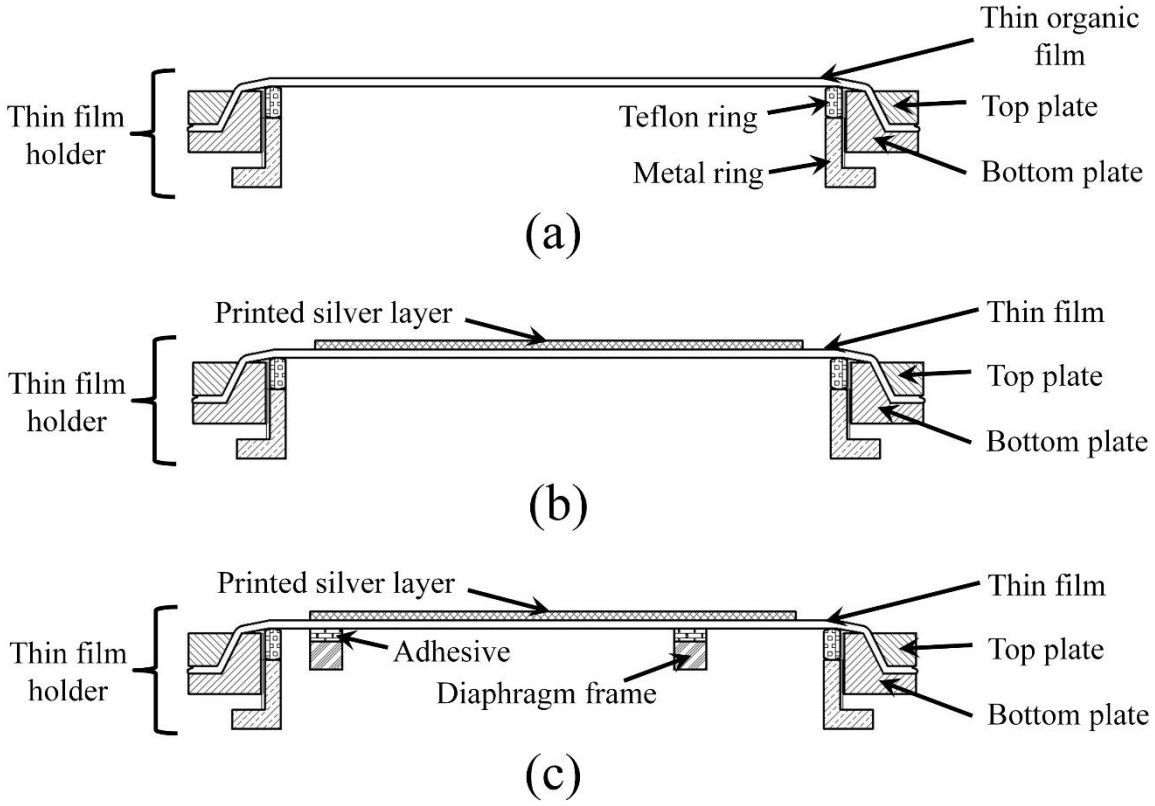

Figure 4.7: *Schematic diagram of the membrane fixed on the thin film holder (a) top view, (b) cross-sectional view after printing and sintering the conductive layer, (c) cross-sectional view after gluing the diaphragm frame to the thin film.*

With reference to Figure 4.7(a), thin organic film is mounted and fixed between the bottom and top plate of the thin film holder. Metal ring and Teflon ring can move up and down to adjust the required tension applied to the thin film. The electrically conductive silver ink layer is printed on the pre-stressed thin organic film using 2D inkjet printing techniques as illustrated in Figure 4.7(b), sintered using conventional thermal curing method in heat oven. With refers to Figure 4.7(c), a rigid diaphragm frame made by 3D printing method is glued to the thin organic film on the opposite surface of the printed conduction layer using adhesive.

Figure 4.8(a) illustrates the top view of the diaphragm. The membrane with printed conductive layer attached on the rigid frame is then cut-off from the film holder, as illustrated in Figure 4.8(b). Then the extended part to the flexible membrane with printed layer is folded over the frame in one corner and glued to the opposite surface of the frame to get the connection from the other side, as showed in Figure 4.8(c).

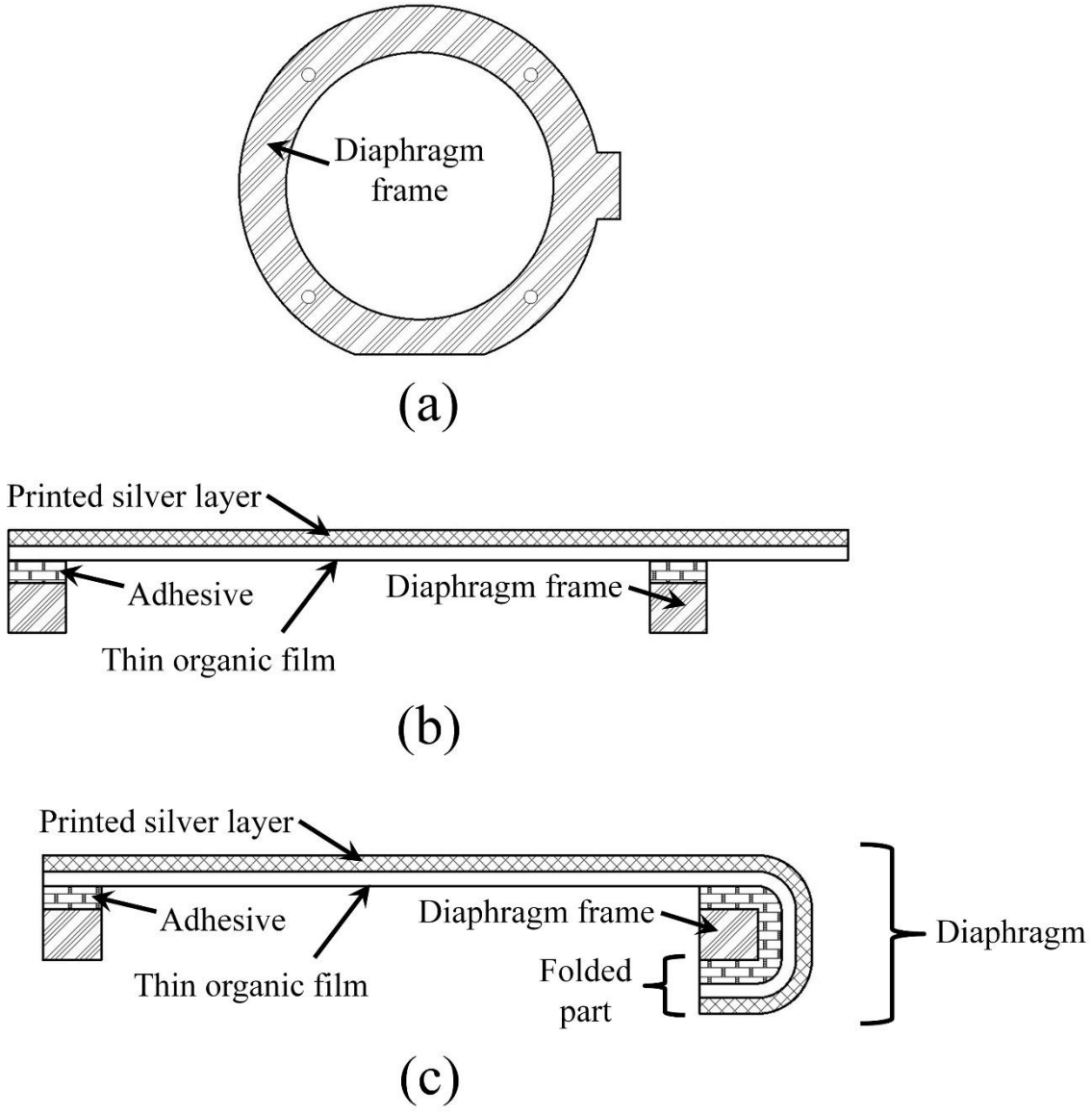

Figure 4.8: *Schematic diagram of the diaphragm with printed electrode fix on the diaphragm frame (a) top view, (b) cross-sectional view after separating from the large film holder, (c) cross-sectional view of the final diaphragm.*

4.3.3. Device assembling

Once the bottom structure and diaphragm are prepared, they are assembled to form the capacitive acoustic transducer, where a spacer is used to separate the diaphragm from the backplate. Figures 4.9(a) and 4.9(b) illustrate the cross-sectional and top view of the spacer respectively. Spacer is fabricated either separately by 3D printing method, or by printing ultraviolet (UV) curing dielectric ink layer directly on the 3D printed structure using 2D inkjet printing or by prototyping thin polyimide (PI) film by laser ablation technique.

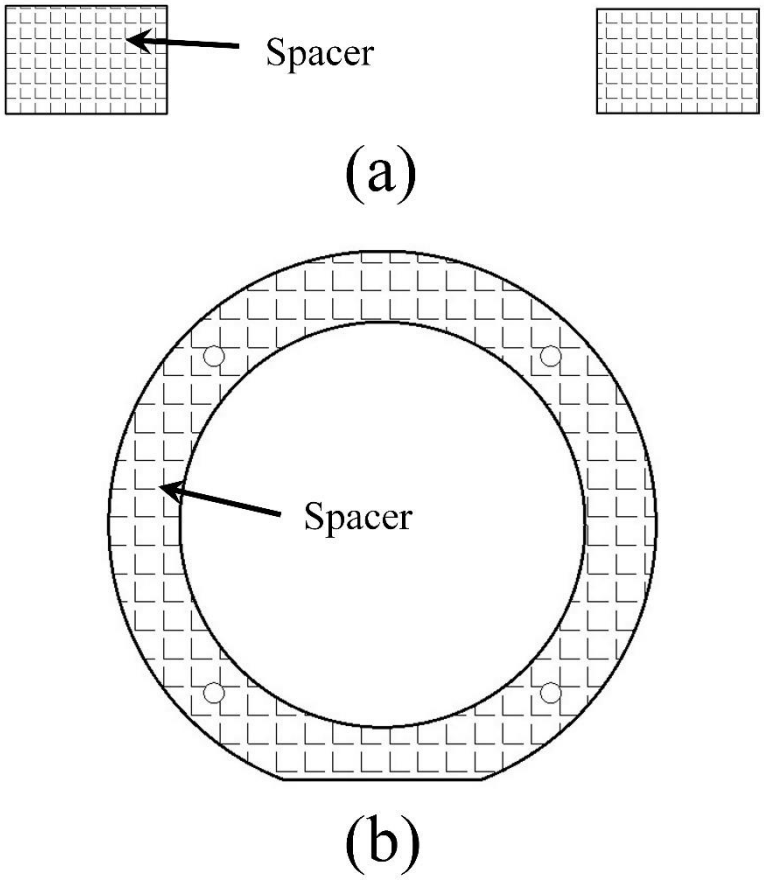

Figure 4.9: *Schematic diagram of the 3D printed spacer (a) cross-sectional view, and (b) top view.*

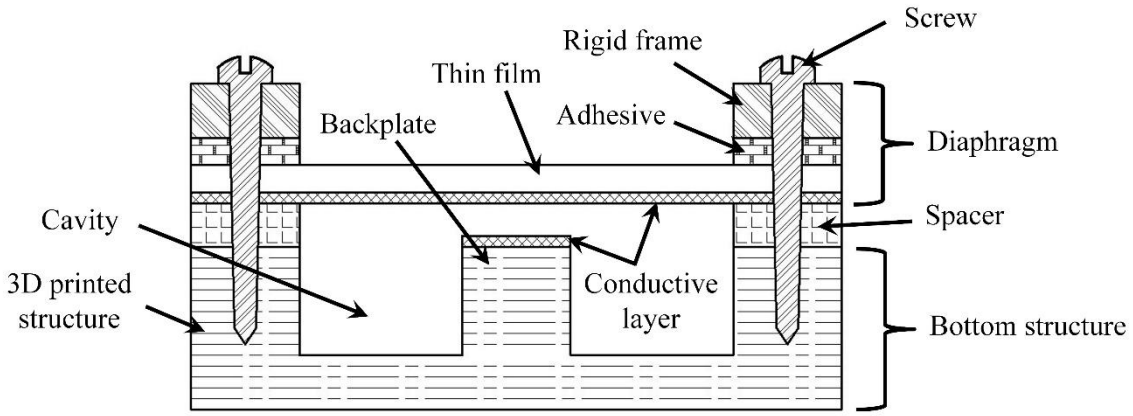

Figure 4.10: *Schematic diagram of the cross-sectional view of the capacitive acoustic transducer after complete assembly.*

The schematic of the capacitive device is presented in Figure 4.10. The bottom part comprises of 3D printed structure with cylindrical rigid backplate of a small radius, a flat annular cavity surrounding the backplate and a printed conductive layer on the backplate. A diaphragm comprises of a printed conductive layer on a thin organic film, which is attached to a rigid frame by adhesive. The bottom electrode and the diaphragm are separated by air-gap created by a spacer. All the parts are joined by screws, in a way that both electrodes are facing each other. The final assembly creates an enclosure that prevents dust particles from entering the system and also protects the printed conductive layers from scratches.

The acoustic transducer could also be assembled by joining the bottom structure and the diaphragm by adhesive rather than screw. However in that case, the air gap will be the accumulated height of the spacer and the adhesive layer, as showed in Figure 4.11.

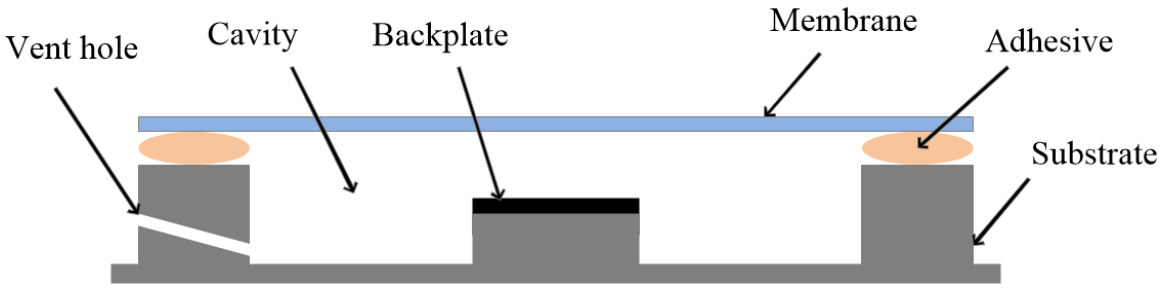

Figure 4.11*: Schematic diagram assembly of the device, where the change of air gap occurs due to the additional height of the adhesive.*

4.4. Development of technological building blocks

The fabrication of the transducer composed of the inkjet printing of conductive silver ink layer on the 3D printed substrate to fabricate the bottom structure of the device, and the inkjet printing of conductive silver electrode on thin film of thickness below 25 µm. The printing process and the characterization of the printed conductive layer are discussed in details below.

4.4.1. Conductive layer printing on 3D printed substrate

Three-dimensional (3D) printing is an emerging technique that allows the building of wide range of structures with complex shapes and sizes. On the other hand, direct write 2D inkjet technique is used for electronic interconnections [10], [11], as well as to develop different devices, such as passive electrical components [11], [12], transistors, solar cells, displays [11]. Although, 3D printing technique and the 2D inkjet printing are two independent methods, the combination of these two techniques could enable us to develop new functional objects.

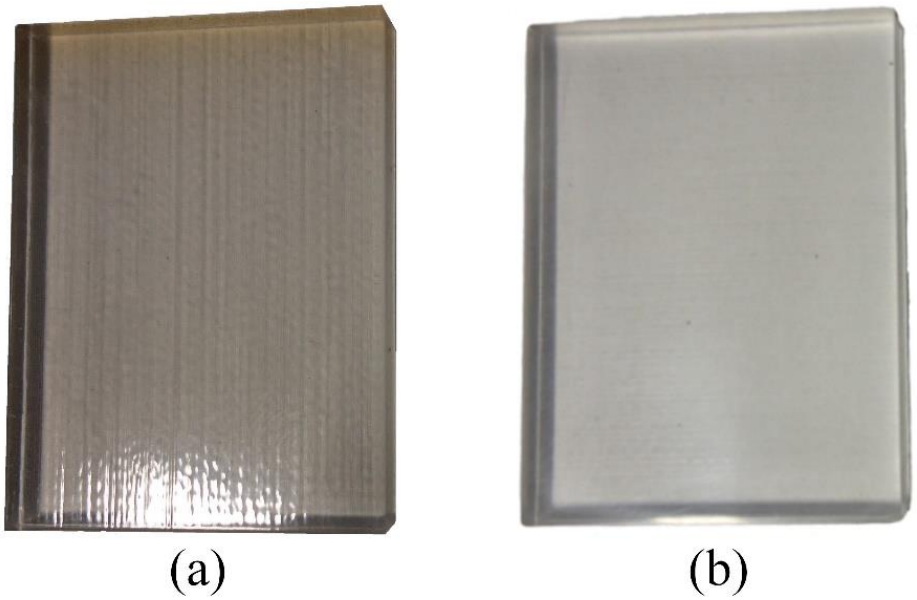

Figure 4.12: *Three-dimensional (3D) printed substrate, (a) as printed, (b) after polishing.*

Generally, inkjet printing of conductive layer requires substrate with smooth surface and appropriate surface energy. However, 3D printed substrates show relatively large surface roughness, as presented in Figure 4.12(a). Therefore, to reduce the surface roughness, the

structure is polished. Polishing of the 3D printed substrate is performed using Struers LaboPol-5 grinding and polishing machine from 50 to 500 rpm. Polishing starts with coarse abrasive grinding paper with particle size of 15.3 µm. Thereafter the polishing is performed using finer abrasive papers (particle size of 6.5 µm and 2.5 µm). Finally, dispersed alumina nanoparticle based polishing suspensions with particle size of 300 nm and 100 nm are used before completing the polishing step with 50 nm of alumina nanoparticles suspension. Figure 4.12(b) presents the 3D printed structure after polishing. The roughness of the as-printed and polished 3D substrates are listed in Table 4.2. The roughness of the surface is correlated with the polishing time as well.

Table 4.2: Roughness of the surface of as printed and polished 3D printed substrates.

Substrate	Code	As-printed		Polished	
		R_a nm	R_q nm	R_a nm	R_q nm
Bio-compatible materials	MED610	1220 ± 120	1450 ± 150	76.5 ± 14	99.4 ± 17
High Temperature	RGD525	1600 ± 610	1930 ± 750	93.4 ± 39	116.6 ± 48
Vero White	RGD875	2410 ± 650	2890 ± 740	118.2 ± 15	154.8 ± 23
Vero Black	RGD835	2280 ± 220	3030 ± 390	114.4 ± 9	148.1 ± 10
Vero Blue	RGD840	2580 ± 620	3200 ± 790	158.0 ± 17	275.7 ± 48
Vero Clean	RGD810	2000 ± 550	2320 ± 620	119.1 ± 16	176.5 ± 27

The surface energy of the polished 3D printed substrates was also measured. In this regard, the contact angle method has been carried out using a goniometer from Dataphysics (OCA200). Three different solvents, namely, H_2O, diiodomethane and ethylene glycol 40% were used. Thereafter, the Owens-Wendt-Rabel-Kälbe (OWRK) method [13]–[15] has been used to calculate the surface energy. The measured surface energies of the 3D printed substrates are listed in Table 4.3.

Table 4.3: Surface energy of the polished 3D printed substrates along with commercially available polyethylene terephthalate (PET) substrate.

Substrate	Code	Surface Energy (γ_{sl}) mN.m^{-1}
Polyethylene terephthalate	PET	40.7 ± 0.2
Bio-compatible materials	MED610	40.7 ± 0.7
High Temperature	RGD525	44.0 ± 0.5
Vero White	RGD875	39.9 ± 0.4
Vero Black	RGD835	38.3 ± 0.6
Vero Blue	RGD840	38.5 ± 0.8
Vero Clean	RGD810	40.1 ± 0.2

It has been observed that the surface energy of the 3D printed substrates is similar to that of the commercially available polyethylene terephthalate (PET) substrate, which permits the inkjet printing of the conductive silver layer on the 3D printed substrates. During this work, inkjet printing of conductive silver layer on the 3D printed MED610 and RGD525 substrates were further investigated, as the MED610 structure exhibits surface energy similar to PET, and RGD525 substrate shows the highest surface energy and has higher heat deflection temperature and low glass transition temperature amongst the tested polyjet materials.

Inkjet printing on the 3D printed substrates has been performed using silverjet ANP DGP-HR ink having 35-40 wt.% of metal content with drop spacing of 30 µm. After printing, the layer is initially dried at 30 °C under vacuum for 15 minutes and then sintered at elevated temperature in atmospheric pressure. Study have showed that to obtain a good conductive layer, sintering of ANP silver nanoparticle based ink needs to be performed at elevated temperature between 120 to 250 °C for sufficient time duration [16]. As the 3D printed substrates have low heat deflection temperature (T_{HD}) and low glass transition temperature (T_g), the sintering process of the conductive layer using conventional thermal heat oven causes the damage of the 3D printed substrate (Figure 4.13(a)). This is confirmed by the optical profilometer observation using WYKO NT110 from Veeco, as presented in Figure 4.13(b). This problem can be solved by sintering the conductive layer using photonic sintering technique [17]–[19], as illustrated in Figures 4.13(c) and 4.13(d).

During this work, Novacentrix PulseForge 3200 with N20-VXI lamp has been used. The lamp produces a high intensity, broad spectrum pulse of light having wavelengths between 225 and 1050 nm. The absorption of the light by the nanoparticles initiates the heating of the sample up to several hundred of degrees within very short time, without significantly rising the temperature of the underlying substrate. After the termination of the pulse, the surface is generally cooled due to heat conduction into the bulk of the substrate which prevents it from being damaged [17]. The maximum energy input that can be used during photonic sintering is mainly limited by the effective heat dissipation which depends on the absorption coefficient, thermal conductivity, heat capacity and also the thickness of the substrate. Therefore, optimization of the photonic sintering process is required to maintain the energy input from the light pulse, so that the heat transfer from the layer to be sintered to the substrate remains below the damaging threshold for the substrate. In case of slow

heat dissipation from metal to substrate the delamination of the conductive layer takes place, whereas too low energy input will not provide the good conductivity due to lack of effective sintering of the printed silver layer.

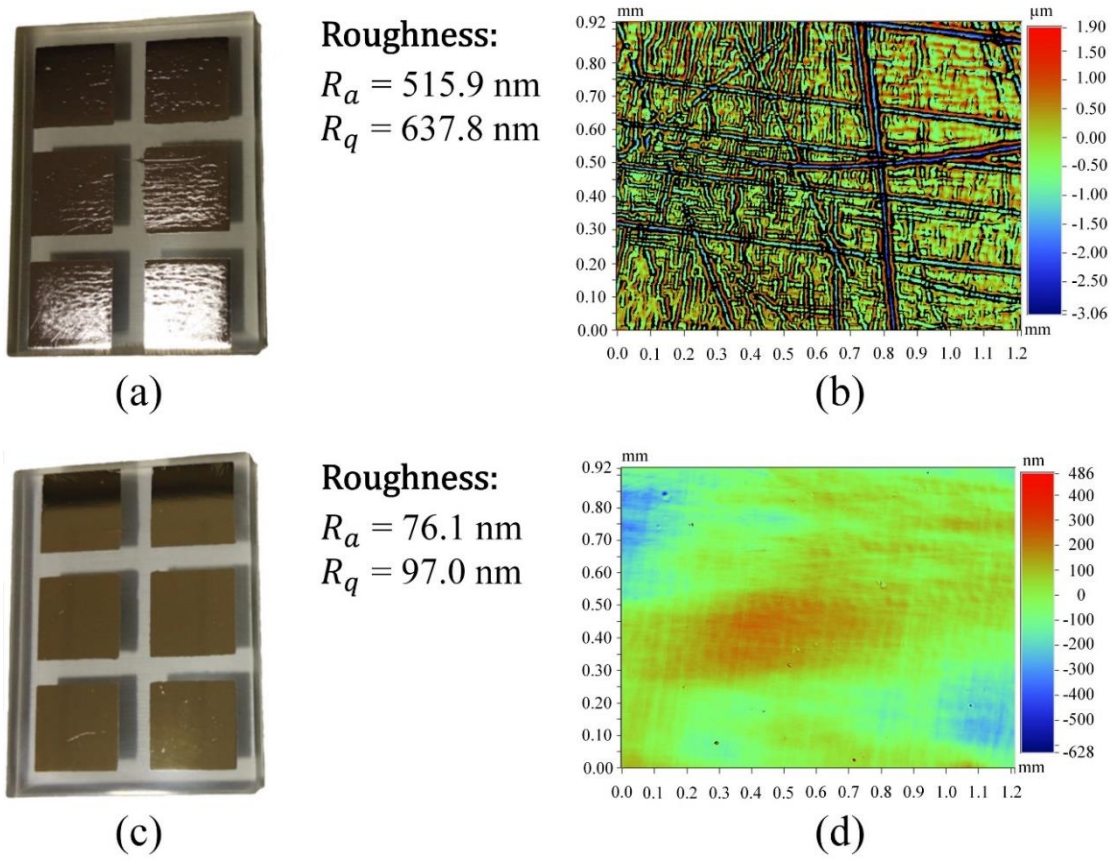

Figure 4.13: *Samples (a) inkjet-printed silver layer on 3D printed substrate after sintering at 140 °C for 20 minutes in thermal heat oven in atmospheric pressure, (b) surface roughness of the conductive layer after thermal oven sintering, (c) sintering of the conductive layer by photonic sintering method, and (d) surface roughness of the conductive layer after photonic sintering.*

In order to study the sintering process in further details, samples are prepared using 3D printed substrates by printing squares having an area of 1 cm^2 using conductive silver ink. After drying the as-printed layers at 30 °C under vacuum for 15 minutes, sintering of the samples were performed using photonic curing technique under different conditions. The varied sintering parameters are voltage (V_B) that corresponds to the exposed energy in J/cm^2, pulse duration (T_{on}), time between two pulses (T_{off}) and number of pulses (N_p). It has been observed that the 3D printed RGD525 substrate allows the use of higher energy input within shorter time duration compared to MED610 substrate. The conductive layers

have then been characterized to study their electrical properties, morphology and roughness.

4.4.1.1. Electrical measurement

The sheet resistance of the printed silver layers, having thickness of 1±0.1 µm as measured using mechanical profilometer (model: XP-2, AMBiOS Technology) and sintered using photonic sintering method for different parameters, has been performed by JANDEL four point probing resistance measurement system (model: RM3-AR). Figures 4.14 and 4.15 show the sheet resistance with respect to number of photonic sintering pulses of the conductive layers on MED610 and RGD525 substrates respectively. Similar results have been observed for both substrates, where the resistivity decreases with the increasing pulse duration.

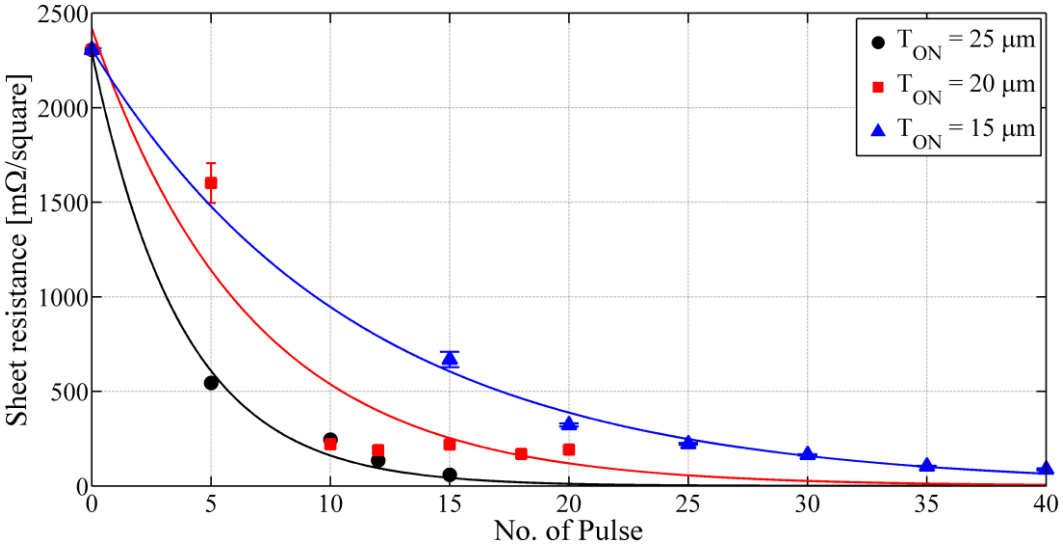

Figure 4.14: *Sheet resistance of the inkjet-printed silver layer on 3D printed MED610 substrate (Dried and photonic sintered for constant V_B=400V, T_{off}=1000µs).*

Sheet resistance as low as 58.7±5.1 mΩ/square on MED610 substrate was achieved for V_B of 400 V, T_{on} of 25 µs, T_{off} of 1000 µs and N_p of 15; however, the pilling-off of the layer was observed. Optimum sintering without any delamination of the conductive layer on the MED610 substrate was achieved for V_B of 400 V, T_{on} of 15 µs, T_{off} of 1000 µs and N_p of 40, where the sheet resistance was 87.5±5.2 mΩ/square. On the other hand, the sheet resistance of 81.2±8.3 mΩ/square was achieved for the optimum sintering without any

pilling-off of the conductive layer on the RGD525 substrate for V_B of 400 V, T_{on} of 20 µs, T_{off} of 1000 µs and N_p of 30. The resistivity (ρ) of the printed silver layers can be calculated using following expression,

$$\rho = R_{sq}.t \quad \ldots\ldots\ldots (4.1)$$

Here R_{sq} represents the sheet resistance and t is the thickness of the inkjet-printed conductive silver layer. Therefore, the electrical conductivity (σ) in S/m, which is reciprocal of the resistivity can be then calculated using equation 4.2.

$$\sigma = \frac{1}{\rho} = \frac{1}{R_{sq}.t} \quad \ldots\ldots\ldots (4.2)$$

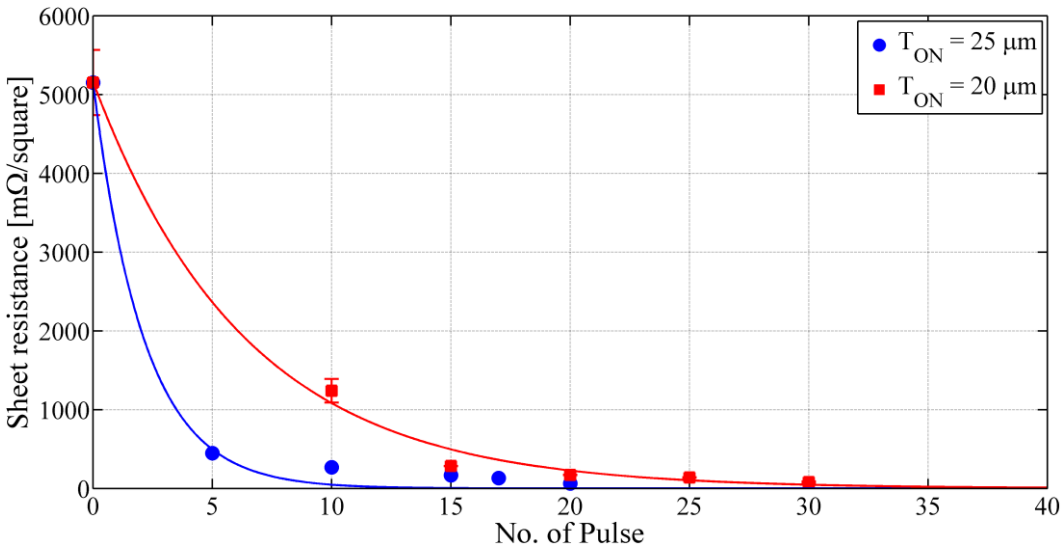

Figure 4.15: *Sheet resistance of the inkjet-printed silver layer on 3D printed RGD525 substrate (Dried and photonic sintered for constant V_B=400V, T_{off}=1000µs).*

The increase in electrical conductivity can be explained by the microstructural evolution due to the sintering of the nanoparticles. The morphology of the inkjet-printed conductive layer after photonic sintering has been studied by scanning electron microscope (SEM) using Ultra 55 from Carl Zeiss. The microstructural evolution of the films was observed, as illustrated in Figures 4.16 and 4.17. The neck formation and the formation of larger particles take place due to the coalescence because of the photonic sintering of the silver nanoparticles.

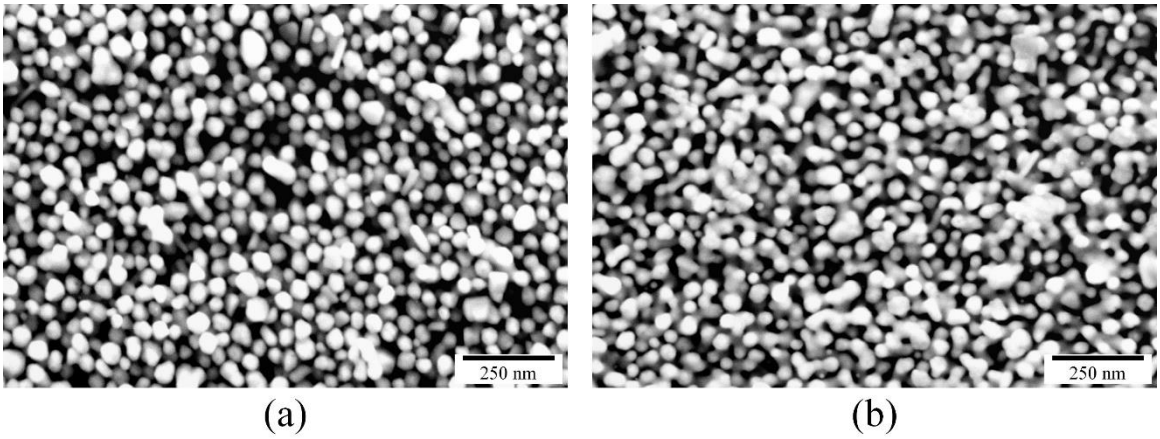

Figure 4.16: *Microstructural evolution of the printed layer on 3D printed MED610 substrate, (a) dried (at 30 °C under vacuum for 10 minutes), and (b) photonic sintered after drying step (at V_B = 400 V, T_{on} = 15 µs, T_{off} = 1000 µs, N_p = 40).*

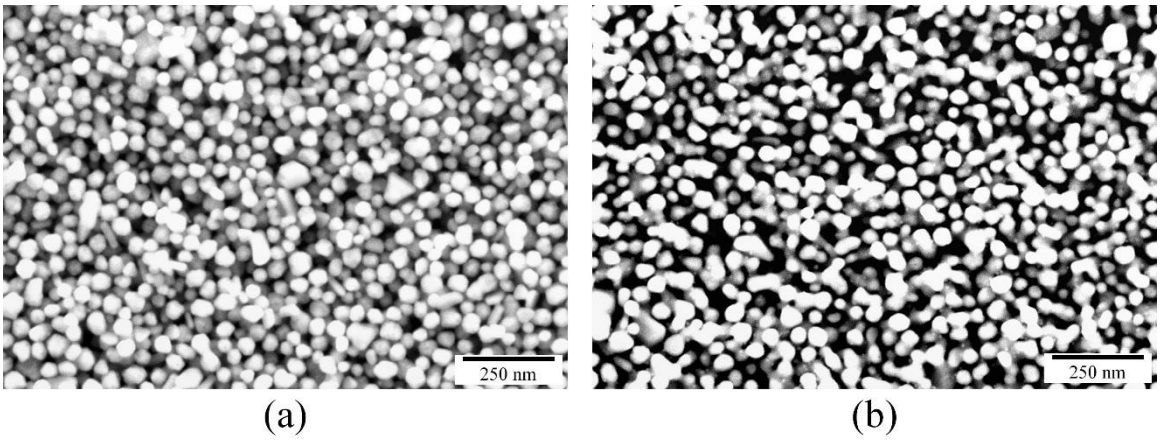

Figure 4.17: *Microstructural evolution of the printed layer on 3D printed RGD525 substrate, (a) dried (at 30 °C under vacuum for 10 minutes), and (b) photonic sintered after drying step (at V_B = 400 V, T_{on} = 20 µs, T_{off} = 1000 µs, N_p = 30).*

4.4.1.2. Grain size measurement

The grain growth can also be estimated from the SEM micrograph using image processing technique. During this study, image processing software, namely, ImageJ software developed by U.S. National Institutes of Health [20], and Gwyddion software [21] have been used to determine the equivalent circle diameter (ECR) of the detected particles based on the determined average surface area (Figures 4.18). The selection of appropriate

threshold value is important during the process for the unprepared samples since the shade in gray scale can either be related to the grains surface or to a grain boundary.

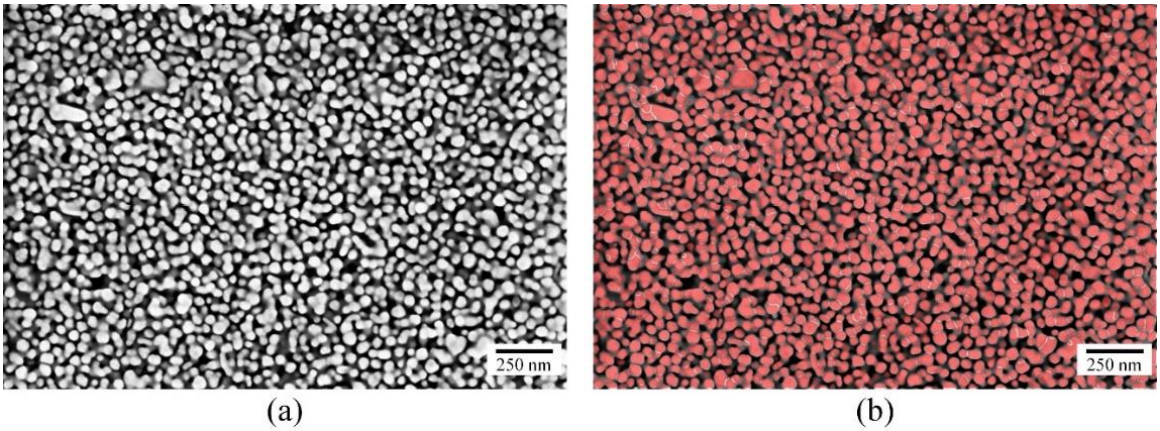

Figure 4.18: *Surface morphology of nanoparticles on 3D printed MED610 substrate, (a) photonic sintered after drying step (at V_B = 400 V, T_{on} = 15 µs, T_{off} = 1000 µs, N_p = 40), and (b) corresponding superimposition of the grain boundary outline resulting from the image analysis process.*

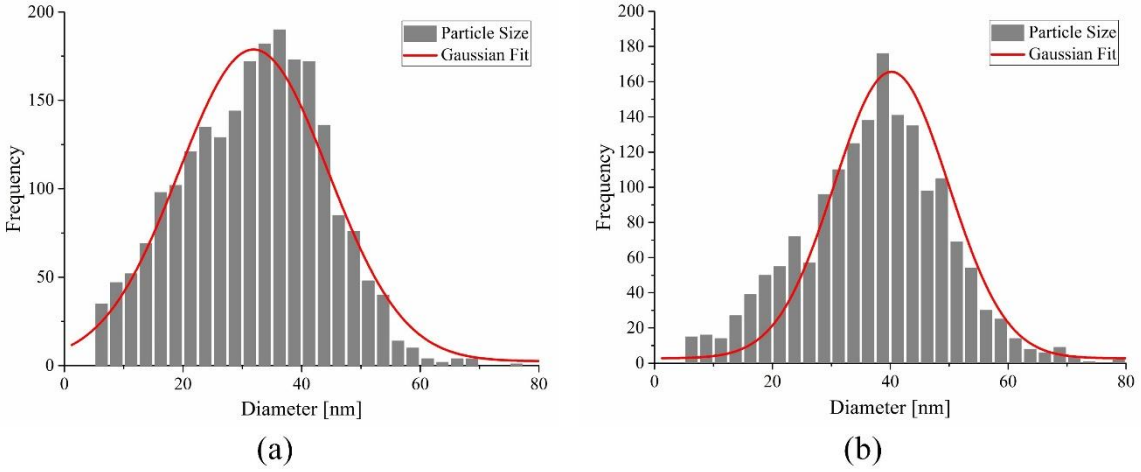

Figure 4.19: *Particle size distribution based on image analysis of the inkjet-printed silver nanoparticles on 3D printed MED610 substrate, (a) dried (at 30 °C under vacuum for 10 minutes), and (b) photonic sintered after drying step (at V_B = 400 V, T_{on} = 15 µs, T_{off} = 1000 µs, N_p = 40).*

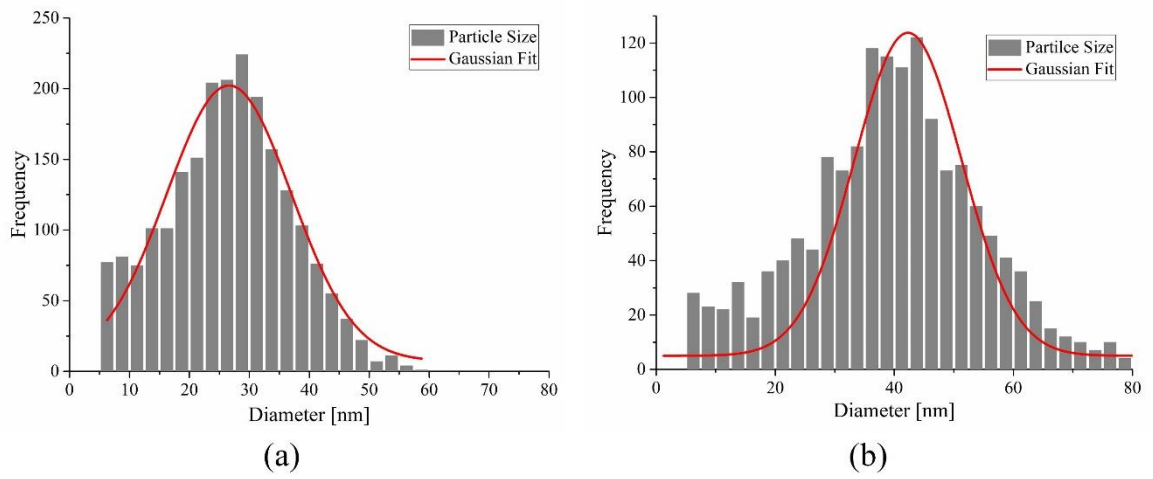

Figure 4.20: *Particle size distribution based on image analysis of the inkjet-printed silver nanoparticles on 3D printed RGD525 substrate, (a) dried (at 30 °C under vacuum for 10 minutes), and (b) photonic sintered after drying step (at V_B = 400 V, T_{on} = 20 µs, T_{off} = 1000 µs, N_p = 30).*

Average grain size of the samples has been calculated using Gaussian fit of the grain size distribution extracted from the SEM images. Figures 4.19 and 4.20 illustrate the grain size distribution of the silver nanoparticles on 3D printed MED610 and RGD525 substrates. The average grain sizes of the sample are listed in Table 4.4.

Table 4.4: Calculated average grain size of the silver nanoparticle on 3D printed substrates after photonic sintering using image analysis.

Substrate	Sample Code	Photonic sintering parameters				Grain Size
		V_B V	T_{on} µs	T_{off} µs	N_p	nm
MED610	M0	-	-	-	-	31.9 ± 12.6
	M1	400	15	1000	15	34 ± 11.8
	M2	400	15	1000	25	35.6 ± 11
	M3	400	15	1000	40	40.2 ± 9.7
RGD525	HT0	-	-	-	-	26.6 ± 10.4
	HT1	400	20	1000	15	29.5 ± 10.9
	HT2	400	20	1000	20	32.9 ± 11.4
	HT3	400	20	1000	30	42.3 ± 9

The image analysis of SEM micrograph shows the growing trends in the grain size for higher number of pulses during photonic sintering. Although, image analysis technique allows fast assessment of grain size, this method is prone to errors and can only refer to estimation of grain size evolution. The precise evaluation of the grain size of the printed silver can be determined using the X-ray diffraction (XRD).

The XRD of the inkjet-printed silver nanoparticles have been studied using X'pert Pro X-ray diffractometer from PANaltical, Cu-Kα X-rays of wavelength (λ) equals to 1.54059 Å and data was taken for the 2θ range of 10° to 90° with the step size of 0.04°. Figure 4.21 illustrates the XRD patterns of the silver nanoparticles after photonic sintering on 3D printed substrates. A number of strong Bragg reflections are present. They correspond to the (111), (200), (220), (311) and (222) reflections of face centered cubic (fcc) silver.

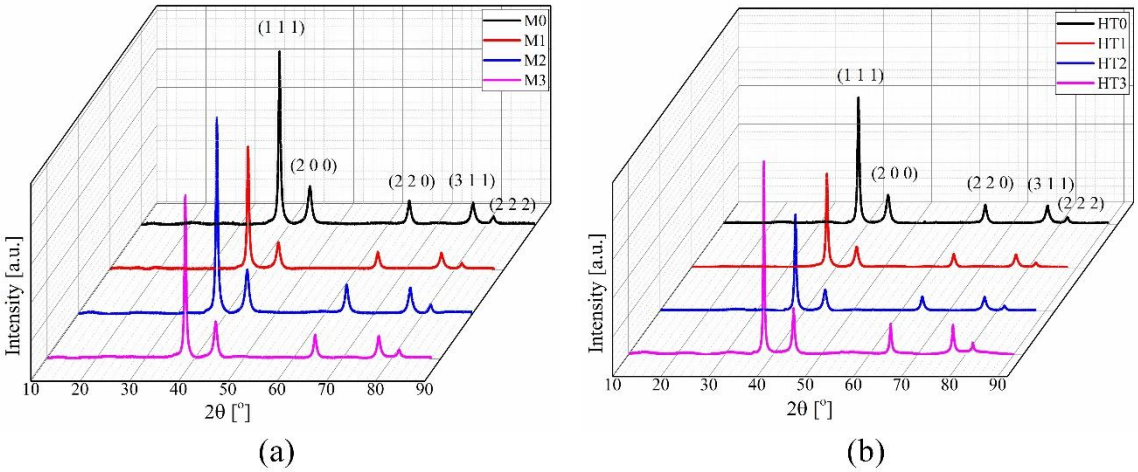

Figure 4.21: *XRD pattern of the inkjet-printed silver nanoparticle on 3D printed MED610 and RGD525 substrates after photonic sintering.*

The XRD pattern can also be used to determine the crystallite size using Rietveld refinement technique. The Rietveld refinement technique, developed by Hugo Rietveld, simultaneously takes into account all the factors affecting the XRD measurement, that is to say the crystal structures, diffraction optic effects, instrumental factors and other sample characteristics. The Rietveld method uses a least square approach to refine a theoretical line profile until it matches the experimental profile. The goal of the Rietveld refinement is to minimize the residual function using a non-linear square algorithm given by equation 4.3 [22], and thus to refine the crystal structure of the particle or compound, namely, cell parameters, atomic positions and Debye-Waller factors.

$$WSS = \sum_i w_i \left(I_i^{\exp} - I_i^{calc}\right)^2, \quad \text{where} \quad w_i = \frac{1}{I_i^{\exp}} \quad \ldots\ldots\ldots (4.3)$$

Here WSS represents the weighted sum of squares, I_i^{exp} presents the experimental intensity, and I_i^{calc} represents the fitted or calculated intensity.

The Rietveld refinement method allows one to separate the refinement of the profile from the refinement of the crystal structure and the extracted intensities can be used for crystal structure determination. The Rietveld refinement requires high quality experimental diffraction pattern, a structural model that makes physical and chemical sense and suitable peak, background functions and instrument calibration file. In this method the crystal structure is described using space group, lattice parameters, atomic positions, atomic site occupations and atomic thermal parameters (both isotropic and anisotropic). The background noise values can either be obtained experimentally from a preliminary measurement or by a method of interpolation between different selected points or by a function describing the background noise. The background noise function is generally refined according to physical criteria, such as thermal diffusion. The instrumental broadening can also be adjusted in order to get proper profile refinement. Therefore, the Rietveld method fits a multivariable structure-background-profile model to experimental data. However, during the process, most important variables, like back ground, instrumental broadening etc., are required to refine at the beginning and then other parameters are refined until the adequate solution can be obtained [23].

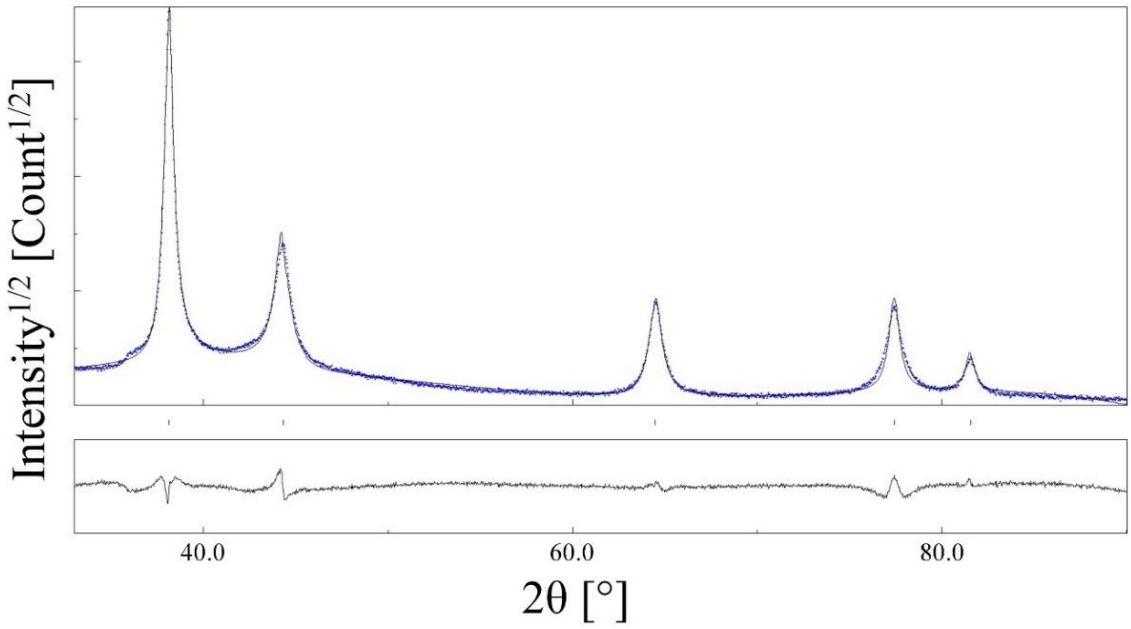

Figure 4.22: *Measured (blue dots) and fitted (black line) spectrum for the inkjet-printed silver nanoparticle based ink on 3D printed MED substrate by the Rietveld texture analysis.*

During this study, the X-ray diffraction patterns of inkjet-printed silver nanoparticle based ink on 3D printed substrates have been studied and refined by Rietveld method using Maud software [24], [25]. Figure 4.22 reports a single plot of a diffraction spectrum as fitted by the program to show the peaks overlap and location. The calculated particle size based on the Rietveld refinement of XRD patterns are listed in Table 4.5.

Table 4.5: Calculated average particle size of the silver nanoparticles on 3D printed substrates from XRD patterns using Rietveld refinement technique.

Substrate	Sample Code	Photonic sintering parameters				Average Grain Size D nm
		V_B V	T_{on} µs	T_{off} µs	N_p	
MED610	M0	-	-	-	-	51.6 ± 1.3
	M1	400	15	1000	15	58.6 ± 0.5
	M2	400	15	1000	25	67.7 ± 2.5
	M3	400	15	1000	40	87.2 ± 4.1
RGD525	HT0	-	-	-	-	56.1 ± 1.5
	HT1	400	20	1000	15	72.2 ± 2.5
	HT2	400	20	1000	20	74.0 ± 3.1
	HT3	400	20	1000	30	99.8 ± 1

The particle size calculation from the XRD patterns confirms the increase in the particle size with the increasing number of pulse for constant values of V_B, T_{on} and T_{off} on 3D printed substrate. However, compared to the image analysis technique, Rietveld refinement analysis provided larger average grain size values. As the image analysis technique based on the SEM micrograph is limited to the 2D analysis of 3D particles, which might leads to the lower grain size values.

Therefore, the reduction of electric resistivity of the photonic sintered silver layer on 3D printed substrate is linked to the grain size growth that has been observed by image analysis of SEM micrograph and then confirmed by the XRD analysis.

4.4.1.3. Surface roughness

The morphology of the photonic cured conductive films on 3D substrates has been further studied by atomic force microscope (AFM) using Veeco Autoprobe CP II in tapping mode. Figures 4.23 and 4.24 present the AFM micrographs of the surface of the photonic sintered samples of silver conductive layers on 3D printed MED610 and RGD525 substrates respectively. The roughness of the layers were also measured from the AFM micrographs and listed in Table 4.6.

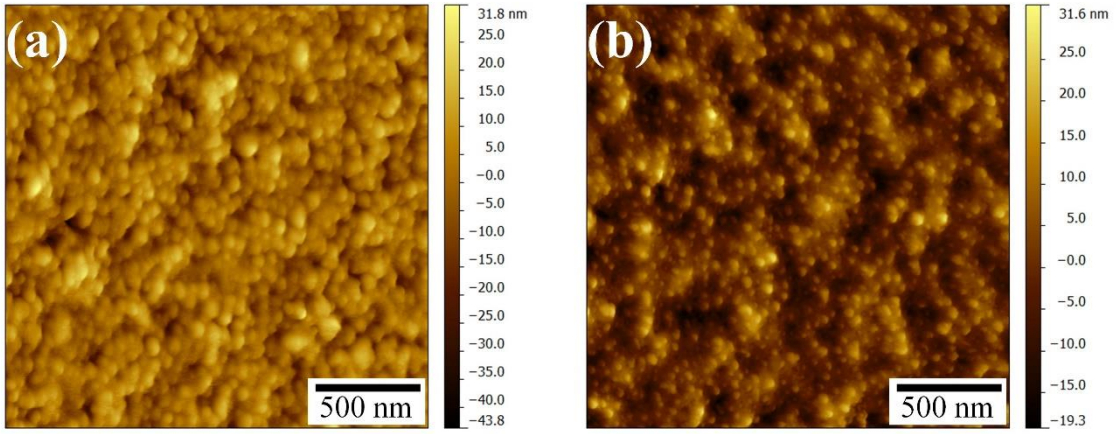

Figure 4.23: *AFM micrograph of inkjet-printed conductive silver layer on 3D printed MED610 substrate, (a) dried, (b) Photonic sintered after drying step (V_B = 400 V, T_{on} = 15 µs, T_{off} = 1000 µs, N_p = 40).*

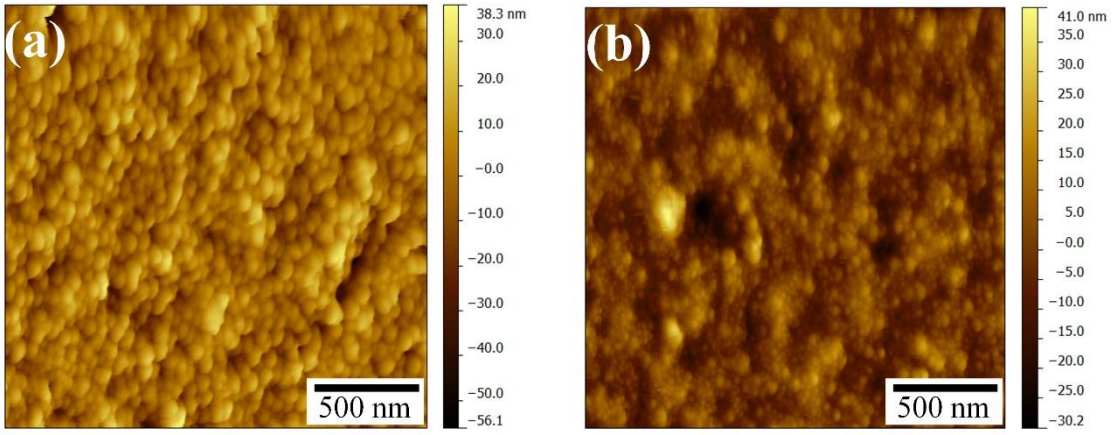

Figure 4.24: *AFM micrograph of inkjet-printed conductive silver layer on 3D printed RGD525 substrate, (a) dried, (b) Photonic sintered (V_B=400V, T_{on}=20µs, T_{off}=1000µs, N_p=30).*

It has been observed that the roughness of the photonic sintered samples on both 3D printed substrates were at around 10 nm. Therefore, the photonic sintered printed silver layer having the thickness of 1±0.1 µm provides smooth surface finish on polished 3D printed substrates.

Table 4.6: Roughness of photonic sintered samples.

	Sample code	Photonic sintering parameters				Roughness	
		V_B V	T_{on} µs	T_{off} µs	N_p	R_a nm	R_q nm
MED610	M0	-	-	-	-	7.1 ± 0.9	9.2 ± 1.3
	M1	400	15	1000	15	6.4 ± 0.6	8.2 ± 0.7
	M2	400	15	1000	25	7.5 ± 0.5	10.3 ± 1.3
	M3	400	15	1000	40	6.0 ± 0.5	7.7 ± 0.7
RGD525	HT0	-	-	-	-	8.2 ± 0.6	10.5 ± 0.7
	HT1	400	20	1000	15	7.1 ± 0 .7	9.0 ± 0.9
	HT2	400	20	1000	20	8.0 ± 0.3	10.3 ± 0.3
	HT3	400	20	1000	30	9.8 ± 3.3	12.3 ± 4.0

R_a → Arithmetic mean of roughness R_q → Root mean square of roughness

During this work, due to the availability of the 3D printing material, MED610 material has been used for the transducer fabrication. Based on the printing tests, the best photonic sintering result on 3D printed MED610 substrate without the delamination of the printed silver layer was obtained for the photonic sintering parameters of V_B of 400 V, T_{on} of 15 µs, T_{off} of 1000 µs and N_p of 40, which is used as one of the building block for the fabrication process of the capacitive acoustic transducer.

4.4.2. Conductive layer printing on thin film

The pre-stressed membrane has been fabricated by inkjet printing of a conductive silver layer on a thin Polyethylene terephthalate (PET) or Mylar film of thickness below 25 µm. To optimize the process, printing tests on thin Mylar film has initially been performed. As it is very difficult to work with very thin film due to static charging, a specific film mounting holder (Figure 4.25(a)) has been designed to apply a tension to the thin film and hold it as a flat surface during inkjet printing process. During this processing, the inkjet printing of the conductive layer is performed using Suntronics U5714 silver nanoparticle based ink from SunChemical, having 40 wt.% of metal content and a mean particle size of 30 – 35 nm, with a drop spacing of 25 µm. The conductive layer is then sintered using conventional thermal heat oven at atmospheric pressure at different sintering temperatures below the glass transition temperature (T_g) of the substrate for different processing times.

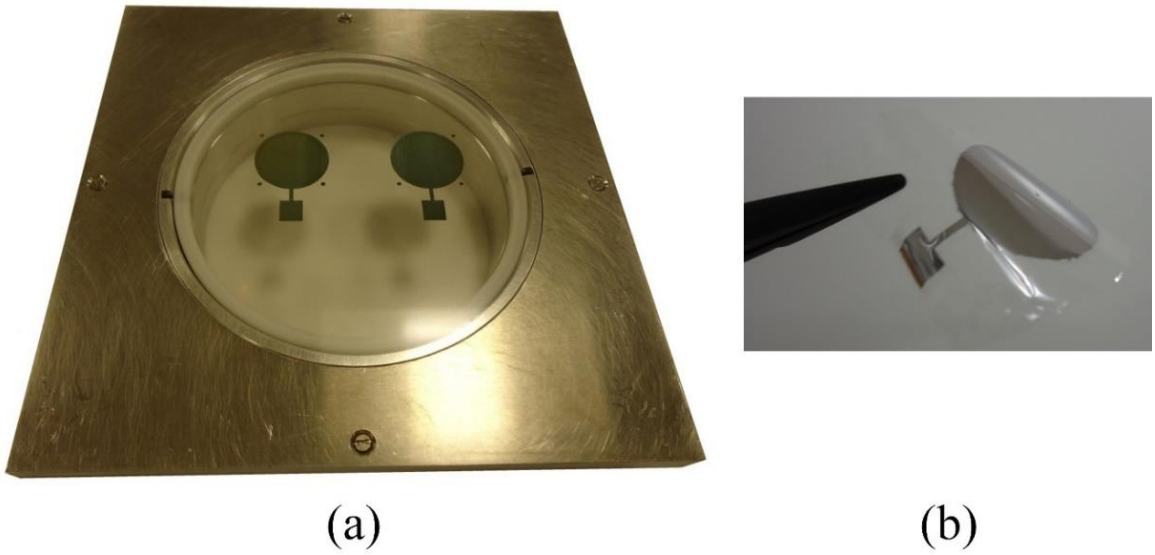

Figure 4.25: *Inkjet printing on thin Mylar film of 8 µm, (a) mounted on thin film holder, (b) thin film after removal from the film holder.*

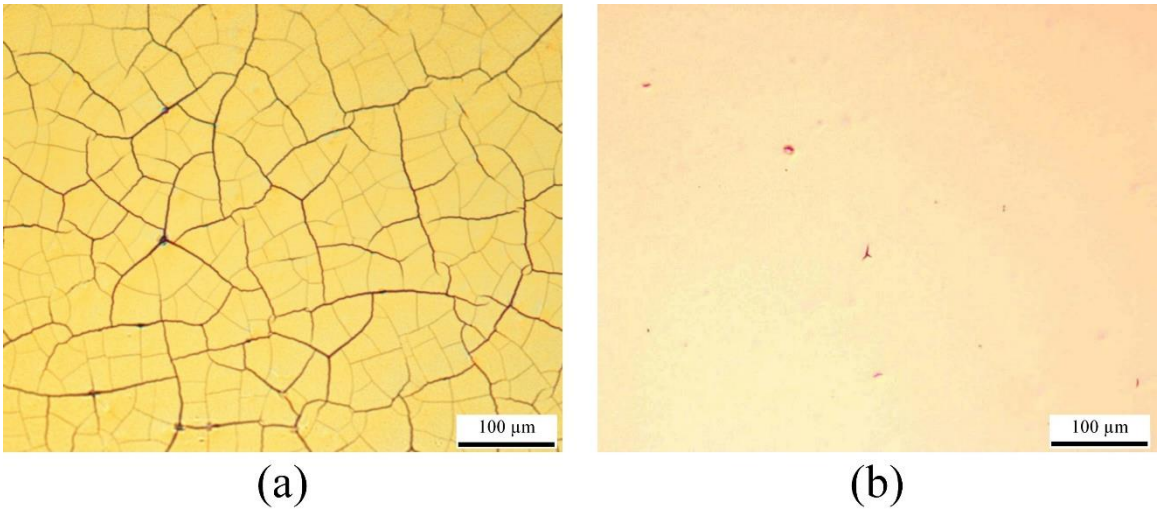

Figure 4.26: *Optical microscopic image of the inkjet-printed conductive silver layer on thin Mylar film of 8 µm sintered at 140 °C for 30 minutes, (a) tension applied after the printing and sintering of the layer, and (b) tension applied before the printing of the conductive layer.*

Thereafter, the thickness of the printed layers was measured using mechanical profilometer (model: XP-2, AMBiOS Technology), and the electrical sheet resistance of the printed conductive layers has been characterized using JANDEL (RM3-AR Test unit) four point probe measurement method. The microstructural evolution of the layer due to different sintering times was studied using ZEISS Supra 40 scanning electron microscope (SEM).

It has been observed that the resistivity of the printed silver layer increases and eventually becomes non-conductive, if the tension is applied at the periphery of the thin film after printing and sintering the conductive layer. This is caused by the formation of cracks on the conductive layer (Figure 4.26(a)). This problem can be solved by applying the tension on the thin Mylar film before printing and sintering of the conductive layer, as shown in Figure 4.26(b). However, in this case, the occasional readjustment of the membrane tension is required as the tension is released during thermal heating.

Finally, after successful printing and sintering the conductive layer having the average thickness of 500±50 nm on the pre-tensed thin film; the electrical measurement has been performed. The measurement showed that the conductivity increases with the increasing sintering temperature and time as well, as listed in Table 4.7. For example, the sheet resistance of the printed layer decreases from 1226±43 mΩ/square for sintering at 90 °C for 30 minutes to 344±18 mΩ/square for sintering at 140 °C for 30 minutes.

Table 4.7: Sheet resistance of inkjet-printed silver nanoparticles layers with different thermal sintering temperature and time.

Sintering parameters		**Sheet Resistance**
Temperature °C	**Time** Minutes	mΩ/square
90	30	1226 ± 43
120	30	582 ± 23
140	10	378 ± 14
140	30	344 ± 18
140	60	265 ± 14

The increase in electrical conductivity can be explained by the microstructural evolution. The microstructural evolution of the silver nanoparticles on thin films is presented in Figure 4.27. The shaping of larger particles by neck formation due to the coalescence has been observed for the thermal heating of the silver nanoparticles. These printed samples were also studied using X-ray diffractometer, as presented in Figure 4.30.

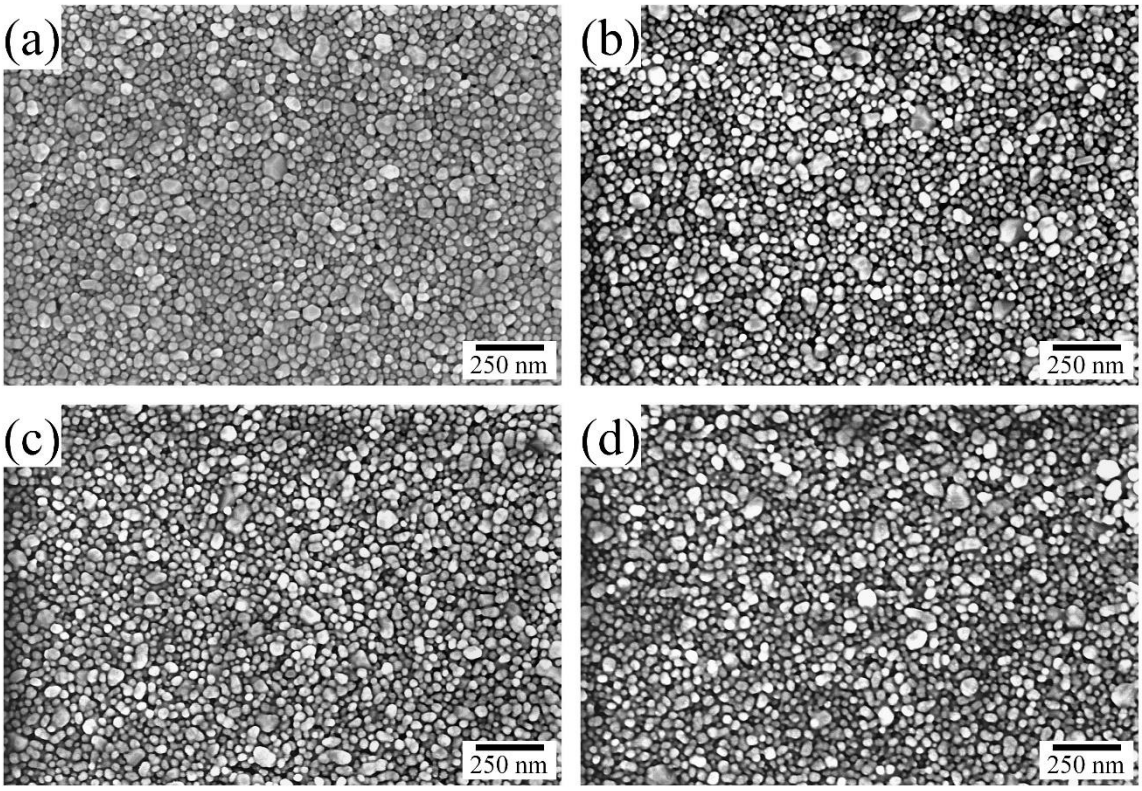

Figure 4.27: *SEM micrograph of Ag nanoparticle layer printed on thin Mylar film of thickness of 8 µm, (a) dried (at 90 °C for 30 minutes), (b) sintered at 120 °C for 30 minutes, (c) sintered at 140 °C for 30 minutes, and (d) sintered at 140 °C for 60 minutes.*

The grain sizes of the printed silver layers on thin film for different sintering temperatures and times have also been calculated using image analysis, and tabulated in Table 4.8. Image analysis of the SEM micrograph using imageJ and Gwyddion image processing software have estimated very mild increment of the particle size with the processing time and temperature. As the image analysis of the SEM micrograph is not a very reliable technique to detect the particle growth, Rietveld analysis on XRD pattern were performed as well to examine the grain size. Results are listed in Table 4.8. Rietveld refinement confirms that the average particle size increases with the increasing temperature and sintering time. However, during this experiment, the grain size increment was small as relatively low sintering temperature of 140 °C was used.

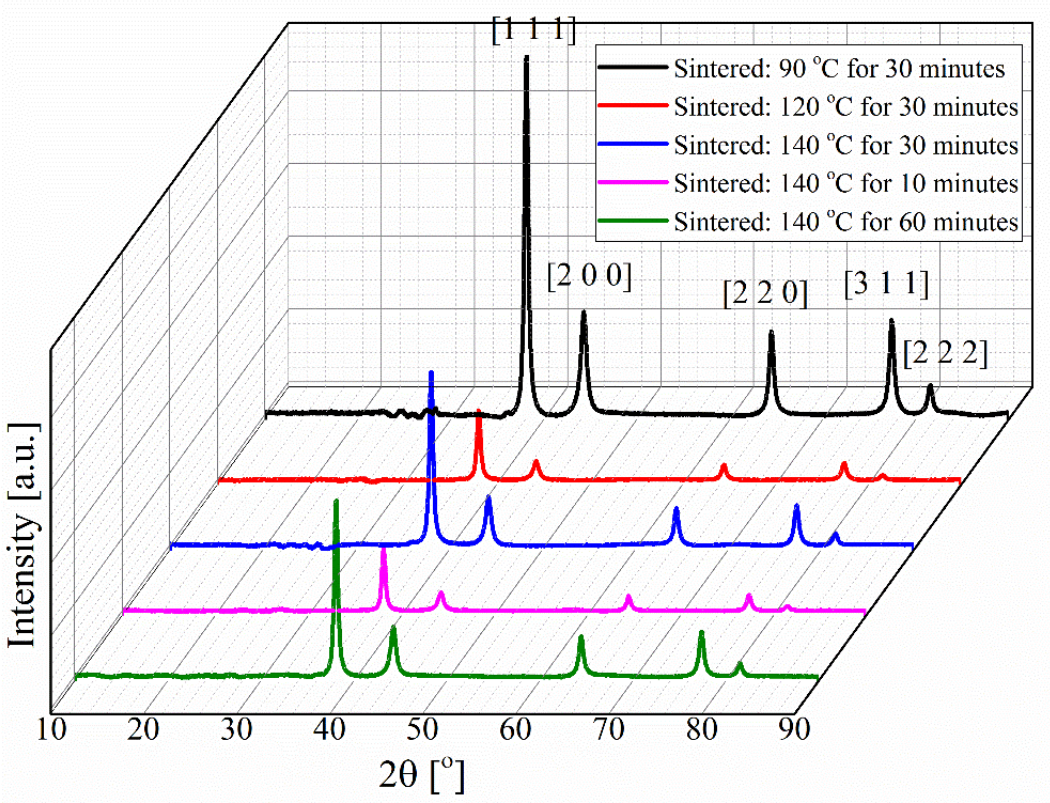

Figure 4.28: *XRD pattern of the inkjet-printed silver nanoparticle layer on thin Mylar film after conventional thermal sintering.*

Table 4.8: Calculated particle size of the silver nanoparticles based on image analysis and Rietveld refinement

Sintering parameters		**Grain Size**	
Temperature °C	**Time** Minutes	**Image Analysis** nm	**Rietveld refinement** nm
90	30	27 ± 9.3	42.9 ± 0.8
120	30	27.7 ± 8.5	45.3 ± 1.3
140	10	29.9 ± 9.5	48.1 ± 1.3
140	30	32.2 ± 10	51.3 ± 1.5
140	60	34 ± 9.3	54.6 ± 2.2

Based on the printing tests performed on thin Mylar film of thickness below 25 µm, during the device fabrication process, the printed conductive layer for membrane fabrication was performed on pre-stressed thin film and then sintered at 140 °C for 30 minutes. In addition, the mechanical behavior of the printed layer on thin Mylar film has also been performed and shows good adhesion, for details see Appendix D.

4.5. Characterization of the capacitive acoustic transducer

After the fabrication, the performances of the printed capacitive acoustic transducers have been characterized to understand static behavior and dynamic behavior under the acoustic pressure. In this regard, static and dynamic measurements have been performed and are discussed in details below.

4.5.1. Static measurement

Initially, the static capacitance measurement of the capacitive acoustic transducer with respect to frequency has been performed using an AC impedance spectrometer (model: 4284A Precision LCR Meter from Agilent). It has been observed that the static capacitance of the transducer does not depend on the bias voltage and the state of charge of the capacitor. Figure 4.29 shows the frequency response of the capacitance of the transducer between 1 kHz to 1 MHz for different dc bias voltages.

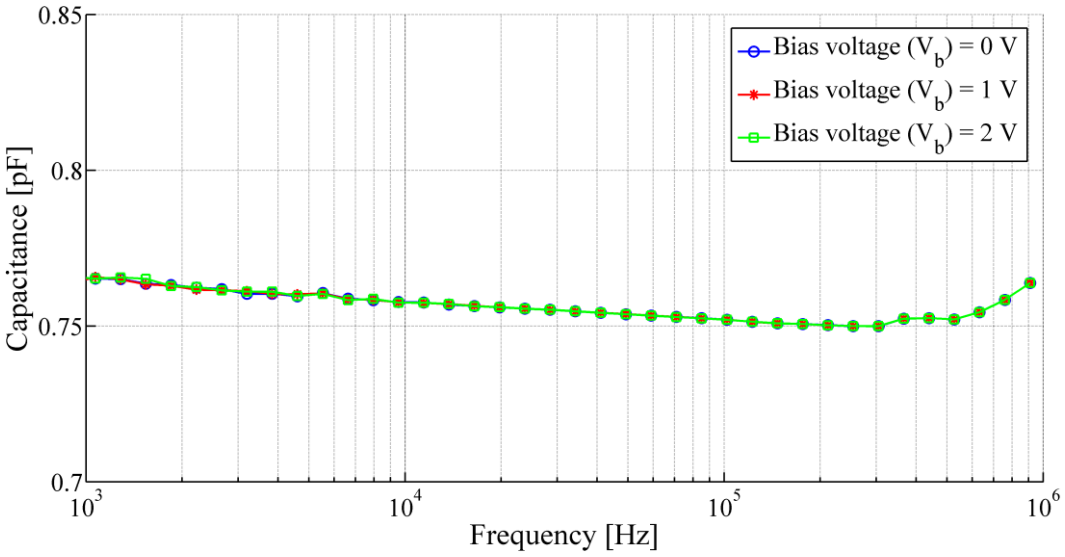

Figure 4.29: *Frequency response of the capacitance of the capacitive acoustic transducer with the membrane radius of 8.1 mm, backplate radius of 871 µm and air gap of 67.7 µm.*

The frequency response of the capacitive acoustic transducer shows almost no dependency for the applied bias voltage between 0 and 2 V. At frequencies between 1 kHz to 1 MHz, the static capacitance of the printed capacitive transducer remains almost constant. Slight fluctuations of the capacitance at higher frequencies may occur due to the skin effect [26] or due to change in parasitic inductance [27] of the printed electrodes.

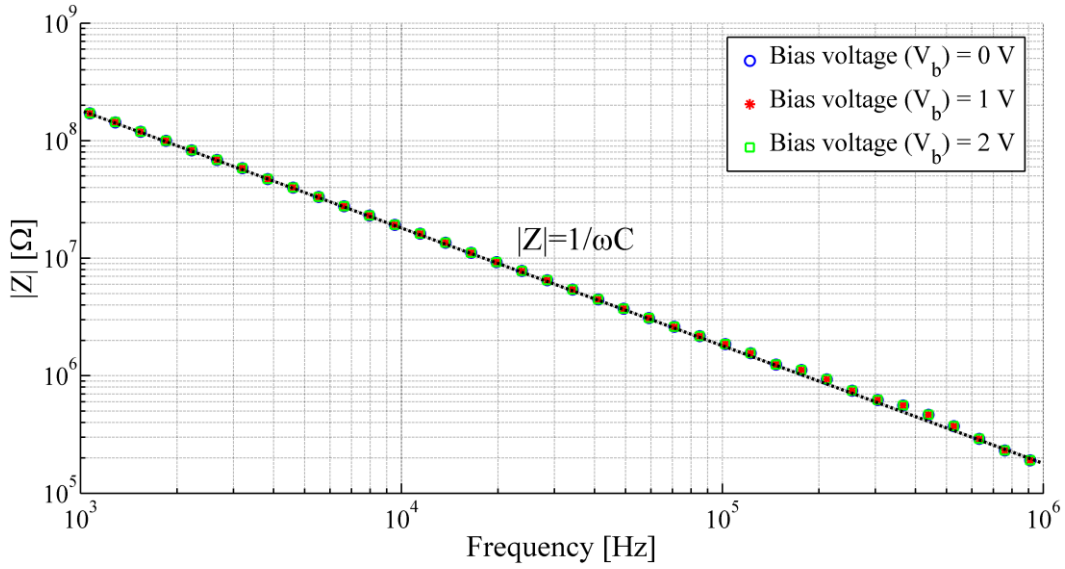

Figure 4.30: *Frequency response of the impedance of the capacitive acoustic transducer with the membrane radius of 8.1 mm, backplate radius of 871 µm and air gap of 67.7 µm.*

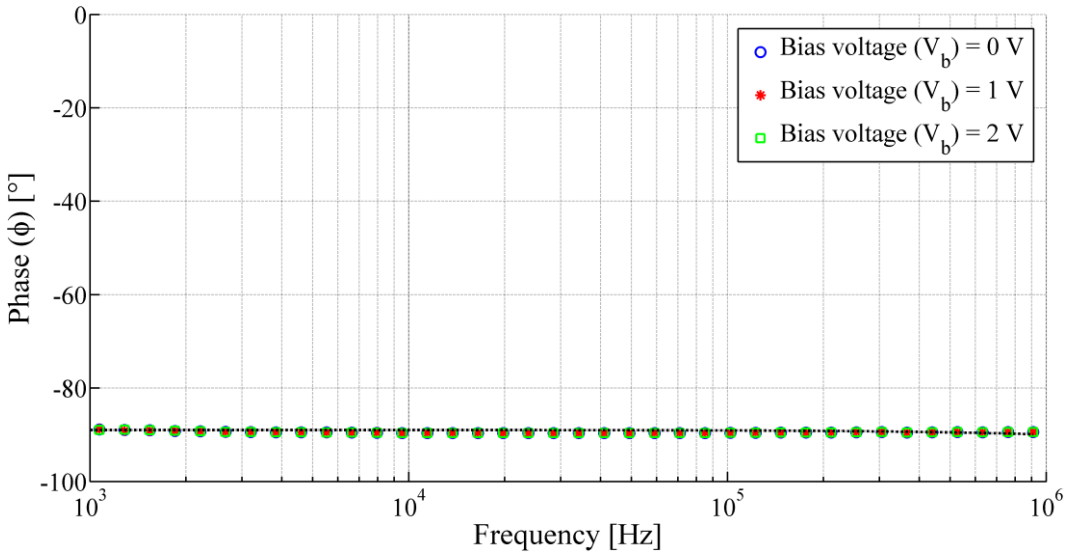

Figure 4.31: *Frequency response of the phase of the capacitive acoustic transducer with the membrane radius of 8.1 mm, backplate radius of 871 µm and air gap of 67.7 µm.*

In addition, Figure 4.30 exhibits the impedance behavior of the printed transducer with respect to frequency. It has been observed that the impedance |Z| decreases inversely with the frequency. This behavior is in agreement with the behavior of an ideal capacitor. Indeed the impedance Z of an ideal capacitor can be expressed as follows:

$$Z = \frac{1}{j\omega C} \quad \ldots\ldots\ldots (4.4)$$

where ω is the angular frequency and C represents the electrostatic capacitance of the capacitor.

Moreover, the voltage has a phase shift (ϕ) of around -90° with some fluctuations, as observed from the Figure 4.31, which shows that the current and voltage of the transducer are not in phase with respect to each other. This is also in agreement with that of an ideal capacitor. Therefore based on the experiment, the fabricated printed acoustic transducer is acting as capacitor.

During this work, 3D printed spacers having the thicknesses of few tens to hundreds of microns have been used to create the air gap of the capacitive acoustic transducer. Because of the low thickness, the 3D printed spacer is relatively soft, and thus compressed under applied pressure. As the screw system is used to assemble the final device, it has been observed that the achieved air gap is much smaller than the spacer height. For the maximum tightening of the screws during the transducers assembly, the achieved air gap of the device is measured by measuring the capacitance (C_0) of the system at 1 kHz for bias voltage of 0 V and then calculating the air gap (h_g) using following expression as showed by equation 4.5,

$$h_g = \frac{\varepsilon_0 \varepsilon_r S_e}{C_0} = \frac{\varepsilon_0 \varepsilon_r \pi R_e^2}{C_0} \ldots\ldots\ldots (4.5)$$

where ε_0 represents the vacuum dielectric constant ($\varepsilon_0 = 8.854 \times 10^{-12} F \cdot m^{-1}$), ε_r is the relative static permittivity of the material between the electrodes (for vacuum, $\varepsilon_r = 1$), and S_e and R_e represent the effective area and effective radius respectively.

However, in reality often the edge correction of a parallel plate capacitor structure is required [28]. As in an acoustic sensor, the membrane is backed by the small backplate electrode, considering the edge correction, the equation for air gap can be expressed as follows,

$$h_g = \frac{\varepsilon_0 \varepsilon_r \pi (R_e + E_{eff} h_g)^2}{C_0} \ldots\ldots\ldots (4.6)$$

where E_{eff} represents the empirical edge effect factor, which is equal to 0.52 [29]. The relative relation between the spacer height and the air gap is illustrated in Figure 4.32.

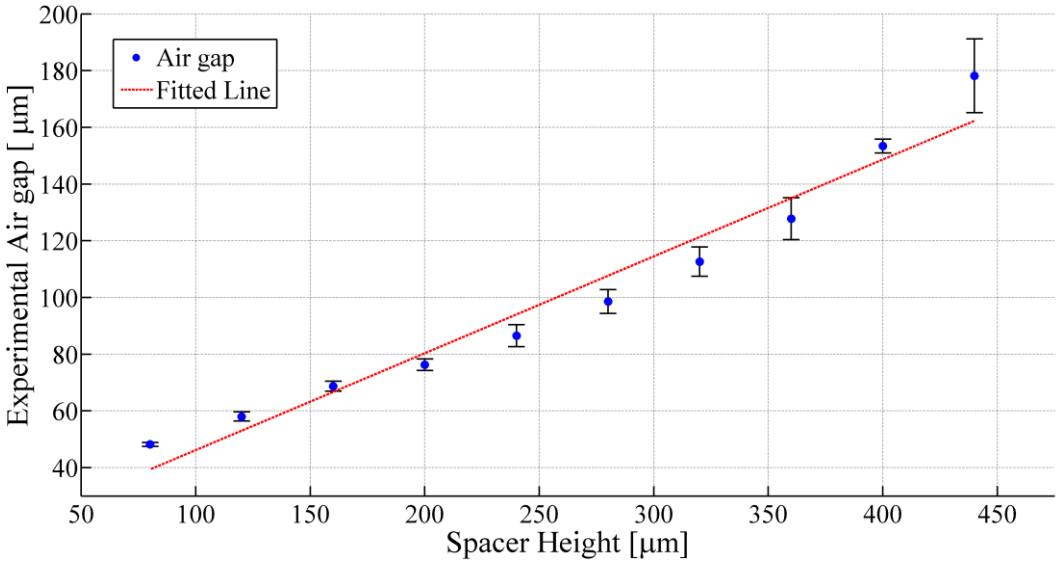

Figure 4.32: *Relation between 3D printed spacer height and the achieved air gap of the transducer for a device having the following parameters: membrane radius of 8.1 mm, backplate radius of 871 µm, cavity height of 4000 µm, and membrane thickness of 8 µm (considering the edge effect).*

4.5.2. Dynamic measurement using laser Doppler vibrometer

Dynamic characterization of the membrane alone and of the printed capacitive acoustic transducers have been performed using non-contact lase Doppler vibrometer (LDV) (Model: Polytec PSV-400 Scanning laser Vibrometer (Waldbronne, Germany)) to understand their behavior under acoustic pressure harmonic excitation between 20 to 20 kHz. During this work, acoustic pressure excitation has been generated by loudspeaker (B&C-DE-700-8, Italy) and corresponding response recorded using LDV in single-point mode and scanning mode. Figures 4.33 and 4.34 show the experimental setup of the measurement using LDV. In the case of single-point measurement mode, the laser spot is fixed at the center position of the membrane (to acquire the response spectrum); whereas during scanning measurement mode, the laser spot scans through the defined points (Figure 4.34(c)) on the surface of the membrane of the acoustic transducer (to acquire the surface deflection modes). Finally, the experimental observation of the transducer's response is compared to the numerical result performed using COMSOL Multiphysics software.

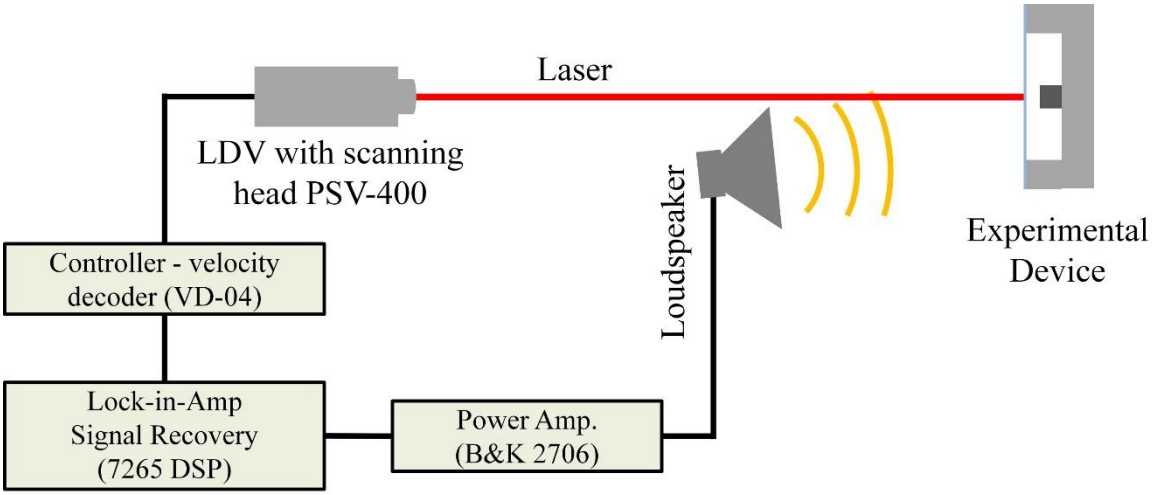

Figure 4.33: *Schematic diagram of the experimental setup for the LDV measurement.*

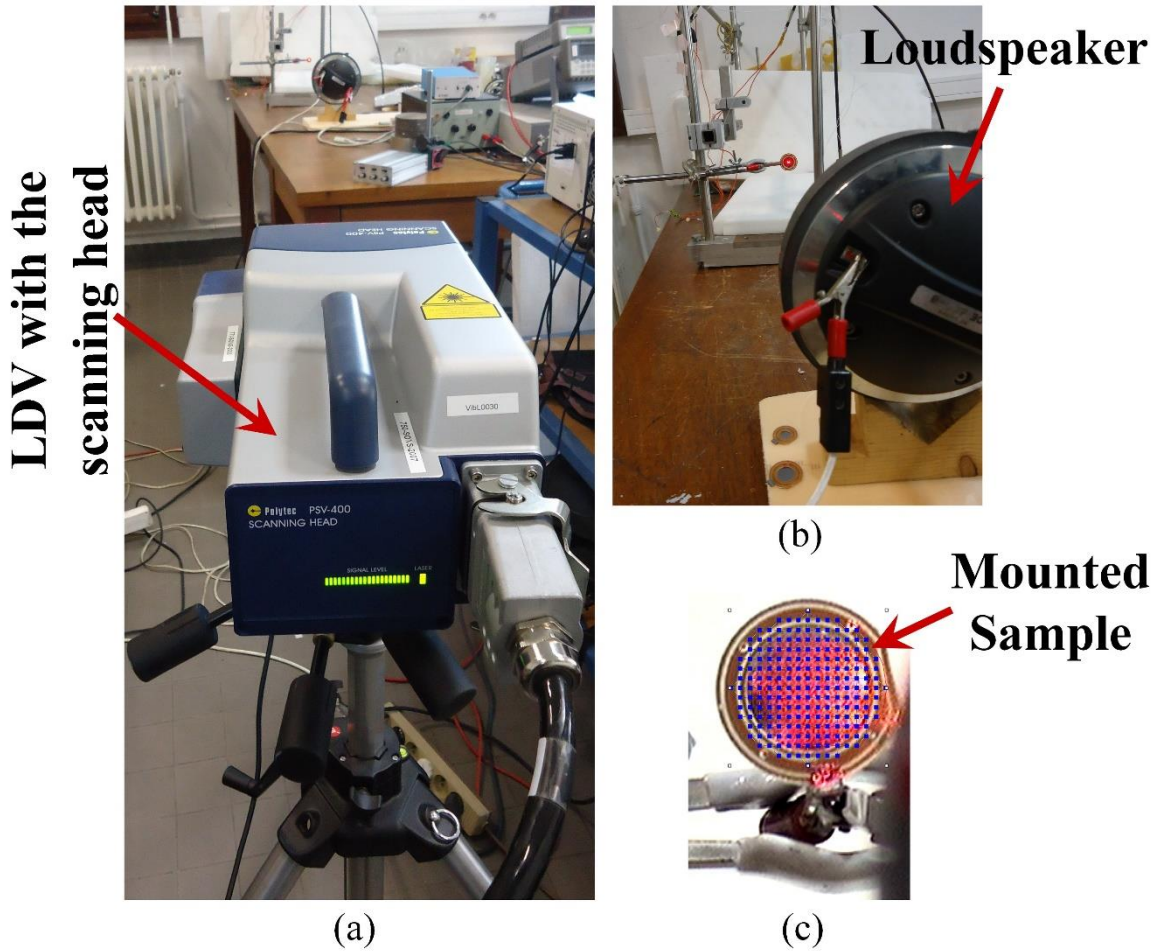

Figure 4.34: *Setup for the dynamic response measurement of the membrane and transducer using LDV (a) full setup, (b) close view, and (c) selection of points during scanning mode LDV measurement.*

4.5.2.1. Characterization of the membrane

As the behavior of the capacitive acoustic resonator depends on its membrane structure, therefore initially the membrane itself is solely characterized using single-point mode and then scanning mode. Figure 4.35 illustrates the frequency response of the membrane having membrane radius of 10 mm and membrane thickness of 8 µm fixed at its periphery. The shapes of some of the observed modes of the vibrating membrane are presented in Figure 4.36.

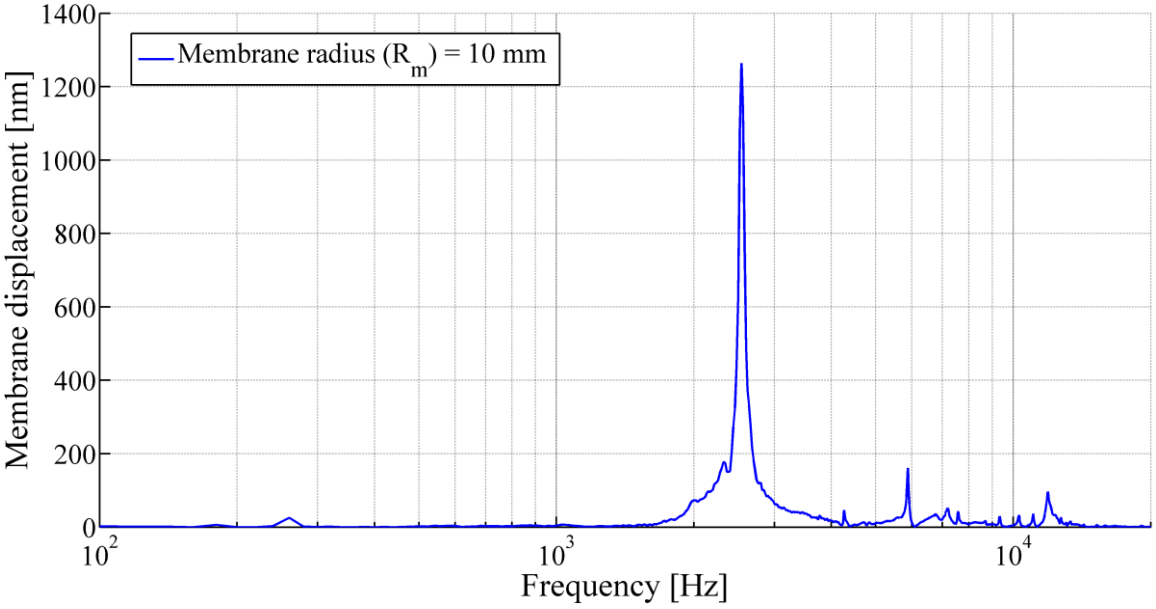

Figure 4.35: *Frequency response of the circular membrane with membrane radius of 10 mm and membrane thickness of 8 µm under acoustic pressure (using LDV in single-point mode).*

The tension (T_m) of the membrane can be calculated from the resonant frequencies (f_{ij}) based on the equation 4.6 [30], [31]. During this work, the membrane tension is calculated from the first vibrational mode.

$$T_m = t_m \rho_m \left(\frac{2\pi f_{ij} R_m}{k_{ij}} \right)^2 \quad \ldots\ldots\ldots (4.7)$$

Here. k_{ij} represent the constants for different modes of vibration of the circular membrane, and integers (i, j) represent the mode shape, R_m, t_m and ρ_m represent the membrane radius, thickness and density respectively. For the first resonant frequency (f_{10}) (Figure 4.36(a))

the value of k_{10} is 2.4048. The calculated membrane tension along with the maximum membrane displacement observed using LDV is tabulated in Table 4.9.

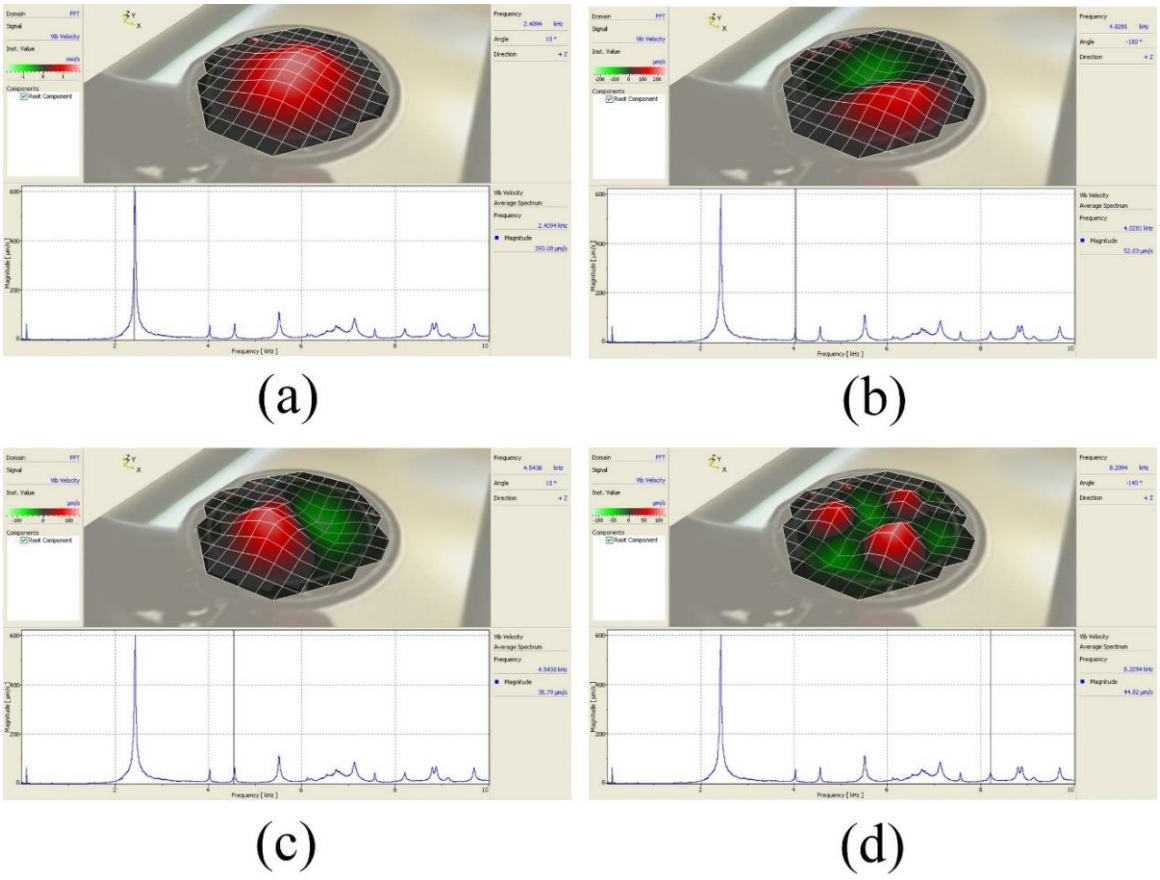

Figure 4.36: *Different modes of vibrating circular membrane with a membrane radius of 10 mm and a membrane thickness of 8 µm (using LDV in scanning mode).*

Table 4.9: Measured membrane displacement and calculated membrane tension of different membrane sizes (having membrane thickness (t_m) = 8 µm and density (ρ_m) = 1390 kg/m^3)

Membrane radius (R_m) mm	**First resonant frequency (f_{10})** Hz	**Maximum membrane displacement at 1st resonant frequency ($\langle\xi\rangle$)** nm	**Calculated membrane tension (T_m)** N/m
4	7980	249	77.34
6	4780	376.2	62.4
8	3840	727.2	71.6
10	2540	1264	49

It has been observed that, with the increasing membrane radius, the resonance moves towards the lower frequencies, while the membrane displacement increases. The scanning

mode allows to identify the defects of the membrane. Figure 4.37 shows the defects at the boundary of the membrane, which may occur due to gluing problem of the pre-tension film with the membrane frame. The defects cause the non-linear membrane tension and thus disturb the membrane vibration.

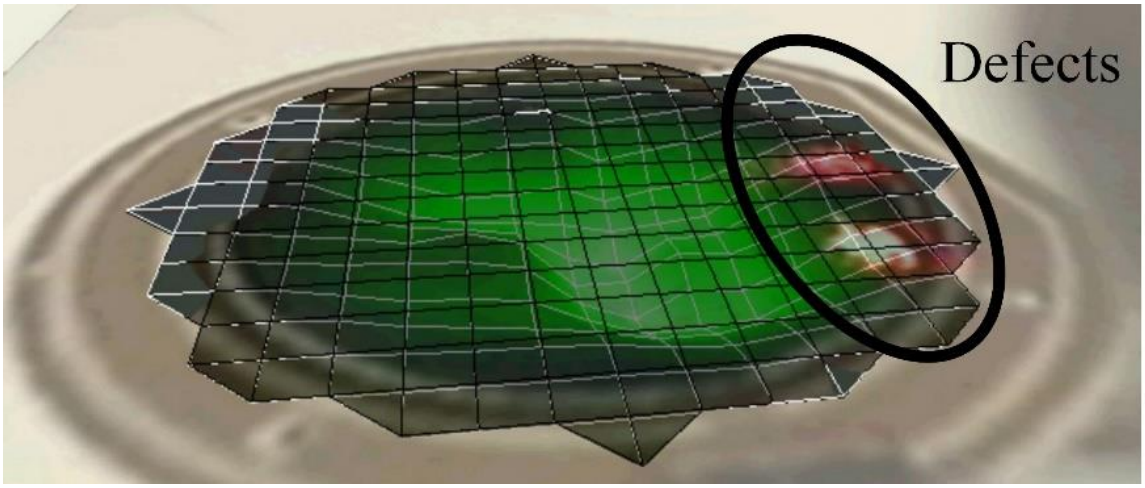

Figure 4.37: *Observation of the defects on the fabricated printed membrane using pre-tension Mylar thin film using LDV in scanning mode.*

4.5.2.2. Characterization of the transducer

The capacitive acoustic transducers have also been characterized by LDV in single-point mode and scanning mode. It has been observed that the printed capacitive transducer exhibits strong sensitivity at its first resonant frequency. Experimental results are compared with the numerical simulations. Figures 4.38 and 4.39 present the frequency response of transducers having different device specifications under acoustic pressure.

According to Figures 4.38 and 4.39, the experimental and the numerical measurements show good correlation between them. However, experimental results exhibit slightly different membrane displacement compared to simulated results. In addition, experimental measurements present some additional peaks or noise that could occur because of defects or non-linearity in the system. The defects might be generated during the assembly process due to the different tightness of the screws, which might lead to the non-linearity in membrane tension and also deforms the membrane. The maximum membrane displacement and Q-factor of the resonators with different specifications are listed in Table 4.10. In most cases, the simulated Q-factor of the transducers is higher than that of the

experimental Q-factor, and occasionally slight shift of resonant frequency is observed as well.

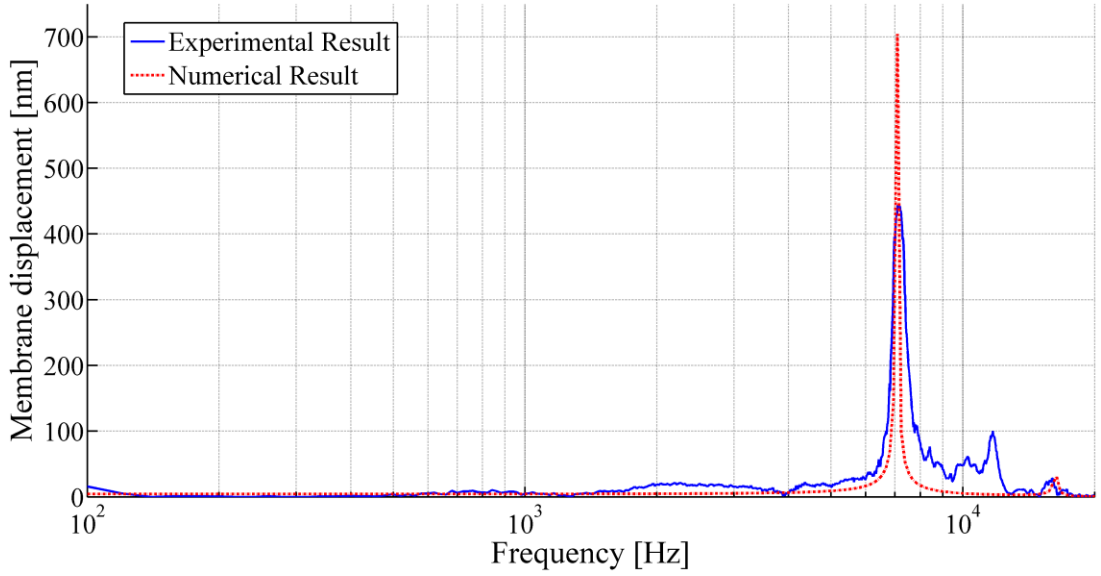

Figure 4.38: *Frequency response of the printed acoustic transducer having membrane radius of 4 mm, backplate radius of 1 mm, cavity height of 2800 µm, air gap of 50 µm, membrane thickness of 23 µm and membrane tension of 102 N/m.*

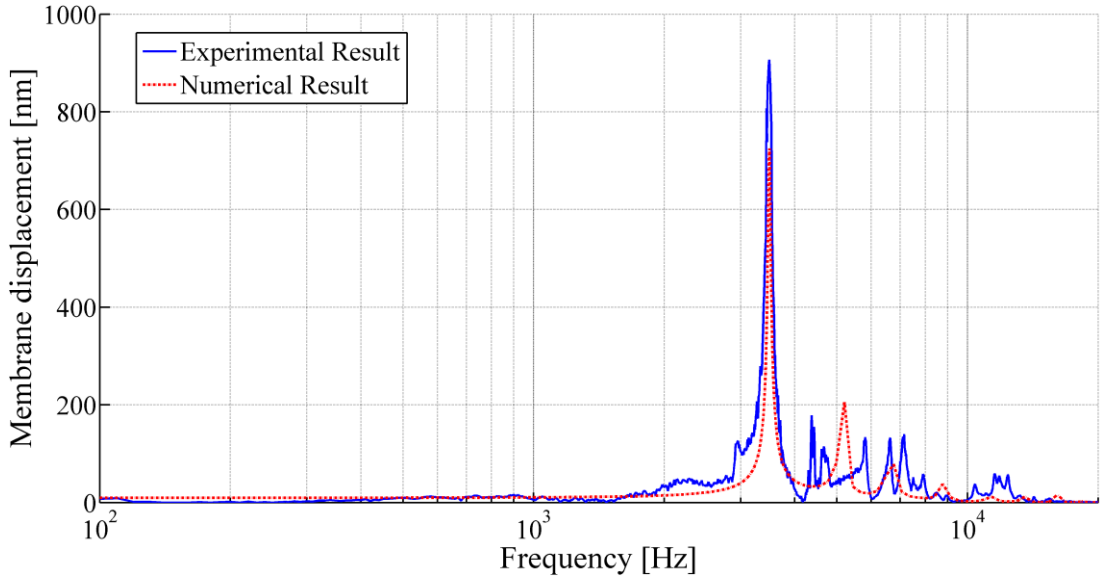

Figure 4.39: *Frequency response of the printed acoustic transducer having membrane radius of 8.1 mm, backplate radius of 871 µm, cavity height of 3990 µm, air gap of 67.7 µm, membrane thickness of 23 µm and membrane tension of 48 N/m.*

Table 4.10: Experimental results for the acoustic resonators

Device parameters						Numerical Results		Experimental Results	
R_m mm	R_b mm	h_c mm	h_g µm	T_m N/m	t_m µm	f_{10} Hz	Q_f	f_{10} Hz	Q_f
4	0.25	3000	12.5	60	8	10162.5	21.2	10310	11
4	0.75	3200	18	30	8	10327.6	8.5	10300	11
4	1	2800	49.7	102	23	7185.2	19.4	7100	16.9
6	0.75	5230	65.8	235	23	6406.2	138.9	6380	33.5
8.1	0.87	3990	67.7	48	23	3489.2	61.6	3490	34
8.1	0.87	4000	66.1	110	23	4622.1	100.2	4660	33
10	0.50	3080	28	67	8	5240.5	28.2	5240	11.2
10	0.75	1050	32.7	110	8	5988.5	18.6	6110	23

The use of scanning mode LDV measurement confirms that the first response peak corresponds to the first resonance of the membrane (Figure 4.40). As the developed printed acoustic transducer, during this work, consists of a much smaller backplate electrode compared to the membrane size, considering the membrane deformation at the center as uniform movement over the whole backplate electrode, the relative capacitance variation (ΔC) can also be calculated using following expression as presented in equation 4.8.

$$\Delta C = C_i \frac{\left|\langle \xi \rangle_{Se}\right|}{h_g} \quad \ldots\ldots\ldots (4.8)$$

where C_i represents the static capacitance, h_g represents the air gap of the acoustic transducer and $|\langle \xi \rangle_{Se}|$ represents the membrane displacement under acoustic pressure.

As an example, for the printed acoustic transducer with a membrane radius of 8.1 mm, backplate radius of 871 µm, cavity height of 3990 µm, air gap of 67.7 µm, membrane thickness of 23 µm and membrane tension of 48 N/m, having a static capacitance of 0.76 pF, an approximate capacitance variation of 4.2 fF and Q-factor of 34 at its resonant frequency of 3490 Hz have been computed. The calculated values exhibited close proximity with the numerical results. Figure 4.41 presents the calculated capacitance variation based on the membrane displacement of the backplate electrode. Therefore, the printed acoustic transducers performed as capacitive acoustic resonator that exhibits adequate sensitivity and selectivity.

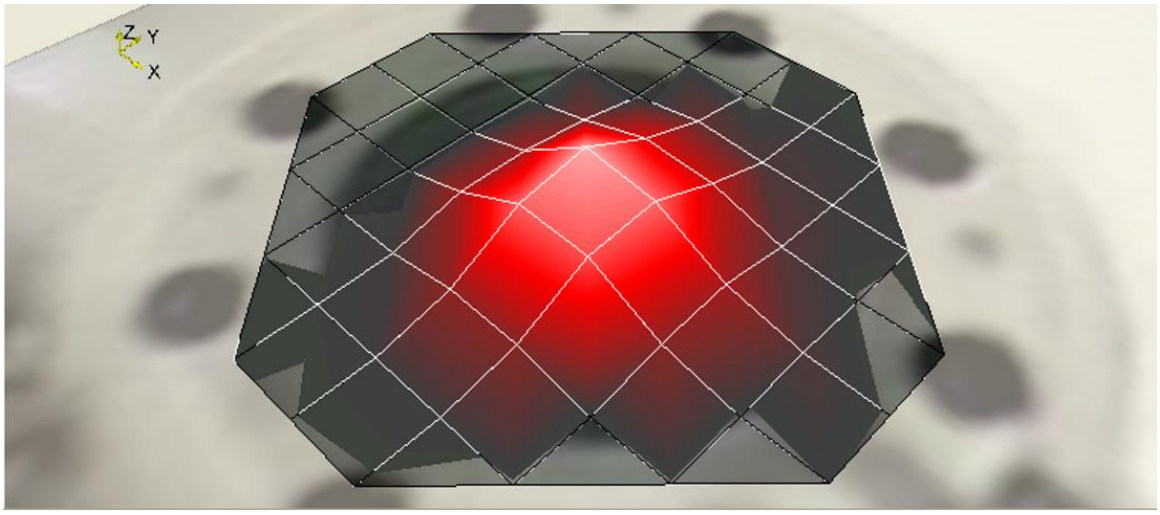

Figure 4.40: *Modal shape of the membrane of the capacitive acoustic resonator, with membrane radius of 8.1 mm, backplate radius of 871 µm, cavity height of 3990 µm, air gap of 67.7 µm, membrane thickness of 23 µm and membrane tension of 48 N/m under acoustic pressure, at the resonance.*

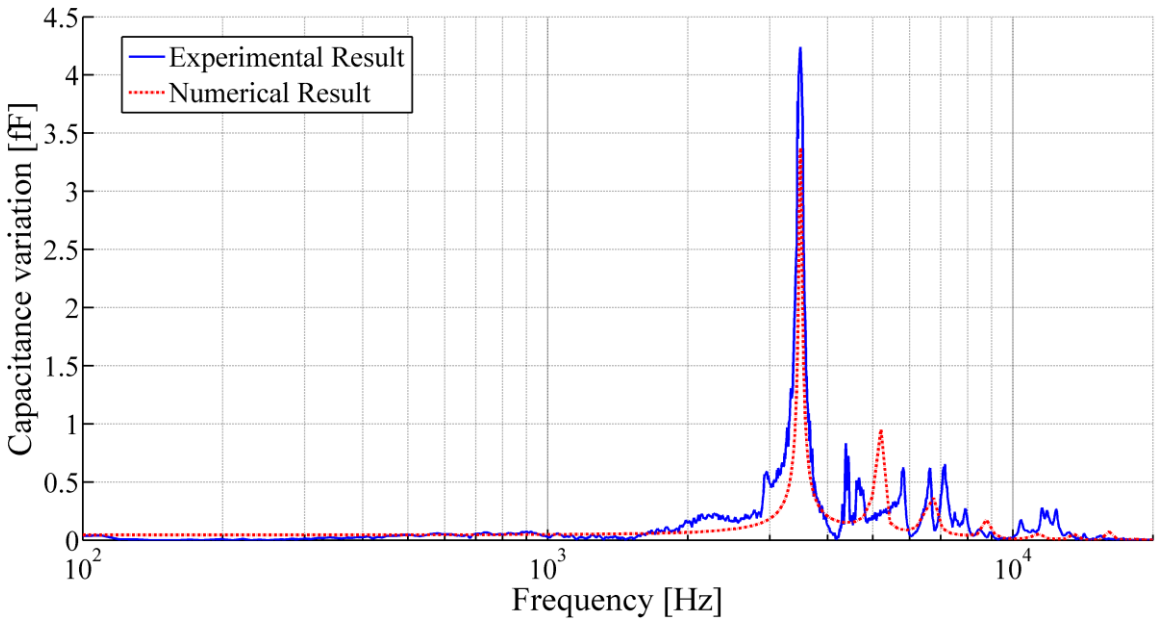

Figure 4.41: *Capacitance variation with respect to the frequency of the printed acoustic transducer with the membrane radius of 8.1 mm, backplate radius of 871 µm, cavity height of 3990 µm, air gap of 67.7 µm, membrane thickness of 23 µm and membrane tension of 48 N/m.*

4.6. Summary

New approach to fabricate capacitive acoustic transducer has been described, where 3D printing and direct write 2D inkjet printing techniques are combined. Polyjet 3D printed materials have low heat deflection temperature. Therefore, photonic sintering technique is used, since it allows the sintering of printed silver nanoparticles on 3D printed substrate without damaging it. The membrane is fabricated using thin organic polymer film having thickness below 25 µm. Experiment has revealed that printing on the thin film has to be performed on pre-tensed film to fabricate the conductive membrane, because in case of applying tension after printing and sintering, the conductivity of the silver layer was deteriorated due to the formation of cracks.

Static capacitance measurement exhibits that the fabricated printed transducer works as a capacitor, and the dynamic measurement using LDV shows that the printed capacitive acoustic transducer has been performing as acoustic resonator that exhibits adequate sensitivity and selectivity at its first resonant frequency with quality factor that was in agreement with the device requirement. The experimental results exhibit good correlation with the numerical simulations. Although in most occasion the experimental Q-factor value is lower than that of the simulated one.

However, there are still some problems related to the fabrication steps. The use of screws to assemble the transducer sometimes causes unexpected non-linearity in membrane tension and also deforms the membrane due to different tightness. In addition, lack of appropriate adhesive to fix the pre-tensioned Mylar film on the membrane frame, leads to problem related to the durability of the membrane tension over time.

References

[1] Alexey Podkovskiy, Petr Honzík, Stéphane Durand, Nicolas Joly, and Michel Bruneau, "Miniaturized Electrostatic Receiver with Small-Sized Backing Electrode," in *Proceedings of Meetings on Acoustics*, Montreal, Canada, 2013, vol. 19, p. 030047.

[2] Petr Honzík, Alexey Podkovskiy, Stéphane Durand, Nicolas Joly, and Michel Bruneau, "Analytical and Numerical Modeling of an Axisymmetrical Electrostatic Transducer with Interior Geometrical Discontinuity," *Journal of the Acoustical Society of America*, vol. 134, no. 5, pp. 3573–3579, 2013.

[3] Petr Honzík, Alexey Podkovskiy, Stéphane Durand, and Nicolas Joly, "Experimental Investigation on the Electrostatic Receiver with Small-Sized Backing Electrode," in *Forum Acusticum*, Krakow, Czech Republic, 2014, vol. 7.

[4] Sawyer B. Fuller, Eric J. Wilhelm, and Joseph M. Jacobson, "Ink-Jet Printed Nanoparticle Microelectromechanical Systems," *Journal of Microelectromechanical Systems*, vol. 11, no. 1, pp. 54–60, 2002.

[5] Robert Horning, Thomas Ohnstein, and Daniel Youngner, "Method for Making Devices using Ink Jet Printing," US7112463 B2, Sep-2006.

[6] Daniel Harris Brean, "Asserting Patents to Combat Infringement via 3D Printing: It's No'Use'," *Fordham Intellectual Property, Media & Entertainment Law Journal*, vol. 23, no. 3, 2013.

[7] Eliahu M. Kritchman and Hanan Gothait, "Apparatus and Method for Three Dimensional Printing," US20050104241A1, 19-May-2005.

[8] Stratasys, "Polyjet Materials," 2015. [Online]. Available: http://www.stratasys.com/materials/polyjet. [Accessed: 29-Apr-2015].

[9] Stratasys, "Dental Materials: Advance Materials for Superior Digital Dentistry and Orthodontics." Stratasys, 2014.

[10] Jolke Perelaer, "Postprinting Processes for Inorganic Ink for Plastic Electronics Applications," in *Inkjet-Based Micromanufacturing*, Jan G. Korvink, Patrick J. Smith, and Dong-Youn Shin, Eds. Weinheim, Germany: WILEY-VCH Verlag GmbH & Co. KGaA, 2012, pp. 111–125.

[11] David Wallace, Donald Hayes, Ting Chen, Virang Shah, Delia Radulescu, Patrick Cooley, Kurt Wachtler, and Arunkumar Nallani, "Ink-Jet as a MEMS Manufacturing Tool," in *First International Conference on Integration and Commercialization of Micro and Nanosystems*, Sanya, Hainan, China, 2007, pp. 1161–1168.

[12] Byung Ju Kang, Chang Kyu Lee, and Je Hoon Oh, "All-Inkjet-Printed Electrical Components and Circuit Fabrication on a Plastic Substrate," *Microelectronic Engineering*, vol. 97, pp. 251–254, Sep. 2012.

[13] Daniel K. Owens and R. C. Wendt, "Estimation of the Surface Free Energy of Polymers," *Journal of Applied Polymer Science*, vol. 13, no. 8, pp. 1741–1747, 1969.

[14] D. H. Kaelble, "Dispersion-Polar Surface Tension Properties of Organic Solids," *The Journal of Adhesion*, vol. 2, no. 2, pp. 66–81, Apr. 1970.

[15] Dimitri Janssen, Randy De Palma, Stijn Verlaak, Paul Heremans, and Wim Dehaen, "Static Solvent Contact Angle Measurements, Surface Free Energy and Wettability Determination of Various Self-Assembled Monolayers on Silicon Dioxide," *Thin Solid Films*, vol. 515, no. 4, pp. 1433–1438, 2006.

[16] Advanced Nano Products (ANP) Co. LTD, "Silver Jet Ink." [Online]. Available: http://anapro.com/eng/product/silver_inkjet_ink.html. [Accessed: 13-Apr-2015].

[17] Stan Farnsworth and Kurt Schroder, "Photonic Curing for Millisecond-Drying of Thin Films," *Specialist Printing Worldwide*, no. 4, pp. 34–36, 2012.

[18] K. A. Schroder, "Mechanisms of Photonic Curing™: Processing High Temperature Films on Low Temperature Substrates," in *Nanotech*, vol. 2, CRC Press, 2011, pp. 220–223.

[19] K. A. Schroder, S. C. McCool, and W. F. Furlan, "Broadcast Photonic Curing of Metallic Nanoparticle Films," *NSTI-Nanotech*, vol. 3, pp. 1–4, 2006.

[20] National Institutes of Health, "ImageJ," *ImageJ*. [Online]. Available: http://imagej.nih.gov/ij/. [Accessed: 14-May-2015].

[21] David Nečas and Petr Klapetek, "Gwyddion," *Gwyddion*. [Online]. Available: http://gwyddion.net/. [Accessed: 14-May-2015].

[22] Luca Lutterotti, "Introduction to Diffraction and the Rietveld Method," University of Trento, Italy.

[23] L. B. McCurker, R. B. Von Dreele, D. E. Cox, D. Louër, and P. Scardi, "Rietveld Refinement Guidelines," *Journal of Applied Crystallograph*, vol. 32, pp. 36–50, 1999.

[24] Luca Lutterotti, "Maud - Materials Analysis Using Diffraction," 1997. [Online]. Available: http://www.ing.unitn.it/~maud/index.html. [Accessed: 01-May-2015].

[25] L. Lutterotti, S. Matthies, and H. R. Wenk, "MAUD (Material Analysis Using Diffraction): A User Friendly Java Program for Rietveld Texture Analysis and More," in *Proceeding of the Twelfth International Conference on Textures of Materials (ICOTOM 12)*, Montréal, Canada, 1999, vol. 1, p. 1599.

[26] Pornanong Pongpaibool, "A Study of Cost-Effective Conductive Ink for Inkjet-Printed RFID Application," in *Proceedings of International Symposium on Antennas and Propagation (ISAP)*, Nagoya, Japan, 2012, pp. 1248–1251.

[27] Murata Manufacturing Co., LTD., "What are impedance/ ESR frequency characteristics in capacitors?," *muRata: Innovator in Electronics*, 14-Feb-2013. [Online]. Available: http://www.murata.com/en-us/products/emiconfun/capacitor/2013/02/14/en-20130214-p1. [Accessed: 23-Jun-2015].

[28] Arnold H. Scott and Harvey L. Curtis, "Edge Correction in the Determination of Dielectric Constant," *Journal of Research of the National Bureau of Standards*, vol. 22, pp. 747–775, 1939.

[29] COMSOL, "Axisymmetric Condenser Microphone with Electrical Lumping." COMSOL, 2012.

[30] Allan F. Bower, *Applied Mechanics of Solids*. New York: CRC Press, 2010.

[31] Philip M. Morse and K. Uno Ingard, *Theoretical Acoustics*. Princeton, New Jersey: Princeton University Press, 1986.

CHAPTER 5

INK FORMULATION AND INKJET PRINTING OF PVDF-TRFE

In this chapter, the formulation of polyvinylidene fluoride – trifluoroethylene (PVDF-TrFE) ink for drop-on-demand (DoD) inkjet printing system is discussed. The inkjet-printed PVDF-TrFE films were then developed and characterized to investigate their morphology, crystallinity and piezoelectric properties. Vapor pressure and viscosity of the solvent strongly influence the quality of the printed layer. Modified waveform and very low jetting frequency have been used to accommodate the relaxation time of the polymeric ink during jetting. Crystallographic studies confirm the presence of β-phase, which exhibits the largest spontaneous polarization per unit cell.

5.1. Background

With the rapid development of technologies, electroactive polymers (EAPs) are gaining growing amount of interest as intelligent/smart materials [1]. There are different EAPs, namely, Nylon-11 [2], polylactide and aniline pentamer copolymer [3], poly(lactic-co-glycolic acid) (PLGA) [4], and poly(vinylidene fluoride) (PVDF) and its copolymers [5]–[10]. Amongst them PVDF and its copolymers exhibit the best electroactive properties, like piezo-, pyro- and ferro-electricity. As a result, they are the polymer of choice for the increasing number of possible microelectronics applications, like sensors, actuators, energy harvestors, memories, biomimetic robotics [11]–[16] etc.

The properties of piezoelectric polymers are different from that of inorganic materials. Studies show that in comparison to inorganic ceramics, polymers exhibit much higher piezoelectric stress constant (g_{31}), which relates to the production of electric field by a mechanical stress. For example, piezoelectric stress constant of poly(vinylidene) fluoride is 240 mV-m/N to compare with 11 mV-m/N of Lead Zirconium Titanate (PZT) [17]. Therefore, for sensor applications, polymers are more preferable. In the case of polymers, piezoelectricity depends on the presence of permanent molecular dipoles, on the orientation or alignment ability and stability of the molecular dipoles and on the ability of the material to undergo large strains when mechanically stressed [18]. Moreover, polymers are light weight and more suitable for flexible electronics applications.

Generally, solution processes, such as spin-coating and dip-coating are used to deposit these polymers to fabricate devices [9], [10], [19], [20]. Although, spin-coating and dip-coating are simple and well-established techniques, deposition of material on desired positions requires the use of photolithographic technique. Photolithography, which

involves masking, deposition and cleaning processes, exhibits higher production cost, longer process time, and causes lots of material waste. Thus, quest for new fabrication techniques to deposit material on desired locations without mask at lower cost with reduction of material losses, leads toward the emerging direct write inkjet printing techniques.

In recent years, with the growing research interest into the manufacturing of plastic electronic devices, whose main benefits are their flexibility, low cost, light weight and ease of processability, inkjet printing of polymer has received a lot of attention [21]. However, unlike well dispersed nanoparticles based inks, polymer solutions exhibit non Newtonian rheological properties [22], which create the complexity to dispense these kinds of media through an orifice [23]–[25]. When subjected to a shear flow, polymer solutions generally exhibit a shear-thinning behavior with a Newtonian plate at low and very high shear rates [26], [27], and the boundaries between these behaviors can greatly vary from one medium to another [28].

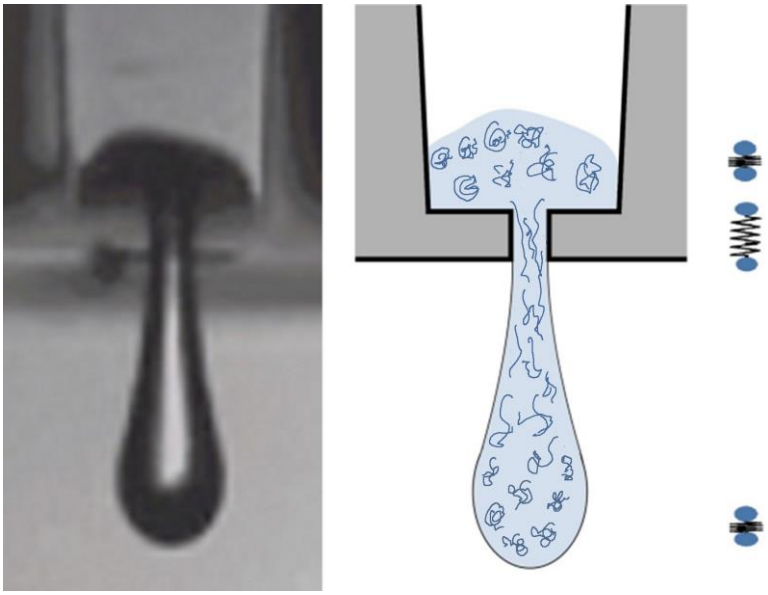

Figure 5.1: *Behavior of polymer fluid during inkjet printing.*

In the case of inkjet printing, droplets are ejected through nozzles with diameters of a few tens of micrometers at velocities typically higher than 10 $m.s^{-1}$ [29], [30]. As a result, polymer solutions undergo a high elongational deformation [31], which causes stretching and orientation of polymer macromolecules to a greater extent (Figure 5.1) than ordinary shear flow [32]. High molecular weight polymer solutions are known to develop a strong

resistance to elongational deformation that results in an increase of elongational viscosity [33], [34], which is overcome by farther decreasing of the shear viscosity induced by shear-thinning behavior in the case of rapid elongational flows [35]. This high resistance to extensional flow occurs when the macromolecular chains undergo a transition from an initial coiled state to a stretched state which results in the development of a marked restoring force. This force is essentially of an entropic nature: an imposed elongation reduces the number of possible configurations and therefore the entropy [22].

The effect of viscoelasticity of non-Newtonian fluids can be incorporated using a dimensionless group, called the Weissenberg number (W_i), which is expressed as follows [36],

$$W_i = \frac{v\tau}{D} = \varepsilon \cdot \tau \quad \ldots\ldots\ldots (5.1)$$

Here τ is the characteristic relaxation time of the fluid, 'v' is the velocity, 'D' is a characteristic length, which is equal to the jet or drop diameter, and ε represents the strain rate. Coil-stretch transitions are observed if the strain rate is higher than a critical value (ε_{crit}) at which the rate of deformation of the macromolecular chain exceeds its rate of relaxation [37]. In this case, the Weissenberg number is greater than 0.5 as described in the equation 5.2,

$$W_i = \varepsilon_{crit} \cdot \tau_1 > 0.5 \quad \ldots\ldots\ldots (5.2)$$

where τ_1 represents the longest relaxation time of macromolecular chains [31], [38].

Taking into account that strain rates typically encountered in inkjet processes are greater than $5 \times 10^4\ s^{-1}$, the above described critical value is exceeded at the pinch region where the ligament is attached to the nozzle tip meniscus for all polymers having M_w higher than $5 \times 10^4\ g.mol^{-1}$ [31], [39]. Thus, inks formulated with PVDF-TrFE copolymer ($M_w = 5 \times 10^5\ g.mol^{-1}$) will exhibit a complex rheological behavior regardless of the ejection parameters used.

The development of the restoring force causes by the macromolecular stretching can prevent the ink from detaching from the nozzles, which might cause the discontinuous ink flow as encountered in inkjet processes. The droplets that flow out of the nozzles and still

attached with a ligament, generally decelerate, stop and then eventually move towards the reverse direction through the nozzles to the printhead chamber [40]. This phenomenon can be avoided by increasing droplet velocity when the ligament is at its maximum extensibility and about to break. According to Xu *et al.* [39], an increase of droplet speed at rupture is observed when higher jetting voltage is applied.

The objectives of this work are to formulate inkjet printable ink with high-molecular weight PVDF-TrFE, thereafter to inkjet print PVDF-TrFE film and finally to characterize the printed layer to understand the morphology, crystallinity and piezoelectric properties.

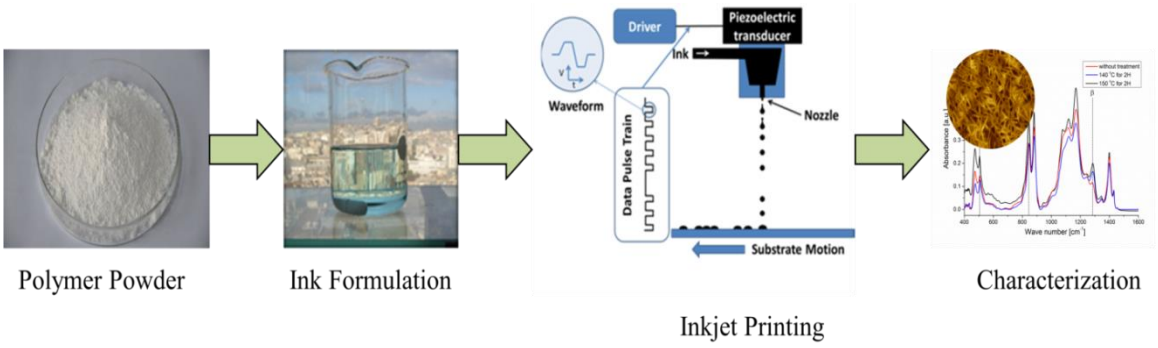

Figure 5.2: *Schematic diagram of the objective of this work.*

5.2. PVDF and its copolymers

Poly (vinylidene fluoride) (PVDF) is a high molecular-weight thermoplastic. It is a fluorocarbon, usually produced by free radical polymerization of $CH_2 = CF_2$ under high temperature (50 to 150 °C) and pressure (10 to 300 atm) where inorganic or organic peroxides are generally used as catalysts [5]. The chemical formula of PVDF is $-(CH_2-CF_2)_n-$, whose structure is essentially head to tail, i.e. $-CF_2-(CH_2-CF_2)_n-CH_2-$ [41]. The structure formula of PVDF is illustrated in Figure 5.3.

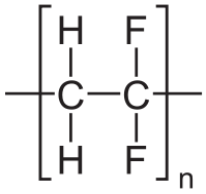

Figure 5.3: *Structure formula of PVDF [42].*

In addition, PVDF is a semicrystalline polymer consisting of more than one phase. Their mechanical properties depend both on the volume fraction of crystalline phases and on the orientation of the molecular chains. The upper limit of the working temperature depends on the melting temperature of the crystallite regions. Moreover, the piezoelectricity of PVDF depends on the amount of polar crystalline phase, for example β-phase PVDF [17]. Generally polymer crystals are very small and are arranged into spherically symmetric poly-crystalline aggregates, known as spherulite structure. During the polymer crystal's growth from melt, lamellae (the platelet-like crystals) grow from the center and are aligned in such a way that well defined crystalline and amorphous regions are created. These aggregates are called spherulites and have no net polarization. The amorphous regions that exhibit the properties of supercooled liquid may occupy more than half of the total volume. PVDF generally shows crystalline fraction of about 50% to 70% [42], [43].

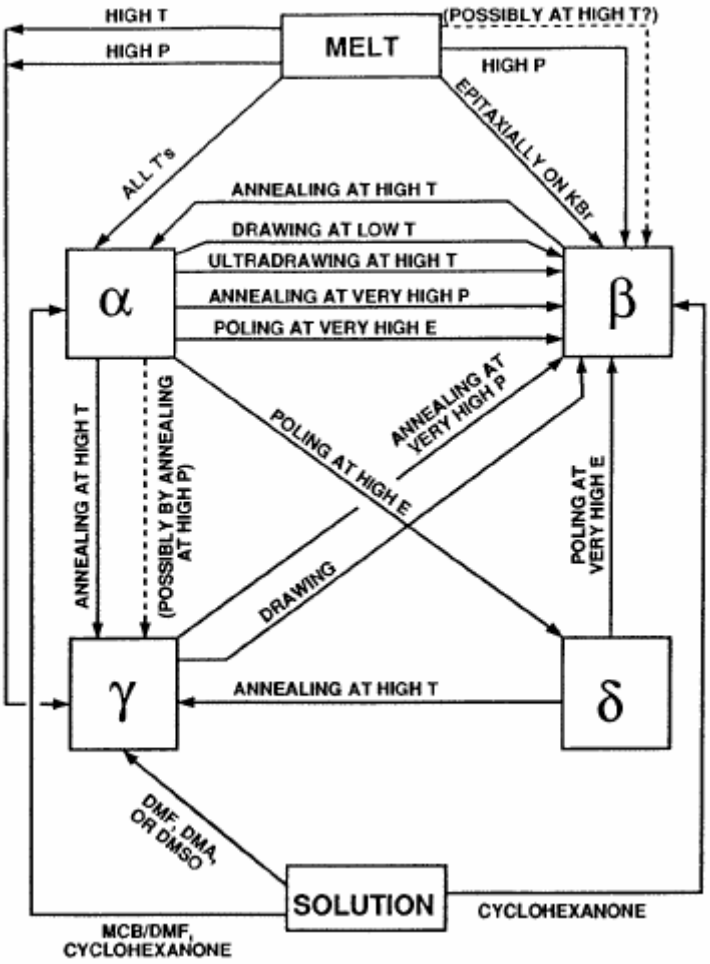

Figure 5.4: *Inter relation among the four well established phases of PVDF [44].*

Polyvinylidene fluoride (PVDF) shows polymorphism and exhibits at least four major crystalline phases, designated as α-, β-, γ- and δ-phase [5], [42]–[45]. Amongst them, three phases, namely, β, γ and δ are polars. The different crystal structures of PVDF are interchangeable and can be converted among the various phases by employing physicochemical techniques, as illustrated in Figure 5.4.

5.2.1. α-phase of PVDF

The conformation of α-phase consists of polymer backbone of alternative *trans* and *gauche* sequences or $TGT\bar{G}$, which is monoclinic and belongs to space group C_{2h} with lattice parameters a=4.96 Å, b=9.64 Å and c=4.62 Å. Generally, α-phase can be produced by crystallization of polymer from the melt at atmospheric pressure at all temperatures [5], [42]. There are two molecules per unit cell and they are aligned in the opposite directions, as presented in Figure 5.5. As a result, self-cancellation among them occurs, the net polar moment is zero and thus α-phase is not polar [46]. However, by poling, the non-polar α-phase can be transformed into polar α-phase [5], [42].

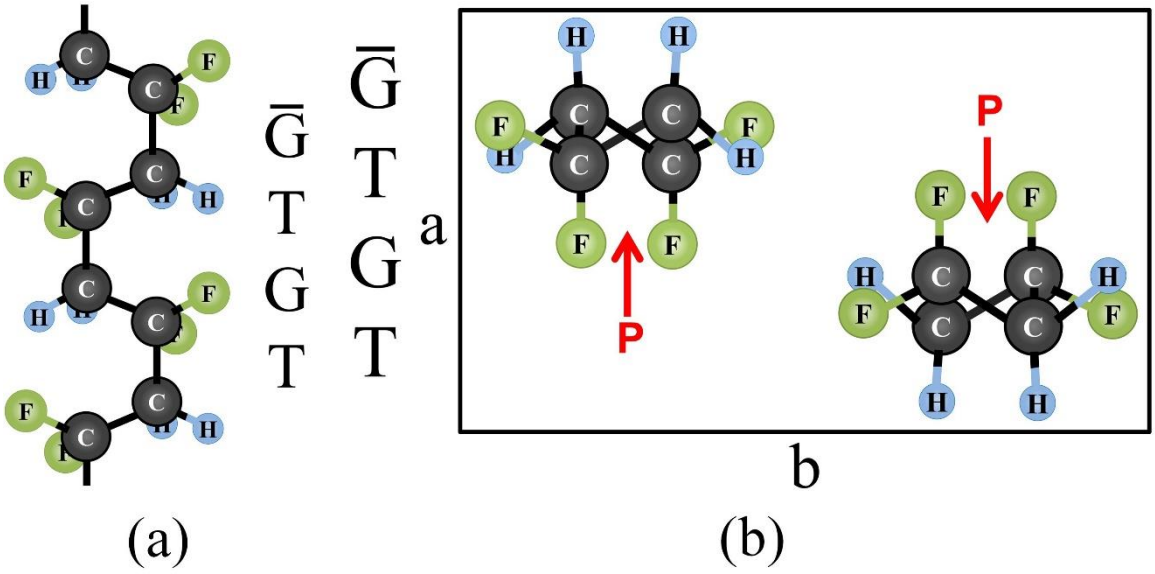

Figure 5.5: *Schematic diagram of (a) molecular structure and (b) crystalline structure of α-phase of PVDF (Adapted from [5]).*

5.2.2. β-phase of PVDF

The β-phase of PVDF is formed of two chains in an "all trans-planar zigzag" configuration that has an orthorhombic structure, and belongs to the space group C_{2v} with lattice constants

a=8.58 Å, b=4.91 Å and c=2.56 Å [43]. In β-phase chain backbone, the dipoles of monomer units are aligned in such a way that fluorine atoms are positioned on one-side of the unit cell. As a result, spontaneous polarization occurs, which give rise to a net dipole moment. This phase of PVDF exhibits piezoelectric as well as pyro- and ferro-electric properties [5], [47]. Figures 5.6(a) and Figure 5.6(b) show the molecular structure and the crystalline structure of β-phase, respectively.

The β-phase is prepared most typically by stretching the unoriented α-phase, which is obtained by cooling the melt at room temperature at a normal cooling rate (10-20 °C) [5]. Moreover, β-phase of PVDF can be casted from the hexamethylphosphoric triamide and can also be yield by stretching γ-phase at high temperature (285°C) and high pressure (400 atm) [48].

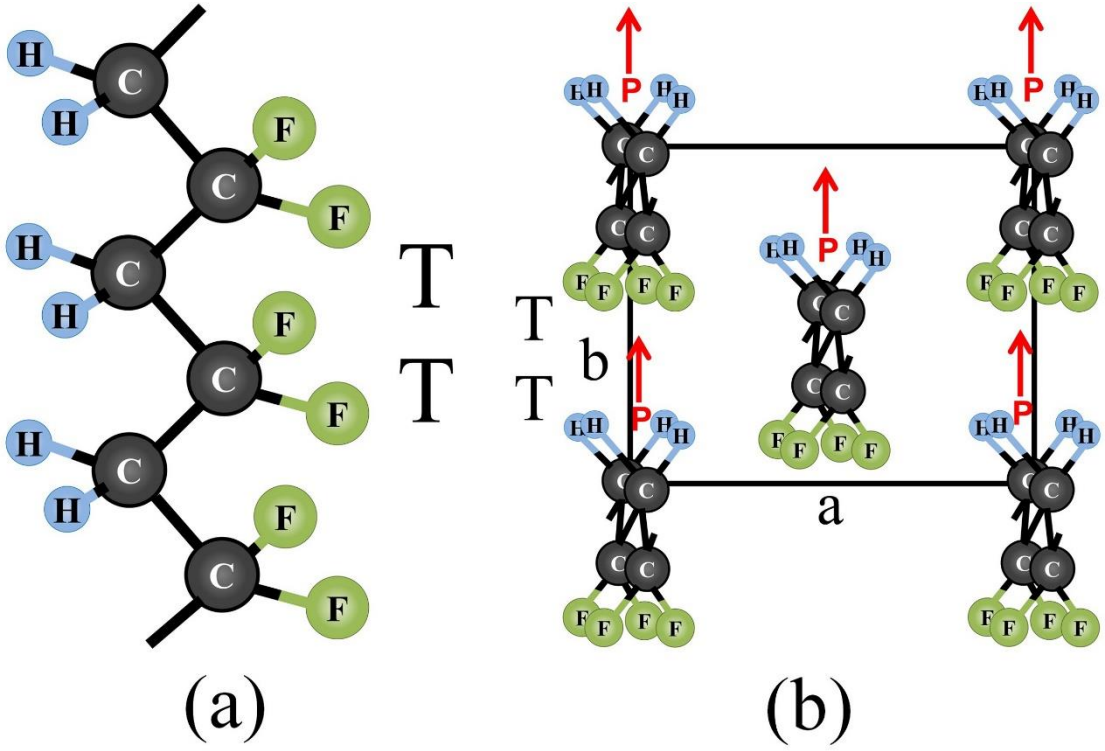

Figure 5.6: *Schematic diagram of (a) molecular structure and (b) crystalline structure of β-phase of PVDF (Adapted from [5]).*

5.2.3. γ-phase of PVDF

The γ-phase of PVDF consists of $TT\bar{G}TTTGT$ configuration with lattice dimensions of a=4.96 Å, b=9.58 Å and c=9.23 Å. Studies show that *γ-phase* can exist in two different configurations. At high temperature, the crystallization of the *γ-phase* results in the

monoclinic modification with regular chain packing [42], [49], [50]. On the other hand at low temperature the crystallization of the *γ-phase* results in the orthorhombic modification [42], [51]. Even at high temperature, *γ-phase* transform from orthorhombic to monoclinic. In addition, *γ-phase* can be obtained from melt crystallization under high pressure and as well as from α-phase by heat treatment at 285°C [42]. Figure 5.7(a) presents the molecular structure and Figure 5.7(b) shows the crystalline structure of form-III (γ-phase), where crystal exhibits planar zigzag conformation. It is regarded as a distorted version of β-phase and is polar.

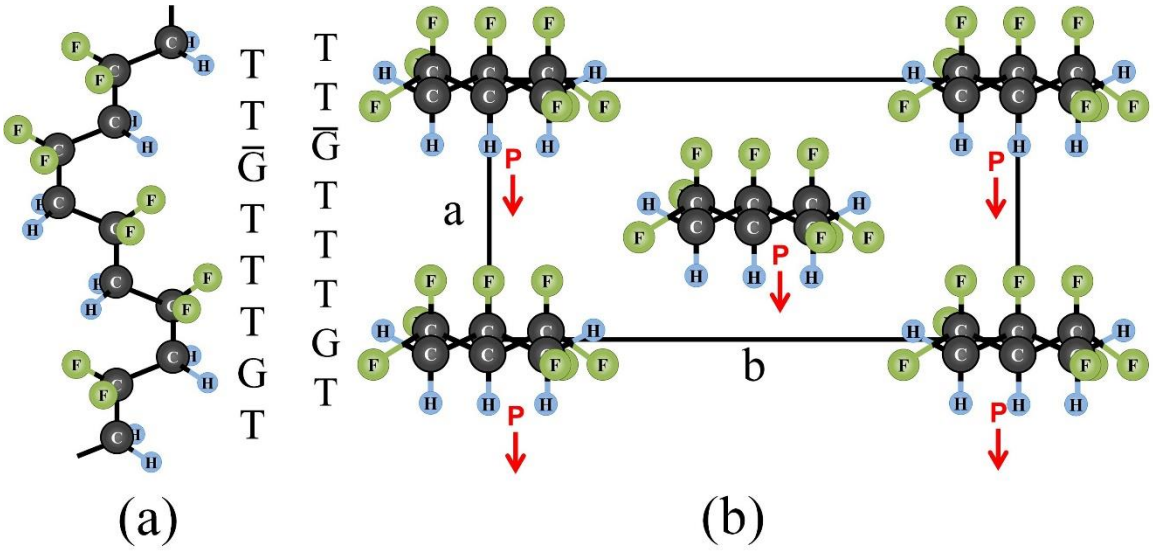

Figure 5.7: *Schematic diagram of (a) molecular structure and (b) crystalline structure of γ-phase of PVDF (Adapted from [5]).*

5.2.4. δ-phase of PVDF

The *δ-phase of PVDF,* which is electrically polar, analog of the *α*-phase, exhibits orthorhombic structure with the lattice constants, a=4.96 Å, b=9.64 Å and c=4.62 Å [5], [42]. In *δ-phase,* each molecule contains two chains aligned in the same direction. Thus, it exhibits pyroelectric and piezoelectric properties. The *δ*-phase can be obtained from *α*-phase by applying high electric fields [42]. Figure 5.8(a) presents the molecular structure and Figure 5.8(b) illustrates the crystalline structure of *δ*-phase of PVDF.

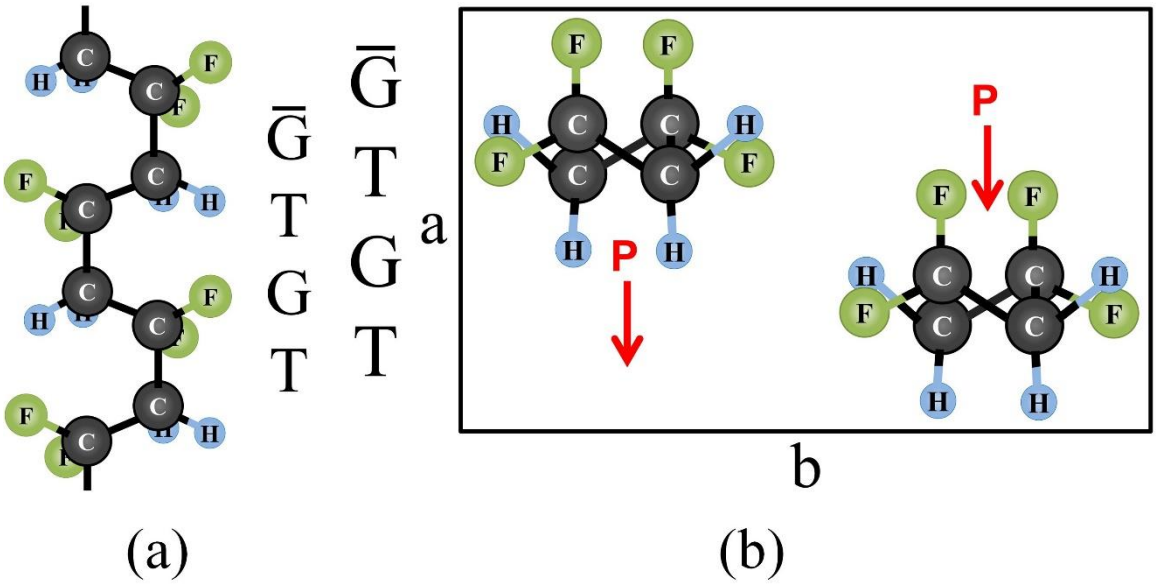

Figure 5.8: *Schematic diagram of (a) molecular structure and (b) crystalline structure of δ-phase of PVDF (Adapted from [5]).*

In addition, copolymerization of vinylidene fluoride (VDF) with other fluorocarbons, namely, trifluoroethylene (TrFE) and tetraethylene (TtFE) are also studied extensively. These copolymers contain about 50-80 mol% of VDF and their electrical properties varies over a wide range depending on formulation [42], [52], [53]. The copolymers are of great advantages to VDF homopolymer, when technical applications, such as sensing and actuation, are concerned. The copolymerization of VDF with other fluorocarbon monomers promotes the most desirable crystal modification, which inherits interesting pyro-, piezo- and ferroelectric properties. They also exhibit a polymorphism similar to PVDF and the transformation between various crystallographic phases can be accomplished by physicochemical techniques. Amongst them, the copolymer, especially with TrFE, is the most attractive one due to its structural stability and exhibition of homogeneous spontaneous polarization [42]. Moreover, PVDF-TrFE provides much higher crystallinity than PVDF [54].

5.2.5. Poly(vinylidene fluoride-trifluoroethylene) (P(VDF–TrFE))

Since the discovery of Poly(vinylidene fluoride-trifluoroethylene) (P(VDF–TrFE)), this copolymer of PVDF is the most studied piezo- and ferroelectric polymer [54]. The molecular structure of VDF-TrFE is shown in Figure 5.9. The P(VDF-TrFE) copolymer

exhibits some advantages over pure PVDF polymer, as the copolymer typically shows much higher crystallinity and thus, exhibits a larger piezoelectric response [5], [42], [54].

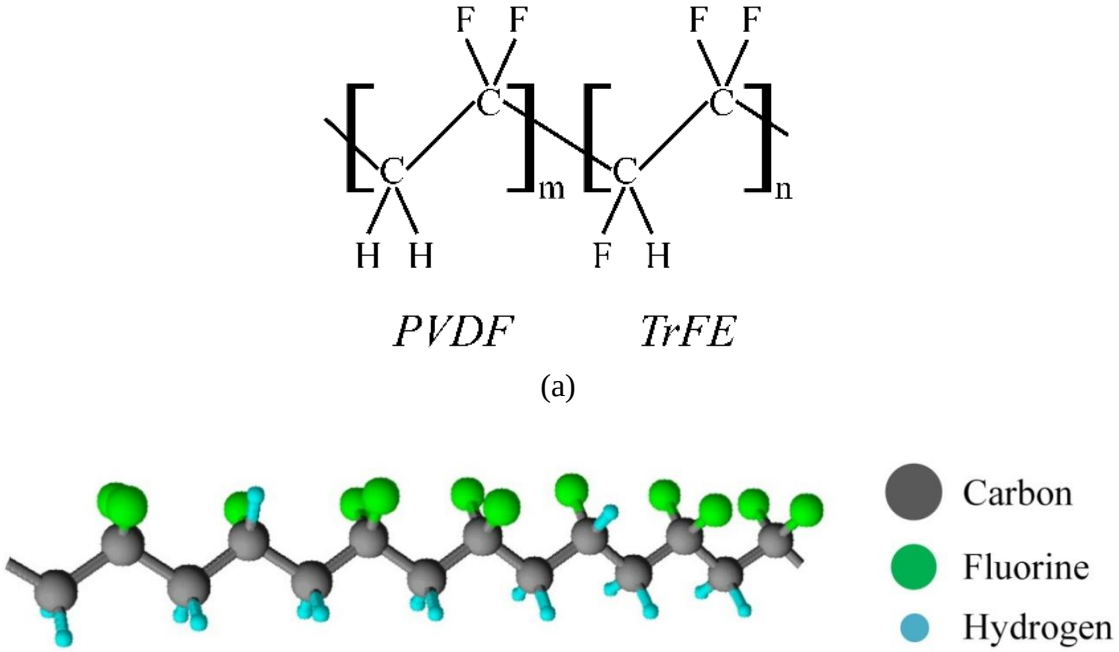

Figure 5.9: *Schematic diagram of (a) molecular structure [42], and (b) chain structure of P(VDF-TrFE).*

This copolymer exhibits "all-trans" structure both in the melt crystallized and solution casted films. The crystalline form of P(VDF–TrFE) varies, depending on their molar content ratios of VDF (m) and TrFE ($n = 1-m$), and on crystallization conditions [55]–[57]. The addition of trifluoroethylene (TrFE) introduces more fluorine atoms into the polymer chain and prevents the molecular chains from accommodating a "trans-gauche-trans-gauche" conformation due to the steric hindrance imparted by the bulky fluorine atoms. As a result, the copolymer is normally oriented directly in the extended "all-trans" conformation even without the application of any physical methods, such as stretching, annealing or quenching [42], [52], [53]. Therefore, the introduction of the TrFE generally stabilized the formation of β crystalline phase [58]. However, the addition of higher or lesser molar ratio of TrFE ruins the transition temperature by reducing the average dipole moment of the chains, expanding the lattice, and introducing defects [59]. It has been observed that the copolymer of VDF with more than 17 mol% of TrFE contains more extended all-trans conformation or a polar crystalline phase (β phase) [42], [55], [60], [61], and thus exhibits spontaneous polarization. P(VDF-TrFE) exhibits strong piezoelectric

property. At 120°C under an electric field of 40 MV/m, when the sample was polarized for half an hour, the highest value of piezoelectric constant d_{31}=49 pC/N was obtained [42], which is higher than PVDF itself.

In the present study, the composition of 70% VDF and 30% TrFE molar ratio is chosen, because of its distinct ferroelectric properties, and higher percentage of crystallinity without stretching treatments.

5.3. Experimental details

5.3.1. Materials

Polyvinylidene fluoride-trifluoroethylene (PVDF-TrFE, $M_w \approx 500{,}000\ g.mol^{-1}$, random copolymer) was provided by Piezotech. Butan-1-ol (MEK), tetrahyrofuran (THF), dimethyl sulfoxyde (DMSO), N-methyl-2-pyrrolydone (NMP), Ethylene glycol (EG), Diethyl phthalate (DEP), Propylene glycol (PG), N-cyclohexyl-2-pyrrolidone (CHP) were purchased from Sigma-Aldrich. Commercial silver nanoparticle ink used to make bottom electrode was DGP 40LT-15C from Advanced Nano Product (ANP). Isopropanol (VLSI standard) was obtained from Technic France. All products were used as received.

Printings on flexible substrate were carried out on polyimide Apical 500 AV (125 µm) and polyethylene terephthalate (PET, 480 µm) purchased from Technifilm company. Prior to the printing, the surface of these polymer films were rinsed with isopropanol and dried using blown nitrogen.

5.3.2. Experimental procedure

In order to prepare the PVDF-TrFE ink, solutions with different weight percentages of PVDF-TrFE are prepared using various solvents or mixture of solvents. The viscosity and surface tension of the prepared inks were characterized using a Brookfield viscometer DV1+ mounted with an ULA-DIN-86 spindle, and an OCA goniometer from Apollo Instruments respectively. Inkjet printings were performed with a Dimatix 2800-DMP from Fujifilm using 10 pL cartridges with 16 nozzles having a 23 µm diameter. Initially silver nanoparticle layers were inkjet-printed using drop-spacing of 25 µm on polyimide and PET substrates, and sintered by employing photonic sintering technique using a Pulseforge 3200 from Novacentrix. The printed silver electrode had the thickness of 500±50 nm, and the

average surface roughness (R_a) of 25±2.5 nm and root mean square roughness (R_q) of 32±3.5 nm. Thereafter, PVDF-TrFE layers were inkjet-printed on the silver layer. Then, the samples were dried at room temperature with air flow inside the oven (model: Heratherm oven from Thermo Scientific) for 24 hours, and then at 90 °C for half an hour to ensure the evaporation of the solvents. Finally, the samples were sintered at temperature between 140 and 150 °C in air for different time scales. The aluminum top electrodes were deposited by physical vapor deposition technique using the DP650 equipment from Alliance-Concept. Thickness of the films was measured using mechanical profilometer (model: XP-2, AMBiOS Technology). The poling step of PVDF-TrFE films have been carried out by applying voltage across the thickness of the film. Scanning Electron Microscope (SEM) images were recorded with a ZEISS Supra 40 and the surface topography was characterized using atomic force microscope (AFM) in tapping mode (SPII-Veeco apparatus). Furthermore, Fourier transform infrared spectroscopy (FTIR) and X-ray diffraction (XRD) of the samples were performed by Vertex 70 from Bruker and X'pert Pro X-ray diffractometer from PANaltical respectively. Electrical characterizations were performed with a 4200-SCS parameter analyzer from Keithley, and piezoelectric characterization through d_{33} coefficient measurement was performed with Polytec OFV3001 laser Doppler vibrometer (LDV) with OVD02 decoder to measure top surface displacement.

5.4. Results and discussions

5.4.1. PVDF-TrFE ink formulation

In the field of microelectronics, butan-2-one (MEK), a good solvent of PVDF-TrFE is generally used for solution based deposition, like spin coating [62]–[66]. Some researchers also used dimethylformamide [67], [68]. However, because of its high toxicity, this product has not been taken on. Moreover, even disregarding the viscosity and surface tension, which can vary greatly with the addition of the polymer, it is possible to observe in Table 5.1 that MEK does not match with the specifications of the Dimatix inkjet printer.

MEK exhibits very low density and is highly volatile. Generally, a solvent with a high evaporation rate can leads to rapid formation of a solid polymer membrane in the nozzles where ink is in contact with air and causes the cartridge clogging. Therefore during this

work, MEK has been mixed with other solvent having high boiling point and low vapor pressure.

Table 5.1: Physical properties of MEK and optimum fluid specifications for Dimatix [30]

Physical property	Dimatix specifications	MEK
Viscosity (mPa·s)	10 – 12	0.43
Surface tension ($mN \cdot m^{-1}$)	28 – 33	24.6
Boiling point (°C)	> 100	79.6
Density (g/cm^3)	> 1	0.8
Pressure vapor (Pa)	low*	10500 (very high)

**No precise value is advised by the constructor*

Alongside the need to adjust the physical properties of the ink, it seems interesting to study the effect of the solvent quality on the maximum concentration that can be printed. Effectively, with a decreased solvent quality, coils formed by the macromolecules contract to form structures with a smaller diameter [22], [69]. This decrease in diameter has a significant impact on coil unraveling when the fluid is under elongational flow and consequently on rheological properties of polymer solutions [70]. For example, in case of a good solvent, the macromolecules unravel faster and the onset of coil-stretch transition occurs at lower strains [71]. Thus, three different solvents, as mentioned in Table 5.2, with physical properties complementary to those of MEK and with a variable affinity for the PVDF-TrFE copolymer, have been tested for the ink formulation.

Table 5.2: Additional solvents description

Physical property	DMSO	CHP	DEP
Viscosity (mPa.s)	1.9	11.5	10.5
Surface tension ($mN.m^{-1}$)	43.5	43.2	37.5
Boiling point (°C)	190.8	284	295
Density (g/cm^3)	1.1	1	1.1
Pressure vapor (Pa)	59.4	66.64	2800
Solvent quality	Good	Latent	Bad

After ink formulation, the viscosity and the surface tension of each composition were measured. As a result of the non-Newtonian behavior of the PVDF-TrFE solutions, tests performed with Brookfied viscometer do not reflect the rheological properties of the inks being ejected during the printing process. Experimentally, all the prepared inks exhibit a constant viscosity over the entire range of analysis of this apparatus which corresponds to the low shear rate Newtonian plate generally observed with polymer solutions. So, Brookfield characterizations of the inks will be only used to determine their zero-shear viscosity.

Amongst the different mixtures tested, three compositions, containing a significant amount of copolymer, are inkjet printable. These solutions, described in Table 5.3, were prepared with a zero-shear viscosity lower than Dimatix specifications to anticipate the increase in elongational viscosity during the printing process.

Table 5.3: Inkjet printable PVDF-TrFE solutions

Solvents				Sovent Mixture		PVDF-TrFE Ink		
MEK	DMSO	CHP	DEP	Viscosity	Surface tension	Maximum printable polymer concentration	At maximum polymer concentration	
							Viscosity	Surface tension
wt.%	wt.%	wt.%	wt.%	mPa.s	mN/m	wt.%	mPa.s	mN/m
20	0	80	0	3.8	34.7	0.3	6.5	36.8
20	80	0	0	1.4*	36.7	1.25	5.2	33.6
30	50	0	20	2.1	41.8	0.75	5.6	31.5

**Viscosity of DMSO/MEK mixture was too low to be accurately measured. It has been determined using the data communicated by Gokavi et al. [72]*

After the addition of the polymer, all the inks exhibit a suited surface tension for inkjet printing. Zero-shear viscosity of the solutions at maximum printable polymer concentration is different for each solution, thus no critical value can be identified as a limit for printability. The solvent quality does not have a significant impact on the maximum printable concentration too. The influence of this parameter even seems to have the opposite effect to that intended as the mixture of two good solvents (DMSO/MEK) made possible to obtain the higher printable concentration. In fact, viscosity of the pure solvent without polymer in it is the only influential parameter; the lower it is, the higher is the maximum printable concentration. The poor influence of the solvent quality and hence the initial configuration of macromolecule coils on the ink printability suggests that the coils are nearly stretched at their maximum extensibility during the printing process in all samples that have been studied. So, the use of low viscosity solvents appears as being the only way to compensate the increase in the elongational viscosity during the ejection of the droplets, allowing the physical properties of the ink to remain in a printable range. In these circumstances, the amount of printable polymer concentration in ink may only be maximized by decreasing the solvent viscosity, by incorporating solvent with low viscosity in its composition, comparable to DMSO/MEK (80/20 wt.%) mixture or lower. Even in this case, the improvement would probability be very limited.

Maximum jettable concentration with a solvent mixture of DMSO and MEK was 1.25 wt.% but instabilities occurred during the printing process, leading to discontinuous layers. In

fact, 1.25 wt.% is the critical concentration at which the ink become impossible to print. At this composition, the detachment of the ink droplet from the printer nozzles has often been prevented, which impedes printing even after the use of frequent cleaning procedure. Thus, other printing tests have been carried out using the same solvent but with gradually reduced concentrations of the copolymer. The different results obtained after drying for the inkjet printing of PVDF-TrFE layers on previously printed silver electrode on polyimide foil as a function of PVDF-TrFE concentration ($C_{PVDF\text{-}TrFE}$) are presented in Figure 5.10.

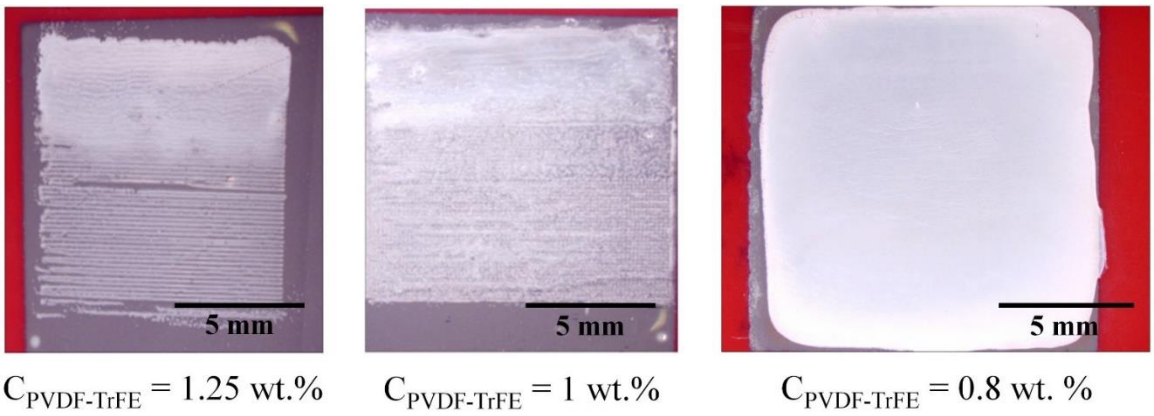

Figure 5.10: *Inkjet-printed layers obtained with DMSO/MEK (80/20 wt.%) at different concentrations of PVDF-TrFE ($C_{PVDF\text{-}TrFE}$).*

Inks with a PVDF-TrFE content equal to 0.8 wt.% made possible to obtain well defined patterns with a satisfactory continuity. Furthermore, drop-analysis of all the ink compositions, which is systematically conducted before printing, revealed that all of the 16 nozzles were always jetting for the ink with the composition of DMSO/MEK (80/20 wt.%) mixture and 0.8 wt.% of PVDF-TrFE content. Therefore, this composition has been used in the next step of this study.

5.4.2. Printing of polymeric ink

The stable printing of relatively high viscosity polymeric piezoelectric PVDF-TrFE ink requires the optimization of several printing parameters, namely, jetting frequency, voltage, nozzle temperature etc. The different printing conditions that have been implemented during this work are described in Table 5.4. In addition, a waveform, adapted to the rheological behavior of the polymer had also to be defined. It is depicted in Figure 5.11.

Table 5.4: Printing conditions

Parameter	Value
Drop spacing	20 µm
Firing voltage	40 V
Jetting frequency	2 kHz
Nozzle temperature	40 °C
Substrate temperature	Room temperature
Meniscus vacuum	2 inches H_2O or 498.2 Pa
Cartridge height	0.8 mm

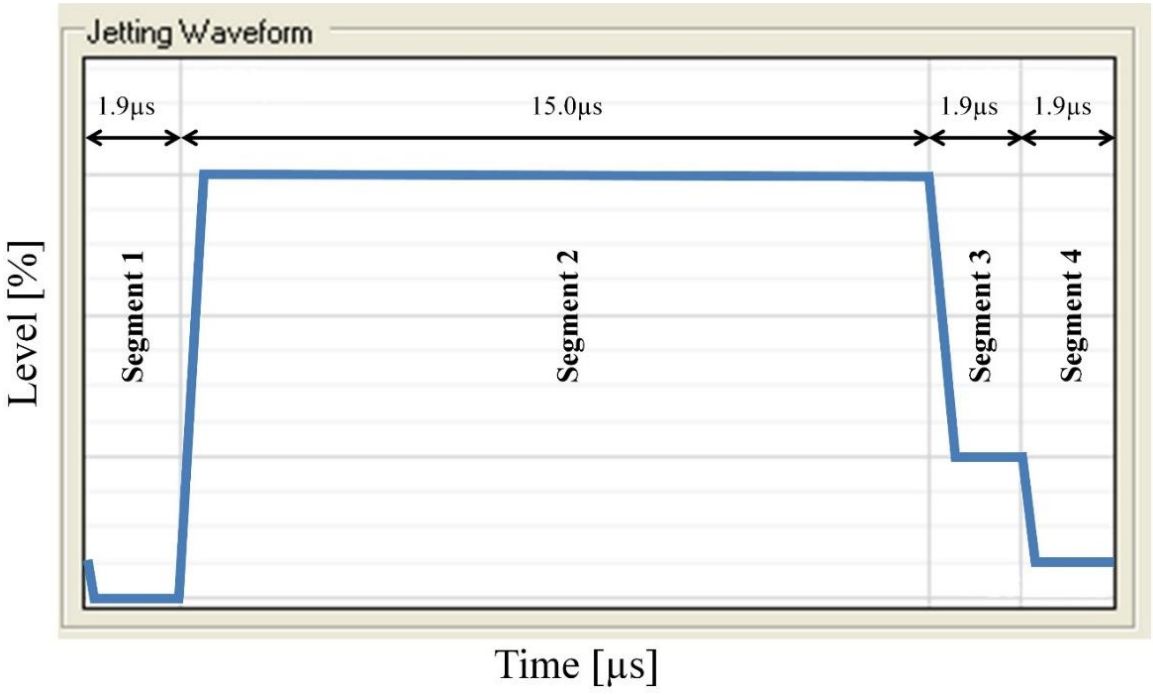

Figure 5.11: *Jetting waveform of DoD Inkjet-printer.*

The level (in ordinate) indicates the percentage of the firing voltage. Duration of each segment has been indicated in the graphical representation of the waveform. Compared to the default waveform, the duration of segment 1, linked to the ink quantity injected in the printhead chamber, has been reduced in order to increase the droplets velocity [30]. Duration of segment 2, corresponding to the ejection step, has been greatly extended to be adapted to drop deceleration due to the increase in viscosity during ejection. The slew rates of all segments have been set near their maximum values. For segments 1 and 2, this choice was motivated by the need to overcome viscoelastic behavior of the ink that opposes its flow. Concerning segments 3 and 4 which correspond to the fluid drop break-off and return to standby position, a sharper slope made possible to increase the droplets velocity and facilitate their breakup [30].

During this work, jetting voltage was set at the maximum value of 40 V that the printing system can deliver. Furthermore, for stable ejection of the polymeric ink, low jetting frequency of 2 kHz was employed. It has been observed experimentally that stable ejection was possible only at low jetting frequency, typically 2 kHz or less. Above this value, the jetting is disrupted and eventually completely stopped at higher frequency. This phenomenon is not consistent with the relaxation time generally observed with polymer in solution which is in the range of 10^{-5} to 10^{-6} s [73] and should be compatible with higher jetting frequencies. The need of a low jetting frequency during inkjet printing can thus be attributed to the time required between the droplet ejection and its detachment from the nozzle, induced by the viscoelastic behavior of polymer solution. In addition, printing an ink with this type of rheological behavior also requires high nozzle temperature and high firing voltage to compensate the increase in elongational viscosity during ejection.

5.4.3. Thickness measurement

A study carried out by Tseng *et al.* [65], shows that thicknesses in a range of few microns are the more suited for the fabrication of sensors based on the piezoelectric properties of PVDF-TrFE. On the other hand, Sharma *et al.* [63] reported a decrease in the rate of beta phase for thicknesses above 6 µm, so the fabricated layers thickness should have to be within 2 to 5 microns.

Table 5.5: Thickness of the inkjet-printed PVDF-TrFE layer (for drop spacing of 20 µm) sintered at 145 °C for 1 hour

No. of Layers	**Total thickness** µm	**Thickness per layer** µm
6	0.69 ± 0.04	0.12 ± 0.01
15	1.94 ± 0.13	0.13 ± 0.01
20	2.53 ± 0.27	0.13 ± 0.014

After drying and sintering, the thickness of the inkjet-printed layers of PVDF-TrFE on inkjet-printed silver (Ag) electrodes was measured using mechanical profilometer. The values are tabulated in Table 5.5. It has been observed that the thickness of each inkjet-printed layer of developed PVDF-TrFE ink with 20 µm drop spacing is between 120 and 130 nm. Thus, the ink is concentrated enough to obtain film thickness of around 2 µm with fifteen printing steps.

5.4.4. Surface morphology

Morphological investigations of inkjet-printed PVDF-TrFE films have been performed by scanning electron microscope (SEM) on untreated sample and samples sintered at 145°C for 1 hour and 24 hours respectively. Figures 5.12(a) to 5.12(c) illustrate the surface microstructure of the inkjet-printed PVDF-TrFE layers on printed silver electrode. The untreated sample exhibits undefined crystalline structure and inhomogeneous layer with a large number of holes within the film. In general, PVDF-TrFE films are sintered between Curie and melting temperature. The formation of homogeneous films with acicular grains (needle-like crystals) in edge-on lamellae are observed when films are sintered at 145 °C. However, the length of elongated crystallite decreases with the increasing time of sintering, as observed for the film sintered at 145 °C for 24 hours (Figure 5.12(c)) compared to film sintered at 145 °C for 1 hour (Figure 5.12(b)).

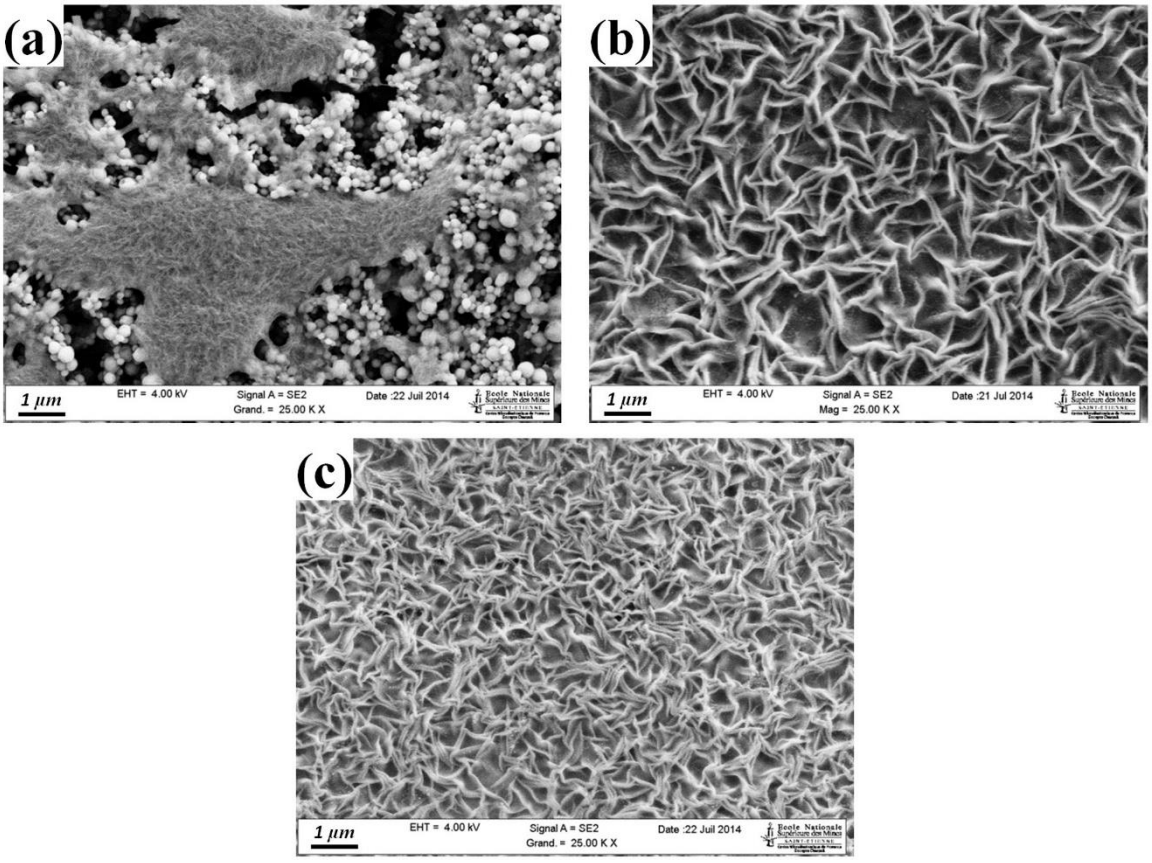

Figure 5.12: *Inkjet-printed PVDF-TrFE (15 layers) film (a)untreated, (b) sintered at 145°C for 1 hour, and (c) sintered at 145°C for 24 hours.*

The topographies of the samples sintered at 145 °C for 1 hour and 24 hours were further investigated by AFM using tapping mode, as illustrated in Figures 5.13(a) and 5.13(b). It has been found that tightly compact crystalline grains were formed for the PVDF-TrFE samples sintered at 145 °C. AFM image analysis reveals that the average size of the crystalline grains with length of 0.9±0.08 µm and width of 0.22±0.07 µm were obtained for the sample sintered at 145 °C for 1 hour, whereas the average grain size reduced to the length of 0.61±0.07 µm and width of 0.11±0.01 µm for the sample sintered at 145 °C for 24 hours. Therefore, higher sintering time reduces the crystalline grain size.

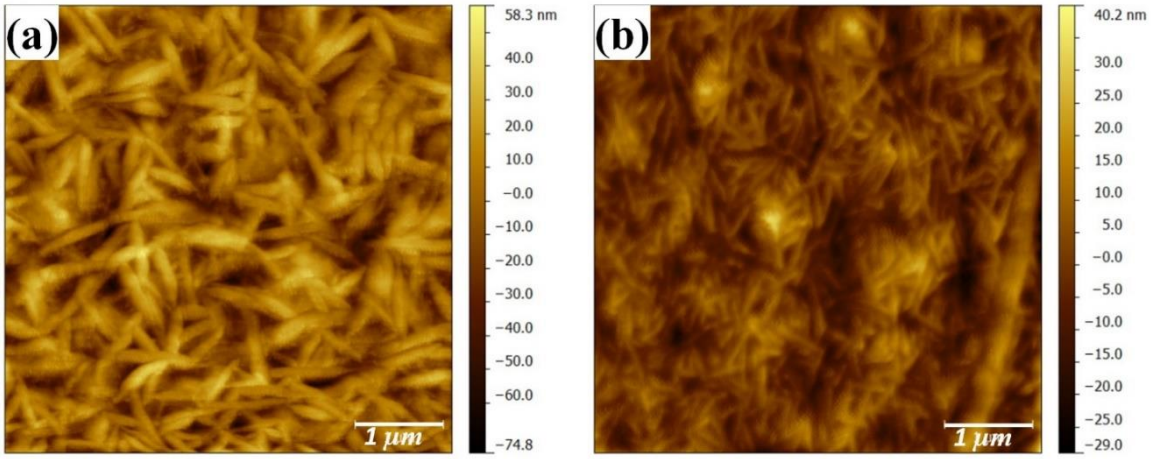

Figure 5.13: *Topographies of inkjet-printed PVDF-TrFE thin film (15 layers) sintered at 145 °C for (a) 1 hour and (b) 24 hours.*

Table 5.6: Roughness of the inkjet-printed PVDF-TrFE samples on silver layer printed on polymer substrates (scan area: 50×50 µm^2)

Sample	**No. of Layer(s)**	**Thermal Treatment**		**Crystal grain size**		**Average Roughness**	
		Temperature °C	Time Hour(s)	Length µm	Width µm		nm
P01	15	145	*1*	0.9 ± 0.08	0.22 ± 0.07	R_a	78.8 ± 8.7
						R_q	103.3 ± 10.7
P02	15	145	*24*	0.61 ± 0.07	0.11 ± 0.01	R_a	40.6 ± 0.4
						R_q	52.8 ± 0.5

The arithmetic roughness (R_a) and the root mean square roughness (R_q) of the printed PVDF-TrFE layer are also measured from AFM micrographs and tabulated in Table 5.6. Roughness of the film decreases significantly with the increasing sintering time. Long sintering time at 145 °C, which is very close to the melting temperature of PVDF-TrFE,

may cause melting of the polymer crystallites and thus eventually reduce the surface roughness.

5.4.5. Crystallinity

Generally, the absorbance of infrared (IR) light of each phase of the PVDF-TrFE generates a characteristic spectral-fingerprint, based on the frequencies at which the material absorbs infrared light and the intensity of those absorptions. Therefore, the FTIR spectra of PVDF-TrFE samples are a reliable and crucial technique to obtain valuable information about their structure and also help to elucidate the different crystalline phases.

According to the literature, the absorption bands at 510, 850 and 1288 cm^{-1} are assigned to β-crystalline phase of the PVDF-TrFE copolymer [74]. Peaks at 766, 855 and 976 cm^{-1} represent the α-phase [11] and bands at 1400, 1250 and 1100 cm^{-1} correspond to the amorphous region of the copolymer [75].

The FTIR spectra of PVDF-TrFE samples, sintered at different temperatures are illustrated in Figure 5.14. All the samples contain β-crystalline peaks. Studies show that the presence of small amount of TrFE into the PVDF-TrFE copolymer generally leads to the formation of polar β-crystalline phase. It has been found that more than 80% β-crystallinity is generally obtained after the annealing of the PVDF-TrFE films, and for stretched annealed films, the crystallinity can reach up to 90% [76].

The crystalline phase content of PVDF-TrFE can be quantified using FTIR spectrum. The absorption coefficients K_α and K_β, at the respective wavenumber of 766 and 848 cm^{-1} for α and β-phase are calculated, based on the assumption that the FTIR absorption follows the Lambert-Beer law [77]. In this way, according to Gregorio et al, the relative fraction of the β-phase in a sample containing just α and β-VDF can be expressed as follows,

$$F(\beta) = \frac{A_\beta}{\left(K_\beta / K_\alpha\right) A_\alpha + A_\beta} \times 100\% \quad \ldots\ldots\ldots (5.3)$$

where $F(\beta)$ is the content of β-crystalline phase, A_α and A_β represent the absorption at 766 and 840 cm^{-1} in arbitrary unit respectively, K_α and K_β correspond to the absorption

coefficient at the respective wavenumber. Their values are 6.1×10^4 cm^2/mol and 7.7×10^4 cm^2/mol respectively.

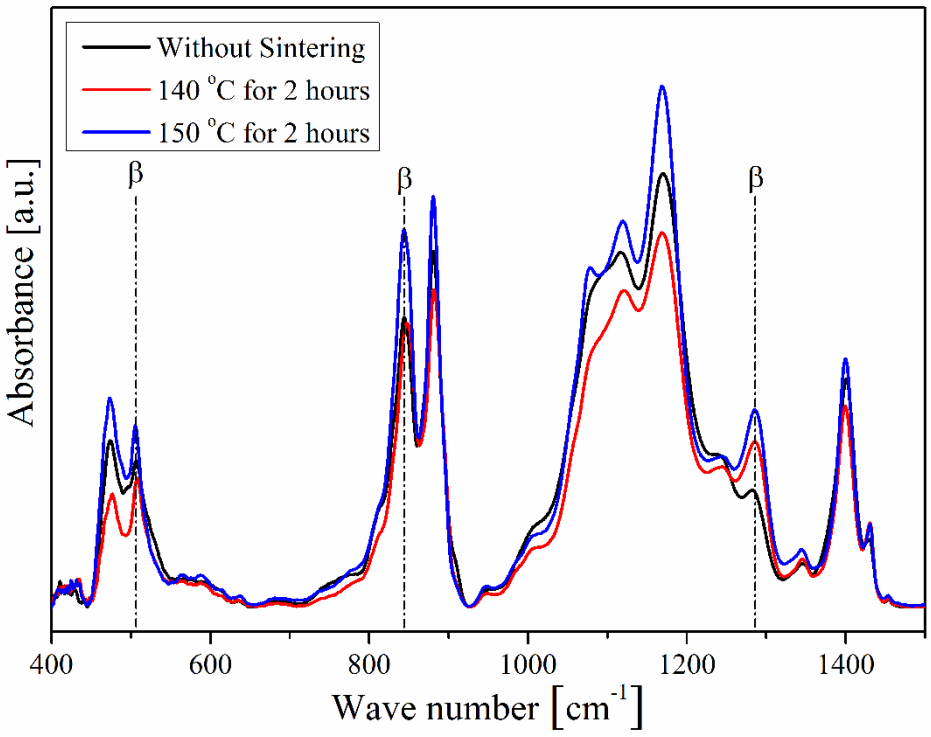

Figure 5.14: *FTIR spectra of PVDF-TrFE samples with different sintering conditions.*

Table 5.7: Relative fraction of polar β-crystalline phase with respect to α-phase

Sample	$F(\beta)$ %
Without sintering	88.6
140 °C for 2 hours	92.8
150 °C for 2 hours	91.5
150 °C for 8 hours	89.6

The content of the β-crystalline phase for the inkjet-printed samples sintered at different temperature and time was calculated (Table 5.7). It has been observed that both the sintering time and temperature influenced the β-crystalline phase content in the samples. The percentage of β-phase has been reduced for the samples sintered at 150 °C from 2 hours to 8 hours by 1.9%. In addition, the percentage of β-crystalline phase reduced from 92.8% to 91.5% for the sample sintered at 140 and 150 °C for 2 hours respectively. Therefore, according to the FTIR spectra analysis, it has been observed that the samples were mainly composed of β-crystalline phase and almost negligible amount of α-phase.

The unit cell of β-crystalline phase of PVDF-TrFE is orthorhombic. Characteristic X-ray diffraction peak of the β-crystalline phase assigned to (110/200) reflection planes generally appears around 2θ = 19.90° [74]. Figure 5.15 illustrates the X-ray diffraction pattern for inkjet-printed PVDF-TrFE sintered at 140 °C for 2 hours, and 150 °C for 2 hours and 8 hours respectively along with unsintered sample.

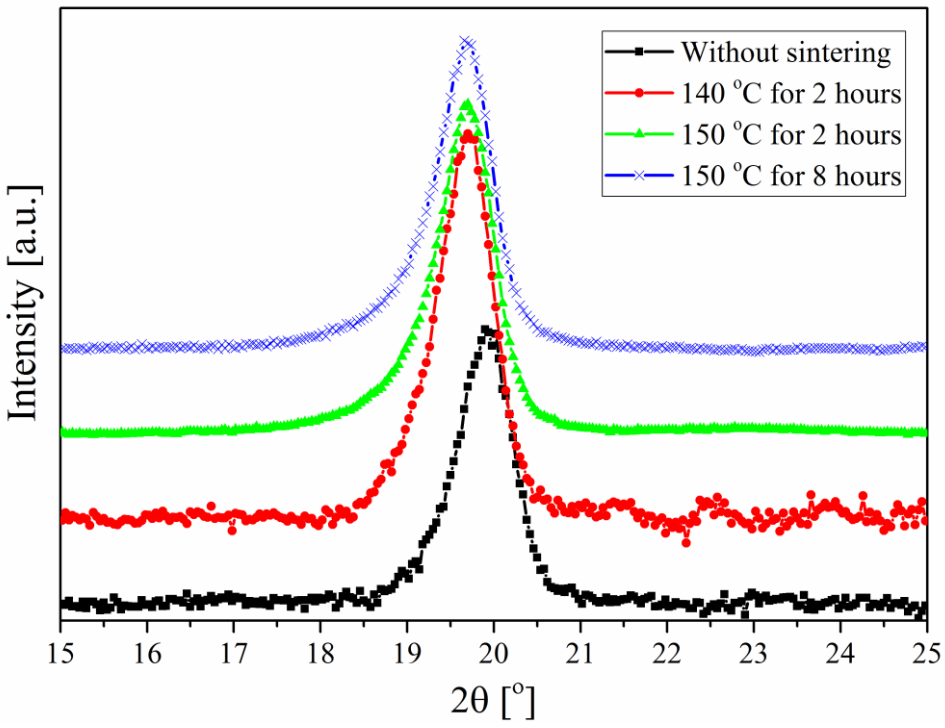

Figure 5.15: *XRD pattern of the inkjet-printed PVDF-TrFE samples (sinters at different temperature and time).*

XRD pattern can also be used to calculate the total crystallinity (X_C) of the PVDF-TrFE samples [74]. In this regard, two peaks corresponding to crystalline and amorphous phase were resolved, as presented in Figure 5.16, taking into account that the samples are composed of β-crystalline phase. The percentage of crystallinity can then be calculated as follows [65],

$$X_C = \frac{A_C}{A_C + A_A} \times 100\% \quad \ldots\ldots\ldots (5.4)$$

where A_C is the peak area of the crystalline phase and A_A corresponds to the amorphous phase. Calculated crystallinity of inkjet-printed PVDF-TrFE samples sintered at different temperatures and times is presented in Table 5.8.

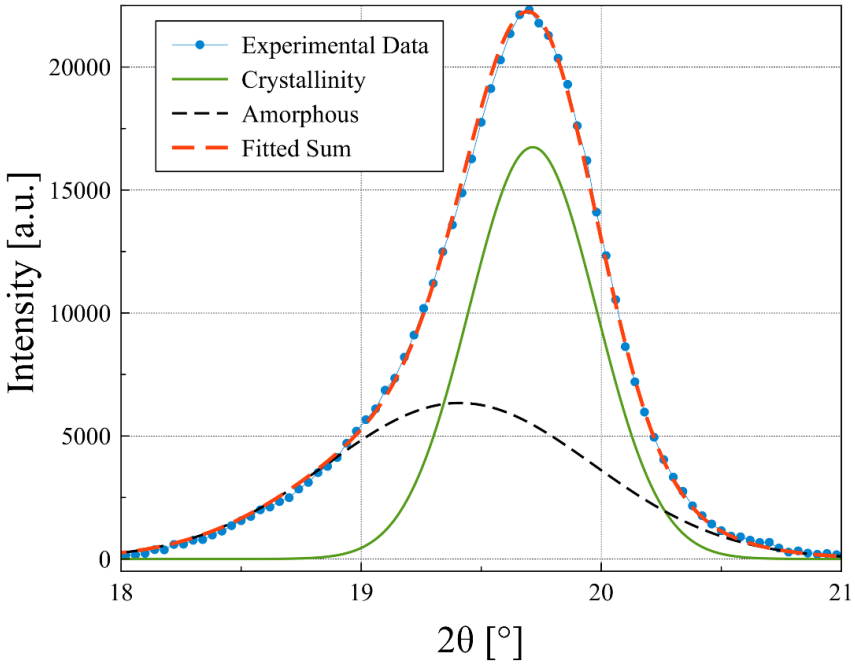

Figure 5.16: *Deconvolution of the XRD pattern for PVDF-TrFE thin film sintered at 150 °C for 2 hours.*

Table 5.8: Crystallinity of PVDF-TrFE films versus sintering conditions

Sample	X_C (%)
Without sintering	53.0 ± 1.4
140 °C for 2 hours	71.0 ± 1.6
150 °C for 2 hours	61.0 ± 0.5
150 °C for 8 hours	56.2 ± 1.5

The percentage of total crystallinity of samples was influenced both by the sintering temperature and time. Crystallinity increases for the sintered samples. However, decrease of crystallinity from 72.6% for sample sintered at 140 °C for 2 hours to 61.4% for sample sintered at 150 °C for 2 hours is observed. On the other hand, crystallinity also decreases from 61.4% to 57.2% for the samples sintered at 150 °C for 2 hours and 8 hours respectively. Therefore, maximum crystallinity is achieved at 140 °C for a duration of 2 hours.

5.4.6. Electrical characterization

For electrical measurement, aluminum (Al) top electrodes with radius of 0.75 mm were prepared using physical vapor deposition technique. Figure 5.17 illustrates the top and cross-section view of the sample after top electrode deposition. Figure 5.18 shows an optical image of the inkjet-printed PVDF-TrFE film after top electrode deposition.

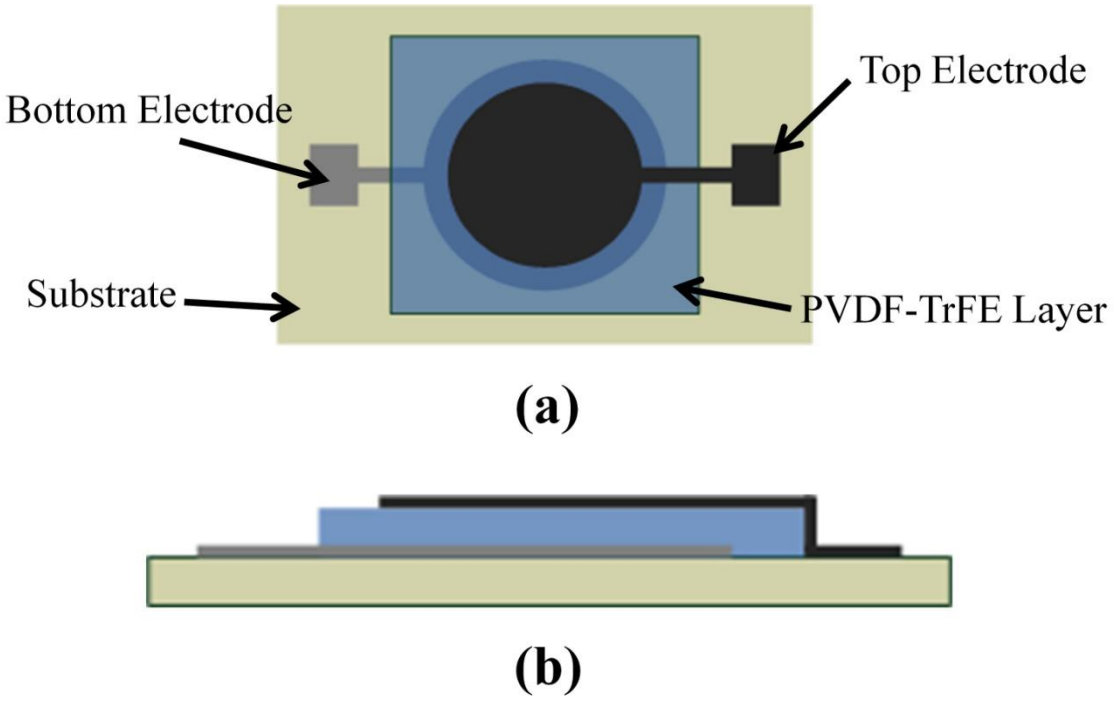

Figure 5.17: *Schematic diagram of PVDF-TrFE sample (a) top view, and (b) cross-sectional view.*

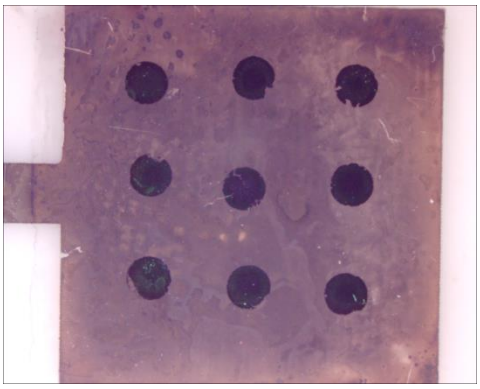

Figure 5.18: *Inkjet-printed PVDF-TrFE film after aluminum (Al) electrode deposition.*

Initially, capacitance measurements were performed to check the quality of the deposited film. Table 5.9 shows the measured capacitance values. Capacitance of 0.19±0.01 pF was obtained, which is very low compared to the theoretical value of 50 pF, calculated using an effective dielectric constant of 8 for PVDF-TrFE.

Table 5.9: Measured capacitance of PVDF-TrFE

Film Thickness	Top electrode radius	Relative dielectric constant	Capacitance (C_p)		Resistance (R_p)
			Theoretical	Experimental	
µm	mm		pF	pF	GΩ
2.5	0.75	8	50	0.19 ± 0.01	8.6 ± 0.2

The polarization of the PVDF-TrFE film is performed before piezoelectric coefficient ($d_{33,f}$) measurement. Figure 5.19 shows the setup for thin film $d_{33,f}$ characterization process, where Polytec OFV-3001 laser Doppler vibrometer (LDV) is used to measure the displacement (u_3) of the layer when sine wave voltage ($V = V_0.cos(\omega_0 t)$) with a frequency of $f_0 = 150\ kHz$ is applied to electrodes using a probe station. Relation between displacement (u_3), piezoelectric coefficient (d_{33}) and applied voltage (V) can be expressed as follows,

$$u_3 = d_{33,f} V \ldots \ldots \ldots (5.5)$$

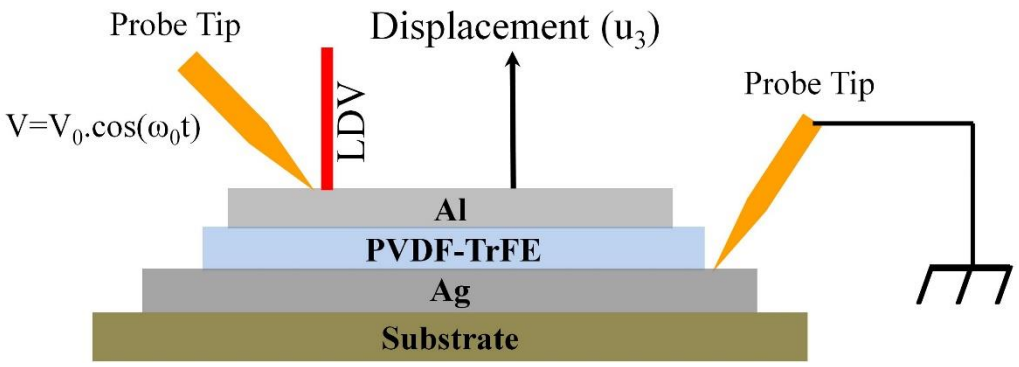

Figure 5.19: *Schematic diagram of piezoelectric coefficient ($d_{33,f}$) measurement approach, where V_0 represents the maximum voltage amplitude and ω_0 is the angular frequency.*

According to the measurement, a $d_{33,f}$ value of 2 pC/N or 2 pm/V was observed for the inkjet-printed PVDF-TrFE film. The measured value is about 10 times smaller than expected [78]. The low value of dielectric properties and piezoelectric coefficient could be due to the poor top electrode quality, as well as to microcracks in the printed PVDF-TrFE layer. Study shows that the surface reaction of PVDF-TrFE generally takes place with the deposited aluminum top electrode, and thus aluminum (Al) is probably not the best suitable material to fabricate electrode on PVDF-TrFE [75], [79]. Aluminum reacts with fluorine to form thin aluminum fluoride (AlF_3) layer, and in the process, reduces the fluorine content

in the polymer [79], which might cause the reduction of the piezoelectric properties of the printed PVDF-TrFE layer. New materials like gold or poly(3,4-ethylenedioxythiophene) polystyrene sulfonate (PEDOT:PSS) for the top electrode will be investigated.

5.5. Summary

With the growing interest towards flexible electronics, piezoelectric material, like PVDF-TrFE copolymer has been used for many applications because of its flexibility. However, high flexibility was observed only for high molecular weights. During this work, inkjet printable ink of PVDF-TrFE (70/30) with a molecular weight (M_w) equal to 500,000 g/mol has been developed. It has been observed that the viscosity of the solvent is the only parameter of the ink composition that plays an important role to develop stable jettable ink with a significant concentration of PVDF-TrFE for DoD inkjet system. The presence of polymer increases the solvent viscosity, which could be solved by preparing compositions with low viscosity solvent along with MEK. During this work, best jettability was observed for the ink composed of a solution mixture of MEK/DMSO. This particular solvent composition permits the fabrication of stable PVDF-TrFE ink with 0.8 wt.% high molecular weight polymer content. For uninterrupted jetting, low jetting frequency of 2 kHz or below was used and the waveform used for DoD printing process was also modified by taking into account the rheological behavior of the fluid. Morphological analysis shows that PVDF-TrFE, in the printed thin layers exhibits high crystallinity percentage and β phase after sintering at 140 °C for 2 hours. Tests performed at higher temperature and longer times led to a decrease in crystallinity percentage, β phase ratio and crystal grain size coupled with a reduction of the surface roughness. A $d_{33,f}$ value of 2 pm/V was obtained, which is 10 times smaller than the expected value. This could be caused by the poor quality of the deposited top electrode.

The results were quite promising. However, further improvements of the ink and the printing process are required before stepping towards the piezoelectric based transducer and device fabrication. Future work will be focused to enhance the polymer concentration in the ink, printing of more homogeneous printed PVDF-TrFE layer and to improve the quality of the top electrode deposition to obtain better piezoelectric properties, and to develop the inkjet printable PVDF-TrFE devices.

References

[1] Pierre-Jean Cottinet, Daniel Guyomar, Benoit Guiffard, Laurent Lebrun, and Chatchai Putson, "Electrostrictive Polymers as High-Performance Electroactive Polymers for Energy Harvesting," in *Piezoelectric Ceramics*, Ernesto Suaste-Gomez, Ed. Croatia: InTech, 2010, pp. 185–208.

[2] S. C. Mathur, J. I. Scheinbeim, and B. A. Newman, "Piezoelectric Properties and Ferroelectric Hysteresis Effects in Uniaxially Stretched Nylon-11 Films," *Journal of Applied Physics*, vol. 56, pp. 2419–2425, 1984.

[3] Lihong Huang, Xiuli Zhuang, Jun Hu, Le Lang, Peibiao Zhang, Yu Wang, Xuesi Chen, Yen Wei, and Xiabin Jing, "Synthesis of Biodegradable and Electroactive Multiblock Polylactide and Aniline Pentamer Copolymer for Tissue Engineering Applications," *Biomacromolecules*, vol. 9, no. 3, pp. 850–858, 2008.

[4] David J. Bryan, Jin Bo Tang, Stephen A. Doherty, David D. Hile, Debra J. Trantolo, Donald L. Wise, and Ian C. Summerhayes, "Enhanced Peripheral Nerve Regeneration Through a Poled Bioresorbable Poly (Lactic-co-Glycolic Acid) Guidance Channel," *Journal of neural engineering*, vol. 1, no. 2, pp. 91–98, 2004.

[5] Kohji Tashiro, "Cystal Structure and Phase Transition of PVDF and Related Copolymers," in *Ferroelectric Polymers: Chemistry, Physics, and Applications*, Hari Singh Nalwa, Ed. New York: Marcel Dekker, Inc., 1995, pp. 63–180.

[6] R. Glen Kepler, "Ferroelectric, Pyroelectric, and Piezoelectric Properties of Poly(vinylidene Fluoride)," in *Ferroelectric Polymers: Chemistry, Physics, and Applications*, Hari Singh Nalwa, Ed. New York: Marcel Dekker, Inc., 1995, pp. 183–232.

[7] Eiichi Fukada, "History and Recent Progress in Piezoelectric Polymers," *IEEE Transactions on Ultrasonics, Ferroelectrics and Frequency Control*, vol. 47, no. 6, pp. 1277–1290, 2000.

[8] A. Salimi and A. A. Yousefi, "Analysis Method: FTIR Studies of β-Phase Crystal Formation in Stretched PVDF Films," *Polymer Testing*, vol. 22, no. 6, pp. 699–704, 2003.

[9] T. Furukawa, Y. Takahashi, and T. Nakajima, "Recent Advances in Ferroelectric Polymer Thin Films for Memory Applications," *Current Applied Physics*, vol. 10, no. 1, pp. e62–e67, 2010.

[10] Insung Bae, Seok Ju Kang, Youn Jung Park, T. Furukawa, and Cheolmin Park, "Organic Ferroelectric Field-Effect Transistor with P(VDF-TrFE)/PMMA Blend Thin Films for Non-volatile Memory Applications," *Current Applied Physics*, vol. 10, no. 1, pp. e54–e57, 2010.

[11] P. Martins, A. C. Lopes, and S. Lanceros-Mendez, "Electroactive Phases of Poly (vinylidene fluoride): Determination, Processing and Applications," *Progress in Polymer Science*, vol. 39, no. 4, pp. 683–706, 2014.

[12] Iwao Seo and Dechun Zou, "Electromechanical Applications," in *Ferroelectric Polymers: Chemistry, Physics, and Applications*, Hari Singh Nalwa, Ed. New York: Marcel Dekker, Inc., 1995, pp. 699–734.

[13] EisoYamaka, "Pyroelectric Applications," in *Ferroelectric Polymers: Chemistry, Physics, and Applications*, Hari Singh Nalwa, Ed. New York: Marcel Dekker, Inc., 1995, pp. 669–698.

[14] Thomas R. Howarth and Kurt M. Rittenmyer, "Transduciton Applications," in *Ferroelectric Polymers: Chemistry, Physics, and Applications*, Hari Singh Nalwa, Ed. New York: Marcel Dekker, Inc., 1995, pp. 735–770.

[15] Munehiro Date, "Ferroelectric Optical Memory," in *Ferroelectric Polymers: Chemistry, Physics, and Applications*, Hari Singh Nalwa, Ed. New York: Marcel Dekker, Inc., 1995, pp. 771–790.

[16] Danilo De Rossi, Elisa Stussi, and Claudio Domenici, "Biomedical and Robotic Applications of Ferroelectric Polymers," in *Ferroelectric Polymers: Chemistry, Physics, and Applications*, Hari Singh Nalwa, Ed. New York: Marcel Dekker, Inc., 1995, pp. 771–790.

[17] J. S. Harrison and Zoubeida Ounaies, "Piezoelectric Polymers," in *Encyclopedia Of Polymer Science and Technology*, vol. 3, Wiley Online Library, 2002, pp. 474–498.

[18] M. G. Broadhurst and G. T. Davis, "Piezo-and Pyroelectric Properties," in *Electrets*, Gerhard M. Sessler, Ed. Berlin, Heidelberg: Springer, 1987, pp. 285–319.

[19] Ronald C. G. Naber, Cristina Tanase, Paul W. M. Blom, Gerwin H. Gelinck, Albert W. Marsman, Fred J. Touwslager, Sepas Setayesh, and Dago M. de Leeuw, "High-Performance Solution-Processed Polymer Ferroelectric Field-Effect Transistors," *Nature Materials*, vol. 4, no. 3, pp. 243–248, 2005.

[20] Haisheng Xu, Xuerang Fang, Xiaobing Liu, Shan Wu, Yingjun Gu, Xiangjian Meng, Jinglan Sun, and Junhao Chu, "Fabrication and Properties of Solution Processed All Polymer Thin-film Ferroelectric Device," *Journal of Applied Polymer Science*, vol. 120, no. 3, pp. 1510–1513, 2011.

[21] Emine Tekin, Patrick J. Smith, and Ulrich S. Schubert, "Inkjet Printing as a Deposition and Patterning Tool for Polymers and Inorganic Particles," *Soft Matter*, vol. 4, no. 4, pp. 703–713, 2008.

[22] I. Teraoka, *Polymer Solutions: An Introduction to Physical Properties*. New York: John Wiley & Sons, 2002.

[23] N. F. Morrison and O. G. Harlen, "Viscoelasticity in Inkjet Printing," *Rheologica acta*, vol. 49, no. 6, pp. 619–632, 2010.

[24] X. B. Chen, "Modeling and Control of Fluid Dispensing Processes: A State-of-the-Art Review," *The International Journal of Advanced Manufacturing Technology*, vol. 43, no. 3–4, pp. 276–286, 2009.

[25] C. Clasen, P. M. Phillips, Ljiljana Palangetic, and J. Vermant, "Dispensing of Rheologically Complex Fluids: The Map of Misery," *AIChE Journal*, vol. 58, no. 10, pp. 3242–3255, 2012.

[26] R. H. Colby, D. C. Boris, W. E. Krause, and S. Dou, "Shear Thinning of Unentangled Flexible Polymer Liquids," *Rheologica acta*, vol. 46, no. 5, pp. 569–575, 2007.

[27] V. N. Kalashnikov, "Shear-Rate Dependent Viscosity of Dilute Polymer Solutions," *Journal of Rheology*, vol. 38, no. 5, pp. 1385–1403, 1994.

[28] L. Zhang, C. Yang, and Z.-S. Mao, "Numerical Simulation of a Bubble Rising in Shear-Thinning Fluids," *Journal of Non-Newtonian Fluid Mechanics*, vol. 165, no. 11, pp. 555–567, 2010.

[29] Brian Derby, "Inkjet Printing of Functional and Structural Materials: Fluid Property Requirements, Feature Stability, and Resolution," *Annual Review of Materials Research*, vol. 40, pp. 395–414, 2010.

[30] FujiFilm, "Dimatix Materials Printer." FujiFilm Dimatix, Inc., 2008.

[31] K. A-Alamry, K. Nixon, R. Hindley, J. A. Odell, and S. G. Yeates, "Flow-Induced Polymer Degradation during Ink-Jet Printing," *Macromolecular Rapid Communications*, vol. 32, no. 3, pp. 316–320, 2011.

[32] D. E. Smith, H. P. Babcock, and S. Chu, "Single-Polymer Dynamics in Steady Shear Flow," *Science*, vol. 283, no. 5408, pp. 1724–1727, 1999.

[33] G. H. McKinley, "Dimensionless Groups for Understanding Free Surface Flows of Complex Fluids," *Bulletin of the Society of Rheology*, vol. 2005, pp. 6–9, 2005.

[34] G. H. McKinley, "Visco-Elasto-Capillary Thinning and Break-up of Complex Fluids," *Rheology Reviews*, vol. 3, pp. 1–49, 2005.

[35] M. Ochowiak, L. Broniarz-Press, S. Rozanska, and J. Rozanski, "The Effect of Extensional Viscosity on the Effervescent Atomization of Polyacrylamide Solutions," *Journal of Industrial and Engineering Chemistry*, vol. 18, no. 6, pp. 2028–2035, 2012.

[36] K.K.B. Hon, L. Li, and I.M. Hutchings, "Direct Writing Technology-Advances and Developments," *CIRP Annals - Manufacturing Technology*, vol. 57, no. 2, pp. 601–620, 2008.

[37] P. G. De Gennes, "Coil-Stretch Transition of Dilute Flexible Polymers Under Ultrahigh Velocity Gradients," *The Journal of Chemical Physics*, vol. 60, no. 12, pp. 5030–5042, 1974.

[38] C. McIlroy, O. G. Harlen, and N. F. Morrison, "Modelling the Jetting of Dilute Polymer Solutions in Drop-on-demand Inkjet Printing," *Journal of Non-Newtonian Fluid Mechanics*, vol. 201, pp. 17–28, 2013.

[39] D. Xu, V. Sanchez-Romaguera, S. Barbosa, W. Travis, J. de Wit, P. Swan, and S. G. Yeates, "Inkjet Printing of Polymer Solutions and the Role of Chain Entanglement," *Journal of Materials Chemistry*, vol. 17, no. 46, pp. 4902–4907, 2007.

[40] A. V. Bazilevskii, J. D. Meyer, and A. N. Rozhkov, "Dynamics and Breakup of Pulse Microjets of Polymeric Liquids," *Fluid Dynamics*, vol. 40, no. 3, pp. 376–392, 2005.

[41] P. Pantelis, "Properties and Application of Piezoelectric Polymers," *Physics in Technology*, vol. 15, pp. 239–261, 1984.

[42] H.S. Nalwa, "Recent Development in Ferroelectric Polymers," *Journal of Macromolecular Science - Reviews in Macromolecular Chemistry & Physics*, vol. C31, no. 4, pp. 341–432, 1991.

[43] Ryozo Hasegawa, Yasuhiro Takahashi, Yozo Chatani, and Hiroyuki Tadokoro, "Crystal Structure of Three Crystalline Forms of Poly (vinylidene fluoride)," *Polymer Journal*, vol. 3, no. 5, pp. 600–610, 1972.

[44] Andrew J. Lovinger, "Poly(Vinylidene Fluoride)," in *Developments in Crystalline Polymers—1*, D.C. Bassett, Ed. Netherlands, 1982, pp. 195–273.

[45] L.T. Chen and C.W. Frank, "The Influence of Head-to-Head Defects on the Crystallization of PVF2," *Ferroelectrics*, vol. 57, no. 1, pp. 51–62, 1984.

[46] G.R. Davies, "Comment on Dielectric Behaviour and Morphology of Poly(vinylidene fluoride)," *Journal of Materials Science*, vol. 11, pp. 782–784, 1976.

[47] Qiming Zhang and Jerry Scheinbeim, "Electric EAP," in *Electroactive Polymer (EAP) Actuators as Artificial Muscles: Reality, Potential, and Challenges*, Second., Yoseph Bar-Cohen, Ed. Bellingham, Washington, USA: SPIE PRESS, 2004, pp. 95–150.

[48] M. Fujii, V. Stannett, and H.B. Hopfenberg, "Transitions in Poly(vinyl fluoride) and Poly(vinylidene fluoride)," *Journal of Macromolecular Science-Physics*, vol. B15, no. 3, pp. 421–431, 1978.

[49] Bruces S. Morra and Richard S. Stein, "Melting Studies of Poly(vinylidene Fluoride) and Its Blends with Poly(methyl Methacrylate)," *Journal of Polymer Science: Polymer Physics Edition*, vol. 20, no. 12, pp. 2243–2259, 1982.

[50] Bruce S. Morra and Richard S. Stein, "Morphological Studies of Poly(vinylidene Fluoride) and Its Blends with Poly(methyl Methacrylate)," *Journal of Polymer Science: Polymer Physics Edition*, vol. 20, no. 12, pp. 22461–2275, 1982.

[51] Raymond F. Boyer, "Glassy Transitions in Semicrystalline Polymers," *Journal of Polymer Science: Polymer Symposia*, vol. 50, no. 1, pp. 189–242, 1975.

[52] G.R. Davies and H. Singh, "Evidence for a New Crystal Phase in Conventionally Poled Samples of Poly(vinylidene Fluoride) in Crystal Form II," *Polymer*, vol. 20, pp. 772–774, 1979.

[53] Y. Murata and N. Koizumi, "Curie Transition in Copolymers of Vinylidene Fluoride and Tetrafluoroethylene," *Polymer Journal*, vol. 17, no. 9, pp. 1071–1074, 1985.

[54] Takeo Furukawa, "Ferroelectric Properties of Vinylidene Fluoride Copolymers," *Phase Transitions*, vol. 18, no. 3–4, pp. 143–211, Aug. 1989.

[55] J.B. Lando and W.W. Doll, "The Polymorphism of Poly(vinylidene fluoride). I. The Effect of Head-to-Head Structure," *Journal of Macromolecules Science, Part B: Physics*, vol. 2, no. 2, pp. 205–218, 1968.

[56] K. Tashiro, K. Takano, M. Kobayashi, Y. Chatani, and H. Tadokoro, "Structural Study on Ferroelectric Phase Transition of Vinylidene Fluoride-Trifluoroethylene Copolymers (III) Dependence of Transitional Behavior on VDF Molar Content," *Ferroelectrics*, vol. 57, no. 1, pp. 297–326, Jun. 1984.

[57] Hiroji Ohigashi, "Piezoelectric Polymers-Materials and Manufacture," *Japanese Journal of Applied Physics*, vol. 24, pp. 23–27, 1985.

[58] B.L. Farmer, A.J. Hopfinger, and J.B. Lando, "Polymorphism of Poly(vinylidene Fluoride): Potential Energy Calculations of the Effects of Head-to-Head Units on the Chain Conformation and Packing of Poly(vinylidene Fluoride)," *Journal of Applied Physics*, vol. 43, no. 11, p. 4293, 1972.

[59] Andrew J. Lovinger, G. E. Johnson, H. E. Bair, and E. W. Anderson, "Structural, Dielectric, and Thermal Investigation of the Curie Transition in a Tetrafluoroethylene Copolymer of Vinylidene Fluoride," *Journal of Applied Physics*, vol. 56, no. 9, p. 2412, 1984.

[60] M. Latour and R. L. Moreira, "A Spectroscopic Study in the PIM Region of Poly(vinylidene Fluoride) and Copolymers," *Electrical Insulation, IEEE Transactions on*, no. 3, pp. 525–528, 1986.

[61] Helen L.W. Chan, Z. Zhao, K. W. Kwok, C. L. Choy, C. Alquié, C. Boue, and J. Lewiner, "Polarization of Thick Polyvinylidene Fluoride/Trifluoroethylene Copolymer Films," *Journal of applied physics*, vol. 80, no. 7, pp. 3982–3991, 1996.

[62] J. Chang, C. H. Shin, Y. J. Park, S. J. Kang, H. J. Jeong, K. J. Kim, C. J. Hawker, T. P. Russell, D. Y. Ryu, and C. Park, "Polymeric Gate Dielectric Interlayer of Cross-Linkable Poly(styrene-r-methylmethacrylate) Copolymer for Ferroelectric PVDF-TrFE Field Effect Transistor Memory," *Organic Electronics*, vol. 10, no. 5, pp. 849–856, 2009.

[63] T. Sharma, S.-S. Je, B. Gill, and J. X. Zhang, "Patterning Piezoelectric Thin Film PVDF–TrFE Based Pressure Sensor for Catheter Application," *Sensors and Actuators A: Physical*, vol. 177, pp. 87–92, 2012.

[64] Y. J. Park, S. J. Kang, Y. Shin, R. H. Kim, I. Bae, and C. Park, "Non-Volatile Memory Characteristics of Epitaxially Grown PVDF-TrFE Thin Films and Their Printed Micropattern Application," *Current Applied Physics*, vol. 11, no. 2, pp. e30–e34, 2011.

[65] Hong-Jie Tseng, Wei-Cheng Tian, and Wen-Jong Wu, "P(VDF-TrFE) Polymer-Based Thin Films Deposited on Stainless Steel Substrates Treated Using Water Dissociation for Flexible Tactile Sensor Development," *Sensors*, vol. 13, pp. 14777–14796.

[66] A. A. Prabu, K. J. Kim, and C. Park, "Effect of Thickness on the Crystallinity and Curie Transition Behavior in P(VDF/TrFE) (72/28) Copolymer Thin Films using FTIR-Transmission Spectroscopy," *Vibrational Spectroscopy*, vol. 49, no. 2, pp. 101–109, 2009.

[67] H. J. Hwang, J. H. Yang, S. C. Kang, C. Cho, C. G. Kang, Y. G. Lee, and B. H. Lee, "Novel Multi-Bit Memory Device Using Metal/PVDF–TrFE/Graphene Stack," *Microelectronic Engineering*, vol. 109, pp. 87–89, 2013.

[68] S.-W. Jung, S.-M. Yoon, S. Y. Kang, I.-K. You, J. B. Koo, K.-J. Baeg, and Y.-Y. Noh, "Low-Voltage-Operated Top-Gate Polymer Thin-Film Transistors with High-Capacitance P(VDF-TrFE)/PVDF-Blended Dielectrics," *Current Applied Physics*, vol. 11, no. 3, pp. S213–S218, 2011.

[69] Michel Fontanille and Yves Gnanou, *Chimie et physic-chimie des polymères*. Paris: Dunod, 2002.

[70] C. A. Cathey and G. G. Fuller, "The Optical and Mechanical Response of Flexible Polymer Solutions to Extensional Flow," *Journal of Non-Newtonian Fluid Mechanics*, vol. 34, no. 1, pp. 63–88, 1990.

[71] S. Somani, E. S. Shaqfeh, and J. R. Prakash, "Effect of Solvent Quality on the Coil-Stretch Transition," *Macromolecules*, vol. 43, no. 24, pp. 10679–10691, 2010.

[72] G. S. Gokavi, J. R. Raju, T. M. Aminabhavi, R. H. Balundgi, and M. V. Muddapur, "Viscosities and Densities of Binary Liquid Mixtures of Dimethyl Sulfoxide with Chlorobenzene, Pyridine, and Methyl Ethyl Ketone at 25, 35, 45 and 55 °C," *Journal of Chemical and Engineering Data*, vol. 31, no. 1, pp. 15–18, 1986.

[73] D. C. Vadillo, W. Mathues, and C. Clasen, "Microsecond Relaxation Processes in Shear and Extensional Flows of Weakly Elastic Polymer Solutions," *Rheologica acta*, vol. 51, no. 8, pp. 755–769, 2012.

[74] Rahman Ismael Mahdi, W. C. Gan, and W. H. Majid, "Hot Plate Annealing at a Low Temperature of a Thin Ferroelectric P (VDF-TrFE) Film with an Improved Crystalline Structure for Sensors and Actuators," *Sensors*, vol. 14, no. 10, pp. 19115–19127, 2014.

[75] Dipankar Mandal, "Ultra-Thin Films of a Ferroelectric Copolymer: P(VDF-TrFE)," Master's Thesis, Brandenburgischen Technischen Universität, Cottbus, 2008.

[76] F. Fang, M. Z. Zhang, and J. F. Huang, "Deformation and Fracture Behavior of Poly(vinylidene fluoride-trifluorethylene) Ferroelectric Copolymer Films Under Uniaxial Tension," *Journal of Polymer Science Part B: Polymer Physics*, vol. 43, no. 22, pp. 3255–3260, 2005.

[77] Rinaldo Gregorio Jr and Marcelo Cestari, "Effect of crystallization temperature on the crystalline phase content and morphology of poly (vinylidene fluoride)," *Journal of Polymer Science Part B: Polymer Physics*, vol. 32, no. 5, pp. 859–870, 1994.

[78] Piezotech, "P(VDF-TrFE) Ferrolelectric & Piezoelectric Copolymers." [Online]. Available: http://www.piezotech.fr/fr/2-products-piezoelectric-polymers/news/news-32-p-vdf-trfe-ferrolelectric-&-piezoelectric-copolymers.html. [Accessed: 16-Jan-2015].

[79] K. Müller, Y. Burkov, D. Mandal, K. Henkel, I. Paloumpa, A. Goryachko, and D. Schmeißer, "Microscopic and Spectroscopic Characterisation of Interfaces and Dielectric Layers for OFET Devices," in *Physical and Chemical Aspects of Organic Electronics*, Christof Wöll, Ed. Weinheim, Germany: Wiley-VCH, 2009, pp. 445–468.

CHAPTER 6

CONCLUSIONS AND PERSPECTIVES

This chapter summarizes the overall goals, objectives and the main results of the thesis. The major contributions of this research are also discussed. Finally, some perspectives are drawn.

6.1. Summary

The main objectives of this work can be divided into three parts. Firstly, the study of the basic design of the capacitive acoustic sensor developed by the "Spinnaker" consortium and the design optimization to achieve a capacitive acoustic resonator with appropriate sensitivity and selectivity. Secondly, the development of the fabrication steps of the transducer using printing techniques. And finally, the characterization of the device and the comparison with simulation. In addition, within the timeframe of this thesis, stable inkjet-printable polyvinylidene fluoride – trifluoroethylene (PVDF-TrFE) ink was also developed. This ink can be used to fabricate piezoelectric acoustic transducer, which could stand up as a potential alternative candidate to capacitive transducer.

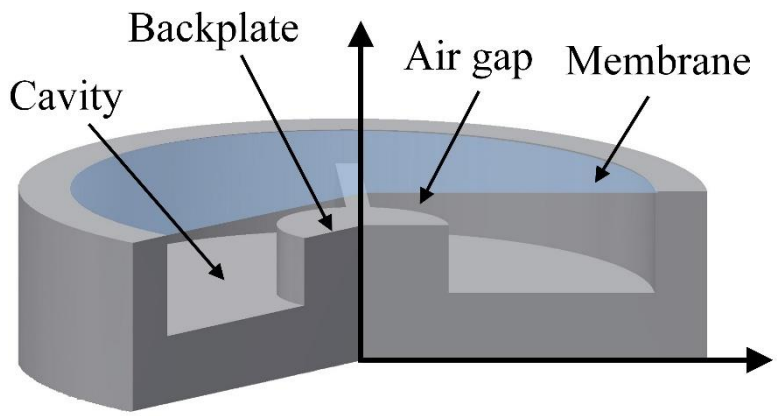

Figure 6.1: *Schematic diagram of the design of the capacitive acoustic transducer.*

Acoustic sensors that provide output responses due to the variation of acoustic pressure acting upon a flexible diaphragm have been used in many civilian and military applications [1]–[3]. Amongst different types of acoustic sensor, this work was focused on capacitive acoustic transducer. For years, many capacitive acoustic transducers have been designed and developed, mainly targeted towards audio applications, with constant sensitivity over a wide bandwidth. To develop radio frequency identification (RFID) system with improved localization, TAGSYS RFID has been planning to incorporate a capacitive acoustic resonator to RFID system. In this regard, a new design of the capacitive acoustic transducer

was proposed by the "Spinnaker" consortium (Figure 6.1). This work was undertaken to explore the possibilities of designing and developing new capacitive acoustic transducer with good sensitivity and selectivity using low cost manufacturing techniques, such as printing techniques.

Over a period of time, printed electronics technologies, especially inkjet printing technique, emerge as a promising way to fabricate electronic goods on different types of substrate and to reduce the production cost. Inkjet printing technique is a direct maskless writing technique performed at ambient temperature under atmospheric pressure. Therefore, this technique is cheaper than vacuum based technologies and also reduces the processing complexity and fabrication steps in comparison to photolithographic technique. There are several factors that influence the inkjet printing process in terms of ink, printing parameters and substrates, as illustrated in Figure 6.2.

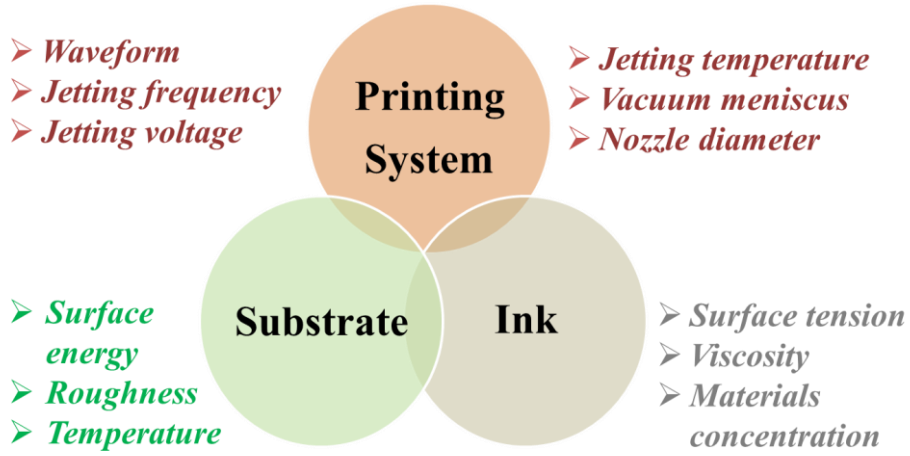

Figure 6.2: *Summary of important factors that influence the inkjet printing process.*

The printing of the material layer is generally followed by curing steps, such as thermal heating using conventional oven. The development of an alternative curing technique, namely, the photonic sintering technique facilitates the use of low cost substrate, like paper, and plastic substrates with low glass transition temperature.

Within the framework of this thesis, we proved that the design of the capacitive acoustic sensor proposed by the "Spinnaker" consortium can be used to build capacitive acoustic resonator with the required specifications. In this regard, the basic design of the transducer has been investigated and optimized using numerical simulation and design of experiment

(DOE) approach, as presented in Chapter 3. The virtual prototyping of the transducer was modeled using COMSOL multiphysics software. The use of DOE allowed the study of linear, quadratic and interaction effects of different parameters on the output responses of the transducer with a reduced number of conducted experiments. The empirical model for each output response has then been developed based on the response surface method (RSM). The empirical model is far less complex than the numerical simulation. Therefore, the use of DOE reduces the computation efforts during the sensor optimization process. Since multiple outputs have to be optimized simultaneously, multi-criteria desirability functions have been employed. Finally, based on the optimization result, cross-verification using numerical simulation was performed. It has been observed that the optimized set of parameters will provide an acoustic transducer with static capacitance of 0.50 pF, capacitance variation of 2.6 fF and quality-factor of 522, along with capacitance ratio of 0.5% and output voltage of 20 mV at first resonant frequency of the acoustic sensor for an incident acoustic pressure level of 80 dB_{SPL}. Hence, the approach that combines numerical simulation and DOE has guided us towards the optimum set of parameters that satisfies the targeted output responses of the acoustic resonator, and set the foundation for the development of the transducer using printing technologies.

Generally, inkjet printing technique is used to develop circuit interconnections [4], [5], and electronic components, such as capacitor, resistor, inductor, thin film transistor [5], [6] etc. This technique can also be used to fabricate 3D structures MEMS structures using complex sacrificial layer technique [7], [8]; however, their dimensions are limited to micrometer scale range. As the optimization suggested that the transducer should have a large cavity of few millimeters and relatively large membrane radius compared to the backplate electrode, the two-dimensional inkjet printing technique alone was not suitable for this kind of device fabrication. Since the constraint was the use of printing techniques, therefore a new manufacturing approach has been developed to address this issue, as discussed in Chapter 4. During this thesis, emerging three-dimensional (3D) printing technique has been combined with direct write 2D inkjet technique. However, this work required to deal with several issues, namely, surface roughness of 3D printed structure, surface energy and the thermal stability. Generally, 3D printed materials have low heat deflection temperature and therefore, to avoid any damage, photonic sintering has been used to sinter the inkjet-printed silver nanoparticle on the 3D printed structure. To manufacture the membrane of the transducer, silver layer has been inkjet-printed on thin organic polymer film, having

thickness below 25 µm. However, the membrane development needed to deal with the problem related to the application of the membrane tension. It has been observed that to fabricate the membrane with tension, the printing of conductive layer on the thin film needed to be performed on pre-tensed film. Indeed, if the tension is applied on the periphery of the film after printing the conductive layer, the conductivity decreases due to appearance of cracks on the printed conductive layer.

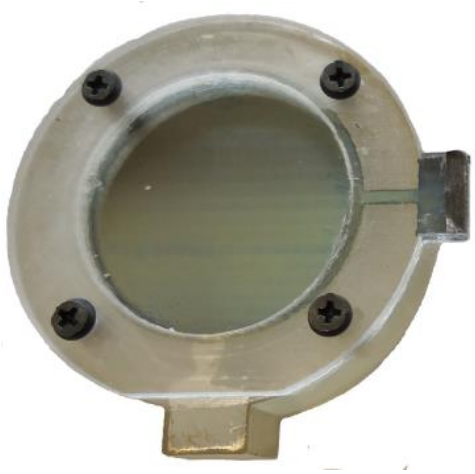

Figure 6.3: *Printed capacitive acoustic transducer.*

Final assembly (Figure 6.3) has been performed using screw system, where membrane and backplate were separated by a 3D printed spacer. Electrical characterization of the printed acoustic transducer has shown that the fabricated transducer acted as a pure capacitor in static mode. The dynamic behavior of the device was characterized using laser Doppler vibrometer (LDV). The sensor exhibited high sensitivity and selectivity at its first resonant frequency (Figure 6.4). Experimental results have also been successfully compared with the numerical simulation results. Therefore, it can be concluded that the printed capacitive transducer performs as an acoustic resonator with relatively good Q-factor.

As the fabrication of the devices has been performed manually, there were some problems associated with the fabrication steps. Occasionally, unexpected non-uniformity in the membrane tension and some deformations of the membrane have been observed due to the different tightness of the screws. In addition, lack of appropriate adhesive to fix the pre-tensed Mylar film on the membrane frame leads to problem related to the durability of the membrane tension over time.

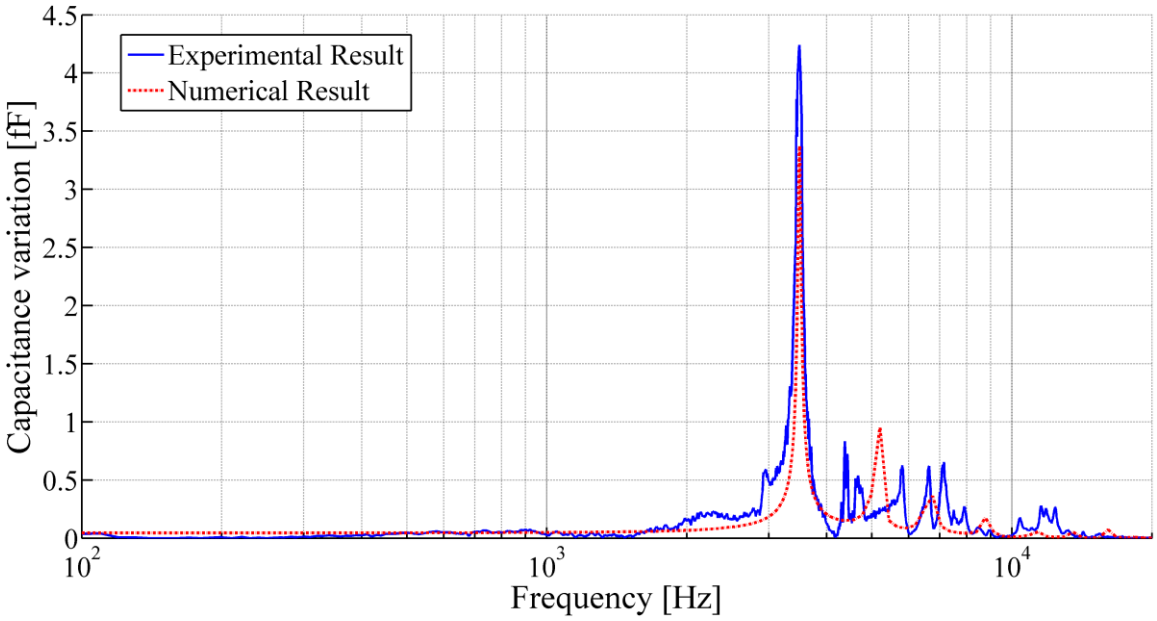

Figure 6.4: *Capacitance variation with respect to the frequency of the printed acoustic transducer with the membrane radius of 8.1 mm, backplate radius of 871 µm, cavity height of 3990 µm, air gap of 67.7 µm, membrane thickness of 23 µm and membrane tension of 48 N/m.*

Piezoelectric acoustic transducer could be an interesting alternative to the capacitive acoustic transducer. Since piezoelectric transducer does not require a backplate electrode, the damping effect will be drastically reduced. This will lead to larger membrane displacement. In addition, the piezoelectric transducer will directly provide an output voltage while capacitive transducer requires an additional capacitance to voltage converter. However, the lack of inkjet-printable piezoelectric ink inspired us to develop an inkjet printable polymeric piezoelectric using polyvinylidene fluoride – trifluoroethylene (PVDF-TrFE) ink, as presented in chapter 5. The development of polymeric ink requires the optimization of several ink and printing parameters to obtain stable jettability. It has been noticed that the viscosity of the solvent of the ink was the main influencing factor to achieve stable jettable ink with a significant concentration of PVDF-TrFE. The ink viscosity, which generally increases due to the addition of the polymer, could be controlled by preparing compositions with low viscosity solvent along with butan-2-one (MEK). The ink composition with a solvent mixture of MEK and dimethyl sulfoxide (DMSO) provides the best jettability, and allows the development of ink with 0.8 wt.% of the PVDF-TrFE (70/30) polymer concentration having a molar weight of 500000 g/mol. The uninterrupted jetting of this polymeric ink requires the use of low jetting frequency of 2 kHz or below, the

optimized waveform for the piezoelectric DoD printing system and nozzle temperature to accommodate the rheological behavior of the fluid. The printed PVDF-TrFE layers were then dried and sintered between the Curie temperature and the melting temperature of PVDF-TrFE. Finally, the samples were characterized. It has been observed that the printed PVDF-TrFE samples consists mainly of β-crystalline phase, and its concentration depends on the sintering temperature and time. The crystalline grains size decreases with the increasing time close to the melting temperature, and the surface roughness reduces also for higher sintering time. Aluminum top electrode was deposited using physical vapor deposition method to perform the electrical characterization. A value of the piezoelectric coefficient ($d_{33,f}$) of 2 pm/V was obtained, which was smaller than the expected value. This could be caused by the surface reaction of the aluminum with PVDF-TrFE layer. However, due to the limitation of the timeframe of the thesis work, the further improvement and the development of the piezoelectric based transducer could not be performed.

6.2. Future perspectives

This work was initiated by TAGSYS RFID, a French company, to develop an acoustic resonator using printing technology. It has allowed the close collaboration between industrial and academic research. The study has shown promising results; however, further improvements of the device might be possible to enhance the performance of the capacitive acoustic transducer. The gluing of the membrane film to the frame and evenly the assembling by precisely controlling the screws are two possibilities. It could even be interesting to develop improved assembly technique without the use of screw which will reduce the complexity.

Beside 3D printing method, the bottom structure of the acoustic transducer with cavity and backplate can also be developed using alternative manufacturing technique, such as mechanical micromachining and laser ablation technique, for details see Appendix E. However, further study is required before implementing these techniques.

The optimization of the acoustic transducer, during this work, has been performed by combining numerical simulation and DOE method, where multiple output responses were optimized simultaneously to achieve global optimization of the transducer that fulfilled the desired requirements. Similar approach could be implemented to optimize other physical sensors as well.

During this thesis, part of the capacitive acoustic transducer has been manufactured by printing conductive silver layer on 3D printed substrates. The technological building blocks that have been developed, could profitably be used to fabricate other 3D electronic devices and components.

In addition to the application of capacitive acoustic resonator into a RFID system to improve the localization of the RFID tag, this transducer can be used for other interesting applications, such as navigation of drones, autonomous system or bio-mimetic development based on animal instincts [9]. Study shows that the insect, like cricket, can navigate using sound sources in complex environments. The same principle can be explored to fabricate autonomous micro-flying objects [9]. Since the acoustic resonator developed in this project exhibits good sensitivity and selectivity without the use of any passive and electronic filters, this sensor can be an ideal candidate for such bio-mimetic applications. The frequency of the transducer can be tuned by controlling the membrane tension or by changing the dimension of the device.

Finally, the newly developed polymeric PVDF-TrFE based piezoelectric ink can be used to develop piezoelectric acoustic transducer, as well as many other applications, such as pressure sensing, energy harvesting etc. However, still some experiments are required to improve the top electrode deposition on the polymer layer for the fabrication process. The future work will be focused on increasing the polymer concentration in the ink, improving the curing process, and enhancing the quality of the deposited top electrode by using conductive polymer like poly(3,4-ethylenedioxythiophene) polystyrene sulfonate (PEDOT:PSS) or gold to obtain better piezoelectric properties.

References

[1] D. T. Martin, "Design, Fabrication, and Characterization of a MEMS Dual-backplate Capacitive Microphone," Doctoral Thesis, University of Florida, Gainesville, FL, USA, 2007.

[2] Dimitrios Chatzopoulos, "Modeling the Performance of MEMS Based Directional Microphones," Master's Thesis, Naval Postgraduate School, Monterey, CA, USA, 2008.

[3] B. Kaushik, D. Nance, and K. K. Ahuja, "A Review of the Role of Acoustic Sensors in the Modern Battlefield," in *11th AIAA/CEAS Aeroacoustics Conference*, Monterey, CA, USA, 2005, p. AIAA 2005–2997.

[4] Jolke Perelaer, "Postprinting Processes for Inorganic Ink for Plastic Electronics Applications," in *Inkjet-Based Micromanufacturing*, Jan G. Korvink, Patrick J. Smith, and Dong-Youn Shin, Eds. Weinheim, Germany: WILEY-VCH Verlag GmbH & Co. KGaA, 2012, pp. 111–125.

[5] David Wallace, Donald Hayes, Ting Chen, Virang Shah, Delia Radulescu, Patrick Cooley, Kurt Wachtler, and Arunkumar Nallani, "Ink-Jet as a MEMS Manufacturing Tool," in *First International Conference on Integration and Commercialization of Micro and Nanosystems*, Sanya, Hainan, China, 2007, pp. 1161–1168.

[6] Byung Ju Kang, Chang Kyu Lee, and Je Hoon Oh, "All-Inkjet-Printed Electrical Components and Circuit Fabrication on a Plastic Substrate," *Microelectronic Engineering*, vol. 97, pp. 251–254, Sep. 2012.

[7] Sawyer B. Fuller, Eric J. Wilhelm, and Joseph M. Jacobson, "Ink-Jet Printed Nanoparticle Microelectromechanical Systems," *Journal of Microelectromechanical Systems*, vol. 11, no. 1, pp. 54–60, 2002.

[8] Robert Horning, Thomas Ohnstein, and Daniel Youngner, "Method for Making Devices using Ink Jet Printing," US7112463 B2, Sep-2006.

[9] Franck Ruffier, Simon Benacchio, Fabien Expert, and Erick Ogam, "A Tiny Directional Sound Sensor Inspired by Crickets Designed for Micro-Air Vehicles," in *IEEE Sensors*, Limerick, Ireland, 2011, pp. 970–973.

APPENDIXES

APPENDIX A: Membrane displacement

Design of the proposed acoustic sensor consists of a central cylindrical rigid backing electrode of small radius surrounded by a flat annular cavity below a vibrating membrane clamped at its periphery separated by air gap (Figure A1) [1], [2].

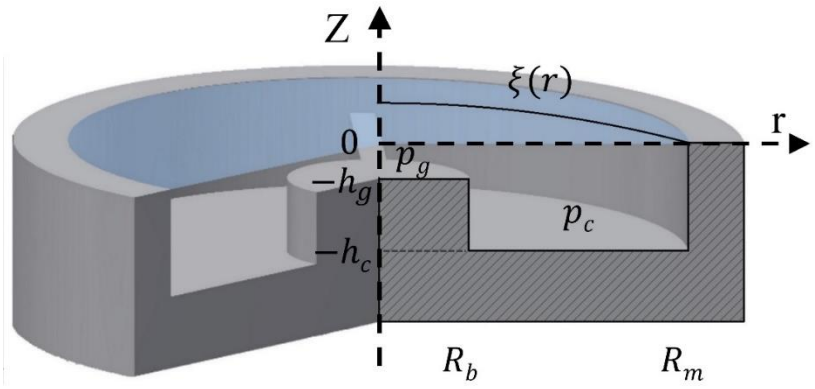

Figure A1: *Schematic diagram of an acoustic transducer.*

Equations governing the membrane displacement

The equation governing the vibration of the thin circular membrane of radius R_m, thickness t_m, and density ρ_m under constant radial force per unit length (T_m) acting on its edge, driven by uniform harmonic incident acoustic pressure p_i over the membrane surface, loaded by the pressure field $p(r)$, also known as reaction pressure at the membrane surface, can be expressed as [1]–[4],

$$T_m\left(\Delta_r + K^2\right)\,\xi(r) = p_i - p(r), \quad 0 < r < R_m \quad \ldots\ldots\ldots (1)$$

Here, $\xi(r)$ is the vertical membrane displacement, Δ_r (equals to ∇_r^2) represents the Laplace operator, and K^2 defines the wavenumber of the free flexural vibration of the membrane,

$$K^2 = \frac{\omega^2 \rho_{ms}}{T_m} = \frac{\omega^2}{c^2}; \quad c = \sqrt{\frac{T_m}{\rho_{ms}}} \qquad \text{and} \qquad \rho_{ms} = t_m \rho_m \quad \ldots\ldots\ldots (2)$$

Where, c denotes the speed of sound in the membrane, ρ_{ms} is the surface density or mass per unit area of the membrane and ω is the angular frequency. The membrane is supported on a rigid circular frame at its periphery $r = R_m$ (Dirichlet boundary condition), therefore

$$\xi(R_m) = 0 \quad \dots\dots\dots (3)$$

The reaction pressure $p(r)$, loading the diaphragm, is due to the underlying air layer squeezed in air gap and in the annular cavity under the membrane, where

$$p(r) = \begin{cases} p_g(r) & r \in (0, R_e) \\ p_c = \text{const} & r \in (R_e, R_m) \end{cases} \dots\dots\dots (4)$$

Here $p_g(r)$ and $p_c(r)$ represent the pressure in the air gap and the pressure in the cavity volume which is assumed to be quasi-uniform respectively, and R_e represents the effective radius and is equal to the radius of the backplate electrode (R_b).

The incident acoustic signal (with the time factor given by $e^{j\omega t}$) triggers the membrane displacement $\xi(r)$, which is assumed to be small and harmonic ($\xi(r)e^{j\omega t}$). The general solution for the displacement of the membrane $\xi(r)$ is the eigenfunction expansion and can be written as [2],

$$\xi(r) = \sum_n \xi_n \Psi_n(r) \quad \dots\dots\dots (5)$$

where eigenfunctions $\Psi_n(r)$ is,

$$\Psi_n(r) = \frac{1}{\sqrt{\pi} R_m J_1(K_n R_m)} J_0(K_n r) \quad \dots\dots\dots (6)$$

Where K_n is given by the equation $J_0(K_n R_m) = 0$ (zero order Bessel function of the first kind). The constants ξ_n can be expressed based on the orthogonality properties of the eigenfunctions $\Psi_n(r)$ as follows:

$$\xi_n = \frac{1}{T\left(K^2 - K_n^2\right)} \iint_{S_m} (p_i - p(r)) \Psi_n dS_m \quad \dots\dots\dots (7)$$

Here $S_m = \pi R_m^2$ represents the surface of the membrane.

Equations governing the fluid motion:

A set of linear homogeneous equations that govern the small amplitude distribution of the fluid are as follows. For details see [4], [5].

The Stokes-Navier equation that reduces to the Poiseuille law for compressible fluid is expressed as,

$$\left(\partial_{ct} - l'_v \partial^2_{zz}\right) v_{r(g,c)}(r,z) = -\frac{1}{\rho_0 c_0} \partial_r p_{g,c}(r) \quad \ldots\ldots\ldots (8)$$

Where $l'_v = \dfrac{\mu}{\rho_0 c_0}$ represents the viscous characteristic length.

The conservation of mass equation of the fluid layer with the thickness, h_g in the air gap and h_c in the cavity, is considered as a first order differential element

$$h_{g,c}\, \mathrm{div_r}\left\langle v_{r(g,c)}(r,z)\right\rangle + j\omega\xi(r) = -\frac{j\omega}{\rho_0} h_{g,c}\left\langle \rho'_{g,c}(r,z)\right\rangle \quad \ldots\ldots\ldots (9)$$

Where the left hand side of the equation is the volume flux amplitude, and $\xi(r)$ is the amplitude of relative displacement of the membrane and is considered as the driving term for the fluid motion.

The state equation taking into account that the density variation $\rho'_{g,c}(r,z)$, regarded as a function of the independent variables $\rho_{g,c}(r)$ and $\tau_{g,c}(r,z)$, is considered as the total differential

$$\left\langle \rho'_{g,c}(r,z)\right\rangle = \frac{\gamma}{c_0^2}\left[p_{g,c}(r) - \beta\left\langle \tau_{g,c}(r,z)\right\rangle\right] \ldots\ldots\ldots (10)$$

Here $\gamma = C_P/C_V$ is the specific heat ratio, where C_P the heat coefficient at constant pressure per unit of mass and C_V the heat coefficient at constant volume per unit of mass, and $\beta = (\partial_T P)_\rho = (\partial P/\partial T)_\rho$ is the increase in pressure per unit increase in temperature at constant density.

The Fourier equation for conduction of heat, expressing that the equation taking into account the entropy variation regarded as a function of the independent variables p and τ, is considered as the total differential

$$\left(\partial_{ct} - l_h \partial_{zz}^2\right) \tau_{g,c}(r,z) = \frac{(\gamma-1)}{\beta\gamma} \partial_{ct} p_{g,c}(r) \quad \ldots\ldots\ldots (11)$$

Where the thermal characteristic length l_h is defined as $l_h = \frac{\lambda_h}{\rho_0 c_0 C_P}$, λ_h being the thermal conductivity, ρ_0 is the density of gas, c_0 is the adiabatic speed of sound.

Equations governing the pressure variations:

As the no-slip condition is applied, the velocity of the particle in the fluid gap vanishes on the membrane, on the backing electrode and on the bottom of the cavity, and thus $v_{r(g,c)}(z)$ is assumed to be equal to zero throughout the fluid film. Therefore,

$$v_{r(g,c)}(r,0) = v_{r(g,c)}(r,-h_{g,c}) = 0 \quad \ldots\ldots\ldots (12)$$

The temperature variation $\tau_{g,c}(r,z)$ is also required to vanish on the walls, as the thermal conductivity and the specific heat per unit volume of the materials of the membrane and the rigid backing plate greatly exceed the corresponding quantities for the fluid, and thus we can write

$$\tau_{g,c}(r,0) = \tau_{g,c}(r,-h_{g,c}) = 0 \quad \ldots\ldots\ldots (13)$$

Since the pressure variation $p_{g,c}(r)$ does not depend on the z-coordinate, the usual solutions of equations (8) and (11) by taking into account the equations, (12) and (13) give the radial velocity of the particles, $v_{r(g,c)}(r,z)$, and temperature variation, $\tau_{g,c}(r,z)$, and can be expressed as follows:

$$v_{r(g,c)}(r,z) \cong -\frac{1}{j\omega\rho_0} \partial_r p_{g,c}(r) \qquad \text{and} \qquad \tau_{g,c}(r,z) = \frac{(\gamma-1)}{\beta\gamma} p_{g,c}(r) \quad \ldots\ldots\ldots (14)$$

The integration of these equations across the thickness of the fluid leads to the mean values of the radial velocity of the particles ($v_{r(g,c)}(r,z)$) and temperature variation ($\tau_{g,c}(r,z)$), and is expressed as

$$\left\langle v_{r(g,c)}(r,z)\right\rangle_z = -\frac{1}{j\omega\rho_0}\partial_r p_{g,c}(r)F_{v(g,c)} \quad \ldots\ldots\ldots (15)$$

and

$$\left\langle \tau_{g,c}(r,z)\right\rangle_z = \frac{(\gamma-1)}{\beta\gamma} p_{g,c}(r)F_{h(g,c)} \quad \ldots\ldots\ldots (16)$$

With $k_v = \frac{(1-j)}{\sqrt{2}}\sqrt{\frac{\rho_0\omega}{\mu}}$, $k_h = \frac{(1-j)}{\sqrt{2}}\sqrt{\frac{\rho_0\omega C_P}{\lambda_h}}$ and $F_{v,h(g,c)} = 1 - \frac{\tan\left(k_{v,h}h_{g,c}/2\right)}{k_{v,h}h_{g,c}/2}$

Where k_v is the wavenumber associated with the vertical movement due to viscosity effects (with a time factor given by $e^{j\omega t}$), ρ_0 and μ are the density and the shear viscosity coefficient of the gas respectively. k_h is the wavenumber associated with the entropic movement due to conduction effects (with a time factor given by $e^{j\omega t}$) and, λ_h is the coefficient of thermal conductivity of the gas respectively.

The combination of equations (16) and (10) gives

$$p_{g,c}(r) = C^2\left\langle \rho'_{g,c}(r,z)\right\rangle \quad \ldots\ldots\ldots (17)$$

Where,

$$C^2 = \frac{1}{\rho_0\chi T[1+(\gamma-1)(1-F_{h(g,c)})]}$$

Equation (17) represents a poly-tropic compressibility law which tends to an isothermal, respectively adiabatic, law for a very thin, respectively very large, layer of fluid compared to the characteristic length $l_h = -\frac{j\omega}{c_0 k_h^2}$.

Finally, combining equations (16) and (9) we get the wave equation for the acoustic pressure

$$(\Delta_r + \chi_{g,c}^2)p_{g,c}(r) = \zeta_{g,c}\xi(r) \quad \ldots\ldots\ldots (18)$$

Where $\chi_{g,c}$ represents the complex wavenumber, and is defined as

$$\chi_{g,c} = \frac{\omega}{c_0}\sqrt{\frac{1+(\gamma-1)(1-F_{h(g,c)})}{F_{v(g,c)}}} = k_0\sqrt{\frac{1+(\gamma-1)(1-F_{h(g,c)})}{F_{v(g,c)}}} \quad \ldots\ldots\ldots (19)$$

$$\text{With } k_0 = \frac{\omega}{c_0}$$

And $\zeta_{g,c}\xi(r)$ with $\zeta_{g,c} = -\frac{\rho_0\omega^2}{h_{g,c}F_{v(g,c)}}$ on the RHS refers to source term.

Acoustic pressure inside the transducer:

The solution of the wave equation (18) for the acoustic pressure in the air gap consists of the general solution, finite at $r = 0$. The pressure in the air gap is

$$p_g(r) = AJ_0(\chi_g r) + \sum_m p_{gm}\Psi_m(r) \quad \ldots\ldots\ldots (20)$$

$$p_{gm} = \frac{\zeta_g\xi_m}{\chi_g^2 - K_m^2} \quad \ldots\ldots\ldots (21)$$

Whereas, the acoustic pressure in the cavity could be either uniform or non-uniform depending on the geometry. If the cavity height is large and the section of the cavity is almost square, then the pressure in the cavity is uniform and is given by,

$$p_c = Z_c w_c \quad \ldots\ldots\ldots (22)$$

$$\text{and } Z_c = \frac{\rho_0 c_0^2}{j\omega V_c}$$

where Z_c represents the acoustic impedance of the cavity, V_c is the volume of the cavity, and w_c is the volume velocity which can be expressed as,

$$w_c = 2\pi R_e h_g \langle \upsilon_{rg}(R_e, z) \rangle_z - j\omega \iint_{S_{em}} \xi(r) dS_{em} \quad \ldots\ldots\ldots (23)$$

where $S_{em} = \pi(R_m^2 - R_e^2)$.

On the other hand, when the radial dimension of the cavity becomes more important than its height, the radial particle velocity predominates and the cavity acts as an annular slit. In this case the acoustic pressure in the cavity is non-uniform and is given by the solution of the equation (18).

$$p_c(r) = B_1 J_0(\chi_c r) + B_2 Y_0(\chi_c r) + \sum_m p_{cm} \Psi_m(r), \qquad p_{cm} = \frac{\zeta_c \xi_m}{\chi_c^2 - K_m^2} \quad \dots\dots\dots (24)$$

A, B_1, B_2 are the integration constant. Details are available in Alexey et al. [2].

Mean displacement of the membrane:

Introducing both parts of the acoustic pressure p_g and p_c to the equation (7) we get,

$$\xi_n T(K^2 - K_n^2) = p_{inc} \iint_{S_m} \Psi_n(r) dS_m - \iint_{S_e} p_g(r) \Psi_n dS_e - \iint_{S_{em}} p_c(r) \Psi_n(r) dS_{em} \quad \dots\dots\dots (25)$$

where $S_e = \pi R_e^2$, known as effective surface area of membrane.

Mean displacement of the membrane over the electrode takes the form

$$\langle \xi \rangle_{Se} = \frac{1}{S_e} \iint_{S_e} \xi(r) dS_e = \frac{2}{\sqrt{\pi} R_e R_m} \sum_n \xi_n \frac{J_1(K_n R_e)}{K_n J_1(K_n R_m)} \quad \dots\dots\dots (26)$$

For further details see [1], [2].

APPENDIX B: DOE experimental data

Nº Exp	R_m	R_b	h_c	h_g	T_m	t_m	C_0	$\|\langle\xi_{Se}\rangle\|_{fr1}$	Q_f	ΔC	$\Delta C/C_0$	V_{out}	$\|\langle\xi_{Se}\rangle\|_{fr2}$
	mm	mm	µm	µm	N/m	µm	pF	nm		fF	%	mV	nm
1	4.0	0.250	1000	3.0	3000	8.0	3.3464	0.4300	10.3200	0.0830	0.0025	0.2870	1.6410
2	10.0	0.250	1000	3.0	100	8.0	7.7734	1.3300	12.0200	0.2570	0.0033	0.8888	5.6821
3	4.0	3.000	1000	3.0	100	8.0	84.1824	0.0690	9.7000	1.9160	0.0023	0.0459	0.1131
4	10.0	3.000	1000	3.0	3000	8.0	88.6094	0.0525	7.0770	1.4620	0.0016	0.0350	0.7420
5	4.0	0.250	4000	3.0	100	8.0	3.3464	17.2730	30.0300	3.3560	0.1003	11.5150	4.2700
6	10.0	0.250	4000	3.0	3000	8.0	7.7734	3.0500	15.9400	0.5900	0.0076	2.0330	8.9893
7	4.0	3.000	4000	3.0	3000	8.0	84.1824	0.0528	19.4040	1.4680	0.0017	0.0350	0.1083
8	10.0	3.000	4000	3.0	100	8.0	88.6094	1.3190	113.7200	36.7100	0.0414	0.8800	2.0654
9	4.0	0.250	1000	80.0	100	8.0	0.1255	491.3900	163.6120	0.1343	0.1070	12.2850	174.9666
10	10.0	0.250	1000	80.0	3000	8.0	0.2915	44.6800	34.0000	0.0121	0.0042	1.1170	22.9508
11	4.0	3.000	1000	80.0	3000	8.0	3.1568	0.5510	4.4540	0.0216	0.0007	0.0138	0.4361
12	10.0	3.000	1000	80.0	100	8.0	3.3229	5.0200	1.7320	0.1960	0.0059	0.1255	2.5247
13	4.0	0.250	4000	80.0	3000	8.0	0.1255	61.8500	414.5600	0.0168	0.0134	1.5460	1.7019
14	10.0	0.250	4000	80.0	100	8.0	0.2915	2940.9600	115.1000	0.8290	0.2844	73.5200	225.5119
15	4.0	3.000	4000	80.0	100	8.0	3.1568	5.5220	2.3500	0.2160	0.0068	0.1380	3.8159
16	10.0	3.000	4000	80.0	3000	8.0	3.3229	9.4400	6.4150	0.3690	0.0111	0.2360	1.1416
17	4.0	1.625	2500	41.5	1550	8.0	1.8965	1.6440	3.5990	0.0700	0.0037	0.0790	0.2336
18	10.0	1.625	2500	41.5	1550	8.0	2.2165	21.5600	8.1500	0.9200	0.0415	1.0390	25.0591
19	7.0	0.250	2500	41.5	1550	8.0	0.4019	371.6200	269.6200	0.3790	0.0943	17.9100	57.0884
20	7.0	3.000	2500	41.5	1550	8.0	6.2455	1.3500	0.6300	0.1960	0.0031	0.0650	1.0635
21	7.0	1.625	1000	41.5	1550	8.0	2.0565	6.3800	5.8800	0.2720	0.0132	0.0307	5.4758
22	7.0	1.625	4000	41.5	1550	8.0	2.0565	8.1800	4.8150	0.3490	0.0170	0.3940	2.5423
23	7.0	1.625	2500	3.0	1550	8.0	28.4487	0.5600	16.6200	4.5500	0.0160	0.3720	0.5963
24	7.0	1.625	2500	80.0	1550	8.0	1.0668	42.2000	27.8600	0.4850	0.0455	1.0550	7.0256
25	4.0	0.250	1000	3.0	100	25.0	3.3464	5.5700	36.0100	1.0800	0.0323	3.7200	11.6079
26	10.0	3.000	1000	3.0	100	25.0	88.6094	0.1229	62.3946	3.4181	0.0039	0.0819	0.2327
27	10.0	0.250	4000	3.0	100	25.0	7.7734	27.4500	77.9900	5.3500	0.0688	18.3000	71.7443
28	4.0	3.000	4000	3.0	100	25.0	84.1824	0.0770	9.9800	2.1410	0.0025	0.0513	0.0760

29	10.0	0.250	1000	80.0	100	25.0	0.2915	395.6900	56.3500	0.1080	0.0370	9.8900	101.8086
30	4.0	3.000	1000	80.0	100	25.0	3.1568	2.5500	3.7900	0.1000	0.0032	0.0640	7.6070
31	4.0	0.250	4000	80.0	100	25.0	0.1255	1657.0600	45.6500	0.4600	0.3666	41.4300	273.3273
32	10.0	3.000	4000	80.0	100	25.0	3.3229	23.5800	2.4000	0.9230	0.0278	0.5900	58.3053
33	10.0	0.250	1000	3.0	3000	25.0	7.7734	1.0040	0.0500	0.1939	0.0025	0.6691	3.9947
34	4.0	3.000	1000	3.0	3000	25.0	84.1824	0.0480	11.2200	1.3350	0.0016	0.0320	0.1531
35	4.0	0.250	4000	3.0	3000	25.0	3.3464	1.2000	9.2600	0.2300	0.0069	0.8000	0.7128
36	10.0	3.000	4000	3.0	3000	25.0	88.6094	0.6980	36.2200	19.4100	0.0219	0.4650	0.0306
37	4.0	0.250	1000	80.0	3000	25.0	0.1255	298.9900	1095.9400	0.0820	0.0653	7.4800	0.5123
38	10.0	3.000	1000	80.0	3000	25.0	3.3229	13.3440	10.4800	0.5200	0.0156	0.3300	3.1628
39	10.0	0.250	4000	80.0	3000	25.0	0.2915	2364.9100	1452.6500	0.6620	0.2271	59.1200	2.7690
40	4.0	3.000	4000	80.0	3000	25.0	3.1568	1.0520	6.8600	0.0410	0.0013	0.0263	0.1097
41	10.0	1.625	2500	41.5	1550	16.5	2.2165	32.8200	11.5900	1.4000	0.0632	1.5800	11.7067
42	7.0	0.250	2500	41.5	1550	16.5	0.4019	611.5600	417.8200	0.6270	0.1560	29.4700	6.2560
43	7.0	1.625	1000	41.5	1550	16.5	2.0565	9.9900	7.8200	0.4300	0.0209	0.4800	3.1932
44	7.0	1.625	2500	3.0	1550	16.5	28.4487	0.9800	18.0300	8.0000	0.0281	0.6540	0.0703
45	7.0	1.625	2500	41.5	100	16.5	2.0565	13.1800	1.0500	0.5600	0.0272	0.6350	30.8702
46	7.0	1.625	2500	41.5	3000	16.5	2.0565	8.7700	9.5800	0.3740	0.0182	0.4220	0.9233
47	5.9	1.322	2266	36.9	1407	15.8	1.5920	12.6200	10.3700	0.4500	0.0283	0.6800	2.3342
48	8.1	1.322	2266	36.9	1407	15.8	1.7240	30.0200	14.2800	1.0700	0.0621	1.6300	8.3485
49	7.0	2.231	2266	36.9	1407	15.8	4.0380	2.6900	1.5700	0.2740	0.0068	0.1460	1.2359
50	7.0	1.625	3202	36.9	1407	15.8	2.3129	9.5900	5.7800	0.5200	0.0225	0.5200	2.1423
51	7.0	1.625	2500	60.1	1407	15.8	1.4201	35.6200	19.1400	0.7200	0.0507	1.1900	6.3362
52	7.0	1.625	2500	41.5	2265	15.8	2.0565	10.0943	9.4500	0.4300	0.0209	0.4900	2.1458
53	7.0	1.625	2500	41.5	1550	20.8	2.0565	14.4900	9.7800	0.6200	0.0301	0.7000	2.8049
54	4.0	0.500	1000	80.0	100	8.0	0.1838	340.0400	107.8000	0.3700	0.2013	8.5000	17.9818
55	4.0	0.500	4000	80.0	3000	8.0	0.1838	59.7000	355.5000	0.0650	0.0354	1.5000	1.5523
56	10.0	0.500	4000	80.0	100	8.0	0.3498	2365.3000	120.3000	2.8500	0.8148	59.1000	97.2469
57	7.0	0.500	2500	41.5	1550	8.0	0.5143	266.9000	189.7000	1.0850	0.2110	12.9000	4.8735
58	7.0	0.500	2500	80.0	1550	8.0	0.2668	600.6000	418.6000	0.6600	0.2474	15.0200	5.0822
59	4.0	0.500	4000	80.0	100	25.0	0.1838	892.7000	102.9700	0.9800	0.5333	22.3200	65.9063
60	4.0	0.500	1000	80.0	3000	25.0	0.1838	214.6200	705.4000	0.2330	0.1268	5.4000	0.7258
61	10.0	0.500	4000	80.0	3000	25.0	0.3498	1954.8000	860.8000	2.2000	0.6290	48.9000	3.9153
62	7.0	0.500	2500	60.1	1407	15.8	0.3551	743.4000	407.1000	1.4500	0.4083	24.7400	4.2702

APPENDIX C: Statistical and mathematical tools

Analysis of Variance (ANOVA)

The analysis of variance (ANOVA) is the basis of the statistical analysis that follows the fitting of the model [6]. General structure of Analysis of variance (ANOVA) table can be given as follows,

Source of variation	Sum of squares	Degrees of freedom	Mean square	Ratio/ F-value	Sig.
Regression	SS_{Reg}	df_{Reg}	MS_{Reg}	$\frac{MS_{Reg}}{MS_{Res}}$	p-value
Residuals	SS_{Res}	df_{Res}	MS_{Res}		
Total	SS_{Total}	df_{Total}			

Sum of Squares

Regression sum of square (SS_{Reg}): The regression sum of square is a quantity that is used to describe how well a model represents the data being modeled.

$$\mathrm{SS}_{\mathrm{Reg}} = \sum_{i=1}^{n} (\hat{y}_i - \bar{y}_i)^2$$

Residuals sum of squares (SS_{Res}): In statistics, the residual sum of squares is the sum of squares of residuals, which is a measure of the discrepancy between the data and an estimated model. SS_{Res} can be given as,

$$\mathrm{SS}_{\mathrm{Res}} = \sum_{i=1}^{n} (y_i - \hat{y}_i)^2$$

Total sum of squares (SS_{Total}): Total sum of squares is a quantity that is defined as being the sum, over all observations, of the squared differences of each observation from the overall mean and can be expressed as follows,

$$\mathrm{SS}_{\mathrm{Total}} = SS_{\mathrm{Reg}} + SS_{\mathrm{Res}} = \sum_{i=1}^{n} (y_i - \bar{y}_i)^2$$

Where, y_i represents actual data or experimental values, $\hat{y}_i$ being the estimated value, and $\bar{y}_i$ represents the mean of actual data and is defined as $\bar{y}_i = \sum_i^n \frac{y_i}{n}$).

Degrees of Freedom

In statistics, the degrees of freedom is the number of values in the final calculation of a statistic that can be varied freely.

Second order polynomial equation is given by,

$$\hat{Y_i} = \beta_0 + \sum_{i=1}^{6} \beta_i x_i + \sum_{i=1}^{6} \beta_{ii} x_i^2 + \sum_{i=1}^{5} \sum_{i<j}^{6} \beta_{ij} x_i x_j + \varepsilon$$

A second order polynomial equation estimates the total numbers of variables or regressors (N_{Reg}) of 28, which consists of 1 constant, 6 linear terms, 6 quadratic terms, and 15 interaction terms. Therefore,

Degrees of freedom of regressions, $df_{\text{Reg}} = \text{k}$

Degrees of freedom of residuals, $df_{\text{Res}} = \text{n - k -1}$

Total degree of freedom, $df_{\text{Total}} = df_{\text{Reg}} + df_{\text{Res}}$

Where, N_{Reg} represents the Total number of regressors, k represents the number of regressors without constant and defined as $k = N_{Reg} - 1$, n represents number of experiments.

Mean Squares:

Regression mean square (MS_{Reg}): The regression mean square is the sum of squares per coefficient, explained by the model and can be expressed as follows,

$$MS_{\text{Reg}} = \frac{SS_{\text{Reg}}}{df_{\text{Reg}}}$$

Residual mean square (MS_{Res}): The residual mean square can be considered as an estimate of the variance and its square root as an estimate of the standard deviation of the experimental technique. MS_{Res} can be expressed as,

$$MS_{\text{Res}} = \frac{SS_{\text{Res}}}{df_{\text{Res}}}$$

Total mean square (MS_{Total}): The total mean square is an estimate of total variance against the grand mean and given by,

$$MS_{Total} = \frac{SS_{Total}}{df_{Total}}$$

F-ratio:

An F-test is a statistical test in which the test statistic has an F-Distribution under the null hypothesis, which investigates whether two populations are equal based on the variances of two samples from those populations. The ratio F is calculated by,

$$F - Ratio = \frac{MS_{\text{Reg}}}{MS_{\text{Res}}}$$

And expressed as, $F(\text{numerator, denominator}) = F(df_{\text{Reg}}, df_{\text{Res}}) = \frac{MS_{\text{Reg}}}{MS_{\text{Res}}}$

Critical value to F-ratio can be obtained from F-distribution table [7] based on the value of numerator (df_1) & denominator (df_2) in the table.

p-value:

The significance (Sig.) or p-value in the table is the probability (between o and 1) of obtaining a ratio of mean squares greater than F-ratio.

$$p - value = \frac{\bar{x} - \mu_0}{\sigma / \sqrt{n}}$$

Where $\bar{x}$ represents the mean of the actual data, μ_0 is the null hypothesis mean value, σ is the variance and n is the number of samples or experiments.

The significance level in the conventional manner is represented as follows:

***	:	< 0.001 (0.1%)
**	:	< 0.01 (1%)
*	:	< 0.05 (5%)
A	:	≥ 0.05 (5%)

R-square (R^2) value:

In statistics, the coefficient of determination, denoted R^2, is a number that provides a measure of how well observed outcomes are replicated by the model. In other words, R^2 is often used to judge the adequacy of a regression model and can be quantified as follows,

$$R^2 = 1 - \frac{\mathrm{SS_{Res}}}{\mathrm{SS_{Total}}} = 1 - \frac{\mathrm{SS_{Total}} - \mathrm{SS_{Reg}}}{\mathrm{SS_{Total}}} = \frac{\mathrm{SS_{Reg}}}{\mathrm{SS_{Total}}}$$

Range of R^2 is in between 0 to 1. The R^2-value of 1 indicates that the regression line perfectly (100%) fits the actual data.

Adjusted R-square (R_a^2) value:

Adjusted R-squared is nothing but the change of R-square that adjusts the number of terms in a model. Adjusted R-square calculates the proportion of the variation in the dependent variable (response) accounted by the explanatory variables (factors).

$$R_a^2 = \frac{\left(MS_{Total} - MS_{\mathrm{Res}}\right)}{MS_{Total}} = 1 - \frac{\frac{\mathrm{SS_{Res}}}{\mathrm{df_{Res}}}}{\frac{\mathrm{SS_{Total}}}{\mathrm{df_{Total}}}} = 1 - \left(1 - R^2\right)\frac{(n-1)}{n-(k-1)-1}$$

APPENDIX D: Bending test of inkjet-printed silver layer on thin film

The mechanical performance, such as the adhesion of the printed conductive silver layer, the flexibility and the lifecycle of the printed conductive silver layer on thin Mylar film of thickness of 8 µm has been evaluated by bending test. In this regard, the bending test has been performed on square shaped inkjet-printed conductive silver layer of thickness of 550±50 nm on thin Mylar film, sintered at 140 °C for 30 minutes. The resistivity of the layer is monitored using JANDEL four point probe system. Printed silver layer exhibits the average sheet resistance of 128±6.3 mΩ/square before bending. The experimental setup of the bending test is illustrated in Figure A2. During the bending test, curvature radius of 5 mm and 25 mm were used under constant tension.

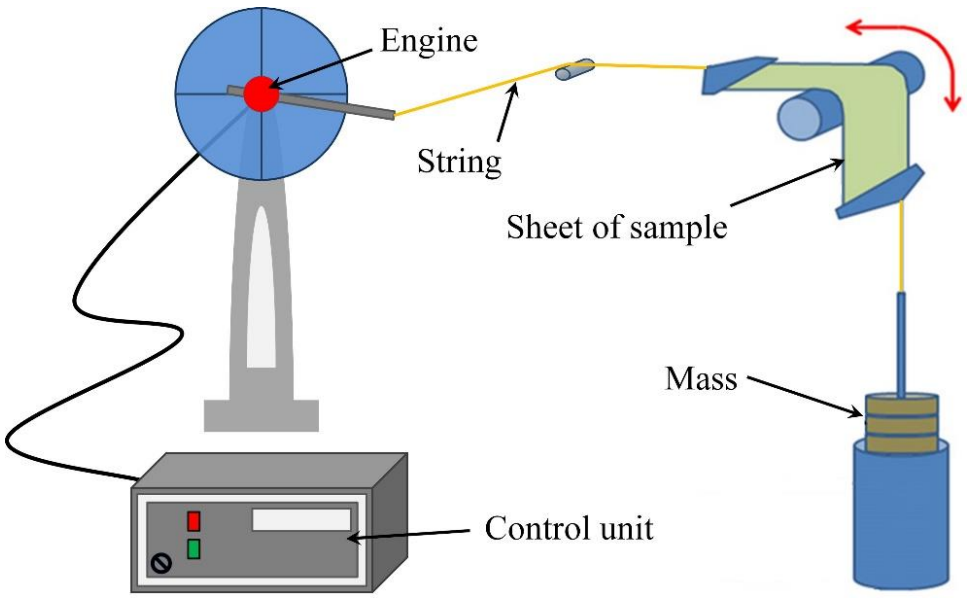

Figure A2: *Schematic diagram of the experimental setup of the bending fatigue machine.*

It has been observed that the printed layers were mechanically well stable. The resistivity of the conductive layers increase with the number of bending cycle (Figure A3). After 10000 cycles, the sheet resistance reaches 195.3±9.8 mΩ/square and 227.6±13.2 mΩ/square for bending radius of 25 mm and 5 mm respectively. This increase in resistance is caused by the formation of local small micro-cracks, as illustrated in Figure A4. Observation has revealed that the use of larger bending radius causes the formation of less number of localized cracks and thus the less deterioration of the electrical properties.

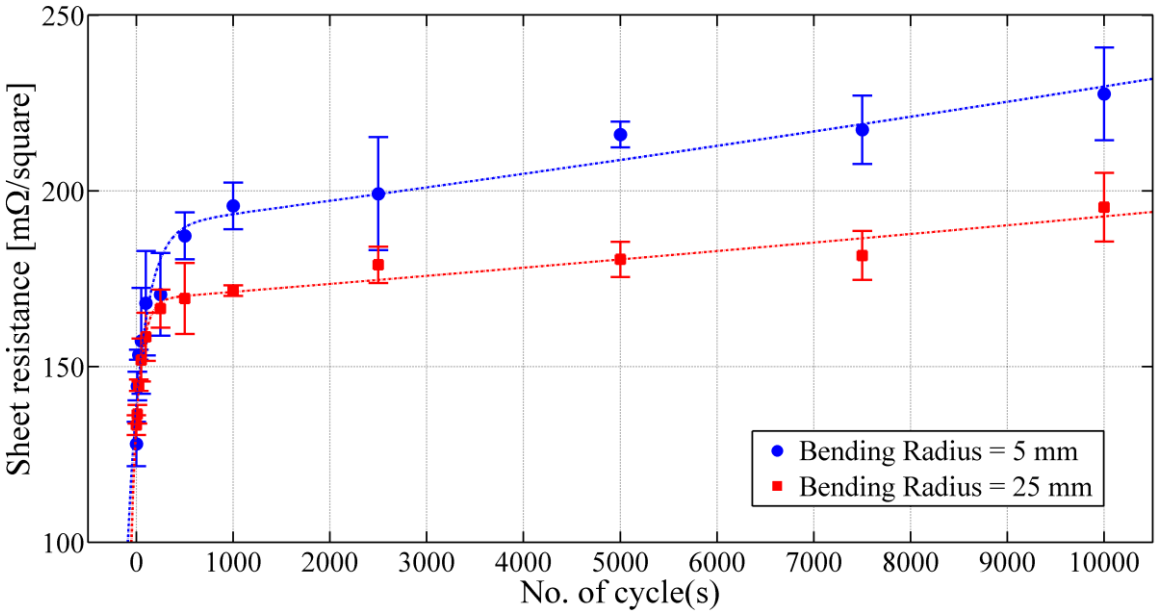

Figure A3: *Sheet resistance (R_s) of the inkjet-printed conductive silver layer on thin Mylar film versus number of bending cycles.*

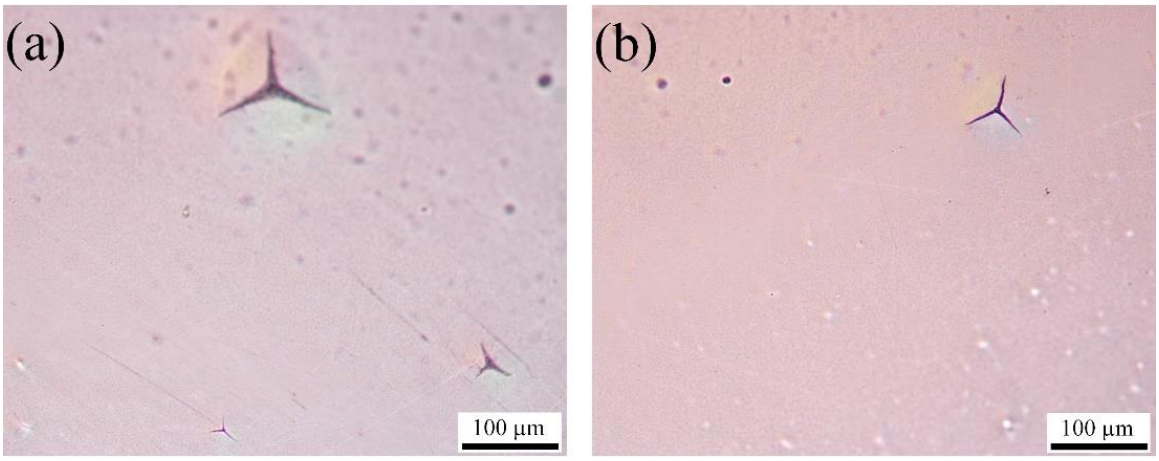

Figure A4: *Optical viewgraph of the inkjet-printed conductive silver layer on thin Mylar film after bending test for 10000 cycles, (a) using curvature radius of 5 mm, and (b) using curvature radius of 25 mm.*

APPENDIX E: Alternative techniques to develop the capacitive acoustic transducer

The three-dimensional (3D) bottom structure of the acoustic transducer with cavity and backplate can also be developed using alternative manufacturing technique, namely, mechanical micromachining and laser ablation technique.

In case of implementation of mechanical micromachining method, thick polyethylene terephthalate (PET) sample having thickness of 480 µm has initially been attached to the printed circuit board (PCB) using adhesive and then patterned using ProtoMat S62 mechanical micromachining tool from "LPKF Lase & Electronics AG" according to the transducer design. Another piece of PCB was patterned as well to create venting hole. Two parts have then been joined together to form the final bottom structure of the transducer having a backplate, a large cavity and venting hole. Finally, backplate electrode has been printed on PET surface using Dimatix inkjet printing technique. The air gap can either be inkjet-printed using UV curable dielectric ink or by using spacer. The membrane is fabricated by printing conductive layer on a thin Mylar film having thingness below 25 µm and then gluing it to the rigid frame. Figure A5 presents the components of an acoustic sensor development using mechanical micromachining tool.

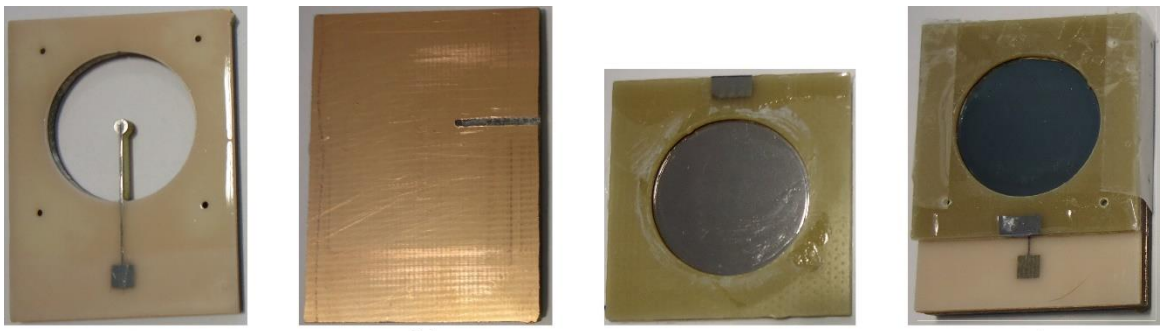

Figure A.5: *Components of an acoustic transducer developed using mechanical micromachining tool (a) bottom structure with printed electrode, (b) parts with the venting channel (c) printed conductive layer on thin film and glued on frame to fabricate membrane, and (d) assembled device.*

However, the device fabricated by above mentioned method using mechanical micromachining technique is relatively complex and is limited to only certain dimension, based on the availability of the thickness of the substrate, and shape. In addition, the fabricated device is quite heavy.

On the other hand, laser ablation technique could be another possible alternating method to fabricate the 3D bottom structure of the transducer. Preliminary laser ablation tests on polyethylene terephthalate (PET), polyimide (PI) and poly carbonate (PC) substrates have been performed using Excimer KrF laser with wavelength of 248 nm and frequency of 10 Hz for different number of shots. Figure A.6 illustrates the confocal microscopic image of the PET substrate after laser ablation.

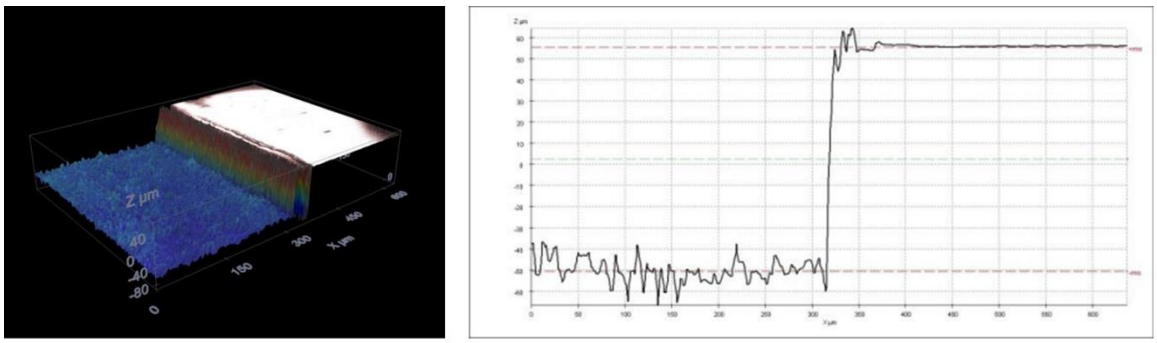

Figure A.6: *Confocal microscopic image (representative) of laser ablated PET substrate.*

Initial tests have revealed that two parameters, namely, fluence in mJ/cm^2 and number of shots (N_s), play an important role during laser ablation. Figure A.7 shows that the step height increases with increasing fluence, whereas roughness decreases with increasing fluence. On the other hand, step height increases with the number of shots; however roughness of the etched surface increases with the increasing number of shots.

The main concerns to use laser ablation to develop the bottom structure are the maximum achievable etching height and the surface roughness for the later inkjet printing of the conductive silver layer. In order to obtain good quality printed conducting layer, low surface roughness is required that should be lower than the thickness of the printed conductive layer. Although the initial test exhibits good promising results; however, further

experiments are required to optimize the laser ablation parameters in order to achieve the required step height with low surface roughness.

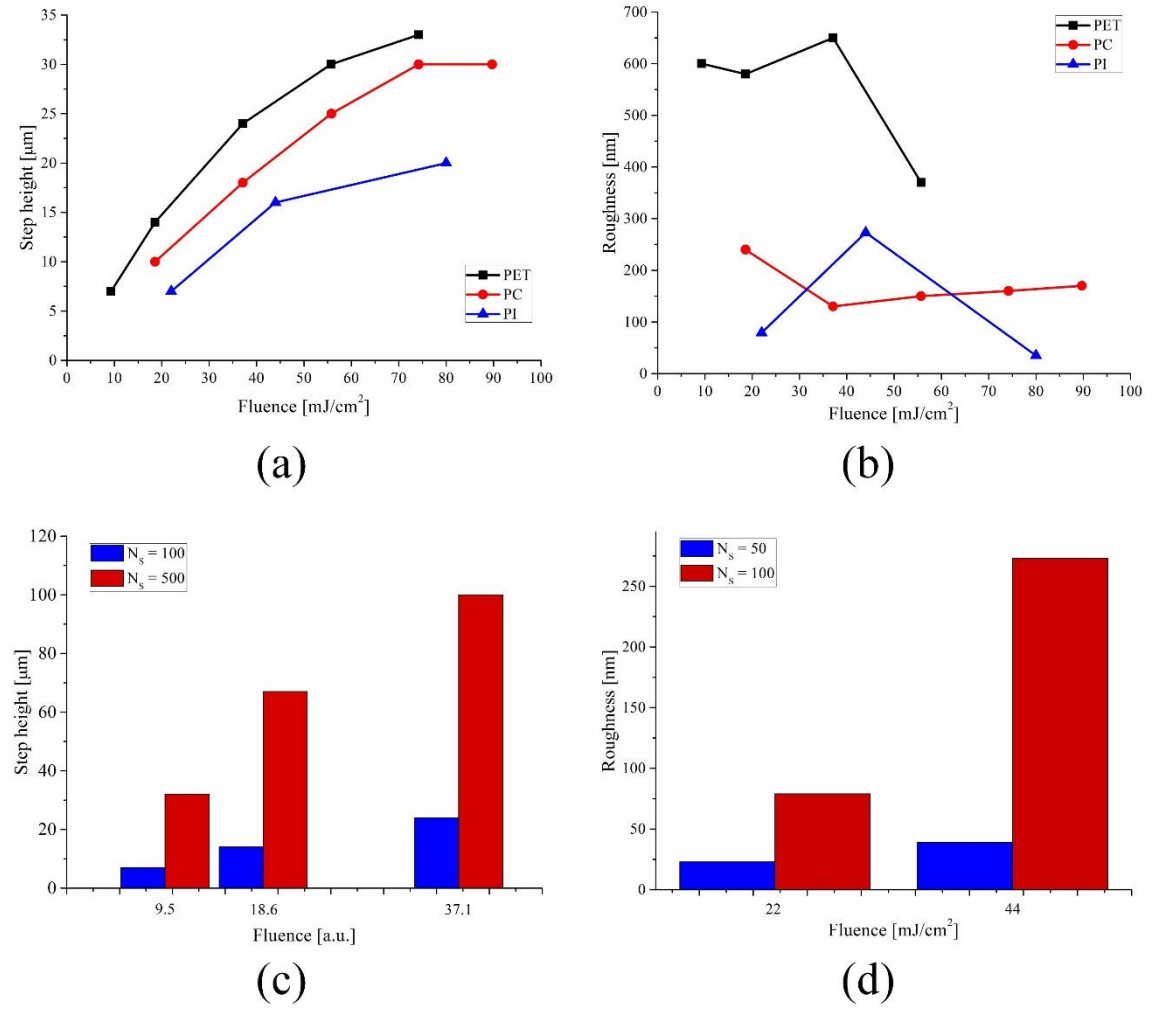

Figure A.7: *Graphical representation of laser ablation of PET, PC-black and Kapton polymer (a) Step height vs Fluence for Ns = 100, (b) Roughness vs Fluence for Ns = 100, (c) Step height vs No. of shot on PET substrate, and (d) Roughness vs No. of shot of PI substrate.*

References

[1] Petr Honzík, Alexey Podkovskiy, Stéphane Durand, Nicolas Joly, and Michel Bruneau, "Analytical and Numerical Modeling of an Axisymmetrical Electrostatic Transducer with Interior Geometrical Discontinuity," *J. Acoust. Soc. Am.*, vol. 134, no. 5, pp. 3573–3579, 2013.

[2] Alexey Podkovskiy, Petr Honzík, Stéphane Durand, Nicolas Joly, and Michel Bruneau, "Miniaturized Electrostatic Receiver with Small-Sized Backing Electrode," in *Proceedings of Meetings on Acoustics*, Montreal, Canada, 2013, vol. 19, p. 030047.

[3] Tomas Lavergne, Stéphane Durand, Michel Bruneau, and Nicolas Joly, "Dynamic Behaviour of the Circular Membrane of an Electrostatic Microphone: Effect of Holes in the Backing Electrode," *J. Acoust. Soc. Am.*, vol. 128, no. 6, pp. 3459–3477, 2010.

[4] Michel Bruneau, Anne-Marie Bruneau, Zdeněk Škvor, and Pierrick Lotton, "An Equivalent Network Modelling the Strong Coupling Between a Vibrating Membrane and a Fluid Film," *Acta Acust.*, vol. 2, pp. 223–232, 1994.

[5] Michel Bruneau, Anne-Marie Bruneau, and Pascal Hamery, "An Improved Approach to Modeling the Behaviour of Thin Fluid Films Trapped Between a Vibrating Membrane and a Backing Wall and Surrounded by a Reservoir at the Periphery," *Acta Acust.*, vol. 1, pp. 227–234, 1993.

[6] Gareth A Lewis, Didier Mathieu, and Roger Phan-Tan-Luu, *Pharmaceutical experimental design*. New York: Dekker, 1999.

[7] Ivo Dinov, "F Distribution Tables," *Statistics Online Computational Resource (SOCR)*. [Online]. Available: http://www.socr.ucla.edu/applets.dir/f_table.html. [Accessed: 20-Mar-2015].

RÉSUMÉ

DESIGN ET DEVELOPPEMENT D'UN CAPTEUR ACOUSTIQUE IMPRIME

Ce travail a été mené dans le cadre d'une thèse CIFRE (Conventions Industrielles de Formation par la REcherche), initiée par le Ministère de l'Enseignement Supérieur et de la Recherche et mise en œuvre par l'Association Nationale de la Recherche et de la Technologie (ANRT). La thèse CIFRE vise à développer les activités de recherche stratégique de l'entreprise et scelle un accord industriel de formation par la recherche. Cette thèse traite du développement d'un nouveau type de capteur acoustique ayant une très haute sensibilité et sélectivité en utilisant les techniques émergentes d'impression.

1. Introduction

Un capteur acoustique est un transducteur qui convertit l'énergie acoustique en énergie électrique. Le principe de fonctionnement d'un capteur acoustique est similaire à celui d'un capteur de pression. Un transducteur acoustique fournit un signal de sortie analogique proportionnel à la pression acoustique exercée sur un diaphragme flexible. Les exemples les plus familiers de capteurs acoustiques sont les microphones, les casques audio, … Il existe différents types de capteurs acoustiques : piézoélectrique, piézorésistif et capacitif [1].

Depuis très longtemps, les capteurs acoustiques ont été utilisés dans des applications civiles et militaires telles que, les aides auditives, les téléphones mobiles, les ordinateurs, les microphones de très haute qualité pour l'enregistrement [2], les sonars pour la détection sous-marine [3] et les systèmes acoustiques pour la surveillance de cibles [4]. A ce jour, la majorité des capteurs acoustiques est dédiée aux applications audio avec une sensibilité quasi-uniforme sur une large bande de fréquence couvrant le spectre humain audible de 20 Hz à 20 kHz.

Dans le cadre du projet Spinnaker, TAGSYS ambitionne de développer des systèmes RFID (Identification Radio Fréquence) avec une géolocalisation améliorée. TAGSYS RFID envisage d'incorporer un capteur acoustique capacitif, présentant une capacité nominale comprise entre 0.5 et 3 pF, une variation de capacité supérieure à 1 fF et un facteur de qualité supérieure à 25 à la résonance fondamentale pour une puissance acoustique égale à 80 dB_{SPL}.

Le principe de fonctionnement du capteur acoustique résonant proposé est similaire à celui d'un microphone à condensateur avec une sensibilité différente. Généralement, le capteur idéal présente une réponse uniforme sur une très large bande de fréquences alors que

TAGSYS RFID souhaite un transducteur acoustique présentant une très haute sensibilité à une fréquence bien précise qui est la résonance fondamentale du système. Ce type de capteur est connu sous le nom de « capteur acoustique résonant » ou « résonateur acoustique ». Toutefois, ce type de composant n'est pas disponible sur le marché.

Par conséquent, un nouveau design de capteur acoustique capacitif a été proposé par le consortium "Spinnaker" (Figure R.1). Ce travail ambitionne d'étudier les possibilités de conception et de développement d'un nouveau transducteur acoustique capacitif, présentant une bonne sensibilité et sélectivité, en utilisant des techniques de fabrication « bas-coût ».

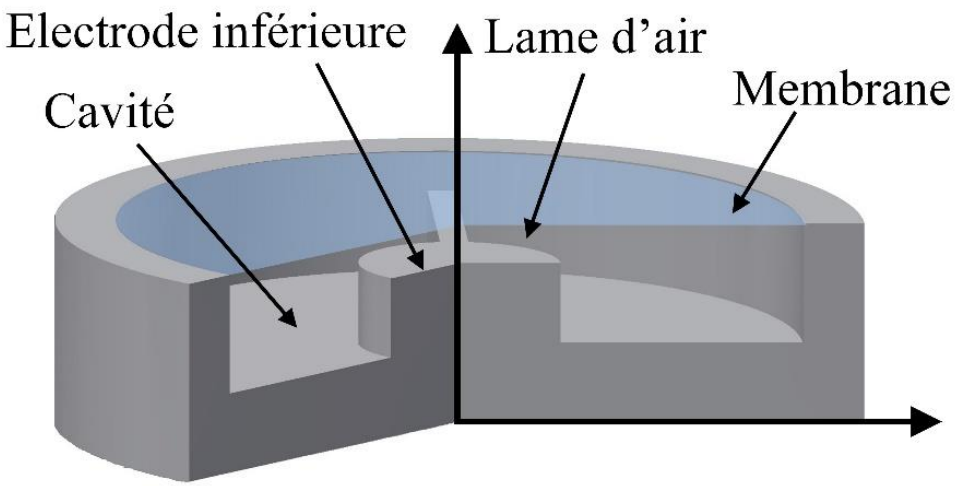

Figure R.1: *Schéma du design du transducteur capacitif acoustique.*

Des méthodes soustractives telles que la photolithographie sont généralement mises en œuvre pour fabriquer des transducteurs acoustiques. Ce procédé comprend plusieurs étapes de dépôt, masquage, gravure et nettoyage pour fabriquer une structure 3D. De plus, cette technique présente un temps et coût de procédé élevés et génère de large quantité de déchets dangereux pour l'environnement. D'autre part, les techniques de dépôt sous vide, pour la fabrication de composants électroniques, consomment beaucoup d'énergie et présentent une faible résolution [5]. Par conséquent, pour satisfaire la demande du marché global pour des produits électroniques de haute qualité peu chers et pour réduire la consommation de matières de premières, la recherche de méthodes innovantes de fabrication amène à de nouveaux procédés de dépôt et de gravure tels que les techniques d'impression.

Parmi les techniques bien maîtrisées, l'impression jet d'encre est une technique additive sans contact permettant de positionner des gouttes de matériau liquide avec précision sur

un substrat. L'impression jet d'encre se fait à température ambiante et utilise peu de produits chimiques dangereux. La transition de la fabrication sous vide poussée de matériaux ultra-purs vers l'impression réduit le coût de fabrication. De plus, cette technique est flexible, versatile, et peut être mise en œuvre assez facilement, puisqu'elle ne requiert pas de masques ou pochoirs [5]–[7]. Par conséquent, l'impression jet d'encre pourrait être une alternative potentielle pour la fabrication microélectronique grâce à sa haute résolution d'impression, son faible coût et sa faible production de déchets. Toutefois, des recherches complémentaires au niveau des matériaux sont requises pour atteindre des produits finis plus performants avec une meilleure fiabilité. Ce travail exploratoire va permettre de développer une plus grande gamme d'applications [8]. En outre, la technologie jet d'encre réduit le nombre d'étapes de procédé par rapport à la photolithographie et ainsi la complexité du procédé.

Le jet d'encre comprend l'impression directe de motifs et le recuit de l'encre déposée pour retirer les solvants, initier la cohésion du film et aboutir à l'optimisation fonctionnelle de la couche imprimée [9]. Le recuit peut se faire de façon conventionnelle dans un four ou à l'aide d'autres techniques sélectives telles que le laser, les micro-ondes, le chauffage par effet joule [10]–[12] et le recuit photonique [5], [13], [14].

La possibilité de concevoir des motifs sans ajout d'étapes additionnelles de procédé augmente le rendement. Cependant, le jet d'encre offre une résolution plus faible que la photolithographie [15], [16]. La résolution du jet d'encre est de quelques dizaines de microns. Elle peut être améliorée en optimisant l'encre, le substrat, le volume de la goutte, la vitesse d'impression et l'espacement entre les gouttes [16]. Généralement, le jet d'encre est mieux adapté pour les matériaux solubles de faible viscosité, tels que les semiconducteurs organiques, alors que des difficultés liées au bouchage des buses d'impression se produisent avec les matériaux de forte viscosité tels que les diélectriques organiques et les encres à base de particules dispersées, telles que les encres métalliques inorganiques [7]. L'encre est déposée sous forme de gouttes et cela peut parfois induire des films minces inhomogènes. Cette technique offre une cadence de production d'environ 100 m^2/h [15]. De plus, l'utilisation simultanée de plusieurs buses peut accroître la productivité.

Le jet d'encre peut être combiné avec d'autres techniques d'impression pour fabriquer des produits électroniques performants peu chers sur de larges substrats; substrats flexibles inclus. L'électronique imprimée peut être employée seule ou combinée avec des

composants microélectroniques conventionnels, tels que des puces en silicium, pour une large gamme d'applications [17].

Les objectifs principaux de ce travail peuvent être décomposés en 3 parties. Premièrement, l'étude du design de base du capteur acoustique capacitif développé par le consortium « Spinnaker » et l'optimisation du résonateur acoustique afin d'atteindre la sensibilité et la sélectivité désirées. Puis, le développement des étapes de fabrication du capteur en utilisant les techniques d'impression. Finalement, la caractérisation du composant et la comparaison avec les résultats de simulation.

En complément au capteur acoustique capacitif, le capteur acoustique piézoélectrique peut être une alternative intéressante car le transducteur piézoélectrique génère directement une tension de sortie induite par le déplacement de la membrane sans l'ajout d'un circuit électronique. De plus, le transducteur piézoélectrique ne nécessite pas d'électrode inférieure ; par conséquent l'effet d'amortissement sera moindre, le déplacement de la membrane plus important et ainsi la sensibilité sera meilleure. Par conséquent, un autre objectif de ce travail de thèse est d'étudier les possibilités de développer un capteur piézoélectrique imprimé. Cependant, il n'existe pas d'encres piézoélectriques commerciales adaptées aux imprimantes à jet d'encre. Par conséquent, le premier challenge de cette partie consiste à développer une encre piézoélectrique imprimable par jet d'encre à base de poly (fluorure de vinylidène - trifluoroéthylène) (PVDF-TrFE). De plus, le développement des briques technologiques du capteur piézoélectrique, telles que le dépôt d'une couche homogène de PVDF-TrFE et le dépôt des électrodes, doit être optimisé avant de pouvoir développer le transducteur.

2. Etat de l'art

Le chapitre 2 présente l'état de l'art des différents types de transducteurs acoustiques. La piézoélectricité, la piézorésistivité et l'effet capacitif sont les techniques de transduction les mieux connues et les plus utilisées [1]. Généralement, les capteurs piézoélectriques et piézorésistifs utilisent la méthode de détection de la déformation, alors que le transducteur capacitif se base sur la détection de la position de la membrane [18].

Dans le cas du transducteur piézoélectrique, un diaphragme mince est fabriqué avec un matériau piézoélectrique ou attaché mécaniquement à un bimorphe, une poutre faite de 2 couches piézoélectriques ayant une polarisation opposée. Le mouvement du diaphragme

induit une contrainte dans le matériau piézoélectrique qui, en réponse, génère une tension électrique [1]. Depuis des années, de nombreux efforts ont été faits pour réaliser des transducteurs piézoélectriques avec différents matériaux piézoélectriques pour réaliser la transduction « mécanique-électrique ». Les premiers composants avaient une faible réponse en fréquence due à la mauvaise maîtrise des contraintes résiduelles dans le diaphragme. Généralement, un capteur piézoélectrique offre 2 avantages principaux : l'absence d'alimentation et une large gamme dynamique [19].

Le transducteur acoustique piézorésistif comprend une membrane avec quatre résistances piézorésistives connectées en pont de Wheatstone. La déflexion de la membrane induit une déformation des piézorésistances qui est fonction de leur position et ainsi, une variation de résistance est observée [1]. De nombreux capteurs de pression et capteurs acoustiques piézorésistifs ont été développés pour diverses applications où le silicium est généralement utilisé comme matériau piézorésistif. Des études ont montré que les premiers composants souffraient d'un haut niveau de bruit. De plus, les capteurs à base de silicium monocristallin présentent une plus grande sensibilité à la température que ceux en silicium polycristallin. Ces composants ont une faible impédance de sortie, ce qui les rend insensibles aux bruits parasites et simplifie la conception de l'amplificateur et du packaging [20].

Le capteur acoustique capacitif détecte, quant à lui, une variation de capacité induite par le changement d'épaisseur de la lame d'air engendré par la déflexion de la membrane [1]. Un transducteur capacitif présente une bonne sensibilité tout en garantissant une très faible consommation. La sensibilité de tels composants se réduit généralement aux hautes fréquences à cause de la résistance au déplacement de l'air dans l'espace étroit entre les deux électrodes [1]. Différentes géométries peuvent être employées pour augmenter la sensibilité en essayant de réduire l'amortissement. Ceci peut être réalisé en utilisant des géométries complexes pour l'électrode inférieure ou la membrane. Une alternative plus simple est de fabriquer un composant avec une membrane beaucoup plus grande que l'électrode inférieure et une grande cavité.

Parmi les différents types de capteurs acoustiques disponibles, le capteur capacitif consomme peu et présente la meilleure sensibilité [21]. De plus, la détection capacitive est insensible aux matériaux utilisés, elle ne dépend que de la variation géométrique de la capacité. Il peut être utilisé comme un composant actif ou passif.

Pour améliorer la localisation spatiale des étiquettes RFID, le développement d'un système hybride, combinant une étiquette RFID existante et un capteur acoustique capacitif sélectif et sensible, est requise. Ainsi, dans le cadre du projet « Spinnaker » et pour respecter la fabrication bas coût du transducteur, les techniques d'impression ont été adaptées pour développer le transducteur capacitif.

Différentes techniques d'impression pour les applications microélectroniques sont aussi discutées dans ce chapitre. Une attention particulière est portée à la méthode du jet d'encre pour sa simplicité de mise en œuvre. Il y a de nombreux facteurs qui influencent le procédé d'impression jet d'encre, comme illustré sur la Figure R.2. Durant ce travail, le système d'impression jet d'encre «goutte à la demande » (DoD : Drop on Demand), Dimatix DMP-2800, avec des cartouches de 10 pL, a été utilisé. Ce système autorise l'impression de différents matériaux sous forme liquide. En fonction du système d'impression, l'encre doit avoir une tension de surface comprise entre 30 et 40 mN/m et une viscosité entre 3 et 20 mPa.s. L'énergie de surface et la rugosité du substrat influence aussi fortement la qualité de l'impression. De plus, des paramètres d'impression tels que la forme d'onde et la tension appliquée à la tête d'impression ainsi que sa température, doivent être optimisées en fonction des propriétés rhéologiques de l'encre.

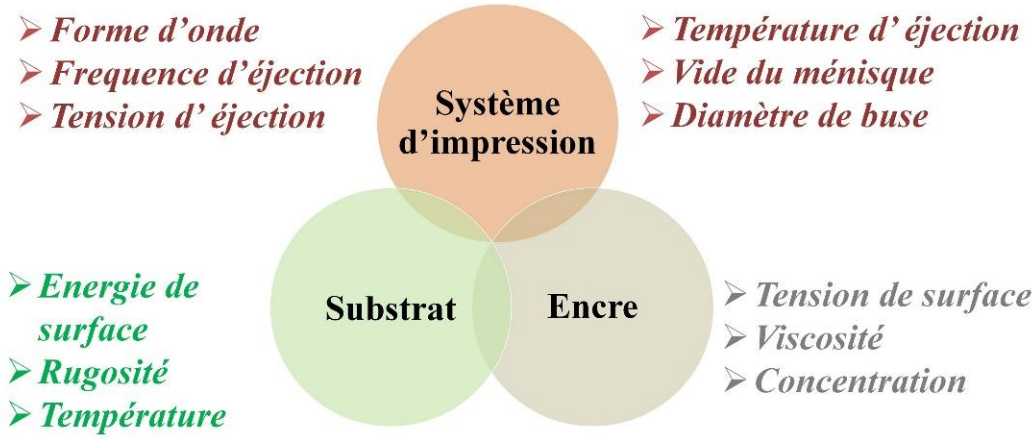

Figure R.2: *Synthèse des facteurs importants influençant le procédé d'impression jet d'encre.*

Généralement, l'impression de la couche est suivie d'étapes de recuit, comme le recuit thermique dans un four conventionnel. Le développement de techniques alternatives, principalement le recuit photonique, facilite l'utilisation de substrats bas coût, comme le papier et d'autres substrats plastiques basse température. La technique du jet d'encre est

utilisée pour réaliser l'interconnexion des circuits [22] ainsi que des composants tels que des capacités, résistances, inductances, transistors en couche mince [23] etc. Cette technique peut aussi être utilisée pour fabriquer des structures MEMS 3D en utilisant un procédé complexe d'oxyde sacrificiel [24], [25].

3. Modélisation et optimisation du capteur acoustique capacitif

Ce chapitre présente le design et l'analyse mathématique simplifiée du capteur acoustique capacitif. La simulation numérique du transducteur acoustique par éléments finis (FEM : Finite Element Method) est discutée ainsi que le plan d'expérience (DOE : Design Of Experiment). Finalement, l'optimisation du dispositif est présentée afin d'obtenir un transducteur avec une bonne sensibilité et sélectivité sur la bande de fréquence expérimentale. Ce type de dispositif est connu sous le nom de « résonateur acoustique capacitif ». L'optimisation du capteur requiert une très bonne connaissance de l'effet de différents facteurs sur les réponses de sortie.

Durant ce travail, le prototypage virtuel du transducteur acoustique, basé sur la Figure R.1, est développé à l'aide du logiciel « multiphysique » COMSOL. Les effets des différents paramètres sur les réponses de sortie du dispositif, telles que le déplacement de la membrane, le facteur de qualité, la variation de la capacité et la tension de sortie, ont été étudiés à l'aide de plans d'expérience. Six paramètres du dispositif ont été considérés : le rayon de la membrane (R_m), le rayon de l'électrode inférieure (R_b), la hauteur de la cavité (h_c), l'espace d'air entre les électrodes (h_g), la tension de la membrane (T_m) et son épaisseur (t_m). En se basant sur les résultats des simulations numériques, la méthode de la « surface de réponse » est ensuite utilisée pour identifier les facteurs significatifs et développer le modèle empirique pour chaque réponse de sortie. Ce modèle est bien moins complexe que le modèle numérique, par conséquent, l'utilisation de plans d'expérience réduit significativement les efforts de calcul durant le processus d'optimisation du capteur. Une série de 62 expériences a été menée par éléments finis pour déterminer les réponses de sortie pour différentes combinaisons des paramètres du dispositif. L'étude confirme que de nombreux termes linéaires, quadratiques et d'interaction influencent le déplacement maximal de la membrane à la résonance fondamentale ($|\langle \xi_{Se} \rangle|_{fr1}$) et le facteur de qualité (Q_f).

Puisque le processus requiert l'optimisation simultanée de plusieurs réponses de sortie du transducteur acoustique, des fonctions de "désirabilité » multicritère ont été employées. Dans cette étude, l'optimisation est réalisée pour obtenir un capteur acoustique résonant pour lequel la valeur du facteur de qualité (Q_f) et la variation de capacité (ΔC) doivent être maximisées et supérieures à 25 et 1 fF respectivement, alors que la valeur de la capacité statique (C_0) doit être comprise entre 0.5 pF et 3.2 pF. Le déplacement de la membrane à la seconde résonance ($|\langle \xi_{Se} \rangle|_{fr2}$) doit être minimisé et inférieur à 3 nm pour garantir une meilleure sélectivité. Les Figures R.3(a) à R.3(d) représentent les fonctions de désirabilité.

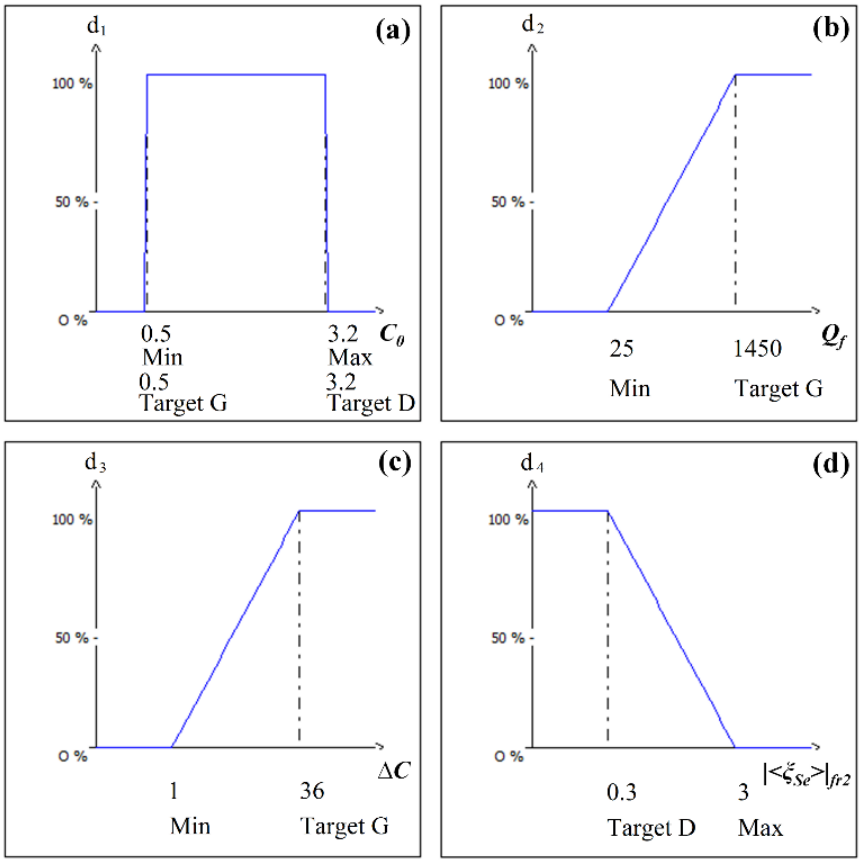

Figure R.3: *Fonctions de désirabilité multicritère pour l'optimisation du capteur acoustique résonant ((a)* $0.5 \leq C_0 \leq 3.2\, pF$*; (b)* $Q_f \geq 25$*; (c)* $\Delta C \geq 1 fF$*; (d)* $|\langle \xi_{Se} \rangle|_{fr2} \leq 3nm$*).*

La solution obtenue par l'optimisation multicritère est représentée par la réponse de surface de la fonction de désirabilité globale selon différents plans sur les Figures R.4(a) à R.4(e), où les zones blanches représentent les zones qui satisfont tous les critères. La valeur optimale des paramètres est déterminée (Table R.1**)** et la désirabilité globale calculée.

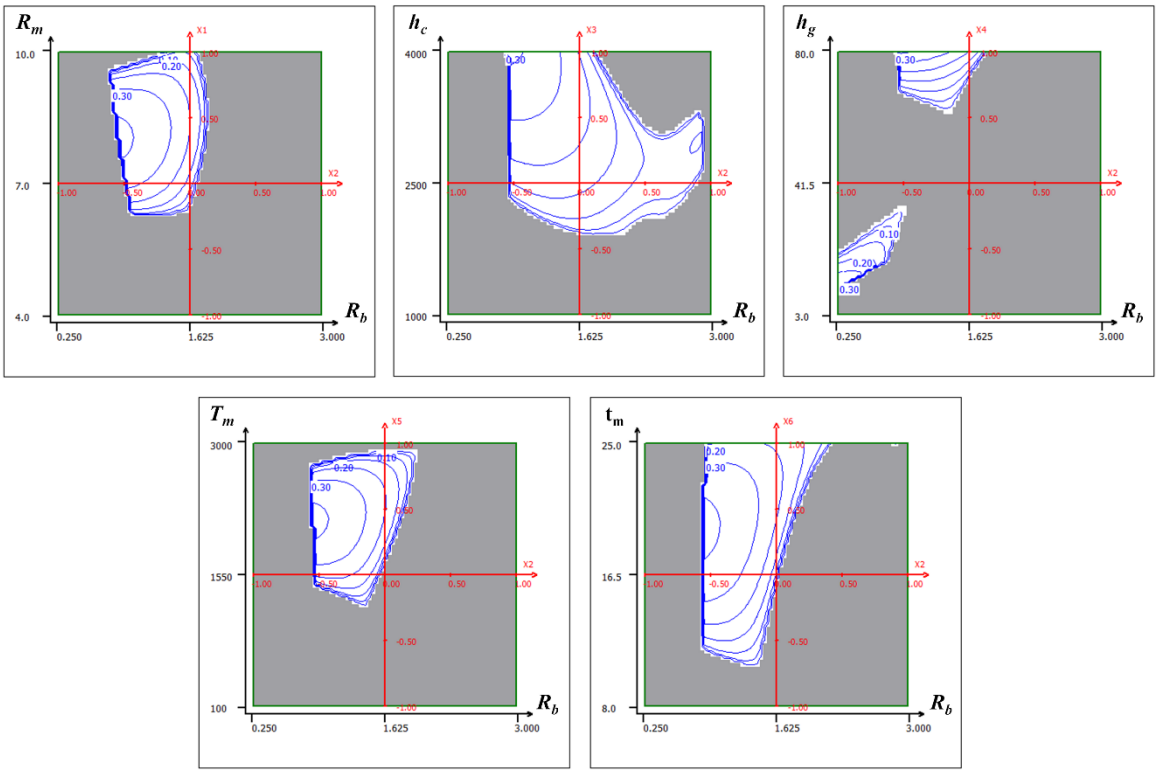

Figure R.4: *Réponse de surface de la fonction de désirabilité globale selon différents plans.*

Table R.1: *Valeur optimale des paramètres obtenue par optimisation multicritère de la fonction de désirabilité*

Facteur	Valeur
Rayon de la membrane (R_m)	8.1 mm
Rayon de l'électrode inférieure (R_b)	0.871 mm
Hauteur de la cavité (h_c)	3987 µm
Lame d'air (h_g)	80.0 µm
Tension de la membrane (T_m)	2158 N/m
Epaisseur de la membrane (t_m)	19.8 µm

Ensuite, une simulation numérique a été réalisée afin de vérifier les réponses du capteur acoustique avec ce jeu de paramètres optimaux. La Figure R.5 représente le déplacement maximal de la membrane du capteur acoustique résonant en fonction de la fréquence. Les résultats de la simulation montrent que les paramètres optimaux permettent d'obtenir un capteur acoustique résonant présentant les caractéristiques suivantes : une capacité statique égale à 0.50 pF, une variation de capacité de 2.6 fF, un facteur de qualité de 522, un rapport ΔC/C de 0.5% et une tension de sortie de 20 mV à la résonance fondamentale, lorsque le

capteur est soumis à une pression acoustique incidente de 80 dB_{SPL}. Ainsi la combinaison optimale des paramètres satisfait la réponse de sortie désirée pour le résonateur acoustique.

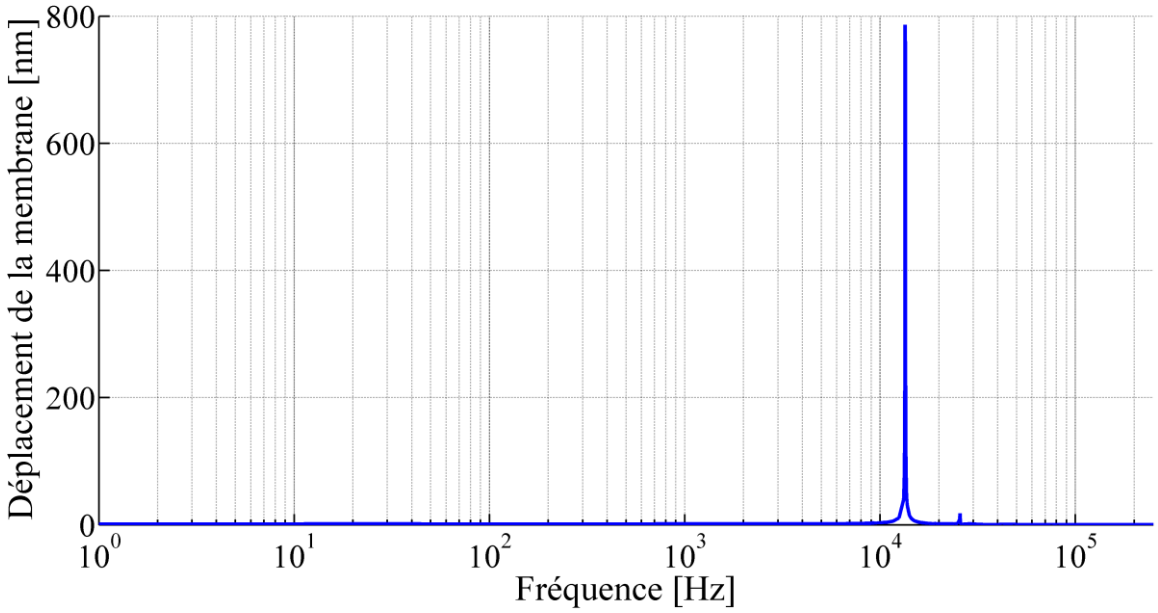

Figure R.5: *Déplacement maximal de la membrane du capteur acoustique résonant avec le jeu de paramètres optimaux (Simulation numérique).*

4. Fabrication et caractérisation du capteur

Dans ce chapitre, le développement d'un résonateur acoustique capacitif par l'utilisation combinée des techniques d'impression 2D et 3D est discutée en détails. La structure basse, avec une électrode arrière rigide et une cavité, est fabriquée directement par impression 3D. Ensuite, l'impression 2D par jet d'encre est employée pour imprimer l'électrode conductrice en argent. Une nouvelle approche est aussi mise en œuvre pour fabriquer le diaphragme du capteur acoustique, où la couche conductrice est imprimée directement, par jet d'encre, sur un film mince organique prétendu. Les étapes du procédé, ainsi que la caractérisation de chaque brique technologique sont aussi présentées précisément.

Durant ce travail, la partie inférieure du transducteur acoustique est structurée sans aucune étape de gravure en utilisant l'impression 3D « polyjet ». Une couche conductrice est ensuite imprimée sur l'électrode arrière à l'aide de la technique d'impression directe 2D. La surface de la structure 3D peut éventuellement nécessiter un polissage pour réduire sa rugosité avant d'imprimer la couche conductrice. Enfin, la couche d'argent imprimée est recuite pour atteindre une conductivité satisfaisante. Généralement, les matériaux 3D

imprimés présentent des faibles températures de déformation. Par conséquent, pour éviter toute dégradation de la structure 3D, un recuit photonique a été effectué pour réaliser la coalescence des nanoparticules d'argent imprimées sur la structure 3D. Le diaphragme du transducteur capacitif est réalisé par impression par jet d'encre d'une couche conductrice sur un film mince organique prétendu. Durant cette étape de fabrication, des films minces organiques d'épaisseur inférieure à 25 µm, tels que le Mylar, le polyéthylene napthalate (PEN) et le polyimide (PI) ont été utilisés. Initialement le film mince est monté sur un support spécifiquement conçu à cet effet et une tension réglable est appliquée. Une couche conductrice est ensuite imprimée sur le film prétendu et recuite. Lorsque la structure inférieure et le diaphragme sont réalisés, ils sont ensuite assemblés après avoir inséré un espaceur afin de séparer la membrane de l'électrode inférieure. La Figure R.6 illustre le déroulement du procédé de fabrication du transducteur acoustique imprimé et la Figure R.7 représente une image de ce dernier.

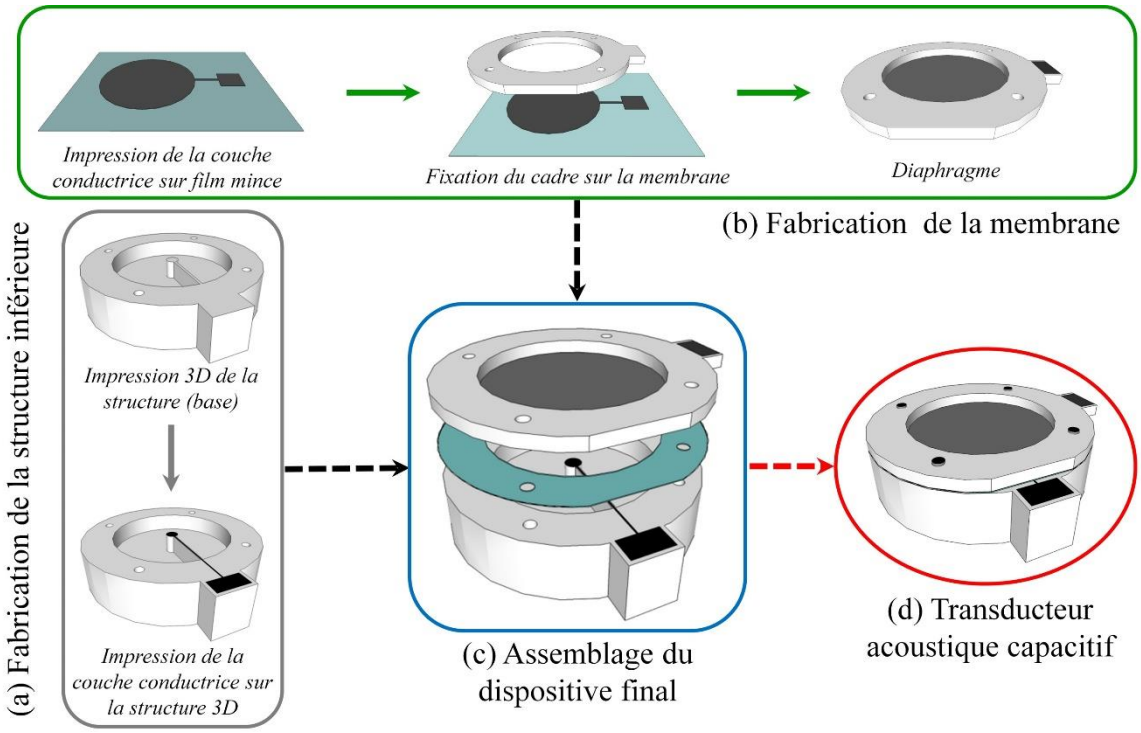

Figure R.6: *Etapes de fabrication du capteur acoustique combinant l'impression jet d'encre et l'impression 3D.*

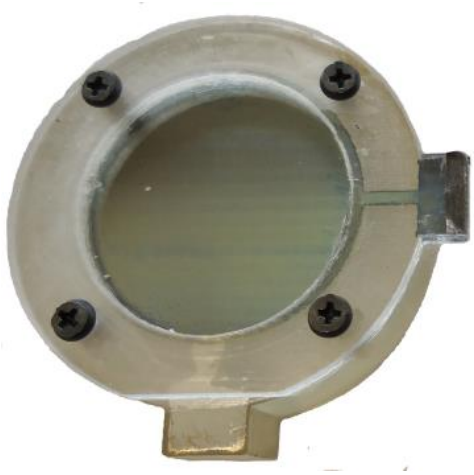

Figure R.7: *Transducteur acoustique capacitif imprimé.*

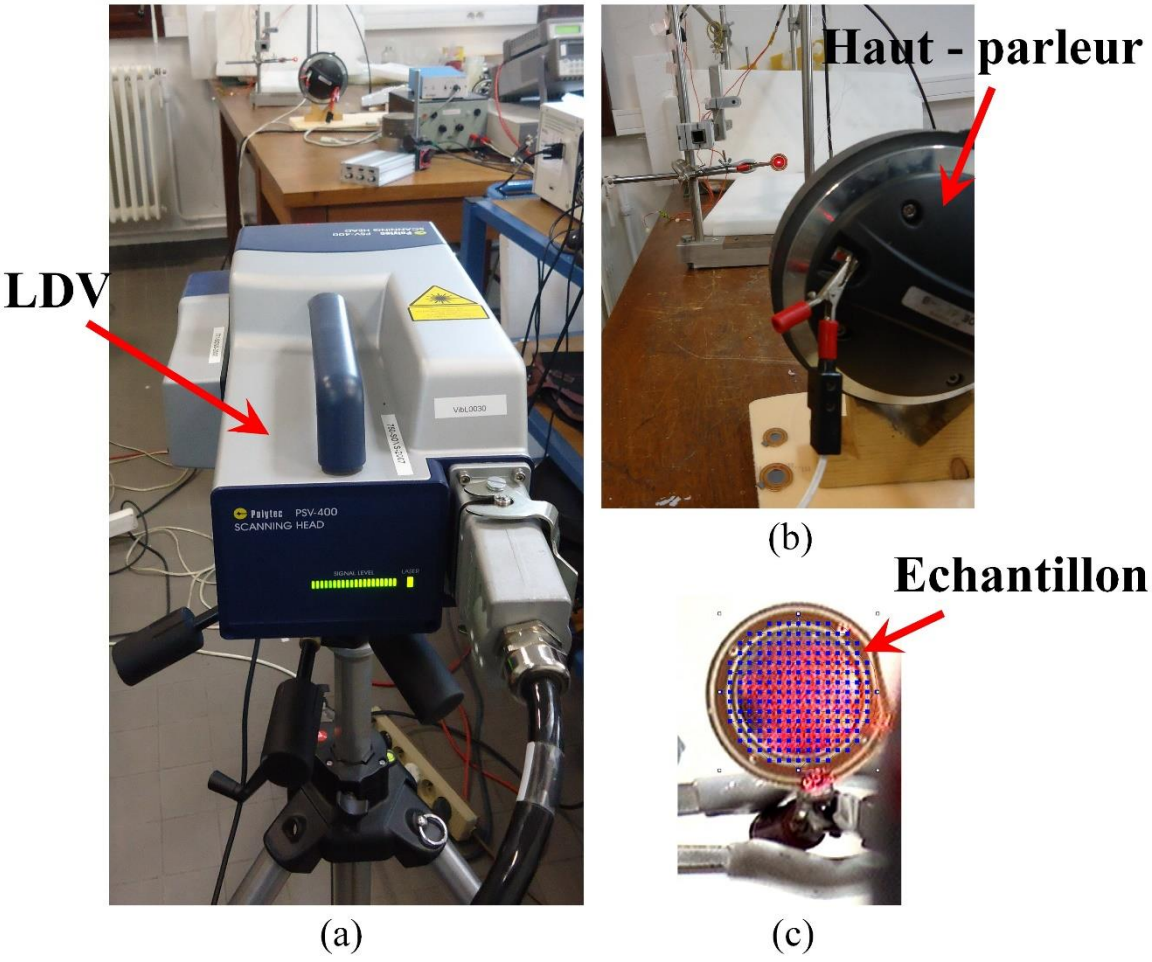

Figure R.8: *Montage expérimental pour la mesure dynamique de la membrane et du transducteur en utilisant la vibromètrie laser LDV (a) montage complet, (b) vue rapprochée, et (c) sélection de points durant la mesure LDV en mode balayage.*

Les mesures d'impédance réalisées à l'aide d'un spectromètre d'impédance (modèle 4284A - Precision LCR Meter - Agilent) confirment que les transducteurs fabriqués se comportent comme des condensateurs. Ensuite, la caractérisation dynamique du transducteur, en mode « ponctuel » ou en mode « balayage », a été faite en utilisant un vibromètre laser à effet Doppler (LDV : laser Doppler vibrometer), comme montré sur la Figure R.8. Les mesures montrent que le transducteur fabriqué se comporte comme une « pure capacité » en mode statique et présente une haute sensibilité et sélectivité à sa fréquence fondamentale de résonance. Les résultats expérimentaux ont été comparés à ceux obtenus par simulation numérique. La corrélation est très bonne comme illustrée sur la Figure R.9. Par conséquent, on peut en conclure que le transducteur capacitif imprimé se comporte comme un résonateur acoustique avec un facteur de qualité relativement élevé. Toutefois, assez souvent la valeur expérimentale du facteur de qualité est sensiblement inférieure à la valeur simulée.

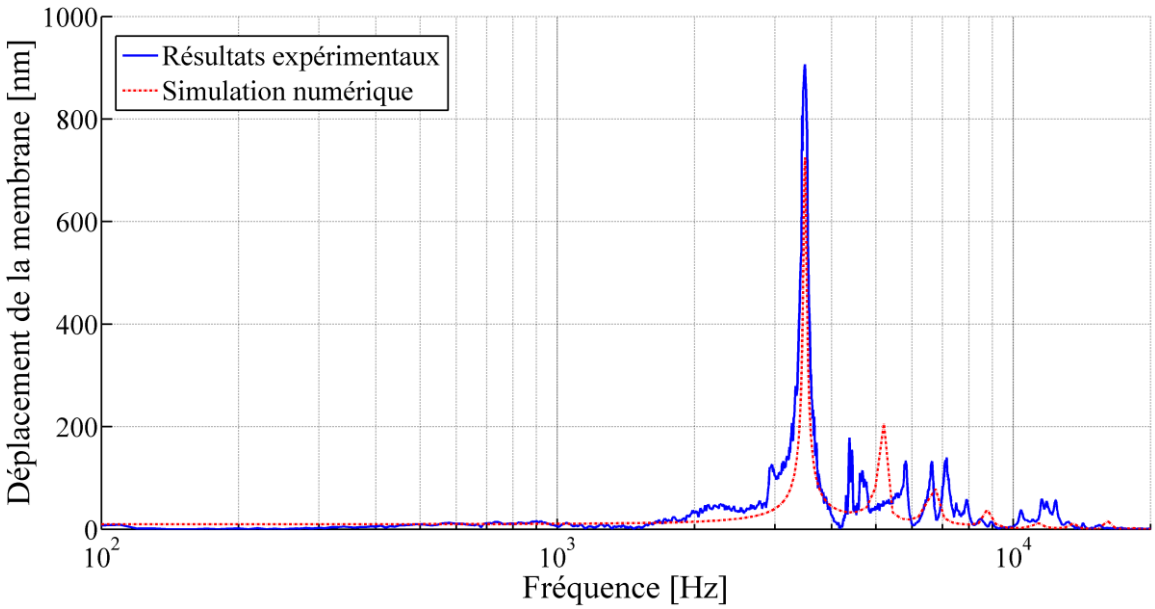

Figure R.9: *Réponse en fréquence du transducteur acoustique imprimé (rayon de la membrane: 8.1 mm, rayon de l'électrode inférieure: 871 µm, hauteur de la cavité: 4 mm, espace inter-électrodes: 68 µm, épaisseur de la membrane:23 µm et tension de la membrane:48 N/m).*

La fabrication de ces dispositifs ayant été faite manuellement, il existe certains problèmes associés aux étapes de fabrication. Occasionnellement, des non-linéarités de la tension de la membrane ainsi que des déformations de cette dernière ont été observées. Elles proviennent de la variabilité du serrage des vis utilisées lors de l'assemblage. De plus, nous

n'avons pas trouvé de colle parfaitement adaptée à la fixation du film prétendu de Mylar sur le cadre de la membrane ; ce qui entraîne des problèmes de stabilité de la tension de la membrane dans le temps.

5. Formulation de l'encre et impression jet d'encre du PVDF-TrFE

Dans ce chapitre, la formulation d'une encre à base du copolymère « polyfluorure de vinylidène – trifluoroéthylène » (PVDF-TrFE) pour les systèmes d'impression jet d'encre « goutte à la demande » est discutée. Ensuite des films de PVDF-TrFE ont été développés et caractérisés afin d'étudier leur morphologie, cristallinité et propriétés piézoélectriques.

Durant ce travail, le copolymère PVDF-TrFE (70/30) avec un poids molaire de 500 Kg/mole a été utilisé. Le développement d'une encre imprimable stable avec une concentration significative de copolymère pour système à impression jet d'encre est principalement influencé par la viscosité du solvant utilisé. Généralement, la viscosité de l'encre augmente avec l'ajout de polymère. Ceci peut être résolu en préparant des mélanges avec un solvant de faible viscosité et de la cétone d'éthyle de méthyle (MEK). Parmi les différents tests réalisés, le mélange de la cétone d'éthyle de méthyle (MEK) et de diméthyl sulfoxyde (DMSO) produit les meilleurs résultats. Le mélange particulier de ces 2 solvants permet de développer une encre imprimable stable avec une concentration de PVDF-TrFE égale à 0.8% en poids.

L'impression continue et stable requiert l'utilisation d'une fréquence d'éjection inférieure ou égale à 2 kHz. La forme d'onde appliquée à la tête d'impression a dû être modifiée pour prendre en compte les propriétés rhéologiques de l'encre. Il a fallu modifier la durée de chaque segment, les temps de montée et de descente ainsi que les tensions appliquées. Des couches de PVDF-TrFE ont ensuite été imprimées. Elles ont été séchées à température ambiante durant plusieurs heures, puis à 90 °C durant 15 minutes pour garantir l'évaporation totale des solvants. Par la suite, les échantillons ont été recuits entre la température de Curie et la température de fusion du PVDF-TrFE, puis caractérisés pour comprendre leur morphologie, cristallinité et propriétés électriques. Il a été observé que la taille des grains décroît avec l'accroissement de la durée du recuit à une température proche de la température de fusion. La rugosité de surface diminue aussi pour des temps de recuit plus longs. L'analyse cristalline montre que la proportion de phase β diminue lorsque le temps et la température de recuit augmentent.

Afin de pouvoir réaliser des caractérisations électriques, des condensateurs ont été réalisés en imprimant l'électrode inférieure avec une encre à base nanoparticules d'argent et en déposant de l'aluminium en phase vapeur pour l'électrode supérieure. La polarisation de la couche de PVDF-TrFE est faite avant de mesurer le coefficient piézoélectrique ($d_{33,f}$). La Figure R.10 montre le dispositif expérimental utilisé pour mesurer ce coefficient. Le déplacement (u_3) de la couche, sous l'effet d'un champ électrique sinusoïdal à la fréquence de 150 kHz, est mesuré par vibromètrie laser (Polytec OFV-3001 laser Doppler vibrometer). La valeur du coefficient piézoélectrique ($d_{33,f}$) obtenue s'élève à 2 pm/V; ce qui environ 10 fois plus faible que la valeur attendue. Ceci s'explique peut-être par la réaction de surface entre l'aluminium et le PVDF-TrFE.

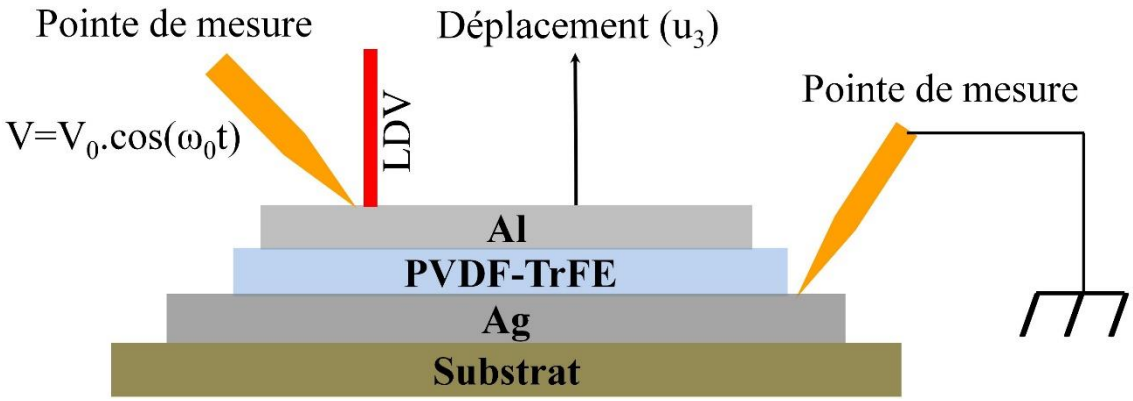

Figure R.10: *Dispositif expérimental utilisé pour la mesure du coefficient piézoélectrique ($d_{33,f}$). V_0 représente l'amplitude maximale de la tension et ω_0, la fréquence angulaire.*

Ces premiers résultats sont encourageants. Toutefois, d'autres améliorations de l'encre et du procédé d'impression sont nécessaires avant d'entreprendre le développement et la fabrication du transducteur piézoélectrique. Les travaux futurs vont se focaliser sur l'augmentation de la concentration du polymère dans l'encre, l'amélioration de la qualité de l'électrode supérieure pour obtenir de meilleures propriétés piézoélectriques et enfin le développement de dispositifs innovants à base de cette encre piézoélectrique.

6. Conclusions et perspectives

A. Résumé

Des capteurs acoustiques, qui fournissent un signal de sortie en réponse à une variation de pression appliquée sur une membrane flexible, ont été utilisés dans de nombreuses applications civiles et militaires [2]–[4]. Parmi les différents types de capteur acoustique, ce travail s'est focalisé sur le transducteur acoustique capacitif. Depuis des années, de nombreux capteurs acoustiques capacitifs ont été conçus et développés, principalement pour des applications audio, avec une sensibilité constante sur une large bande de fréquence. Afin de développer des systèmes RFID (radio frequency identification) avec une meilleure géolocalisation, TAGSYS RFID envisage d'intégrer un résonateur acoustique capacitif au système RFID. Dans ce contexte, un nouveau design de transducteur acoustique capacitif a été proposé par le consortium « Spinnaker ». Ce travail a été entrepris pour explorer les possibilités de concevoir et développer un nouveau transducteur acoustique capacitif avec une bonne sensibilité et sélectivité en utilisant des techniques de fabrication telles que l'impression.

Dans le cadre de cette thèse, nous avons démontré que le design du capteur acoustique capacitif, proposé par le consortium "Spinnaker", pouvait être utilisé pour fabriquer un résonateur acoustique capacitif avec les spécifications requises. Le design de base du transducteur a été étudié et optimisé en utilisant la simulation numérique par éléments finis et des plans d'expérience. L'optimisation multicritère permet d'obtenir un transducteur ayant les spécifications suivantes : une capacité statique égale à 0.50 pF, une variation de capacité de 2.6 fF, un facteur de qualité de 522, un rapport $\Delta C/C$ de 0.5% et une tension de sortie de 20 mV à la résonance fondamentale, lorsque le capteur est soumis à une pression acoustique incidente de 80 dB_{SPL}.

Une nouvelle approche a été proposée et développée afin de pouvoir réaliser ce transducteur en utilisant les techniques d'impression. Durant cette thèse, la technique émergente d'impression 3D a été utilisée conjointement avec la technique d'impression jet d'encre 2D. Plusieurs challenges, tels que l'impression sur un substrat 3D imprimé ainsi que l'impression sur un film organique prétendu d'épaisseur inférieure à 25 microns, ont été relevés. L'optimisation des procédés a permis de fabriquer des transducteurs fonctionnels. La caractérisation électrique de ces dispositifs montre que les transducteurs fabriqués se

comportent comme une capacité idéale dans le mode statique. La caractérisation dynamique, à l'aide de la vibromètrie laser à effet Doppler, montre que le capteur présente une haute sensibilité et sélectivité à sa fréquence de résonance fondamentale. Les résultats expérimentaux ont été comparés avec succès à ceux obtenus par simulation numérique.

L'absence d'encre piézoélectrique imprimable par jet de matière nous a incités à développer une encre imprimable à base du copolymère « polyfluorure de vinylidène – trifluoroéthylène » (PVDF-TrFE) car nous pensons que le transducteur acoustique piézoélectrique pourrait être une alternative intéressante. Dans le délai imparti, une encre imprimable stable, à base de PVDF-TrFE, a été développée. Bien que les résultats soient particulièrement encourageants, des améliorations complémentaires sont nécessaires pour pouvoir fabriquer des dispositifs avec cette encre.

B. Perspectives

Ce travail a été initié par TAGSYS RFID, une entreprise française, pour développer un résonateur acoustique en utilisant la technologie d'impression. Il a permis la collaboration étroite entre la recherche industrielle et académique. Cette étude a montré des résultats encourageants ; toutefois des améliorations complémentaires du dispositif sont souhaitables pour accroître la performance du transducteur acoustique capacitif. Le collage de la membrane sur son cadre et l'assemblage par un contrôle précis du serrage des vis sont 2 possibilités. Il serait même intéressant de développer une technique d'assemblage sans vis afin de réduire la complexité.

L'optimisation du transducteur acoustique a été réalisée en utilisant conjointement la simulation numérique et la méthode des plans d'expérience. Les différentes réponses de sortie ont été optimisées simultanément pour atteindre une optimisation globale du transducteur, conformément aux spécifications requises. Une approche similaire pourrait être mise en œuvre pour optimiser d'autres types de capteur.

Durant cette thèse, une partie du transducteur acoustique a été fabriqué par impression jet d'encre d'une couche conductrice d'argent sur un substrat 3D imprimé. Cette nouvelle brique technologique pourrait être mise à profit pour développer de nouveaux composants et dispositifs électroniques 3D innovants.

Par ailleurs, au-delà de son intégration au sein des systèmes RFID pour améliorer la localisation des étiquettes, ce résonateur acoustique pourrait être utilisé pour d'autres applications intéressantes, telles que l'aide à la navigation des drones, les systèmes autonomes ou des développements biomimétiques basés sur l'instinct animal [26]. Des études ont montré que les insectes, comme le criquet, peuvent naviguer dans des environnements complexes en utilisant des sources sonores. Le même principe peut être exploité pour fabriquer des micro-objets volants autonomes [26]. Puisque le résonateur acoustique, développé durant ce travail de thèse, présente une bonne sensibilité et sélectivité sans l'ajout de filtres électroniques, il est le candidat idéal pour de telles applications biomimétiques ; la fréquence de résonance pouvant être ajustée par la tension de la membrane.

Enfin, la nouvelle encre piézoélectrique développée à base de PVDF-TrFE pourrait être utilisée pour développer des transducteurs acoustiques, ainsi que bien d'autres applications telles que des capteurs de pression, récupérateurs d'énergie … Toutefois d'autres expériences sont encore à mener pour améliorer le dépôt de l'électrode supérieure sur la couche de polymère. Le futur travail sera focalisé sur l'augmentation de la concentration en polymère de l'encre, l'optimisation du procédé de recuit et l'amélioration de la qualité de l'électrode supérieure en utilisant un polymère conducteur comme le poly (3,4-éthylènedioxythiophène) sulfonate de polystyrène (PEDOT:PSS) ou l'or.

Références

[1] P.R. Scheeper, A.G.H. van der Donk, W. Olthuis, and P. Bergveld, "A Review of Silicon Microphones," *Sensors and Actuators A: Physical*, vol. 44, pp. 1–11, 1994.

[2] D. T. Martin, "Design, Fabrication, and Characterization of a MEMS Dual-backplate Capacitive Microphone," Doctoral Thesis, University of Florida, Gainesville, FL, USA, 2007.

[3] Dimitrios Chatzopoulos, "Modeling the Performance of MEMS Based Directional Microphones," Master's Thesis, Naval Postgraduate School, Monterey, CA, USA, 2008.

[4] B. Kaushik, D. Nance, and K. K. Ahuja, "A Review of the Role of Acoustic Sensors in the Modern Battlefield," in *11th AIAA/CEAS Aeroacoustics Conference*, Monterey, CA, USA, 2005, p. AIAA 2005–2997.

[5] Alexander Kamyshny, Joachim Steinke, and Shlomo Magdassi, "Metal-based Inkjet Inks for Printed Electronics," *Open Applied Physics Journal*, vol. 4, pp. 19–36, 2011.

[6] W. T. Wondmagegn, N. T. Satyala, H. J. Stiegler, M. A. Quevedo-Lopez, E. W. Forsythe, R. J. Pieper, and B. E. Gnade, "Simulation Based Performance Comparison of Transistors Designed Using Standard Photolithographic and Coarse Printing Design Specifications," *Thin Solid Films*, vol. 519, no. 6, pp. 1943–1949, 2011.

[7] Matthias Nagel and Thomas Lippert, "Laser-Induced Forward Transfer for the Fabrication of Devices," in *Nanomaterials: Processing and Characterization with Lasers*, S. C. Singh, H. B. Zeng, C. Guo, and W. P. Cai, Eds. Weinheim, Germany: Wiley-VCH, 2012, pp. 255–306.

[8] K.K.B. Hon, L. Li, and I.M. Hutchings, "Direct Writing Technology-Advances and Developments," *CIRP Annals - Manufacturing Technology*, vol. 57, no. 2, pp. 601–620, 2008.

[9] Romain Cauchois, "Microstructuring Inkjet-Printed Deposits: from Silver Nanoparticles Coalescence to the Fabrication of Interconnections for Electronic Devices," École Nationale Supérieure des Mines de Saint-Étienne, Gardanne, 2012.

[10] J. Perelaer, B.-J. de Gans, and U. Schubert, "Ink-jet printing and microwave sintering of conductive silver tracks," *Advanced Materials*, vol. 18, no. 16, pp. 2101–2104, 2006.

[11] M.L. Allen, M. Aronniemi, T. Mattila, A. Alastalo, K. Ojanperä, M. Suhonen, and H. Seppä, "Electrical Sintering of Nanoparticle Structures," *Nanotechnology*, vol. 19, no. 17, p. 175201, 2008.

[12] S. H. Ko, H. Pan, C. P. Grigoropoulos, C. K. Luscombe, J. M. J. Fréchet, and D. Poulikakos, "All-Inkjet-Printed Flexible Electronics Fabrication on a Polymer Substrate by Low-Temperature High-Resolution Selective Laser Sintering of Metal Nanoparticles," *Nanotechnology*, vol. 18, no. 34, p. 345202, 2007.

[13] K. A. Schroder, "Mechanisms of Photonic Curing^{TM}: Processing High Temperature Films on Low Temperature Substrates," in *Nanotech*, vol. 2, CRC Press, 2011, pp. 220–223.

[14] K. A. Schroder, S. C. McCool, and W. F. Furlan, “Broadcast Photonic Curing of Metallic Nanoparticle Films,” *NSTI-Nanotech*, vol. 3, pp. 1–4, 2006.

[15] Ahmed Busnaina, “Nanomaterials-based Manufacturing Platform for Printed Sensors, Electronics, Energy and Material Applications,” presented at the The Tenth U.S.-Korea Forum on Nanotechnology: A New Generation of Nano-technological Products & Processes, Boston, USA, 2013.

[16] K. Pataky, V. Auzelyte, and J. Brugger, “Inkjet Printing for MEMS,” in *Inkjet-Based Micromanufacturing*, Jan G. Korvink, Patrick J. Smith, and Dong-Youn Shin, Eds. Weinheim, Germany: WILEY-VCH Verlag GmbH & Co. KGaA, 2012, pp. 331–345.

[17] Y. Li, D. Lu, and C. P. Wong, *Electrical Conductive Adhesives with Nanotechnologies*. New York, NY, USA: Springer, 2009.

[18] Bin Liu, “Transducers for Sound and Vibration - The Finite Element Method Based Design,” Ph. D. dissertation, Technical University of Denmark, Denmark, 2001.

[19] Ronald G. Polcawich, “A Piezoelectric MEMS Microphone Based on Lead Zirconate Titanate (PZT) Thin Films,” U.S. Army Research Laboratory, ARL-TR-3387, 2004.

[20] Gang Li, Yitshak Zohar, and Man Wong, “Piezoresistive Pressure Sensor Using Metal-Induced Laterally Crystallized Polycrystalline Silicon,” in *International Conference on Electrical Engineering (ICEE)*, Sapporo, Japan, 2004.

[21] P.-C. Hsu, C. H. Mastrangelo, and K. D. Wise, “A High Sensitivity Polysilicon Diaphragm Condenser Microphone,” in *The 11th Annual International Workshop on Micro Electro Mechanical Systems Proceeding*, Heidelberg, Germany, 1998, pp. 580–585.

[22] Jolke Perelaer, “Postprinting Processes for Inorganic Ink for Plastic Electronics Applications,” in *Inkjet-Based Micromanufacturing*, Jan G. Korvink, Patrick J. Smith, and Dong-Youn Shin, Eds. Weinheim, Germany: WILEY-VCH Verlag GmbH & Co. KGaA, 2012, pp. 111–125.

[23] Byung Ju Kang, Chang Kyu Lee, and Je Hoon Oh, “All-Inkjet-Printed Electrical Components and Circuit Fabrication on a Plastic Substrate,” *Microelectronic Engineering*, vol. 97, pp. 251–254, Sep. 2012.

[24] Sawyer B. Fuller, Eric J. Wilhelm, and Joseph M. Jacobson, “Ink-Jet Printed Nanoparticle Microelectromechanical Systems,” *Journal of Microelectromechanical Systems*, vol. 11, no. 1, pp. 54–60, 2002.

[25] Robert Horning, Thomas Ohnstein, and Daniel Youngner, “Method for Making Devices using Ink Jet Printing,” US7112463 B2, Sep-2006.

[26] Franck Ruffier, Simon Benacchio, Fabien Expert, and Erick Ogam, “A Tiny Directional Sound Sensor Inspired by Crickets Designed for Micro-Air Vehicles,” in *IEEE Sensors*, Limerick, Ireland, 2011, pp. 970–973.

École Nationale Supérieure des Mines
de Saint-Étienne

NNT : *2015 EMSE 0794*

Rubaiyet Iftekharul HAQUE

DESIGN AND DEVELOPMENT OF PRINTED ACOUSTIC SENSOR

Speciality : Microelectronics

Keywords : Acoustic sensor, resonator, numerical simulation, design of experiment, printed electronics, 3D printing, piezoelectric polymer.

Abstract :

The objective of this work was to design and fabricate a low cost resonant capacitive acoustic sensor using printing techniques. It falls within the frame of a collaborative research project named “Spinnaker”, set up by TAGSYS RFID, a French company, which has planned to integrate this sensor to improve the geolocalization of their RFID tags. This work started with the design and optimization of the sensor using finite element modeling (COMSOL) and design of experiments (DOE). This first step has enabled the identification of the optimum set of parameters and demonstrated that the output responses were in accordance with the specifications. Then, we have developed the different technological building blocks required for the fabrication of the prototypes using jointly the 2D inkjet printing technique and 3D printing method. The functionality of the sensors has been characterized using both capacitive and acoustic measurements using laser Doppler vibrometer. Experimental results showed that sensitivity and selectivity were within the specifications and in good agreement with the modeling results. Finally, we investigated the piezoelectric approach which could be an interesting option to the capacitive one. Since no inkjet printable piezoelectric ink is commercially available, stable inkjet printable polyvinylidene fluoride-trifluoroethylene (PVDF-TrFE) ink has been developed. PVDF-TrFE layers were then successfully printed and characterized. The results were quite promising, however further improvements of the ink and printing process are required before stepping towards piezoelectric based device fabrication.

École Nationale Supérieure des Mines
de Saint-Étienne

NNT : *2015 EMSE 0794*

Rubaiyet Iftekharul HAQUE

DESIGN ET DÉVELOPPEMENT D'UN CAPTEUR ACOUSTIQUE IMPRIMÉ

Spécialité: Microélectronique

Mots clefs : Capteur acoustique, résonateur, simulation numérique, plan d'expériences, électronique imprimée, impression 3D, polymère piézoélectrique

Résumé :

L'objectif de ce travail était de concevoir et réaliser par impression un capteur acoustique capacitif résonant bas coût. Il s'inscrit dans le cadre d'un projet collaboratif de recherche intitulé « Spinnaker », défini par la société Tagsys RFID qui souhaite intégrer ce capteur afin d'améliorer la géolocalisation des étiquettes RFID. Ce travail a débuté par la conception et l'optimisation du design en utilisant la simulation par éléments finis (COMSOL) ainsi que des plans d'expériences (DOE : Design of Experiment). Cette première étape a permis de déterminer les paramètres optimaux et démontrer que les performances obtenues étaient conformes aux spécifications. Nous avons ensuite développé les différentes briques technologiques nécessaires à la réalisation des prototypes en utilisant conjointement l'impression 2D par inkjet et l'impression 3D. Nous avons vérifié la fonctionnalité de ces capteurs à l'aide de mesures électriques capacitives et acoustiques par vibrométrie laser. Nous avons démontré la sélectivité en fréquence des capteurs réalisés et comparé les résultats expérimentaux à ceux obtenus par simulation. Enfin, nous avons enfin exploré la « voie piezoélectrique » qui nous semble être une alternative intéressante au principe capacitif. En l'absence d'encre piézoélectrique commerciale imprimable par jet de matière, nous avons formulé une encre imprimable à base du co-polymère PVDF-TrFE et démontré le caractère piézoélectrique des couches imprimées. Les résultats sont prometteurs mais des améliorations doivent encore être apportées à cette encre et au procédé d'impression avant de pouvoir fabriquer des premiers prototypes.